



University of Kentucky
UKnowledge

Theses and Dissertations--Mechanical
Engineering

Mechanical Engineering


2019

ENHANCED SURFACE INTEGRITY WITH THERMALLY STABLE RESIDUAL STRESS FIELDS AND NANOSTRUCTURES IN CRYOGENIC PROCESSING OF TITANIUM ALLOY TI-6AL-4V

James R. Caudill

University of Kentucky, jrcaud2@g.uky.edu

Author ORCID Identifier:

 <https://orcid.org/0000-0002-7185-4594>

Digital Object Identifier: <https://doi.org/10.13023/etd.2019.127>

[Right click to open a feedback form in a new tab to let us know how this document benefits you.](#)

Recommended Citation

Caudill, James R., "ENHANCED SURFACE INTEGRITY WITH THERMALLY STABLE RESIDUAL STRESS FIELDS AND NANOSTRUCTURES IN CRYOGENIC PROCESSING OF TITANIUM ALLOY TI-6AL-4V" (2019). *Theses and Dissertations--Mechanical Engineering*. 134.
https://uknowledge.uky.edu/me_etds/134

This Doctoral Dissertation is brought to you for free and open access by the Mechanical Engineering at UKnowledge. It has been accepted for inclusion in Theses and Dissertations--Mechanical Engineering by an authorized administrator of UKnowledge. For more information, please contact UKnowledge@lsv.uky.edu.

STUDENT AGREEMENT:

I represent that my thesis or dissertation and abstract are my original work. Proper attribution has been given to all outside sources. I understand that I am solely responsible for obtaining any needed copyright permissions. I have obtained needed written permission statement(s) from the owner(s) of each third-party copyrighted matter to be included in my work, allowing electronic distribution (if such use is not permitted by the fair use doctrine) which will be submitted to UKnowledge as Additional File.

I hereby grant to The University of Kentucky and its agents the irrevocable, non-exclusive, and royalty-free license to archive and make accessible my work in whole or in part in all forms of media, now or hereafter known. I agree that the document mentioned above may be made available immediately for worldwide access unless an embargo applies.

I retain all other ownership rights to the copyright of my work. I also retain the right to use in future works (such as articles or books) all or part of my work. I understand that I am free to register the copyright to my work.

REVIEW, APPROVAL AND ACCEPTANCE

The document mentioned above has been reviewed and accepted by the student's advisor, on behalf of the advisory committee, and by the Director of Graduate Studies (DGS), on behalf of the program; we verify that this is the final, approved version of the student's thesis including all changes required by the advisory committee. The undersigned agree to abide by the statements above.

James R. Caudill, Student

Dr. I.S. Jawahir, Major Professor

Dr. Alexandre Martin, Director of Graduate Studies

ENHANCED SURFACE INTEGRITY WITH THERMALLY STABLE RESIDUAL
STRESS FIELDS AND NANOSTRUCTURES IN CRYOGENIC PROCESSING OF
TITANIUM ALLOY TI-6AL-4V

DISSERTATION

A dissertation submitted in partial fulfillment of the
requirements for the degree of Doctor of Philosophy in the
College of Engineering at the University of Kentucky

By

James Robert Caudill

Lexington, Kentucky

Co- Directors: Dr. I.S. Jawahir, Professor of Mechanical Engineering

and Dr. Keith Rouch, Professor of Mechanical Engineering

Lexington, Kentucky

2019

Copyright © James Caudill 2019

ABSTRACT OF DISSERTATION

ENHANCED SURFACE INTEGRITY WITH THERMALLY STABLE RESIDUAL STRESS FIELDS AND NANOSTRUCTURES IN CRYOGENIC PROCESSING OF TITANIUM ALLOY TI-6AL-4V

Burnishing is a chipless finishing process used to improve surface integrity by severe plastic deformation (SPD) of surface asperities. As surface integrity in large measure defines the functional performance and fatigue life of aerospace alloys, burnishing is thus a means of increasing the fatigue life of critical components, such as turbine and compressor blades in gas turbine engines. Therefore, the primary objective of this dissertation is to characterize the burnishing-induced surface integrity of *Ti-6Al-4V* alloy in terms of the implemented processing parameters. As the impact of cooling mechanisms on surface integrity from SPD processing is largely unexplored, a particular emphasis was placed upon evaluating the influence of cryogenic cooling with liquid nitrogen in comparison to more conventional methodologies.

Analysis of numerical and experimental results reveals that burnishing facilitates grain refinement via continuous dynamic recrystallization. Application of LN₂ during SPD processing of *Ti-6Al-4V* alloy suppresses the growth of new grains, leading to the formation of near-surface nanostructures which exhibit increased microhardness and compressive residual stress fields. This is particularly true in cryogenic multipass burnishing, where successive tool passes utilizing lower working pressures generate thermally stable work hardened surface layers, uniform nano-level surface finishes, and significantly deeper layers of compressive residual stresses.

KEYWORDS: Surface Integrity, Cryogenic, *Ti-6Al-4V* Alloy, Nanocrystalline, Burnishing, Machining

James Robert Caudill
(*Name of Student*)

April 10th, 2019

Date

ENHANCED SURFACE INTEGRITY WITH THERMALLY STABLE RESIDUAL
STRESS FIELDS AND NANOSTRUCTURES IN CRYOGENIC PROCESSING OF
TITANIUM ALLOY TI-6AL-4V

By

James Robert Caudill

Dr. I.S. Jawahir

Co-Director of Dissertation

Dr. Keith Rouch

Co-Director of Dissertation

Dr. Alexandre Martin

Director of Graduate Studies

April 10th, 2019

ACKNOWLEDGMENTS

I would like to express my deepest gratitude to my advisor Dr. I.S. Jawahir, whose guidance was instrumental to both my scientific and personal growth on a multitude of levels. Dr. Jawahir, through his knowledge and insight into the fundamental nature of manufacturing processes, and his tireless passion for conducting innovative research, inspired me to always search for the governing principles that define any given problem. I am beyond honored to have learned under his tutelage. Furthermore, I would like to sincerely thank my co-advisor, Dr. Keith Rouch, who provided invaluable time and support throughout this process.

Next I wish to thank my committee members, Dr. Fazleena Badurdeen, Dr. David Puleo, and Dr. Julius Schoop for the time and effort they have invested in my research. I would also like to thank the late Charles Arvin, whose technical expertise helped lay the foundation for many of the scientific avenues explored in this dissertation.

Most importantly, I would like to thank my family for their unconditional support throughout this journey, without which none of this would have been possible. My mother and father sacrificed a great deal so that I could follow my dreams, and I lack the words to truly express my deep gratitude for all they have given me.

TABLE OF CONTENTS

ACKNOWLEDGMENTS	iii
LIST OF TABLES.....	vi
LIST OF FIGURES	vii
CHAPTER 1. Introduction.....	1
CHAPTER 2. Background and Literature Review.....	6
2.1 Utilization of <i>Ti-6Al-4V</i> Alloy in Aerospace Applications.....	6
2.2 Processing Background.....	8
2.3 Metal Working Fluids.....	10
2.3.1 Conventional Flood-Cooling	12
2.3.2 Dry and Near-Dry Processing.....	13
2.3.3 Cryogenic Cooling.....	14
2.4 Cryogenic Machining of Titanium Alloy <i>Ti-6Al-4V</i>	15
2.5 Traditional Post-Processing Operations.....	19
2.6 Surface Integrity Investigations	23
2.7 Numerical Modelling of Machining and Burnishing Processes	27
CHAPTER 3. Experimental Analysis of Burnishing-Induced Surface Integrity..	40
3.1 Material Information and Experimental Methodology	40
3.2 Characterization of Surface Quality in Burnished <i>Ti-6Al-4V</i> Alloy.....	46
3.3 Nanostructuring and Microhardness in Burnished Surface Layers of Titanium Alloy <i>Ti-6Al-4V</i>	56
3.4 Sub-surface Microhardness Variation.....	62
3.5 Chapter Conclusions.....	69
CHAPTER 4. Numerical Modeling of Machining and Burnishing Processes	71
4.1 Numerical Modeling of High Speed Machining.....	72
4.1.1 Overview of Modelling Parameters	74
4.1.2 Constitutive Material Modeling.....	74
4.1.3 Implementation of External Cryogenic Cooling.....	87
4.1.4 Numerical Calibration & Experimental Validation	95
4.1.5 Prediction of Surface Integrity Characteristics	99
4.1.6 Impact of High MRR on Cutting Forces and Thermal Fields	108

4.2 Residual Stress Modelling in Burnished Titanium Alloy <i>Ti-6Al-4V</i>	115
4.2.1 Development of Numerical Model	116
4.2.2 Implementation of Displacement-Control and Calibration.....	121
4.2.3 Numerical Characterization of Residual Stresses	126
 CHAPTER 5. Characterization of Residual Stress Fields in Machined & Burnished Titanium Alloy <i>Ti-6Al-4V</i>	 132
5.1 Measurement Techniques	133
5.2 Impact of Cutting Edge Radius.....	139
5.3 Residual Stress Fields in Burnished <i>Ti-6Al-4V</i> Alloy.....	143
5.4 Fatigue Life Implications in Aerospace Applications	158
5.5 Chapter Conclusions.....	169
 CHAPTER 6. Conclusions and Future Work	 170
6.1 Conclusions.....	170
6.2 Future Work	175
6.2.1 Comprehensive Investigation of NTP and Stress Relaxation on Residual Stress Fields and Fatigue Life.....	175
6.2.2 Comparison of Conventionally Wrought and Additively Produced Titanium Alloy <i>Ti-6Al-4V</i>	178
 References.....	 180
 VITA.....	 195

LIST OF TABLES

Table 2-1. Effectiveness of various cooling and lubrication strategies. Reprinted from [42] with permission from Elsevier.....	12
Table 2-2. Summary of experimental burnishing research.....	26
Table 2-3. Summary of modeling software packages and their respective features. Reprinted from [98] with permission from Taylor & Francis.....	31
Table 2-4. Summary of burnishing models presented in literature.....	39
Table 4-1. Johnson-Cook Constants from SHPB experiments.....	87
Table 4-2. Literature survey of heat exchange coefficient in cryogenic cooling.....	89
Table 4-3. Various properties of liquid and gaseous nitrogen. Adapted from [166] with permission from Taylor & Francis.....	90
Table 4-4. Machining parameters utilized during numerical calibration and validation.....	96
Table 4-5. Machining parameters for high MRR simulations.....	109

LIST OF FIGURES

Figure 2-1. <i>Ti-6Al-4V</i> alloy utilization in Boeing 757 (A) landing gear and (B) cockpit window frame. Adapted from [19] with permission from Elsevier.....	7
Figure 2-2. Cross-sectional schematic of turbofan engine depicting the typical utilization of <i>Ti-6Al-4V</i> alloy. Adapted from [23] with permission.....	8
Figure 2-3. Generalized graphical depiction of burnishing process.....	9
Figure 2-4. Comparison of residual stress profiles developed in <i>AISI-304</i> using laser-shock-peening and deep rolling. Reprinted from [71] with permission from Elsevier.....	19
Figure 2-5. (A) Comparison of surface roughness using various post-processing techniques and (B) SEM micrograph of shot-peened <i>Ti-6Al-4V</i> alloy. Adapted from [73] with permission.....	21
Figure 2-6. Illustration of region of high stress concentration location and burnishing clearance issues. Adapted from [23] with permission.....	22
Figure 2-7. Illustration of the effect of loading pressure and NTP on (A) surface hardness, (B), surface roughness, and (C) surface topography. Adapted from [74] with permission from Elsevier	24
Figure 2-8. FEM model of single asperity in ANSYS APDL. Reprinted from [99] with permission.....	34
Figure 2-9. Depiction of (A) workpiece surface including its initial roughness profile and (B) a comparison of experimental and simulated results. Adapted from [101] with permission from SAGE.....	35
Figure 2-10. Projection of 3D burnishing mechanics onto 2D plane and loading /unloading scheme used to predict residual stress fields developed during burnishing. Adapted from [103] with permission.....	37
Figure 3-1. As-received microstructure of titanium alloy <i>Ti-6Al-4V</i> illustrating its two phase structure.....	40
Figure 3-2. Experimental setup for cryogenic burnishing investigation including pneumatically actuated burnishing and LN ₂ delivery systems.....	41

Figure 3-3. Nozzle location for external LN ₂ during cryogenic burnishing.....	42
Figure 3-4. Nozzle configuration for high pressure LN ₂ and MQL in hybrid burnishing.....	43
Figure 3-5. Zygo New View 7300 non-contact scanning white light interferometer.....	44
Figure 3-6. (A) CLARK Digital microhardness tester and (B) NanoTest Vantage nano-indenter.....	45
Figure 3-7. (A) Nikon EPIPHOT 300 optical microscope and (B) Focused Ion Beam (FIB) system.....	46
Figure 3-8. 3D topographies of plastically deformed contact areas for loads of (a) 1000 N, (b) 1500 N, (c) 2000 N, and (d) 2500 N.....	47
Figure 3-9. (A) Annotated plastic flow characteristics and (B) measured deformation as a function of loading force.....	48
Figure 3-10. Burnished surface roughness using conventional flood-cooling and cryogenic cooling with LN ₂	49
Figure 3-11. Surface R_a for all analyzed cooling and lubrication strategies at a constant burnishing speed of 50 m/min.....	51
Figure 3-12. Surface quality comparison in flood-cooled, cryogenic, and dry burnishing at 2500 N.....	53
Figure 3-13. Surface finish as a function of NTP for various cooling/lubricating strategies.....	55
Figure 3-14. Comparison of surface microhardness as a function of cooling/lubrication conditions.....	57
Figure 3-15. Nanocrystalline surface layer in <i>Ti-6Al-4V</i> alloy after hybrid burnishing at 1500 N.....	60
Figure 3-16. Nanocrystalline surface layer in titanium alloy <i>Ti-6Al-4V</i> after hybrid MPB at 1000 N after 4 tool passes.....	61
Figure 3-17. Characterization of near-surface hardness using nano-indentation....	63
Figure 3-18. Sub-surface microhardness variation as a function of the utilized cooling mechanism in SPB at 2500 N.....	64

Figure 3-19. Affected layer depth as a function of utilized cooling mechanism for varying burnishing feed rates.....	65
Figure 3-20. Crystallographic orientations in burnished <i>Ti-6Al-4V</i> alloy.....	67
Figure 3-21. Sub-surface microhardness variation as a function of NTP for hybrid burnishing at 1000 N.....	68
Figure 4-1. FEM flow chart and structural hierarchy.....	74
Figure 4-2. Depiction of cutting tool and workpiece geometry.....	76
Figure 4-3. Implemented tool and workpiece element mesh.....	77
Figure 4-4. Depiction of mesh edge length.....	79
Figure 4-5. Implementation of velocity and temperature boundary conditions.....	80
Figure 4-6. Measured friction coefficient as a function of sliding velocity and lubrication type. Reprinted from [142] with permission from Taylor & Francis.....	81
Figure 4-7. Implemented heat capacity, elasticity modulus, and thermal conductivity functions.....	84
Figure 4-8. Implementation of heat exchange windows to simulate LN ₂ cooling...	88
Figure 4-9. Experimentally calculated heat transfer coefficient values for various pressures. Reprinted from [54] with permission.....	93
Figure 4-10. Cryogenic heat transfer coefficient for increasing values of T_{OH} . Adapted from [168] with permission from Elsevier.....	95
Figure 4-11. Comparison of numerical and experimental cutting forces during the modelling calibration.....	96
Figure 4-12. Comparison of numerical and experimental cutting forces during experimental validation for trial II.....	98
Figure 4-13. Comparison of numerical and experimental cutting forces during experimental validation for trial III.....	98
Figure 4-14. Sub-routine flowchart for prediction of surface integrity characteristics.....	102
Figure 4-15. Predicted ALD and microhardness during cryogenic and flood-cooled machining.....	103

Figure 4-16. Depiction of methodology for grain size measurement in flood-cooling.....	105
Figure 4-17. SEM analysis of near-surface microstructure in cryogenic machining.....	105
Figure 4-18. Comparison of numerically predicted and experimentally measured grain sizes in cryogenic and flood-cooled milling.....	105
Figure 4-19. Comparison of numerically predicted and experimentally measured microhardness variation.....	108
Figure 4-20. Simulated tool temperature distribution for cryogenic and flood-cooled rough machining.....	110
Figure 4-21. Simulated tool temperature distribution for cryogenic and flood-cooled finish machining.....	110
Figure 4-22. Simulated workpiece temperature distribution for cryogenic and flood-cooled rough machining.....	111
Figure 4-23. Simulated tool temperature distribution for cryogenic and flood-cooled finish machining.....	111
Figure 4-24. Simulated maximum tool and workpiece temperatures in flood-cooled and cryogenic machining as a function of cutting speed for rough and finish machining.....	112
Figure 4-25. Simulated mean cutting forces in high MRR rough machining for flood-and cryogenic cooling.....	114
Figure 4-26. Simulated mean cutting forces in high MRR finish machining for flood-and cryogenic cooling.....	114
Figure 4-27. General modeling overview and calibration procedure.....	117
Figure 4-28. 2D plane strain representation of 3D burnishing process.....	118
Figure 4-29. Depiction of mesh characteristics in burnishing tool and workpiece.....	119
Figure 4-30. Depiction of modelling methodology typically used in literature to characterize the impact of burnishing force on residual stress.....	121
Figure 4-31. Implementation of displacement-control procedure for burnishing simulation using 1500 N loading force.....	122

Figure 4-32. Comparison of experimental and simulated burnishing forces using a displacement-control scheme.....	123
Figure 4-33. Five-step depiction of burnishing methodology employed during numerical investigation of residual stresses.....	124
Figure 4-34. Comparison of experimental and simulated burnishing forces to determine transition point to steady-state.....	126
Figure 4-35. Methodology for data extraction in residual stress prediction models.....	127
Figure 4-36. Depiction of numerically simulated compressive residual stresses for cryogenically burnished <i>Ti-6Al-4V</i> alloy in the tangential and axial directions.....	128
Figure 4-37. Simulated residual stress depth variation for various loading forces.....	129
Figure 4-38. Depiction of tangential residual stress fields in MPB.....	130
Figure 4-39. Simulated residual stress variation in MPB.....	130
Figure 5-1. Diffraction of X-rays in crystal lattice. Reprinted from [199] with permission.....	135
Figure 5-2. Example of $\sin^2\psi$ plot as a function of interplanar spacing. Reprinted from [199] with permission.....	135
Figure 5-3. 3D surface topography of electropolished <i>Ti-6Al-4V</i> alloy.....	137
Figure 5-4. Electropolished material removal calibration curve in <i>Ti-6Al-4V</i> alloy.....	138
Figure 5-5. Impact of cutting edge radius on residual stress in machined <i>Ti-6Al-4V</i> alloy.....	140
Figure 5-6. FIB based microstructure analysis of hybrid machined <i>Ti-6Al-4V</i> alloy with 50 μm cutting edge radius.....	142
Figure 5-7. Experimental setup for XRD analysis of burnished <i>Ti-6Al-4V</i> alloy.....	145
Figure 5-8. Residual stress in burnished <i>Ti-6Al-4V</i> alloy for various cooling mechanisms.....	146

Figure 5-9. Residual stresses in laser-shock-peened and deep rolled <i>Ti-6Al-4V</i> alloy. Reprinted from [126] with permission from Elsevier.....	146
Figure 5-10. Surface residual stresses and depths of peak compressive stresses in burnished <i>Ti-6Al-4V</i> alloy.....	148
Figure 5-11. Impact of burnishing force and the NTP on the residual stress state in burnished <i>Ti-6Al-4V</i> alloy.....	150
Figure 5-12. A comparison of surface and peak residual stresses in numerical simulations and experimentally measured.....	151
Figure 5-13. Residual Stresses in burnished <i>Ti-6Al-4V</i> alloy after isothermal heating.....	154
Figure 5-14. Comparison of FWHM variation in hybrid burnished <i>Ti-6Al-4V</i> alloy before and after isothermal heating.....	158
Figure 5-15. Representative curve for crack initiation and growth.....	161
Figure 5-16. Graphical depiction of relevant stress intensity factors.....	162
Figure 5-17. Depiction of crack growth suppression due to autofretting. Reprinted from [213] with permission from Elsevier.....	164
Figure 5-18. Illustration of Goodman Diagram for <i>Ti-6Al-4V</i> alloy. Reprinted from [222] with permission from Elsevier.....	166
Figure 5-19. Modified Goodman diagram based on compressive residual stress field developed from hybrid burnishing. Adapted from [222] with permission from Elsevier.....	167
Figure 5-20. Potential load factor reduction in <i>Ti-6Al-4V</i> alloy based aerospace components due to the presence of compressive residual stresses from MPB.....	168

CHAPTER 1.

INTRODUCTION

Titanium is one of the most abundant structural materials on Earth [1]. In its alloyed form its mechanical strength is comparable to that of high carbon steel and exotic nickel-based super alloys, and with roughly half the density of either it possesses a highly attractive strength to weight ratio. These characteristics, along with its high resistance to wear and corrosion, make it an ideal material choice in certain sectors of the aerospace and biomedical industries [2]. Of the most common titanium alloys, *Ti-6Al-4V* is the most widely utilized, accounting for more than 50% of global titanium usage, and 80% of which is concentrated in these two industries [3].

Conventional processing of *Ti-6Al-4V* alloy into functional components almost exclusively relies upon the subtractive CNC machining of cast or wrought workpieces. However, for numerous reasons *Ti-6Al-4V* alloy is generally classified as a difficult-to-machine material. First, like all metallic alloys, the heat generated during metal cutting always negatively impacts machinability [4]. In *Ti-6Al-4V* alloy, this problem is magnified due to its unique combination of high strength and extremely low thermal conductivity in comparison to typical tool materials such as tungsten carbide. As such, the extreme heat generated during machining will generally not quickly dissipate, but rather concentrate on the cutting edge and faces of the tool. At these high temperatures *Ti-6Al-4V* alloy also has a tendency to chemically react with many commercially available tool materials, providing additional avenues for wear and tool failure to occur. Finally, during machining thermal plastic instabilities give rise to non-uniform, localized shear-strain bands in the generated

chip. This leads to a serrated chip formation mechanism and consequently vibration based cutting force fluctuations, which in combination with the high cutting temperatures generates micro-cyclical fatigue on the tool and accelerated tool-wear and possible catastrophic tool failure [5, 6]. Moreover, these challenges are exacerbated in high speed metal cutting, due to the increased cutting temperatures and associated tool-wear. Consequently, machining productivity is significantly reduced at high material removal rates, and considering that some aerospace components can require removal of up to 90% of the original workpiece material, machining related costs are negatively impacted [7].

Cryogenic machining with liquid nitrogen (LN₂) has emerged as an alternative to conventional machining with oil-based metal working fluids (MWF) at room temperature (20°C). LN₂ has a boiling temperature of -196°C at standard atmospheric pressure (10⁵ Pa), and thus cryogenic coolant significantly increases the heat flux in the cutting zone in comparison to conventional flood-cooling. This increased cooling rate rapidly removes the heat generated during machining, and thus reduce the thermal load imparted onto the cutting edges of the tool and to the workpiece. For difficult-to-machine materials, such as titanium alloy *Ti-6Al-4V*, where a tremendous amount of heat is generated during machining, cryogenic cooling has the potential to significantly increase machinability by decreasing the cutting temperature, which consequently leads to increased tool-life and machining productivity [5-10]. Moreover, LN₂ has no negative impact on the environment or human health, as nitrogen is the most naturally occurring element on our planet.

Cryogenic machining of *Ti-6Al-4V* alloy also has the added benefit of greatly enhancing the surface integrity of processed workpieces. Field and Kahles [11] define the concept of surface integrity as the inherent or enhanced condition of a material surface

produced by machining processes or other surface generation/modification operations. Jawahir et al. [12] recently conducted an extensive international benchmark study on the impact of processing parameters on surface integrity for a variety of alloys. For enhanced functional performance of processed components, it was determined that the most influential surface integrity characteristics are the induced surface quality, microhardness, SPD layer thickness, material microstructure, and residual stress distribution. Surface integrity enhancement is particularly prominent in severe plastic deformation (SPD) processes such as burnishing, where extremely large mechanical and thermal strains facilitate microstructural evolution and grain refinement via dynamic recrystallization (DRX). Application of LN₂ during SPD processing suppresses the growth of new grains, leading to the formation of near-surface nanostructures which exhibit increased microhardness and highly compressive residual stress fields [6, 13-18].

However, the current understanding of the impact of cryogenic cooling on the process-induced surface integrity of *Ti-6Al-4V* alloy is severely limited. This is particularly true for the combined influence of processing parameters and cooling/lubricating mechanisms, upon the resulting workpiece microstructure, mechanical properties, and the likely functional performance of machined or burnished components. For aerospace applications, where components are routinely subjected to cyclical loading at elevated temperatures, post-processing SPD techniques such as shot peening or burnishing are utilized to enact deep surface layers of mechanically refined material in order to increase the wear resistance and fatigue life of employed components. In literature, however, there is little to no research focused upon how cooling mechanisms, and specifically cryogenic cooling with LN₂, affect the formation and characteristics of these surface layers.

Consequently, there is no scientific understanding of how the in-process cooling methodology correlates with the functional performance of aerospace materials. Moreover, there is general lack of consensus in literature on the nature of cryogenic cooling itself, and therefore the impact of LN₂ on the frictional characteristics of the tool-workpiece interface, as well as upon the cutting forces generated during machining. Considering that both have a direct influence on the developed surface tractions during processing, they also therefore also significantly impact tool-life and machining productivity.

Therefore, the primary goal of the research presented in this dissertation to develop fundamental insights into the nature of cryogenic cooling and its impact upon the machining and burnishing-induced surface integrity of titanium alloy *Ti-6Al-4V*. In aerospace manufacturing, post-processing techniques such as burnishing serve as the final step during component fabrication, and as such have a dominant influence on the surface integrity of processed components. Therefore, a particular emphasis was placed upon developing a quantifiable and comprehensive understanding of the burnishing process. This was achieved by conducting an extensive experimental investigation into the impact of all controllable burnishing parameters, including the surface speed and feed rate, the utilized loading force, the number of tool passes (NTP), and the cooling and lubrication methodology. The latter of which includes conventional flood-cooling (emulsion), cryogenic cooling, near-dry minimum quantity lubrication (MQL), and hybrid (MQL+LN₂). In this way a complete picture of the effects of cooling and lubrication can be ascertained and correlated to the measured experimental outputs. Surface integrity was characterized in terms of surface quality/topography, surface and depth variation of micro/nano hardness, affected layer thickness, microstructural evolution (nanostructuring), and perhaps most importantly the

residual stress fields generated during processing. Furthermore, the complex dynamics associated with machining and burnishing and their non-linear impact upon material mechanics necessitated the construction of predictive phenomenological models. These models were used highlight process physics and material behaviour during machining and burnishing of *Ti-6Al-4V* alloy by simulating the impact of processing parameters on critical metrics such as cutting forces, thermal fields, strain, strain-rate, etc., while also providing a means of predicting relevant surface integrity characteristics. Therefore, by utilizing both numerical and experimental based approaches, a detailed picture can be drawn that connects processing parameters to the in-service functional performance of components employed in aerospace applications.

CHAPTER 2.

BACKGROUND AND LITERATURE REVIEW

2.1 Utilization of *Ti-6Al-4V* Alloy in Aerospace Applications

Conventional titanium alloy systems are generally classified into groups based upon their composition and the dominant phase expression at room temperature [19]. *Ti-6Al-4V* alloy possesses an α/β system composed of HCP- α grains within a BCC- $\alpha+\beta$ lamellar matrix. It is generally employed in high temperature applications of up to 400-500°C, and has a high specific strength and excellent corrosion resistance. According to Boyer [19] it is generally considered the workhorse of the titanium industry, accounting for over 60% of total titanium production. It offers excellent weight savings in comparison to high strength steel and nickel-based high temperature super alloys, while exhibiting superior high temperature strength characteristics in comparison to aluminum alloys. Therefore, it is typically employed when the combination of strength, weight, corrosion resistance, and high temperature mechanical properties of steel, nickel, or aluminum alloys are insufficient for a specific application [19-21].

Ti-6Al-4V alloy is heavily utilized as a structural material in all common product forms including, castings, plates, forgings, fasteners, etc., in all major sections of an aircraft. Some common examples of *Ti-6Al-4V* alloy used in structural applications are the landing gear support structures and cockpit window frames of a Boeing 757 jetliner are shown below in Figure 2-1. By implementing *Ti-6Al-4V* alloy in landing gear structures, instead of high strength steel, significant weight savings are gained. Moreover, the wheel-well is known to be as a highly corrosive environment, so the increased corrosion resistance

of *Ti-6Al-4V* alloy provides additional resistance to the corrosion pitting observed in other aircraft using steel alloys. With regards to the cockpit windows, the added strength in comparison to aluminum alloys provides additional resistance to bird strikes and other potential impact hazards [19].

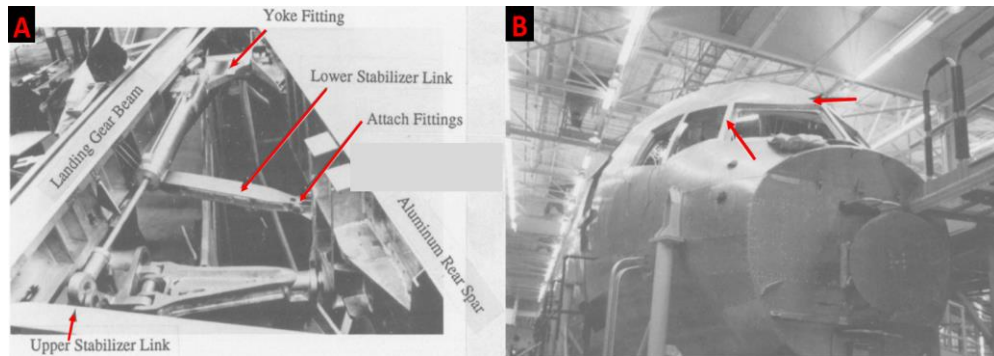


Figure 2-1. *Ti-6Al-4V* alloy utilization in Boeing 757 (A) landing gear and (B) cockpit window frame. Adapted from [19] with permission from Elsevier.

In aircraft multistage gas turbine engines, *Ti-6Al-4V* alloy and *Ni*-based high temperature super alloys are the two most commonly employed metals. Considering the significantly lower density of *Ti-6Al-4V* alloy, for weight savings it would certainly be advantageous to employ this alloy throughout the engine. However, the comparatively lower ideal working temperature of *Ti-6Al-4V* alloy limits its application to the relatively lower thermally stressed regions of the turbine engine, such as the intake fan, low pressure compressor, and about 2/3 of the high pressure compressor [22]. An annotated cross-sectional view of a Pratt & Whitney turbojet engine is shown below in Figure 2-2 to illustrate the typical utilization of *Ti-6Al-4V* alloy in turbine assemblies.

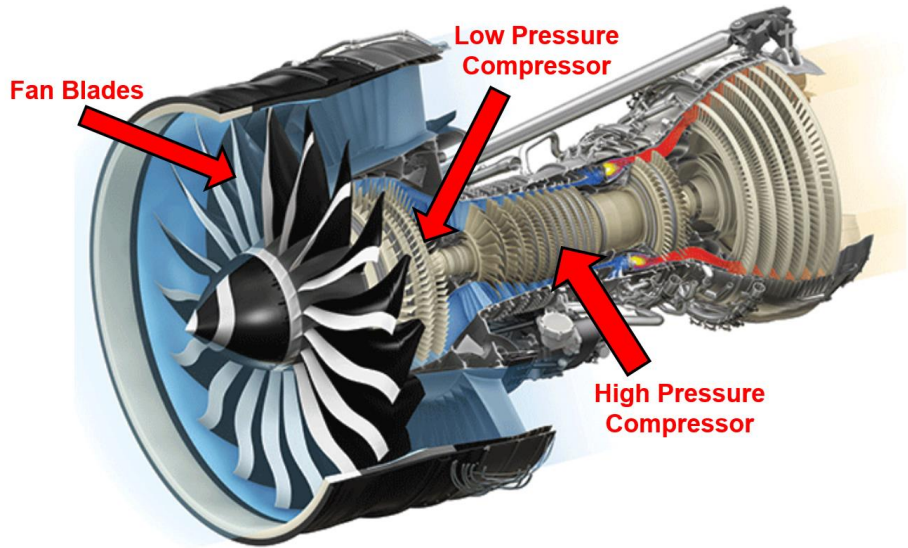


Figure 2-2. Cross-sectional schematic of turbofan engine depicting the typical utilization of *Ti-6Al-4V* alloy. Adapted from [23] with permission.

2.2 Processing Background

Burnishing is a chipless finishing process used to improve the surface integrity of metallic materials by severe plastic deformation (SPD) of surface asperities. This processing technique has particular relevance in gas turbine engines employed in aerospace applications, where surface integrity has a large impact upon the functional performance and fatigue life of critical components such as the fan blades in turbine and compressor assemblies.

During burnishing a CNC turning or vertical milling center is used to bring a highly polished, hardened roller into normal contact with the asperities of a machined surface. If the magnitude of the generated contact stress is greater than the yield strength of the material, the asperities will plastically flow and be compressed into the machined valleys as the tool is fed along the workpiece, producing a homogenous mirror-like surface finish and highly work hardened surface layers exhibiting enhanced mechanical properties.

The only processing distinction between single pass burnishing (SPB) and multipass burnishing (MPB), is that in the latter successive tool passes over the same tool path are employed. Figure 2-3 illustrates the basic mechanisms that characterize this process.

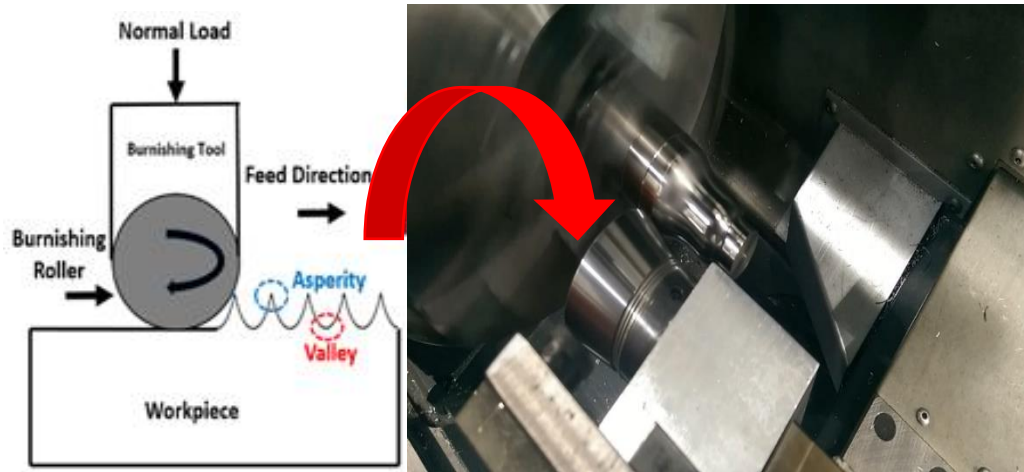


Figure 2-3. Generalized graphical depiction of burnishing process.

Mechanical processing techniques, such as low plasticity burnishing [24, 25] and deep rolling [26, 27], are used to enhance the surface integrity of highly stressed aerospace components by strain hardening and severe plastic deformation (SPD) [28-30]. In high temperature turbine applications, such as the aeroengine assembly shown in Figure 2-2, where parts are routinely subjected to cyclical loading over a range of working temperatures, these methods provide a means to increase fatigue resistance and functional life. Traditional SPD operations, such as shot peening [31, 32], have been used to enhance fatigue life by imparting a compressive residual stress state in the cold worked surface layers. However, without additional polishing steps, shot peening can lead to a degradation in surface quality. At elevated service temperatures, poor surface quality can negatively impact gas flow dynamics and turbine efficiency, as well as increase the probability of fatigue cracking, crack propagation, and eventual component failure [33-

35]. Considering that approximately 20% of the direct operating costs for aerospace companies is directly tied to component maintenance [36], there is a critical need for wear and impact resistant materials that can maintain functionality during high temperature cyclical loading.

Burnishing is a means of increasing the life of such components by inducing highly compressive residual stress states in both the surface and subsurface of processed components, which acts to delay the onset of fatigue crack initiation and/or decrease the rate of fatigue crack propagation [37]. Consequently, the vast majority of research in this field has been on exploring the potential correlation and optimization of processing parameters with residual stresses, fatigue life, and other surface integrity metrics, and many others that seek to simply compare the process-induced surface integrity obtained by burnishing with that obtained by more traditional finishing methods such as a shot-peening or laser-shock-peening. Additionally, for a more complete understanding of complex process mechanics and dynamics, as well as to lay the foundation for practical industrial application, analytic and finite element based constitutive models have been reviewed.

2.3 *Metal Working Fluids*

One of the most effective ways to address some of the challenges associated the machining of *Ti-6Al-4V* alloy is by proper selection and application of metal-working-fluids (MWF). The most recent well-documented CIRP keynote paper by Brinksmeier et al. [38] reviews the most recent developments in MWF application in various machining operations. It was shown that MWF a substantial impact on process productivity, energy and resource efficiency, process sustainability, as well as surface integrity. For difficult-to-machine materials, the proper selection of MWF in general depends upon the desired surface integrity (product quality), machining productivity, sustainability, etc. If surface integrity is more

valued than productivity, then typically low cutting speeds and feeds are employed in order to avoid thermal damage. In such scenarios, MWF with a high degree of lubricity, such as minimum quantity lubrication (MQL), can be employed. Conversely, for moderate and high speed machining, where excessive cutting temperatures can be generated, the MWF should be chosen based upon its cooling capacity. In this scenario, typically flood-cooling or cryogenic cooling can be utilized [39] to efficiently remove heat from the cutting zone. These general rules of thumb are derived from a principle which states that for every combination of workpiece material and tool geometry/material there is an optimal cutting temperature in which machinability is at its highest, and it is here the ratio of the hardness of the cutting tool to that of the workpiece is at its highest [40]. Thus, with sufficient cooling, thermal softening of the tool can be mitigated and tool-life extended by avoiding thermally activated wear mechanisms such as diffusion and adhesion. However, in some cases excessive cooling of the workpiece can increase its microhardness and therefore the cutting forces and tool-wear [41]. This is particularly true when the machining parameters are such that the cutting temperature is significantly lower than this optimal processing temperature. On the other hand, if increased machining productivity is the primary objective of a process, it might be necessary to increase the material removal rate (MRR). However, this in turn will almost certainly generate higher cutting temperatures in the workpiece. This is particularly true for difficult-to-machine alloys such as titanium alloy *Ti-6Al-4V*, and thus proper selection of implementation of cooling methodologies is critical for tool-life, machining productivity, as well as surface integrity. Therefore, for a given machining scenario, there exists a complex interplay between cooling/lubricating and the desired productivity, which furthermore must be balanced with the required material properties and

functionality of the processed component and the desired sustainability of the process. This is summarized quite well in Table 2-1, which was originally presented in Jawahir et al. [42].

Table 2-1. Effectiveness of various cooling and lubrication strategies. Reprinted from [42] with permission from Elsevier.

Effects of the cooling and lubricating strategy		Flood (emulsion/oil)	Dry (compressed air)	MQL (oil)	Cryogenic (LN ₂)	Hybrid (LN ₂ + MQL)
Primary	Cooling	Good	Poor	Marginal	Excellent	Excellent
	Lubrication	Excellent	Poor	Excellent	Marginal	Excellent
	Chip Removal	Good	Good	Marginal	good	Good
Secondary	Machine Cooling	Good	Poor	Poor	Marginal	Marginal
	Workpiece Cooling	Good	Poor	Poor	Good	Good
	Dust/Particle Control	Good	Poor	Marginal	Marginal	Good
	Product Quality (Surface Integrity)	Good	Poor	Marginal	Excellent	Excellent
Sustainability Concerns	Water pollution, microbial infestation, and high cost	Poor surface integrity due to thermal damage	Harmful oil vapor	Initial cost	Initial cost, oil vapor	

2.3.1 Conventional Flood-Cooling

In industrial applications, conventional flood-cooling (emulsion) with water miscible cutting fluids is typically the most common coolant choice. As water has a high thermal conductivity, it is fairly effective and easily implemented means to control between the chip and rake face of the tool as well as between the workpiece and the tool's flank face [6]. For burnishing, as no chip is generated, this refers to the contact region between the roller and the piece. Note, however, that in order to combat the frictional heat generated, additives must be combined with the pure water. These typically take the form of either synthetic, semi-synthetic, or oil soluble water miscible coolants. The primary difference between them being that oil soluble coolants contain mineral oils, while synthetic coolants are composed of either organic or inorganic compounds (Semi-synthetic containing properties of both). All

of these are suitable coolant choices however, depending upon the processing parameters and material being machined [43].

However, there are many economic, environmental, and health related issues associated with the indiscriminate use of water miscible MWF. The cost of procuring and disposal can be as high as 30% of the total manufacturing costs when machining difficult-to-cut materials such as *Ti-6Al-4V* alloy. The cost of disposal can be particularly high, as the spent coolant often requires expensive treatment due to the fact that is non-biodegradable. Moreover, as they typically contain chlorine and sulphur based additives, as well as biocides and other chemicals, they are generally classified as toxic liquids harmful to both human health and the environment. Unfortunately, more than 150 million gallons of this toxic waste is annually disposed of in the natural environment [44]. MWF also are known to be a rich environment for the growth of harmful bacteria and fungi, which can pose as a health hazard to the machinists and other exposed workers [45-48]. All of which decrease the overall sustainability of the machining process.

2.3.2 *Dry and Near-Dry Processing*

A common alternative to flood-cooling is the use of of dry and near-dry minimum quantity lubrication (MQL). Dry machining would obviously be the most sustainable approach, as no MWF is utilized the economic, environmental and societal impact is minimized [49]. However, this is generally only an accepted approach when surface integrity, tool-life, and the geometric accuracy of produced components are not of major concern. Even then it's only a reasonable technique for certain classes of materials with high degrees of machinability. In MQL machining, an aerosol of compressed air and oil is delivered at a very low, pulsating flow rate into the cutting zone [50]. This methodology

has been successfully used to sustainably machine many difficult-to-machine materials within the desired surface quality and accuracy specifications of the machined components [48]. It also been shown to be extremely effective at combating the built-up-edge (BUE) phenomena for a wide variety of materials and machining processes, including *Ti-6Al-4V* alloy [51, 52]. Though MQL can be quite successful at mitigating the frictional adhesion generated during machining, in general however its considered as lubricant rather than a coolant, as it does not address the heat generated from plastic deformation and chip generation. As such, thermally activated tool-wear mechanisms tend to be remain prevalent during MQL machining. Moreover, with no primary cooling mechanism thermal softening of the workpiece may limit or even diminish the process-induced surface integrity in comparison to flood and cryogenic cooling.

2.3.3 *Cryogenic Cooling*

The term cryogenic machining is a term reserved for machining with liquefied gases at temperatures below 120 K (-153.15°C) [53]. There are number of gases which exist in liquid state below this temperature, however liquid nitrogen (LN₂) is most commonly used in machining applications because it is the most abundant naturally occurring element in the atmosphere, and as such is completely safe for both humans and the environment. LN₂ has an extremely low saturation temperature of -196°C at standard atmospheric pressure (10⁵ Pa). Unfortunately, it has a fairly high vapor pressure and a tendency to rapidly absorb heat and evaporate. As the gaseous phase has significantly diminished heat transfer capabilities it is important to ensure boiling heat transfer in the cutting zone. Therefore, the implemented pressure, nozzle dimensions, distance to workpiece, etc., must all be considered to ensure the most effective cooling strategy [54].

During processing, LN₂ is sprayed directly into the cutting zone in order in it to rapidly cool both the tool and workpiece and significantly reduce the cutting temperature. For machining of *Ti-6Al-4V* alloy, where cutting temperatures can exceed 1000°C under high speed conditions, cryogenic cooling with LN₂ has been shown to dramatically increase tool-life and machining productivity [55-57]. Therefore, the reduced cutting temperatures and increased tool-life effectively allows for higher cutting speeds and increased MRR [7, 46, 58]. Moreover, application of LN₂ has been to shown to significantly alter the mechanical properties of both the tool and workpiece. Specifically, cryogenic temperatures have been shown to increase microhardness and resistance to wear [59, 60]. Though increased workpiece hardness can lead to increased cutting forces and potentially tool-wear, this is more than offset by the mitigation of thermally activated tool-wear mechanisms in the machining of difficult-to-cut materials such as *Ti-6Al-4V* alloy. As a pure cooling technique, cryogenic processing is certainly the superior option in comparison to more conventional methodologies. However, unlike flood-cooling and MQL, in general LN₂ lacks a substantial lubricating mechanism, which can lead to a degraded surface quality after machining. Though there is some literature that suggests LN₂ can actually provide significant lubrication by acting as cushion as the liquid evaporates [61-63]. There is also indication that the friction characteristics are altered by the extremely low temperatures, which results in improved machinability [9, 61].

2.4 *Cryogenic Machining of Titanium Alloy Ti-6Al-4V*

Cryogenic machining of *Ti-6Al-4V* alloy via external LN₂ application, is a means to improve machinability by facilitating the rapid dissipation of heat from the cutting zone, and consequently reduce the chemical affinity between the workpiece and cutting tool

material. There has been some preliminary research conducted with the aim of understanding the effect of cooling and lubrication on tool-life during the machining *Ti-6Al-4V* alloy. The vast majority of which are based on continuous machining operations such as conventional turning. Hong and Ding [5] conducted one of the earliest efforts to characterize the effect of external LN₂ application on tool-life during turning of *Ti-6Al-4V* alloy. With minimization of waste a priority, micro-nozzles were used to spray LN₂ on both the rake and flank faces of an uncoated carbide insert. Additionally, micro-nozzles provided a means to proportionally increase the coolant flowrate commensurate with the machining parameters and the amount of generated heat, without excessively pre-cooling the workpiece. In this way over hardening of the workpiece surface can be avoided and the generated cutting forces can be minimized. In comparison to conventional flood-cooling, tool-life with cryogenic cooling was roughly 5 times greater using a cutting speed of 120 m/min. Venugopal et al. [64, 65] compared the wear mechanisms and tool-life in dry, flood, and cryogenic machining of *Ti-6Al-4V* alloy with uncoated carbide inserts. It was determined that the primary wear mechanism is adhesion-dissolution-diffusion at the crater, along with abrasive and chemical attrition on the flank. Moreover, the cutting edges experienced micro and macro cracking due to the sharp thermal gradients. In all cases, cryogenic cooling provided superior tool-life, however this was diminished at higher cutting speeds. It was speculated that this was likely due to the inability of the LN₂ to penetrate the tool-chip interface effectively at these cutting speeds. Proper calibration of the flow rate would have likely facilitated a more efficient transfer of heat from the cutting zone and more substantial tool-life increases. Dhananchezian and Kumar [62] studied the effect of cutting speed and cooling/lubrication upon the tool-life and process-induced

surface integrity of *Ti-6Al-4V* alloy. PVD coated inserts (TiAlN) with specialized holes for internal LN₂ delivery on the flank and nose were utilized, while an additional cooling stream was applied on the rake face. This allowed for a 62% reduction in the measured cutting temperature as compared to flood-cooling. Moreover, at the highest tested cutting speed of 100 m/min, tool-life with cryogenic cooling was 40% longer than that with conventional flood-cooling. Additionally, the measured cutting forces and surface quality (R_a) were also roughly 40% lower. This was attributed to the reduced friction coefficient provided by the LN₂ cushion. Schoop et al. [66] investigated the surface integrity and tool-life in high speed finish machining of *Ti-6Al-4V* alloy using PCD inserts under flood-cooling, cryogenic, and hybrid (LN₂+MQL) cooling. Although typically PCD tools are rarely used in this type of machining scenario, due to their propensity for chemical wear at high cutting speeds and temperatures, LN₂ was effective at mitigating the thermally activated tool-wear. Cryogenic and hybrid machining were 4-5 times more successful at increasing tool-life, likely due to the rapid heat exchange between the cryogenic environment and the high thermal conductivity of the PCD insert. Flood-cooling also showed significant surface damage in comparison, which was hypothesized to be related to the increased thermal softening and side flow at the elevated cutting speed. Finally, both cryogenic and hybrid machining produced deeper surface layers with increased microhardness. Cutting forces, chip morphology, and tool-life in turned *Ti-6Al-4V* alloy were studied by Bermingham et al. [7]. An interesting conclusion drawn was that cryogenic cooling with LN₂ was not only effective at removing the heat generated during machining, but also has the potential to reduce the amount of thermal energy that is actually generated. This is accomplished by reducing the chip-tool contact length by physically

lifting the chip, and by doing so significantly reduce the heat generated in the secondary deformation zone and on the rake face which arise from friction [67]. However, Bermingham et al. [7] also noted that though the main cutting force was reduced due to reduced friction on the flank face from direct application of coolant, the coefficient of friction from LN₂ at the tool-chip interface on the rake face actually increased and this is observed in the increased thrust and feed forces. This highlights the incomplete understanding on the effects of cryogenic cooling on lubrication and friction during machining of *Ti-6Al-4V* alloy. However, the literature is fairly conclusive in regards to the benefits of cryogenic cooling in terms of increasing machining productivity through enhanced tool-life, and facilitating surface integrity enhancement by mitigation of thermal softening mechanisms [15].

Interrupted cryogenic machining of *Ti-6Al-4V* alloy, such as face milling, end milling, etc., is almost completely unexplored in literature. Though some authors have studied the effect of liquid CO₂ [68], compressed nitrogen gas with oil mist [69], and MQL with cooling air [70], none of these techniques utilize true cryogenic temperatures. However, they did all share the common conclusion, that with reduced coolant temperature both tool-life and surface roughness (from a decrease in adhesion) were observed. Shokrani et al. [6] conducted one of the only true experimental investigations of interrupted cryogenic cutting, which in this case was end-milling. Analysis of Variance (ANOVA) was used to statistically analyse the effect of cooling/lubrication, speed, feed, and depth of cut upon the processed microhardness and surface quality. Comparing dry, flood, and cryogenic cooling this analysis revealed that cryogenic cooling produced workpieces with

higher microhardness, as well as fewer surface defects and lower R_a . However, there was little emphasis on the underlying physics and metallurgy that explain these results.

2.5 Traditional Post-Processing Operations

In Altenberger et al. [31, 34], Drechsler et al. [26], and Nikitin and Altenberger [71], the effects of deep rolling (burnishing) on residual stress and fatigue life, were compared with that induced by conventional shot-peening techniques. It was generally observed that deep rolling produced a substantially more compressive residual stress state at deeper depths beneath the processed surface, as is shown in Figure 2-4. This in turn directly led to significant increases of more than 50% in its high cycle fatigue (HCF) life.

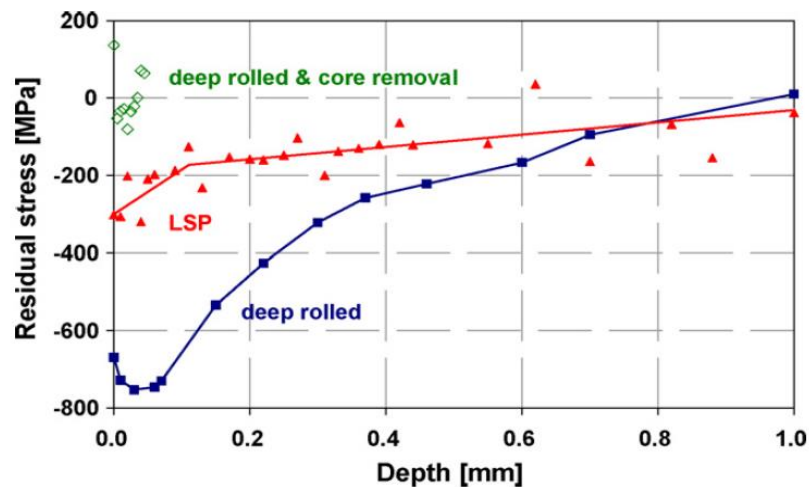


Figure 2-4. Comparison of residual stress profiles developed in *AISI-304* using laser shock-peening and deep rolling. Reprinted from [71] with permission from Elsevier.

Additionally, Altenberger et al. [31, 34] investigated fatigue life at elevated temperatures so as to ascertain the nature of any stress relaxation phenomena. It was discovered that after isothermal heating to 550°C, shot-peened *Ti-6Al-4V* alloy was almost completely annealed into its virgin state and the measured residual stress profile was indistinguishable from that of the as-received material. And while deep rolled workpieces also exhibited some measure of stress relaxation in terms of magnitude, surface layers still

maintained significant amounts of refinement associated with the previous cold working. This included the burnishing-induced nanocrystalline surface layers generated deep rolling of *Ti-6Al-4V* alloy. From an aerospace perspective this is extremely important observation, as most aeroengine components must routinely operate in high temperature environments. Retention of process-induced surface integrity characteristics at these elevated service temperatures gives increased confidence that the in-service functional performance and fatigue life will not be effected by the operational parameters in which the component are employed.

Other researchers [24, 25] conducted similar experimental comparisons using low plasticity burnishing (LPB) as the means of SPD processing. In comparison to deep rolling/burnishing, LPB is a technique specifically designed for aerospace turbine air-foils. As these are thin metallic components which must be processed within extremely tight manufacturing tolerances, minimizing component distortion is a necessity. Thus, in LPB the goal is to not maximize the surface integrity refinement by optimization of process parameters, but rather to only to do so to the limit at which no potential part distortion will occur. Analysis revealed results similar to that observed for deep rolling, where in comparison to shot & laser-shock peening, LPB rolling was far more successful at generating beneficial compressive residual stresses and enhanced fatigue life (though not to the same degree as deep rolling/burnishing). Many other authors [71-73] compared these finishing operations but from the perspective of more complete picture of surface integrity, by including metrics such as induced surface quality and microhardness variation. Certainly in the former burnishing was found to be a superior operation. Shot-peening has a tendency to actually degrade the machined surface quality, whereas with burnishing

surface R_a values on the order of a couple hundred nanometers or smaller can be achieved depending upon the initial surface roughness of the workpiece and the applied burnishing parameters. Figure 2-5 compares the maximum surface roughness in titanium alloy *Ti-6Al-4V* and aluminium alloy *Al-7075* using various post-processing techniques, including ball burnishing (BB), shot-peening (SP), and laser-shock peening (USP). Additionally, an SEM micrograph of *Ti-6Al-4V* alloy is presented which illustrates the rough and irregular surface topography produced from shot-peening processes. From Figure 2-5 it is readily apparent that in aerospace applications, where surface quality can have a significant effect on gas flow dynamics and fatigue life, that additional processing steps such as polishing or lapping are needed after shot-peening in order to improve the surface quality.

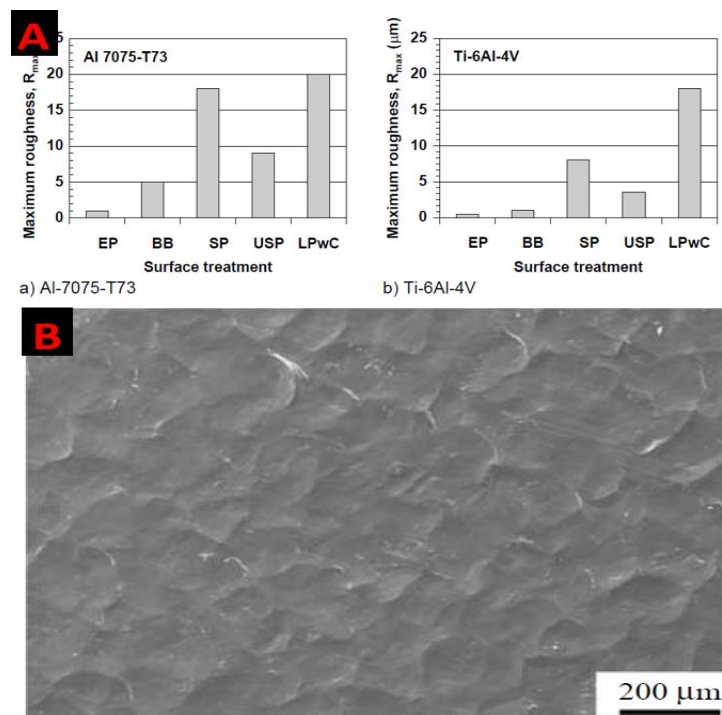


Figure 2-5. (A) Comparison of surface roughness using various post-processing techniques and (B) SEM micrograph of shot-peened *Ti-6Al-4V* alloy. Adapted from [73] with permission.

The most significant advantages of shot-peening and laser-shock peening in comparison to burnishing processes, is that these conventional methods are generally easier to perform on actual components. Typically, aerospace parts and assemblies, and particularly turbine blades, have complex geometries with convex and concave surface profiles with very narrow segments that are very difficult for the burnishing tool to actually reach due to tool clearance issues. For example, such a location is found where the fan blades and shaft are connected as is depicted in Figure 2-6.

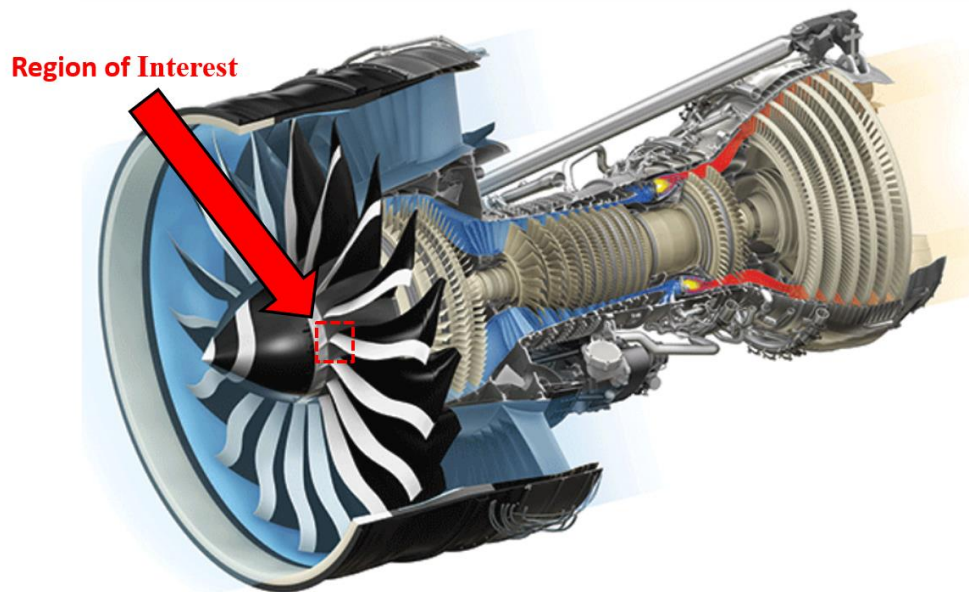


Figure 2-6. Illustration of region of high stress concentration location and burnishing clearance issues. Adapted from [23] with permission.

These locations are notorious for experiencing high concentrations of stress during operation and are often sites where fatigue cracks initiate, and therefore imparting compressive residual stress fields in these regions is extremely important in regards to fatigue life. Most burnishing tools are not designed for geometries such tight clearances, and for those that are it is questionable whether tool stiffness can be maintained while

utilizing high burnishing pressures. Shot-peening, conversely, requires no such considerations. As long as the surface is exposed shot-peening can be performed.

2.6 *Surface Integrity Investigations*

Some research has been conducted on the influence of relevant burnishing parameter on the process-induced surface integrity of metallic alloys [74-83]. In general, they all derived similar conclusions in regards to the ability of burnishing/deep rolling to achieve an optimal measures of surface integrity for various alloys. The imparted surface microhardness and residual stresses, and their variation with depth, were both largely dependent on the loading pressure applied and to a lesser degree the NTP. The general consensus was that both microhardness and the magnitude of the compressive stress field, increase with increased loading until a point in which the material reaches its capacity for strain-hardening. In terms of surface quality, experimental observations indicated that increasing loading pressure and/or NTP only improved surface quality to certain threshold. Beyond which further increases to burnishing force or NTP resulted in surface spalling, smearing, and other forms of surface quality degradation, all of which lead to increased R_a values. In all cases surface quality continuously improved with decreasing feed rate until a stagnation point was reached, which was dependent upon the diameter of the burnishing tool. However, regardless of the tool geometry, no further improvement could be achieved once the limiting feed rate was reached. Burnishing speed, on the other hand, displayed mixed results. In some cases, increased speed was directly associated with decreased hardness and surface quality, but in most research this parameter usually had no statistical effect upon any relevant surface integrity measure. Figure 2-7 depicts these observed behaviours, along with optical micrographs of the processed topographies which illustrate the observed surface quality degradation.

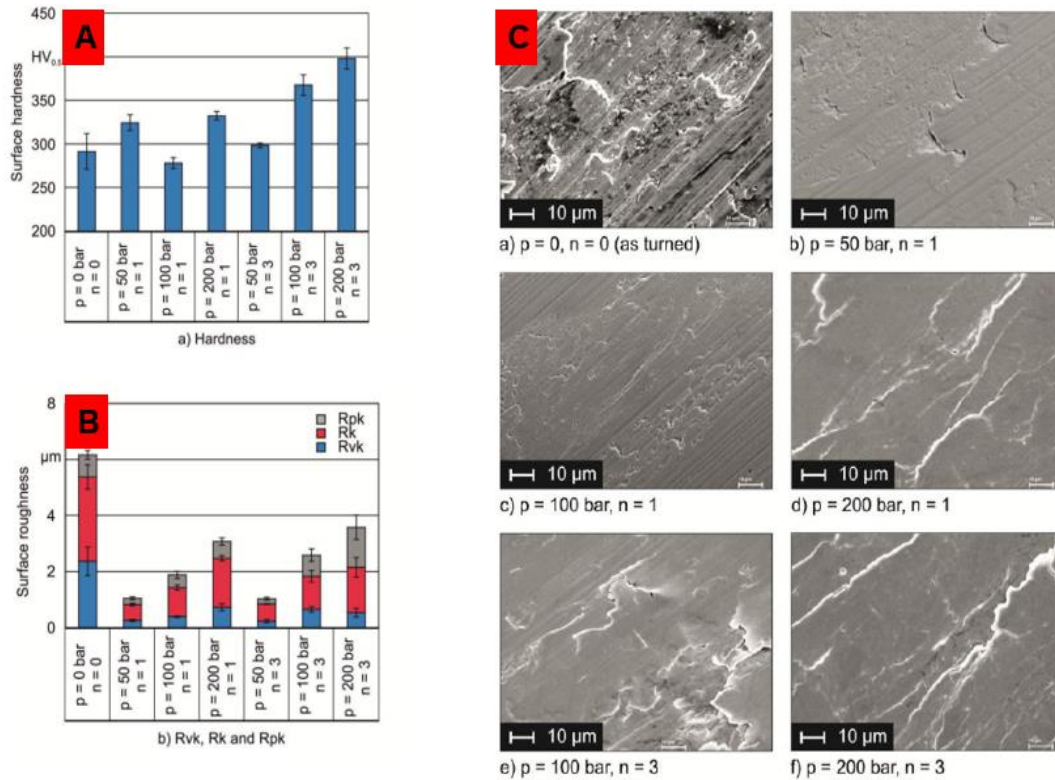


Figure 2-7. Illustration of the effect of loading pressure and NTP on (A) surface hardness, (B), surface roughness, and (C) surface topography. Adapted from [74] with permission from Elsevier.

However, none of the research yet examined has considered the effect of cooling nor lubrication upon the surface integrity of the processed workpiece. The only major attempt to understand the effects of lubrication on the burnished surface integrity was by Hassan [84], in which seven different lubricating oils with varying viscosity were studied. It was noted that while the use of a lubrication during processing improved the surface quality in terms of roughness and hardness, by reducing temperature and contact wear associated with a reduced coefficient of friction, the viscosity itself had no measureable effect. The effect of cooling (CO₂) during burnishing was examined by Meyer [85]. Liquid CO₂ was externally applied at the contact interface of the tool and workpiece, and the resulting surface integrity was compared to that achieved by dry burnishing. It was discovered that the use of CO₂ cooling facilitates an increase in the hardening potential of

the material, but at the expense of increased material embrittlement due to the excessively low temperatures. This in turn lead directly to increased surface R_a values. Similar results were found by Grzesik & Zak [86] in which workpieces were pre-cooled with liquid CO₂ before burnishing. In both CO₂ cooling investigations the material studied was *AISI 5140* steel, and while direct comparison of experimental results is complicated due to the varying diameter of their burnishing tools, external application displayed slightly better results. Pu et al. [87] and Huang [88] studied the effects of external cryogenic (LN₂) application upon the surface integrity produced via 2D multipass burnishing of *AZ31B Mg* and *Al 7050* respectively. In the former application of cryogenics allowed for the creation of nanocrystalline surface layers during dynamic recrystallization, which in large part explained the vast improvement in residual stress and corrosion resistance displayed by cryogenically processed samples. While the later explored the microhardness variation with depth for a variety of processing parameters, and in all cases LN₂ application facilitated vast increases in microhardness relative to dry burnishing. A summary of these findings is illustrated in below in Table 2-2, where SQ, MH, and RS respectively denote surface quality, microhardness, and residual stresses.

Table 2-2. Summary of experimental burnishing research.

Author(s)	Material	Tool Geometry	Cooling/Lubrication	Surface Integrity
Abrao (2014)	<i>AISI 1060 Steel</i>	Spherical ($\phi=6.35$ mm)	NA	SQ, MH, RS
Altenberger (1999)	<i>AISI 304 SS</i>	Spherical ($\phi=6.6$ mm)	NA	RS
Altenberger (2012)	<i>Ti-6Al-4V</i>	Spherical ($\phi=6.6$ mm)	NA	RS, FL
Drechsler (1998)	<i>Ti-10V-2Fe-3Al</i>	Spherical ($\phi=7.0$ mm)	NA	SQ, MH, FL
El-Khaberry (2001)	<i>Al 6061</i>	NA	NA	SQ, MH, RS
El-Taweel (2009)	<i>Brass</i>	Spherical ($\phi=8.0$ mm)	NA	SQ, MH
El-Tayeb (2007)	<i>Al 6061</i>	NA	SAE 20	SQ, MH
Grzesik (2013)	<i>AISI 5140 Steel</i>	Spherical ($\phi=12.0$ mm)	(CO ₂)	SQ, MH
Hassan (2000)	<i>Al & Brass</i>	Spherical ($\phi=10.0$ mm), Roller ($\phi=13.0$ mm)	NA	SQ, MH
Hornbach (2005)	<i>Ti-6Al-4V</i>	NA	NA	RS, FL
Meyer (2012)	<i>Tool Steel</i>	Spherical ($\phi=6.13$)	CO ₂	SQ, MH
Mhaede (2011)	<i>Ti-6Al-4V, Al 7075</i>	Spherical ($\phi=6.0$ mm)	NA	FL, RS, SQ
Nalla (2003)	<i>Ti-6Al-4V</i>	Spherical ($\phi=6.6$ mm)	NA	FL, MH, RS
Nemat (2000)	<i>Mild Steel, Al</i>	Spherical	Engine oil	SQ, MH
Nikitin (2007)	<i>AISI 304 SS</i>	Spherical ($\phi=6.6$ mm)	NA	RS, FL MH
Prevey (2005)	<i>Ti-6Al-4V, In-718</i>	Spherical	NA	RS, FL
Pu (2014)	<i>AZ31B</i>	NA	LN ₂	RS, Corrosion
Revankar (2014)	<i>Ti-6Al-4V</i>	Spherical ($\phi=8.0$ mm)	Engine oil	SQ, MH
Tsuji (2009)	<i>Ti-6Al-4V</i>	Spherical ($\phi=6.0$ mm)	Water soluble oil	SQ, MH, FL
Wagner (2011)	<i>Ti-6Al-4V, Al 7075</i>	Spherical ($\phi=6.0$ mm)	NA	SQ, MH, RS, FL
Brinksmeier (2008)	<i>Steel</i>	Spherical ($\phi=6.0$ mm)	NA	MH
Shirsat (2004)	<i>Al</i>	Spherical ($\phi=12.0$ mm)	Engine oil	SQ, MH
Hassan (1997)	<i>Brass</i>	Spherical ($\phi=10.0$ mm)	7 Lubricants	SQ, MH

From Table 2-2 it becomes readily apparent that only minimal research has been conducted into the impact of cooling mechanism during processing. This is not surprising, though, as burnishing is generally considered a cold working process, and the importance of cooling tends to be considered only for hot working processes and for cases where tool-life can be drastically improved with improved cooling. However, for most materials, and for *Ti-6Al-4V* alloy in particular, temperature has significant effect upon the material flow stress and microstructural evolution. Thus, it cannot be ignored if one wishes to understand the fundamental mechanisms that define this process. Meyer [85] researched the effects of external liquid CO₂ application and found many benefits to its use, but carbon dioxide exists in its liquid form at -78.5°C, whereas liquid nitrogen boils at -196°C. Huang et al. [88] and Pu et al. [87] studied the effects of liquid nitrogen in multipass 2D burnishing, and Grzesik and Zak [86] examined pre-frozen workpieces using LN₂. However, in literature, no research has been conducted studying external LN₂ application in 3D SPB or MPB of any material. Moreover, what research has been conducted on the effect of cooling did not attempt to understand the physics of how cooling mechanisms facilitate surface integrity refinement. Additionally, very little research has been conducted into the role of lubrication and no published literature examines the effect of hybrid (LN₂+MQL) cooling. Finally, almost the entirety of literature has focused on tool geometries that are spherical in nature with maximum loading pressures of approximately 300 bar. Much larger loading scenarios and possible refinement are possible with smaller tool-workpiece contact regions and higher loading pressures.

2.7 *Numerical Modelling of Machining and Burnishing Processes*

According to Merchant [89], efforts to model machining and/or burnishing processes can be divided into three major categories: Empirical based models, analytic

physics-based models, and predictive numerical simulations such as those based on the finite element method (FEM). Each approach has advantages and disadvantages, and as such one methodology will certainly be more appropriate depending upon the complexity and scope of the problem. As most problems in mechanical and aerospace engineering are inherently non-linear, often involving a combination of heat and mass transfer, fluid flow, thermal and mechanical stresses, etc. [90], a quick review of literature will show that the vast majority of modelling efforts have been primarily numerical based. This is largely due to the fact that complex process physics generally cannot be analytically solved in an efficient manner, and also because FEM simulations are less expensive in both time and resources than extensive experimentation [91]. Consequently, it is no surprise that FEM based methodologies have emerged as powerful tools for the simulation of manufacturing processes [92]. This is particularly true for machining and burnishing, as both entail complex processes with extremely complicated boundary conditions, making accurate analytical predictive models very difficult, and in some cases impossible to construct. Typically, such complexities make FEM based simulations an attractive alternative, as the solutions for governing differential equations can be accurately approximated [93]. Though, if not constructed with care, with FEM the understanding of the underlying physics' that drive this process is lost. Therefore, it is extremely important to have a firm understanding of the mathematical implications of the various design choices, and when possible, supplement the existing FEM coding with physics based algorithms.

For burnishing, almost all analytical or empirical based models have been constructed to predict the burnishing-induced surface quality. Kukielka [94] was the first to develop a purely analytic means of predicting of surface roughness based upon the

burnishing parameters. Though there were certainly shortcomings with the implemented approach, namely ignoring the effect of the initial machined surface quality and defining the material behaviour during deformation as Hertzian and thus completely elastic in nature. It was largely successful, however, in predicting the surface quality trends and their dependence upon the various burnishing parameters, by capturing the smoothing mechanism present during burnishing. Unfortunately, the model's accuracy was severely impacted by the accuracy shortcomings that can be inherent in analytic modelling. Luo et al. [95] improved upon this by considering the initial surface roughness of the machined workpiece. Moreover, a smoothing mechanism was developed based on an elastic-plastic contact scenario, utilizing the assumption that the asperities of the machined surfaces are spherical summits whose height accords with Gaussian distribution, and are continuously and smoothly deformed from elastic, through elastic-plastic, to fully plastic deformation. This is certainly more realistic representation of the material physics at play during processing, and as such is reflected in its increased accuracy with experimental results. Further modification was made by Korzynski [96], in which the smoothing mechanism was developed based on the assumption that the relation between surface roughness and force lead to asperities that maintained the shape of a wedge and the plane which burnishing force acts is dominated by uniaxial compression. Uniaxial compression, however, is more suitable for machined asperities with small semi-angle. In finish machining the semi-angle is quite large because the height of the asperities is quite small compared to the cutting feed. The only analytical effort to predict a surface integrity metric other than surface roughness was conducted by Black et al. [97], in which slip-line theory was used to determine factors such as the energy required for burnishing process, the depth of the

deformed surface layer, and the states of stress and strain induced in this as layer as functions of the tool geometry, applied force, workpiece properties, and the friction conditions at the interface. However, this effort was met with mixed results, as the compressive residual stress and plastic strain results predicted by this model were largely inaccurate in comparison to the experimental results.

Numerical simulations have the advantage of being able to more accurately capture the complexities associated with this process. The modelling of machining processes, whether it be in traditional metal cutting and chip generation, or in chipless processes such as burnishing, are largely differentiated based upon a variety of features. Outeiro [98] lists these as:

- (1) Finite element (FE) or meshless methods
- (2) Formulation type
- (3) Time integration algorithms
- (4) Constitutive and damage models
- (5) Friction models

There are many different software packages (Deform, Abaqus, Ls-Dyna, etc.) available for FE simulation, all of which have different combinations of these features, and thus the appropriate software must be chosen for the specific task at hand. Table 2-3 summarizes these features.

Table 2-3. Summary of modeling software packages and their respective features.
 Reprinted from [98] with permission from Taylor & Francis.

	Deform	Abaqus	LS-Dyna	Advantedge
Formulation	Lagrangian; ALE	Lagrangian; Eulerian; ALE	Lagrangian; Eulerian; ALE	Lagrangian
Algorithm of time integration	Implicit	Implicit; Explicit	Implicit; Explicit	Explicit
Constitutive models	Elasto-visco-plastic: <ul style="list-style-type: none"> • Johnson-Cook • Other models • User routine 	Elasto-visco-plastic: <ul style="list-style-type: none"> • Johnson-Cook • Other models • User routine 	Elasto-visco-plastic: <ul style="list-style-type: none"> • Johnson-Cook • Other models • User routine 	Elasto-visco-plastic: <ul style="list-style-type: none"> • Johnson-Cook • Other models
Damage models	<ul style="list-style-type: none"> • Cockcroft-Latham • Brozzo • Other models • User routine 	<ul style="list-style-type: none"> • Johnson-Cook • Other models • User routine 	<ul style="list-style-type: none"> • Johnson-Cook • Other models • User routine 	
Chip formation techniques	<ul style="list-style-type: none"> • Continuous tool indentation and remeshing 	<ul style="list-style-type: none"> • Node-splitting • Element deletion • No separation 	<ul style="list-style-type: none"> • Node-splitting • Element deletion • No separation 	Continuous tool indentation and remeshing
Chip segmentation?		Yes, but only with Lagrangian formulation		
Friction	<ul style="list-style-type: none"> • Coulomb friction • Shear friction • User routine 	<ul style="list-style-type: none"> • Coulomb friction • Shear friction • User routine 	<ul style="list-style-type: none"> • Coulomb friction • Shear friction • User routine 	Coulomb
Analysis		Coupled thermo-mechanical		

Meshless methods are commonly used in extremely large deformation scenarios, such as in high speed impact and astrophysical phenomena, but due to loss of accuracy and an increase in computational time are very rarely used machining simulations. In this context, the two most common types of formulations are Lagrangian and Eulerian. In the former, the element mesh is attached to the workpiece and follows the material during deformation, allowing for large plastic deformation. However, continuous remeshing is required in order to avoid errors that arise from large element distortion. In Eulerian based formulations the mesh is fixed in space, and the workpiece is allowed to flow through the mesh during simulation. This avoids element distortion problems, but is only suitable for steady-state machining and also requires additional experimental information that may not be obtainable. Additionally, Arbitrary Lagrangian-Eulerian (ALE) combines features of

both formulations. The mesh is neither fixed in space nor attached to the workpiece, but rather is allowed to move independently. This additional flexibility makes it an attractive option in operations that induce large plastic strains. However, no physical separation is possible during chip generation which can make it generally unsuitable for traditional machining simulations. Arbitrary Lagrangian-Eulerian formulations, however, in some scenarios have the potential to alleviate the drawbacks associated with these methods by implementing a computational system in which the mesh is neither fixed in space or attached to the workpiece. Rather, the mesh elements can arbitrarily move so as to optimize their shape, while simultaneously the mesh on the domain and contact boundaries is allowed to follow the material through deformation.

Time integration algorithms are classified as either implicit or explicit and are used to guide the solution method of the governing ordinary and partial differential equations. Implicit algorithms use an iterative approach to predict the future state of a system by performing calculations based on information at its current time and at some future incremental change in time. This allows for very large time steps but can be computationally expensive depending upon the size of the model. Explicit algorithms, on the other hand, predict the future state of a system based only on its current state. Model accuracy thus requires small time steps which are several order of magnitudes smaller in comparison to implicit methodologies, and may not be suitable in dynamic situations in which a large amount of time is necessary for steady-state conditions to be achieved. Constitutive models govern the nature of the stress-strain behaviour during simulation. Purely elastic or plastic, elastic-plastic, etc., are the most common types of material models, and thus a constitutive model must be chosen based upon the material properties, the

loading scenario, and the expected deformation type, and the desired outputs of the simulation.

Friction conditions at the interface of the tool and workpiece are extremely important model inputs during the simulation of machining processes, as they have a large effect upon the magnitude and distribution of the forces and heat generated during contact. Typically, these models are either Coulomb-type where the frictional stresses are proportional to the normal stresses and a coefficient of friction, or based on stick-slip scenario, in which a sticking region is defined by large normal stresses and frictional stresses are assumed be equal shear flow stresses, and a sliding region where normal stress is small and Coulomb's theory can be applied. In either case, most software packages allow for unique user sub-routines to be developed in order to tailor the exact frictional conditions to the specific process being modelled.

A survey of literature reveals that there is approximately a fairly equal distribution of 2D and 3D models constructed to model the burnishing process. Those that seek only to predict surface integrity measures are usually 2D in nature, as the extra complexity and computational time associated with 3D models is generally not conducive to the mesh requirements for surface integrity prediction. Rao et al. [99] and Bouzid et al. [100] performed simulations to predict the burnished surface roughness for aluminium and steel alloys respectively. In the former, a single asperity was modelled in ANSYS APDL with minimal success, with elements constructed as shown in Figure 2-8. While in the latter, elastic and elastic-plastic material responses were compared to experimental results.

However, in both cases the initial workpiece was modelled as smooth surface and thus model accuracy for both was significantly impacted.

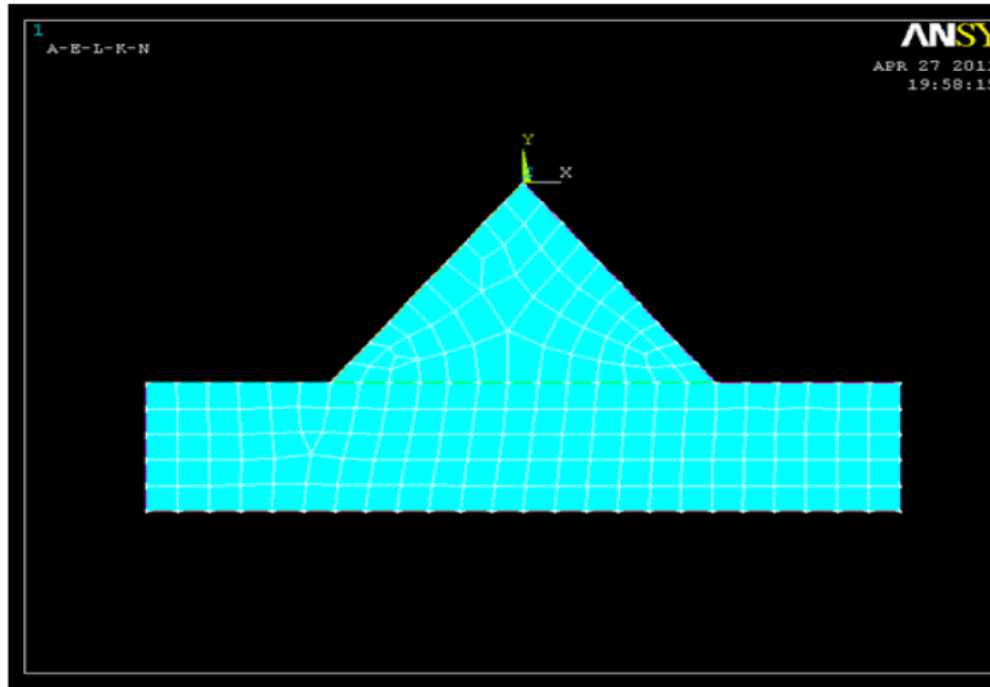


Figure 2-8. FEM model of single asperity in ANSYS APDL. Reprinted from [99] with permission.

Maximov and Duncheva [101] and Roettger [102] improved upon this by including the initial workpiece surface roughness with more accurate results in comparison to experimental values. In the latter, DEFORM was used with a force-control boundary conditions, while in the former Abaqus/implicit was used with displacement boundary controls. For burnishing, regardless of the desired predictive capability of the model, these two forms of boundary controls are the most common found in literature. In Figure 2-9, some of the boundary conditions used for the prediction of surface roughness using a displacement-control mechanism are shown.

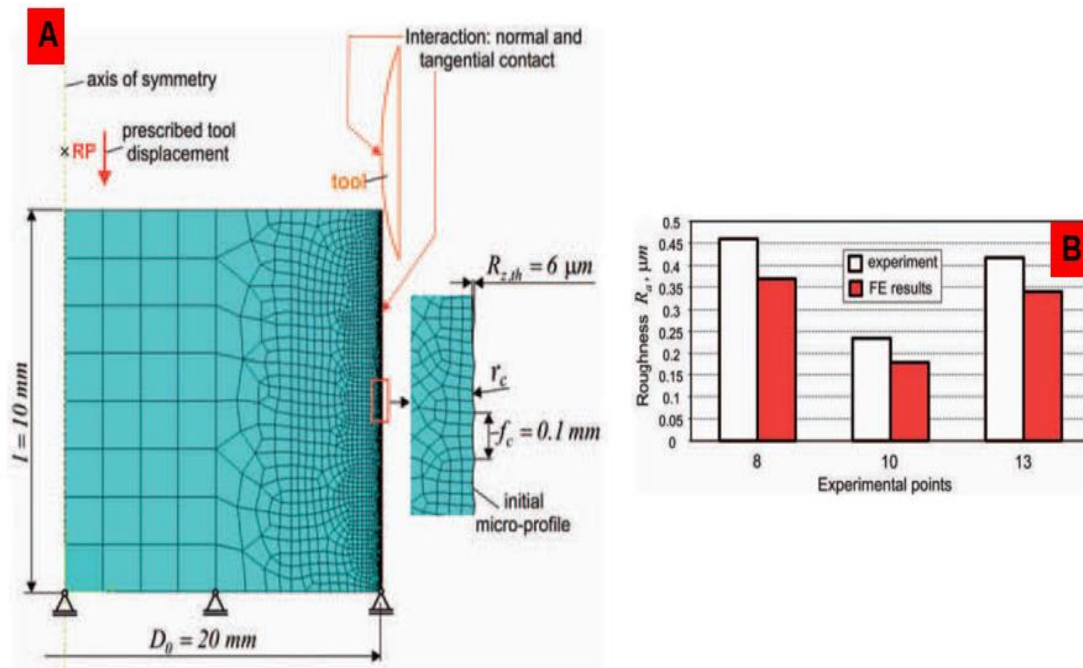


Figure 2-9. Depiction of (A) workpiece surface including its initial roughness profile and (B) a comparison of experimental and simulated results. Adapted from [101] with permission from SAGE.

Most reported FEM models are constructed with the aim of predicting the burnishing-induced surface topography and/or residual stress state. This stress tensor will always have axial, tangential, and radial components, thus requiring a 3D representation to fully capture the stress state. However, the computational time necessary for 3D simulations, particularly those utilizing elastic-plastic constitutive models, can be extraordinarily long. Some researchers have used simplifying assumptions to translate fully 3D models into 2D models under a plane-strain assumption, and discovered that some residual stress components can be predicted with high accuracy with this methodology [103, 104]. Nonetheless, to accommodate the large size of 3D models, explicit time integration is used almost exclusively to reduce computational time in these cases [105-

107], though implicit integration was used by Zhuang and Wicks [108]. A comparison of implicit and explicit time integration was conducted by Sayahi et al. [109] and the authors discovered that mathematically both methods predicted the residual stress field with equal accuracy. However, implicit integration required significantly more computational time as expected.

In these models, the primary motivation was to correlate the implemented burnishing parameters with the predicted residual stress state. Their primary points of differentiation being the constitutive models implemented and the material itself being studied. Regardless of whether 2D or 3D models are utilized, the most accurate modelling methodology tends to be those that utilize displacement-based control schemes. A good example of this is presented in Sartkulvanich et al. [103], where the burnishing tool plastically indents into the material surface to a prescribed depth. The workpiece is then mechanically unloaded as the tool-workpiece contact is broken. At which point the burnishing tool shift based upon the implemented feed rate. This process is then repeated for the duration of the burnishing simulation. A graphical depiction of this process is shown below in Figure 2-10, along with the simplifying assumptions used to project 3D burnishing mechanics onto 2D plane.

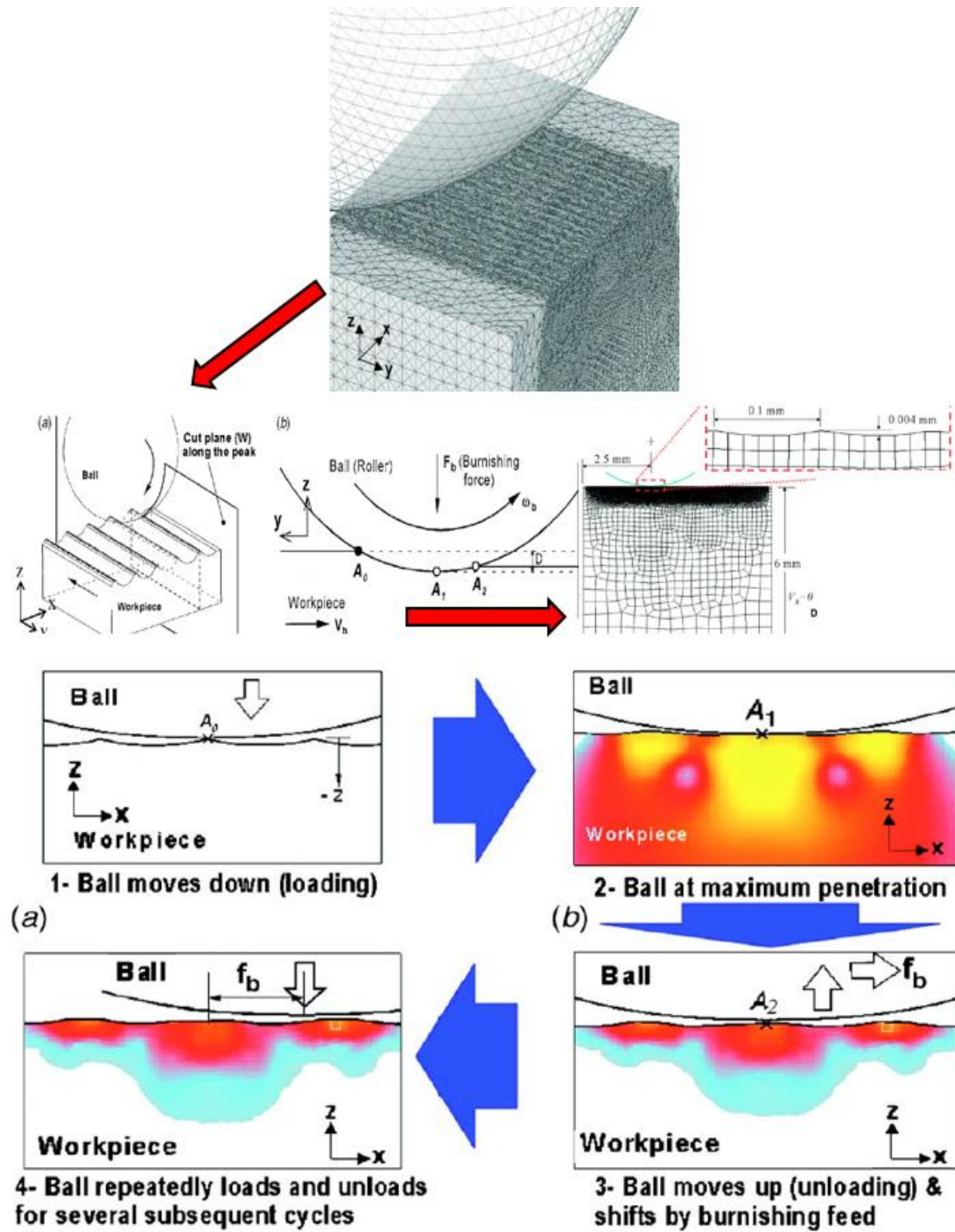


Figure 2-10. Projection of 3D burnishing mechanics onto 2D plane and loading/unloading scheme used to predict residual stress fields developed during burnishing. Adapted from [103] with permission.

Some common threads exist amongst the FEM models reviewed and should be noted. First, all utilized a Lagrangian based formulation. The high burnishing induced strain and strain-rates make this a logical choice. As powerful remeshing techniques can continuously build new surfaces as the tool is fed along the workpiece. Additionally, all utilized a spherical tool geometry with no emphasis on cooling mechanism. Only one study implemented a coefficient of friction during simulations, as the norm was to simply assume that the contact was frictionless. However, there were some attempts to provide increased modelling fidelity.

Huang et al. [110] studied the effects of cryogenic cooling during multipass 2D burnishing of *Al-7050*, and found a high correlation between the simulated burnishing forces and thermal fields, with that measured experimentally. Yen et al. [111] was the only reported simulation that placed significant emphasis on the frictional conditions present, but unfortunately surface quality was beyond the scope of its designed capability. A summary of these findings are shown below in Table 2-4, where again SQ and RS denote surface quality and residual stresses respectively. Like was observed in the experimental burnishing/deep rolling research, almost entirely no modelling emphasis was placed on the cooling and lubrication mechanisms. As this has a fundamental role in the process-induced surface integrity, the scope and accuracy of both analytical and FE based models that do not include this effect are significantly reduced. Moreover, no constructed models considered the influence of the NTP on the process-induced surface integrity. The lack of any investigation into the effect of these parameters limits the predictive capability and application of these models in industrial applications.

Table 2-4. Summary of burnishing models presented in literature.

Author(s)	Type	Software	2D/3D	Tool Geometry	Cooling	Output
Balland (2013)	FEM	ABAQUS	3D	Spherical	NA	Topography
Huang (2015)	FEM	DEFORM	2D	Cylindrical	LN ₂	Force, Temp
Klocke (1998)	FEM	ABAQUS	3D	Spherical	NA	RS, strain
Beres (2004)	FEM	ABAQUS	2D/3D	Spherical	NA	RS, SQ
Rottger (2002)	FEM	DEFORM	2D	Spherical	NA	RS, SQ
Sartkulvanich (2007)	FEM	DEFORM	2D	Spherical	NA	RS, SQ
Bouzid (2004)	FEM	NA	3D	Spherical	NA	SQ
Zhuang (2004)	FEM	ABAQUS	3D	Spherical	NA	RS
Mohammadi (2014)	FEM	ABAQUS	3D	Spherical	NA	RS
Yen (2005)	FEM	DEFORM	2D/3D	Spherical	NA	RS
Maximov (2012)	FEM	ABAQUS	2D	Spherical	NA	RS, SQ
Rao (2011)	FEM	ANSYS-APDL	2D	NA	NA	RS, SQ
Sayahi (2013)	FEM	ABAQUS	2D/3D	Spherical	NA	RS
Kukielka (1989)	Analytic	NA	2D	Spherical	NA	Topography
Luo (2006)	Analytic	NA	2D	Spherical	NA	Topography
Korzynski (2007)	Analytic	NA	2D	Spherical	NA	Topography
Black (1997)	Analytic	NA	2D	Spherical	NA	RS, strain

CHAPTER 3.

EXPERIMENTAL ANALYSIS OF BURNISHING-INDUCED SURFACE INTEGRITY

3.1 Material Information and Experimental Methodology

Titanium alloys, particularly *Ti-6Al-4V* [5], are ideal material choices for aerospace applications due to their unique combination of high strength at elevated temperatures, low weight, and suitable thermo-mechanical properties [21, 112]. The *Ti-6Al-4V* alloy studied in this analysis was supplied by GE Aviation, Cincinnati, Ohio, with an approximate composition (wt. %) of 6.31% *Al*, 4.06% *V*, 1.16% *Fe*, and less than .25% *O*, *Si*, *C*, *Mo*, and the remainder *Ti*. The as-supplied conventionally wrought material features a bimodal material microstructure composed of primary α -grains with a hexagonal close packed (HCP) crystal structure, and lamellar body centered cubic (BCC) $\alpha+\beta$ colonies [11, 23], as is shown in Figure 3-1. The as-received grain size of the HCP α -phase was determined to be $17.2 \pm 4.2 \mu\text{m}$ as determined using the mean intercept methodology. The average microhardness of the virgin material was measured to be $35.7 \pm 1.2 \text{ HRC}$.

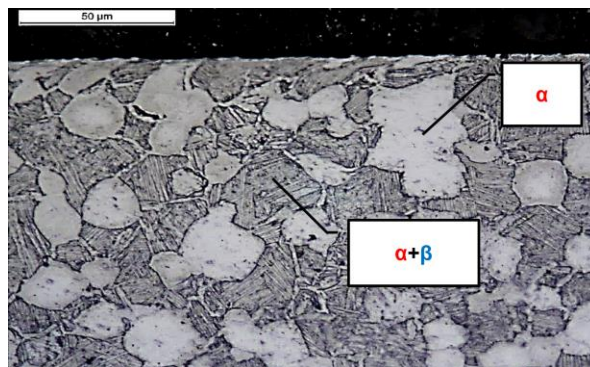


Figure 3-1. As-received microstructure of titanium alloy *Ti-6Al-4V* illustrating its two phase structure.

Burnishing experiments were conducted on a HAAS TL-2 lathe using a pneumatically actuated tool developed by researchers at the University of Kentucky. The system, depicted in Figure 3-2, is capable of delivering a maximum loading force of 2650 N to a tungsten carbide roller with a 1.5 mm radius of curvature. Considering the Hertzian contact area, which is based on the geometries of the tool and workpiece, the maximum available loading pressure is approximately 16 GPa. The unique design of the system employed during this investigation allows for up to 8 mm of travel and at full travel a maximum force deviation of only $\Delta F = 0.14\%$. In this way, the tool itself is capable of following complex surface contours while applying nearly constant loading to the workpiece using CNC turning centers.

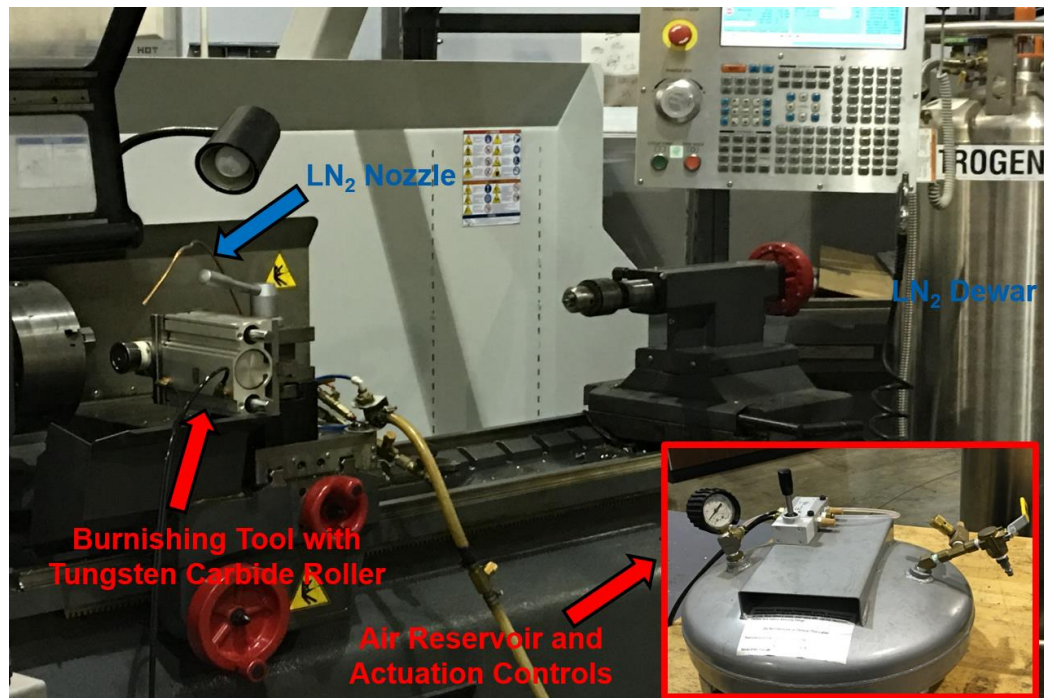


Figure 3-2. Experimental setup for cryogenic burnishing investigation including pneumatically actuated burnishing and LN₂ delivery systems.

Conventional flood-cooled (emulsion), minimum quantity lubrication (MQL), cryogenic (LN₂), and hybrid (LN+MQL) burnishing experiments were conducted using a full factorial design space at loading forces of from 1000 - 2500 N, with burnishing speeds of 25, 50, and 100 m/min and feed rates of 0.025, 0.05, and 0.1 mm/rev. Hybrid burnishing at 1500 N was also investigated using these the additional consideration of MQL flow rate (25 mL/hr and 50 mL/hr). Multipass burnishing experiments (MPB) at 1500 N were conducted for all cooling/lubrication conditions at a fixed speed and feed of 50 m/min and 0.05 mm/rev respectively. Additionally, selected parameters were burnished under dry conditions. With the exception of hybrid burnishing, the location for external LN₂, MQL, and flood-coolant application was the contact interface between the tool and work piece (rake equivalent) as is depicted in Figure 3-3 for cryogenic burnishing.

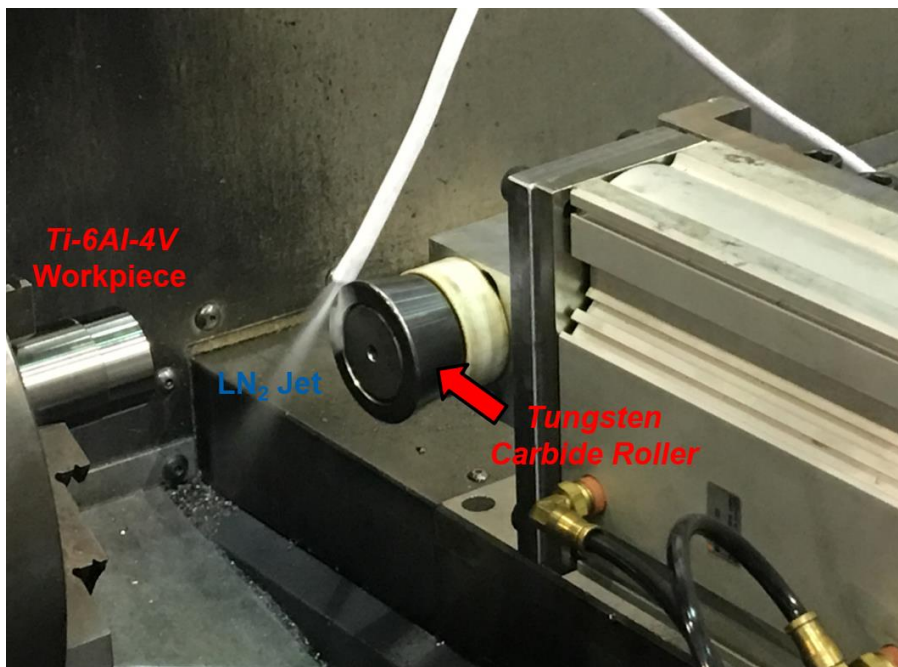


Figure 3-3. Nozzle location for external LN₂ during cryogenic burnishing.

The nature of a hybrid burnishing environment, in which a pressurized air-oil lubricating stream at room temperature is applied simultaneously with high pressure LN₂, necessitates separating the individual flow streams. Otherwise the LN₂ jet dominates the lower pressure MQL, effectively preventing the workpiece from MQL application. By using the workpiece to shield the individual coolant/lubricant streams, both can be effectively applied during processing. The nozzle configuration for hybrid burnishing of *Ti-6Al-4V* alloy is depicted in Figure 3-4, where the MQL nozzle location is in the rake equivalent position. It should be noted that reversing the placement of the nozzles, (i.e., LN₂ in the rake equivalent position) resulted in no measurable difference in the experimentally measured surface integrity characteristics.

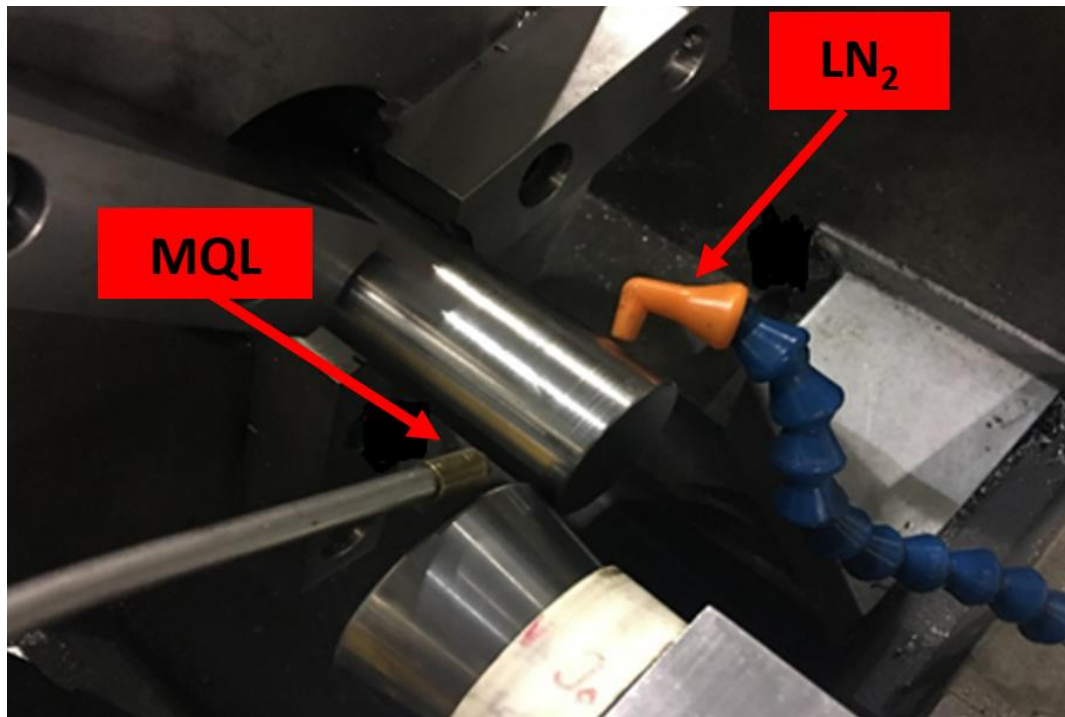


Figure 3-4. Nozzle configuration for high pressure LN₂ and MQL in hybrid burnishing.

Characterization of burnishing-induced surface integrity, including microhardness, surface quality, and material microstructure, was achieved using equipment designed for advanced metallographic and material analysis. Non-contact 3D optical surface profiles of the burnished workpieces were obtained using a Zygo New View 7300 scanning white light interferometer, as is shown in Figure 3-5. The system is capable of a vertical resolution of less than 0.1 nm, facilitating highly accurate surface topography imaging and surface roughness analysis.

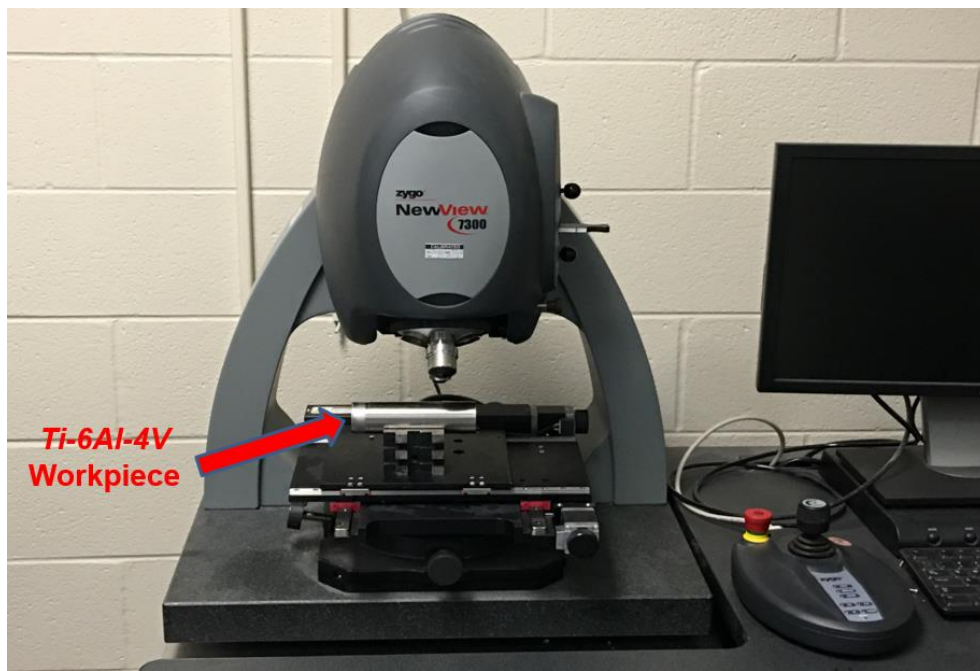


Figure 3-5. Zygo New View 7300 non-contact scanning white light interferometer.

Vickers microhardness measurements were made using a CLARK Digital testing unit with a diamond indenter using a 100 gf loading force and 10 second dwell time. In order to ensure accurate and repeatable measurements, indentations were analyzed using an optical microscope, as this allowed for a higher resolution measurement of the length of the indentation diagonals. All surface and material cross-section microhardness

measurements were made using this methodology. However, near-surface characterization of microhardness required a different technique due to the relative size of the indentation in comparison to the distance to the specimen edge. Accuracy demands that distance between the center of an indentation to the material surface be at least 2.5X the length of the diagonal. When this requirement is not satisfied the measured data is unreliable at best and most likely highly inaccurate. For *Ti-6Al-4V* alloy, the size of the indentation using a 100 gf loading limits measurements to a depth threshold of 25 μm . The only way to obtain data in near-surface regions less than 25 μm to the material surface is to use lower loading forces and smaller indentations. However, in doing so it becomes increasingly difficult to accurately measure the indentation lengths (even using optical microscopes under high magnification). Therefore, nano-indentation using a NanoTest Vantage system was used to characterize the near-surface hardness profiles of burnished workpiece samples. These hardness measuring systems are shown in Figure 3-6.

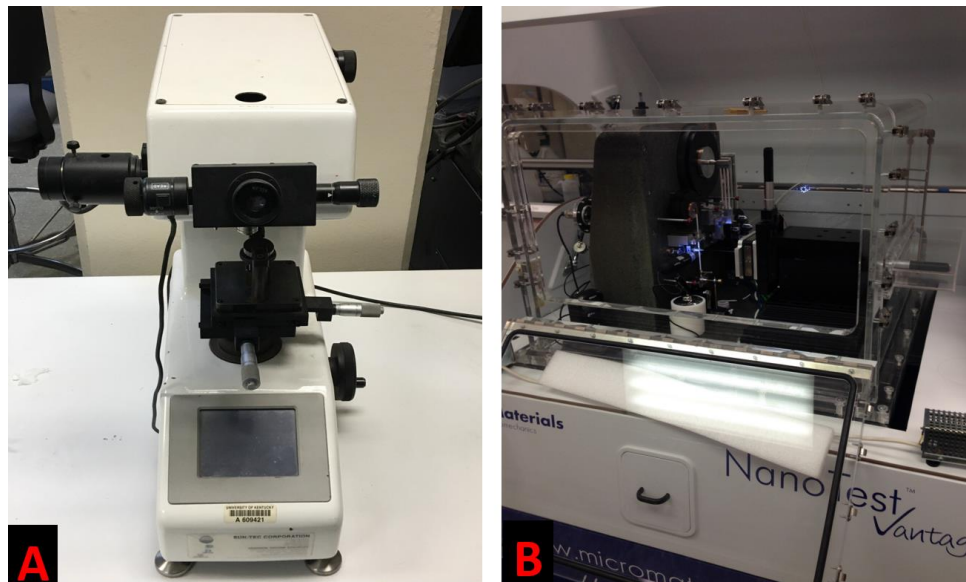


Figure 3-6. (A) CLARK Digital microhardness tester and (B) NanoTest Vantage nano-indenter.

General microstructure analysis was conducted using standard optical microscopy techniques using a Nikon EPIPHOT 300. However, more advanced microscopy techniques, including scanning electron microscopy (SEM) and Focused Ion Beam (FIB) microscopy were necessary to characterize nano-scale grain structures induced in the near surface regions of burnished *Ti-6Al-4V* alloy. These systems are portrayed in Figure 3-7.

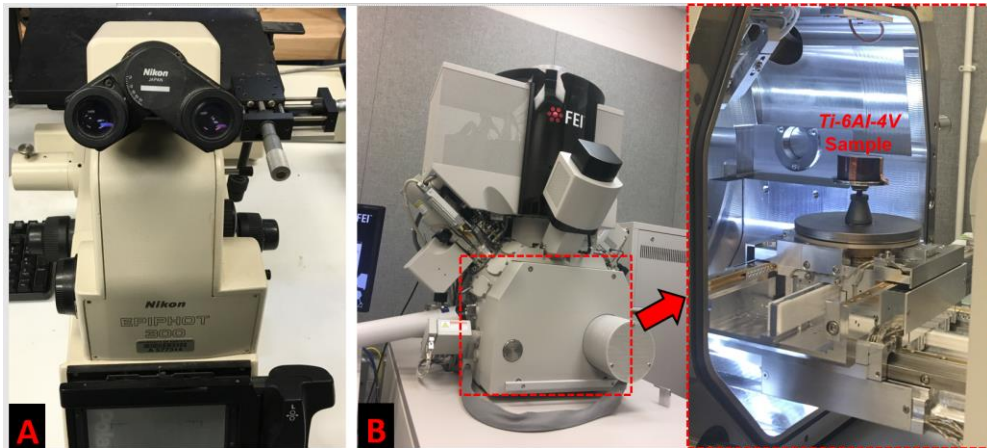


Figure 3-7. (A) Nikon EPIPHOT 300 optical microscope and (B) Focused Ion Beam (FIB) system.

3.2 Characterization of Surface Quality in Burnished *Ti-6Al-4V* Alloy

The surface quality of burnished *Ti-6Al-4V* alloy is in large part defined by the plastically deformed contact area between the tool and workpiece. When the loading pressure exceeds the yield strength of the workpiece, the tool plastically deforms the material surface to a depth prescribed by the loading force. This induces material flow of not only surface asperities, but also the sub-surface, which flows towards the surface as the tool is fed along the workpiece. To quantify this effect, various loading forces were used to plastically deform (indent) a stationary workpiece, after which non-contact scanning white light interferometry was used to characterize the nature of the surface topography and plastic deformation induced from the initial burnishing load. This

effectively isolates the dynamic effect of the loading force on material deformation, from the dynamics effects generated from the burnishing speed and feed. Which is important due to the fact that in literature, the applied loading force was found to be the most influential processing parameter for many of the surface integrity measures.

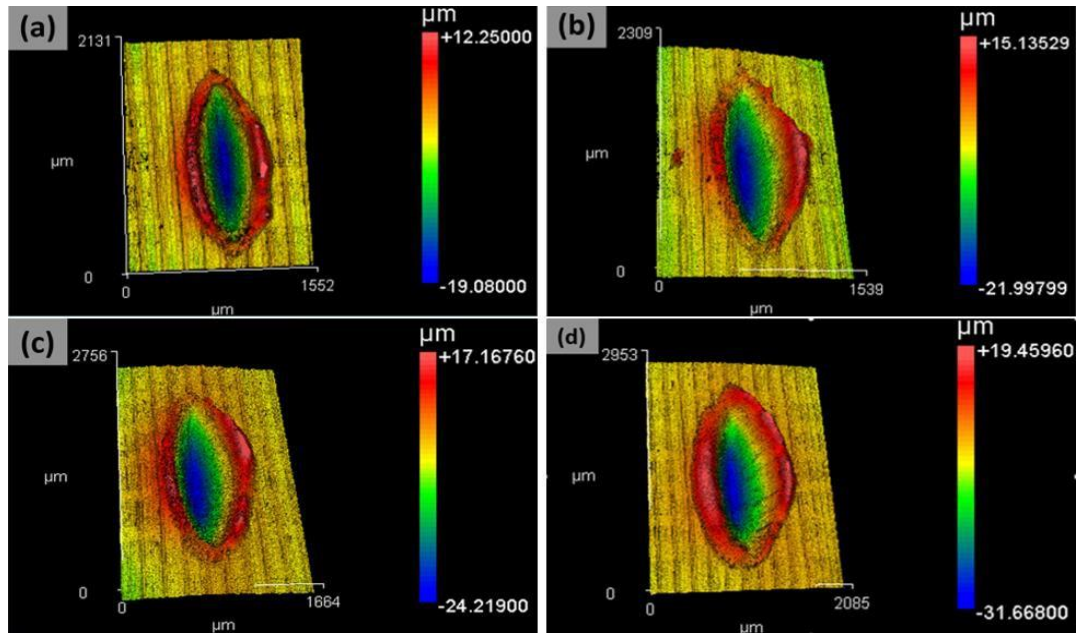


Figure 3-8. 3D topographies of plastically deformed contact areas for loads of (a) 1000 N, (b) 1500 N, (c) 2000 N, and (d) 2500 N.

The plastic behavior observed in the *Ti-6Al-4V* alloy, shown in Figure 3-8, depicts a strong dependency on the implemented loading force. As the load is increased from 1000 to 2500 N, a marked increase in the plastically deformed volume is observed. Though the general shape of the indentation remains unchanged (as the tool geometry was constant), the surface area of the indentation is significantly larger at higher loading forces, which is reflected in a 58.5% increase in the center-line distance to the indentation edge. Additionally, a 65.9% increase in the maximum depth of deformation and a 58.8% increase in maximum pile-up were observed. Insight into the nature of the initial plastic deformation is invaluable to understanding the impact of the other burnishing parameters.

As can be seen in any of the indentations in Figure 3-8, in comparison to the distance between the tool feed-marks (which were generated using a feed rate of 0.15 mm/rev), even at low loading forces the width of the indentation (2X the center-line distance) is notably larger. As such, even high burnishing feed rates will generate significant tool-pass overlap (TPO) on the original plastic indentation. Consequently, at lower feed rates the effect of TPO will be more pronounced. These material flow characteristics are annotated and compared in Figure 3-9.

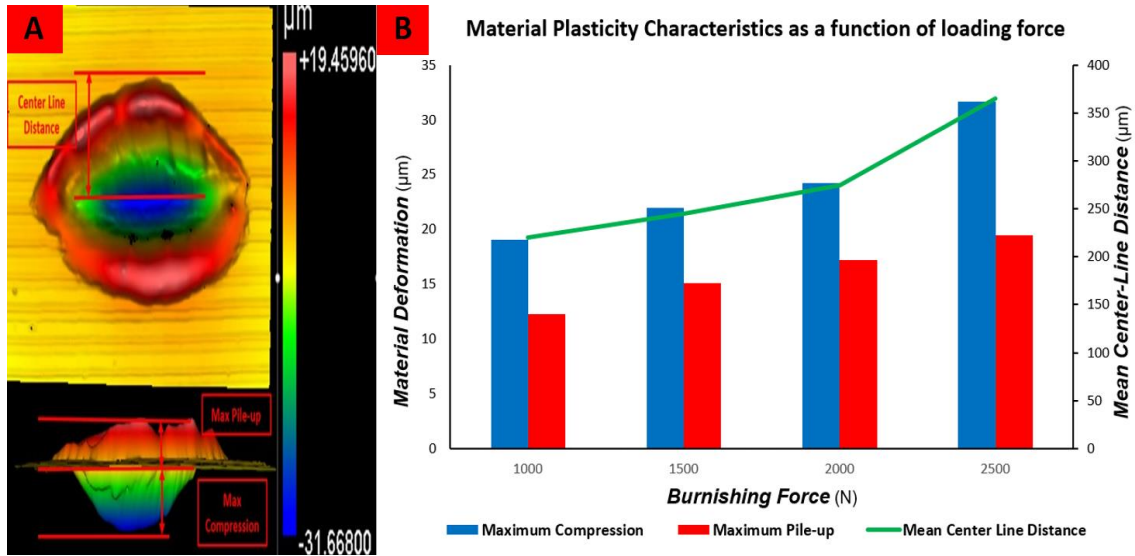


Figure 3-9. (A) Annotated plastic flow characteristics and (B) measured deformation as a function of loading force.

All as-received workpieces were finish machined to an initial Ra of 1.31 μm . In comparison to the machined surface quality, analysis of burnished surface quality revealed a significant reduction in Ra from for all burnishing parameters. In comparing the process-induced surface quality for burnishing experiments conducted with LN_2 and flood-cooling at 1500 N, as illustrated in Figure 3-10, maximum respective Ra reductions of 61% and 64.8% were obtained.

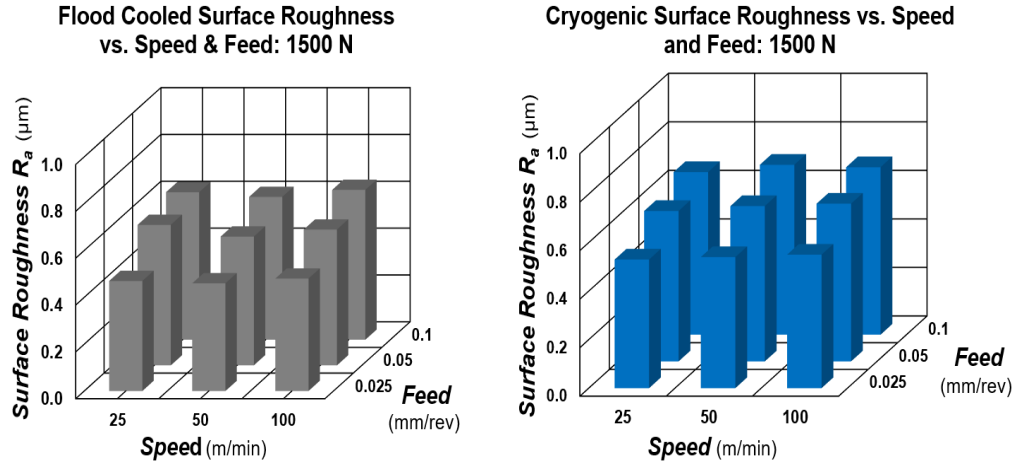


Figure 3-10. Burnished surface roughness using conventional flood-cooling and cryogenic cooling with LN₂.

Furthermore, it was observed that the final surface quality was strongly dependent upon the burnishing feed rate. Specifically, with a constant burnishing force, the burnished surface quality showed continuous improvement with decreasing feed rate. The observed influence of burnishing feed rate on R_a is readily explained by the material plasticity characterization illustrated in Figure 3-8 and the center-line distances shown in Figure 3-9b. Nemat and Lyons [113] showed that for increasing feed rates, the center-line distance between two consecutive indentations grows larger compared to the plastically deformed contact area. Conversely, as feed rate decreases, the TPO on the original indentation contact area increases. This leads to greater surface homogeneity for a given surface area of the processed workpiece, as surface voids and bulges (i.e., material pile-up) are more effectively smoothed, which consequently results in a reduction in R_a .

Considering that *Ti-6Al-4V* alloy exhibits an extremely low thermal conductivity, localized temperature in the burnishing contact zone, which results from the extremely high burnishing pressure and ensuing plastic deformation and frictional effects, tends to accumulate on the material surface. By consequence of the increased heat flux associated

with cryogenic cooling (i.e. increased cooling rate) [54], surface asperities more effectively resist deformation due to an increase in flow stress of *Ti-6Al-4V* alloy with decreasing temperature. Thus, external LN₂ application inhibits plastic flow during burnishing due to a reduction in temperature at the tool workpiece interface. The heat flux associated with flood-cooling, and even more so in near-dry MQL, is significantly lower in comparison. This results in a comparatively higher interface temperature and a thermal softening effect in the *Ti-6Al-4V* alloy workpiece, due to the associated reduction in flow stress. Therefore, the workpiece surface can more easily flow when using conventional cooling methodologies. Moreover, both flood-cooling and MQL generally provide increased lubrication during burnishing in comparison to LN₂, which reduces detrimental frictional based effects such as mechanical adhesion between the tool and workpiece [114]. Both of these factors, namely the increased flow stress and larger interface friction, explain the slightly larger R_a values observed in cryogenic burnishing compared to other analyzed cooling/lubricating strategies at 1500 *N*. However, as shown in Figure 3-11, for SPB the best surface finish was observed in dry burnishing, as the absence of any form of cooling mechanism allows for the material to more readily flow.

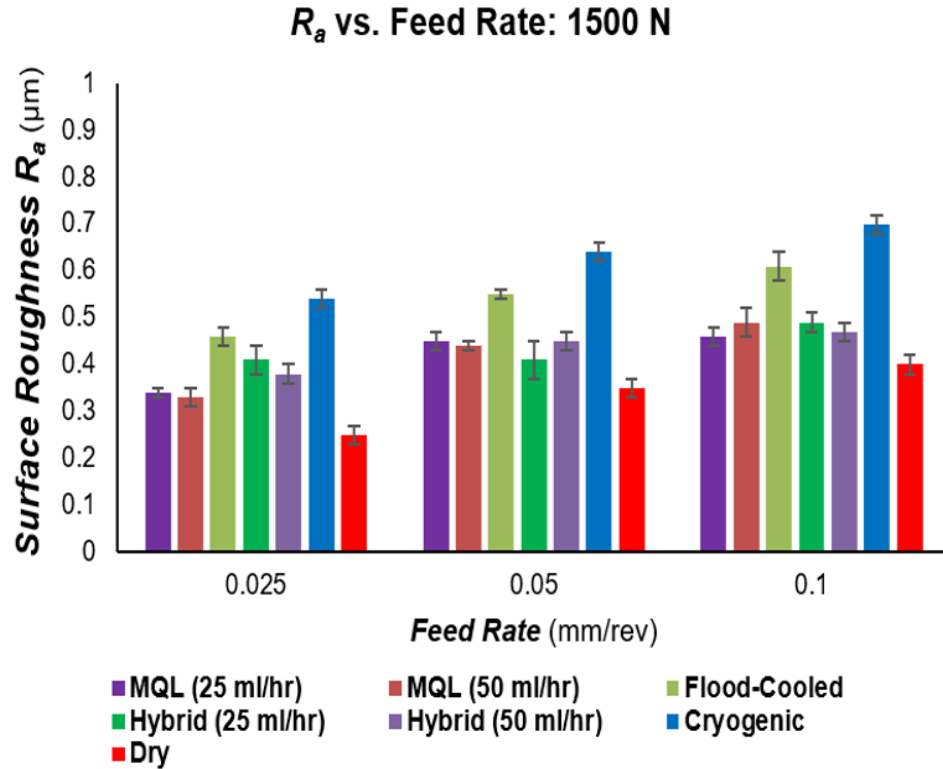


Figure 3-11. Surface R_a for all analyzed cooling and lubrication strategies at a constant burnishing speed of 50 m/min.

As shown in Figure 3-11, MQL as a standalone lubrication mechanism produced improved roughness characteristics compared to flood-cooling at the same loading pressure. Since MQL provides a near-dry burnishing environment with little to no cooling effect, thermal softening allows for greater plasticity of surface asperities, and therefore improved R_a values. Moreover, doubling the MQL flow rate shows no appreciable effect upon the measured surface quality. If the cooling effect in MQL was dominant, it would be expected that increased flow rate would have a strong influence on R_a , as a greater volume of lubricating fluid is capable of carrying away a larger amount of heat. As this was not observed, it reinforces the supposition that increased lubrication is the primary benefit of MQL application. Hybrid burnishing at 1500 N produced significantly improved surface quality in comparison to both cryogenic and flood-cooled

burnishing at the same loading force. In fact, the surface quality is only slightly degraded in comparison to MQL burnishing. This observation underscores the importance of properly controlling the contact friction between the tool and workpiece, as mitigation of mechanical adhesion is just as important to the final surface quality as the materials thermo-mechanical behavior during plastic deformation. Hybrid burnishing introduces a lubricating mechanism, which reduces the effect of friction and adhesion, and consequently leads to improved surface quality at all tested speeds and feeds in comparison to cryogenic burnishing.

When the loading force is increased from 1500 to 2500 *N*, plastic flow likewise increases, as is shown in Figures 3-8 and 3-9b. Specifically, the mean center-line distance increases by 32.9%. This in turn allows for more TPO at a given feed rate and an improved surface finish. Consequently, it can be concluded that at higher loading pressures, the material's resistance to plastic flow, which is more pronounced in cryogenic burnishing, is overcome by the increased energy provided by the extreme pressure of the burnishing tool against the workpiece surface. Moreover, as loading force is increased, the maximum penetration depth and pile-up both significantly increase. This allows for a greater volume of material to be compressed on the burnished surface after a single tool pass. As a result, asperities of the turned surface are more effectively filled, since a greater portion of the burnished surface undergoes significant flow. Shown in Figure 3-12, maximum reductions in *Ra* of 77.8% and 79.3% were achieved for cryogenic and flood-cooled burnishing respectively. Moreover, the previously noted importance of feed rate is again observed.

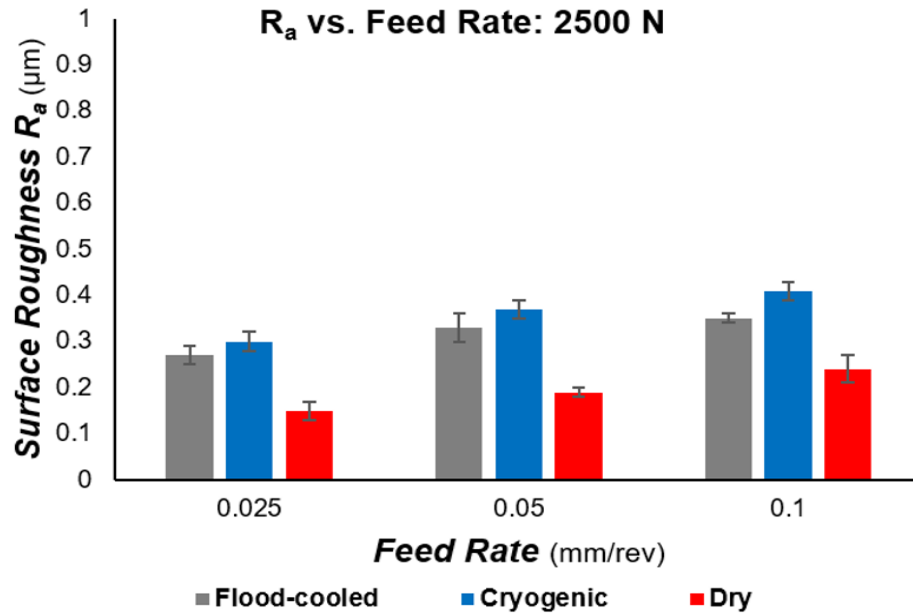


Figure 3-12. Surface quality comparison in flood-cooled, cryogenic, and dry burnishing at 2500 N.

To examine the effect of NTP upon surface quality, burnishing feed, speed, and loading force were kept constant at 0.05 mm/rev, 50 m/min, and 2500 N, respectively. The effect of the NTP upon surface quality has previously been explored by several authors for a variety of materials and tool geometries [115-117]. A common conclusion among the reported literature is that increasing the number of burnishing passes greatly reduces surface R_a by smoothing planar deviations that exist due to surface voids and bulges created by previous passes, effectively doubling the TPO with each successive tool pass. However, it is generally noted that there exists a critical NTP, at which any subsequent tool passes induce excessive work hardening and surface flaking, an effect also known as spalling, which greatly deteriorates final surface quality.

The same behavior described in literature is also observed in this study. For flood-cooled burnishing at 1500 N, the most significant improvement in surface quality occurs

after the 4th tool pass, which is roughly identical to the R_a observed at 2500 N. Thus, roughly the same surface quality can be achieved using significantly reduced burnishing forces by increasing the NTP. This again can be explained by the increasing TPO associated with an increasing NTP. With MQL burnishing, this maximum reduction occurs after only the second burnishing pass. For processing of thin aerospace components, such as turbine or compressor blades, these observations are potentially extremely important, due to the fact that dimensional tolerances have little to no allowance for any part distortion during manufacturing. Utilizing lower loading forces and additional tool passes is advantageous to both this necessity and for surface integrity in general, as it reduces the probability of unwanted part distortion while simultaneously avoiding any decrease in surface quality. However, any further cold-working beyond that generated at the critical NTP, leads to a reduction in surface quality approximately proportionally to the magnitude of the loading force, i.e., more spalling is exhibited at higher loading pressures beyond the optimum number of passes. In Figure 3-13, the burnishing-induced surface roughness R_a observed at 1500 N is characterized as a function of NTP using four cooling/lubrication conditions.

R_a vs. Number of Passes: 1500 N

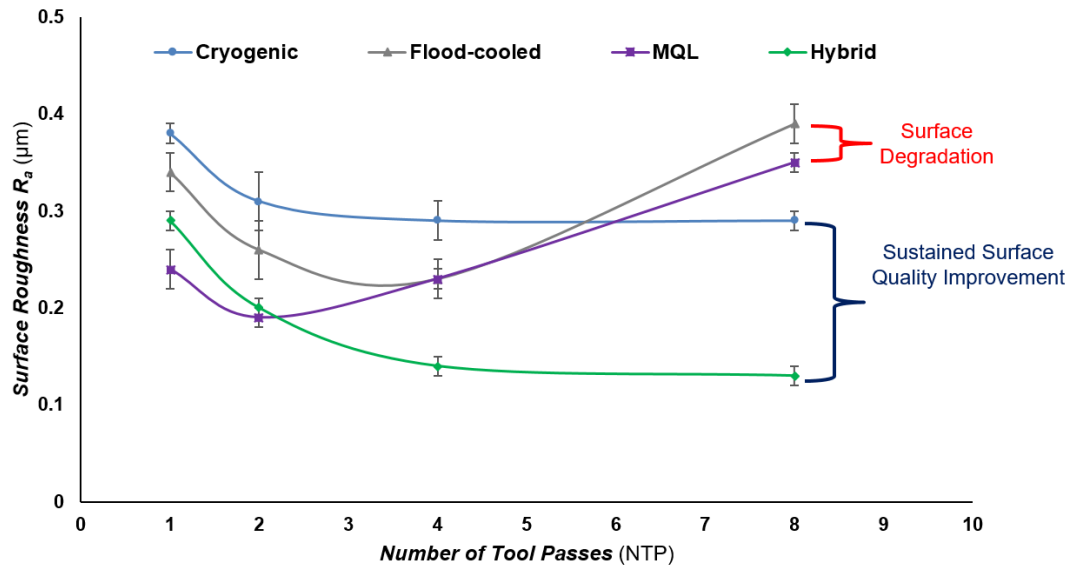


Figure 3-13. Surface finish as a function of NTP for various cooling/lubricating strategies.

Interestingly, cryogenic and hybrid burnishing exhibit a different behavior during MPB than that documented in literature (and also observed in this investigation for flood-cooled and MQL burnishing). In Figure 3-13, it is observed that even after eight tool passes, cryogenic burnishing induced no measurable deterioration in surface quality. The rapid removal of thermal energy from the contact zone mitigates the normally occurring annealing effect of thermal softening. By increasing the yield strength of the workpiece material, cryogenic cooling reduces the amount of catastrophic material failure (i.e., fracture and spalling), and allows for more substantial strain hardening without any deterioration in surface quality. Of course, it is still expected that there exists a critical NTP, beyond which the amount of strain hardening exceeds the yield/spalling strength of the material, leading to increased surface roughness in the same manner as was observed for flood-cooled and MQL burnishing. Practically, though,

as the reduction in R_a observed between four and eight tool passes is only minimal (In fact it is within the statistical margin of error), there would be very little reason to enact an NTP sufficient to induce surface spalling. With hybrid MPB, after four tool passes an approximate nano-level surface finish was achieved ($< 100 \mu\text{m}$). This represents the largest improvement in surface quality of any tested combination of parameters investigated in this study. Application of LN_2 during hybrid burnishing effectively shields the material surface from spalling by increasing the yield strength of *Ti-6Al-4V* alloy, allowing for a significant increase in TPO and continuous improvement in surface quality. These observations suggest that at lower feed rates, which would allow for even a larger TPO per NTP ratio, a lower NTP could be utilized with similar results.

3.3 *Nanostructuring and Microhardness in Burnished Surface Layers of Titanium Alloy Ti-6Al-4V*

Investigation of microhardness after burnishing revealed significant enhancement of surface and subsurface layers in the as-received virgin material. The most significant refinement occurred on the material surface, as is shown in Figure 3-14 for a burnishing force of 1500 *N*.

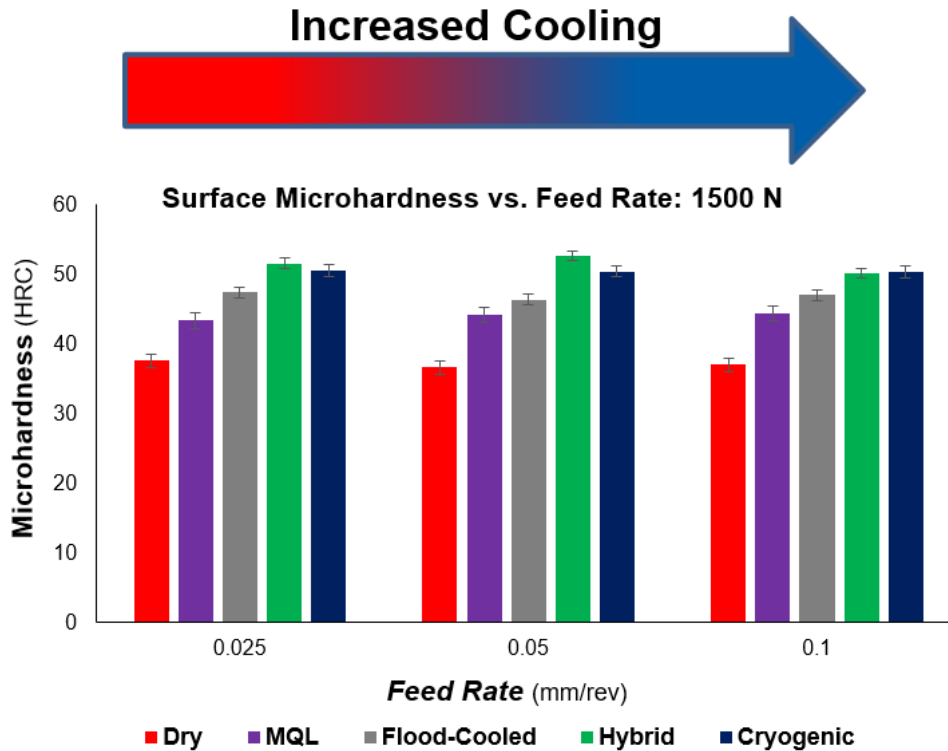


Figure 3-14. Comparison of surface microhardness as a function of cooling/lubricating conditions.

As can be seen in Figure 3-14, cryogenic and hybrid burnishing displayed a maximum hardness increase of approximately 41% from its as-received state, whereas flood cooled and MQL burnishing achieved respective improvements of 25% and 15%. The mechanism through which cryogenic cooling leads to improved surface hardness when compared to MQL and flood-cooling is again hypothesized to be an increased capacity for strain hardening of the workpiece material at low working temperatures. Though plastic deformation during burnishing certainly leads to dislocation multiplication in *Ti-6Al-4V* alloy (As is reflected in the elevated microhardness of the work-hardened surface layers), without a cooling mechanism localized heat accumulation results in the material being locally annealed, i.e., dislocations are continuously relieved through the addition of

thermal energy. This results in reduced flow stress in MQL and flood-cooled burnishing, which ultimately leads to greater plastic deformation at a given loading force and better surface quality, but also reduced work hardening. Application of LN₂ mitigates the effects of thermal softening, allowing for a greater amount of energy to be stored in the rapidly cooled surface layer of the burnished workpiece. This stored energy effectively reduces the amount of thermal energy necessary for dynamic recrystallization (DRX) [118, 119]. This is in contrast to hot working processes, where the onset temperature of dynamic recrystallization (T_{DRX}) is generally believed to occur at approximately 30-50% of the material melting point [120-122], which is also associated with a critical strain value unique to the material. In burnishing of *Ti-6Al-4V* alloy, though local contact temperatures can rise quickly, the interface temperature is certainly below the recrystallization temperature of the material. For burnishing, and other cold working SPD processes, extremely high strains are therefore necessary to generate a sufficient quantity of energy to initiate DRX at temperatures below T_{DRX} . Moreover, in conventional DRX from hot working processes, the recrystallization mechanism is defined by the gradual transformations of sub-grains into nuclei delineated by High Angle Boundaries (HAB). Whereas in DRX driven by SPD processes, which is sometimes referred to as continuous dynamic recrystallization (cDRX), the mechanism is quite different. In cDRX the growth of new grains is defined by increases in sub-boundary misorientations which arise from the continuous accumulation of dislocations [119]. For both hot and cold working however, the minimum grain size is thought to be closely related to the temperature-compensated strain-rate, as is defined by the Zener-Holloman parameter (Z) shown in Eq. 3-1 [123].

$$Z = \dot{\epsilon} \exp\left(\frac{Q}{RT}\right) \quad (3 - 1)$$

where $\dot{\epsilon}$ and T are the respective strain-rate and absolute temperature (K), R is the gas constant ($8.3145 \text{ J} \cdot \text{K}^{-1} \cdot \text{mol}^{-1}$), and Q is the material dependent apparent activation energy (KJ/mol). Thus, cryogenics provides a potentially superior means of producing ultra-fine nano grains by reducing the processing temperature during SPD, which acts to mitigate any relevant thermally activated restoration mechanisms and to suppress the growth of new grains. However, the critical strain threshold for cDRX is drastically increased as the temperature during deformation decreases, and therefore an ever increasing level of strain energy is necessary with decreasing processing temperatures below T_{DRX} [119]. Therefore, burnishing with LN_2 has the potential to substantially reduce grain size in comparison to other cooling mechanisms, but the processing parameters must be sufficient to overcome the impact of cryogenic temperatures on the critical strain and temperature thresholds.

Nanostructuring of surface layers have been observed in cryogenic burnishing of Mg alloys [124, 125] and conventional deep rolling of *Ti-6Al-4V* alloy [126]. However, in the former studies, 2D MPB burnishing mechanisms were investigated. Considering the processing parameters and workpiece dimensions, the NTP on the workpiece surface was such that it is questionable if the process could be considered true burnishing. In the latter, nanoscale features were created, but no information was provided regarding the utilized cooling or lubrication mechanisms. Thus, the investigation almost certainly used either conventional flood-cooling or a dry burnishing condition. Moreover, no information was provided regarding the size of the induced nanostructures. In any case, though microstructural evolution was observed in this investigation for flood-cooled burnishing, grain size reduction was limited to the microscale. During cDRX, application of LN_2

facilitates the formation of nanocrystalline surface layers by grain growth suppression, whereas the reduced heat flux in flood-cooling leads to a less effective suppression mechanism and consequently less grain refinement is observed. Figures 3-15 and 3-16 respectively depict the surface nanostructuring produced by hybrid SPB at 1500 N and MPB at 1000 N after 4 tool passes, as obtained using focused ion beam (FIB) and scanning electron microscopy (SEM). With this methodology, an ion beam is used to remove a volume of material in the near surface region of the processed workpiece in such a way that a steady-state cross-section of the workpiece is able to be analyzed. This is a far more accurate technique to analyze specific regions of the workpiece, as it eliminates any potential thermal damage that can arise from sample cutting.

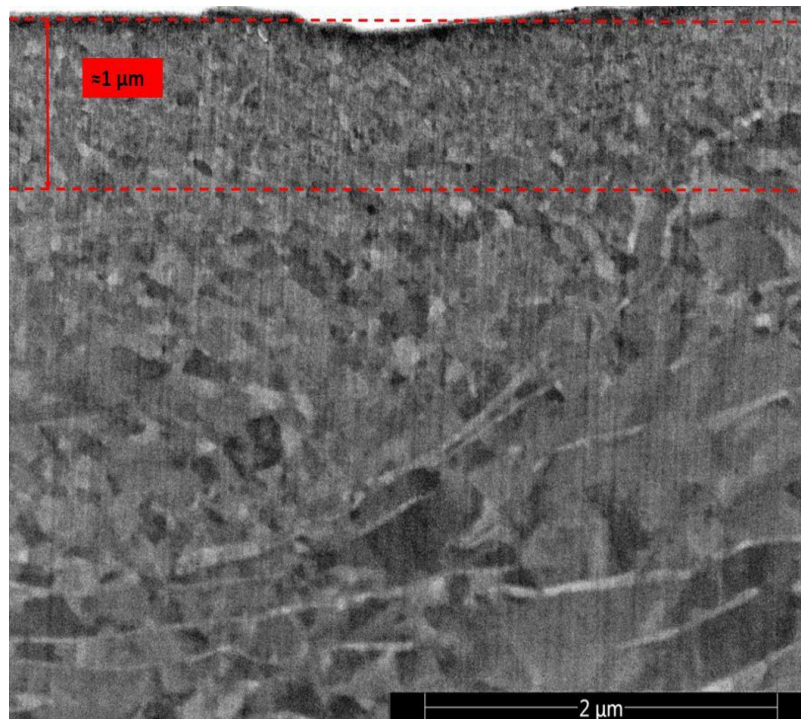


Figure 3-15. Nanocrystalline surface layer in *Ti-6Al-4V* alloy after hybrid burnishing at 1500 N.

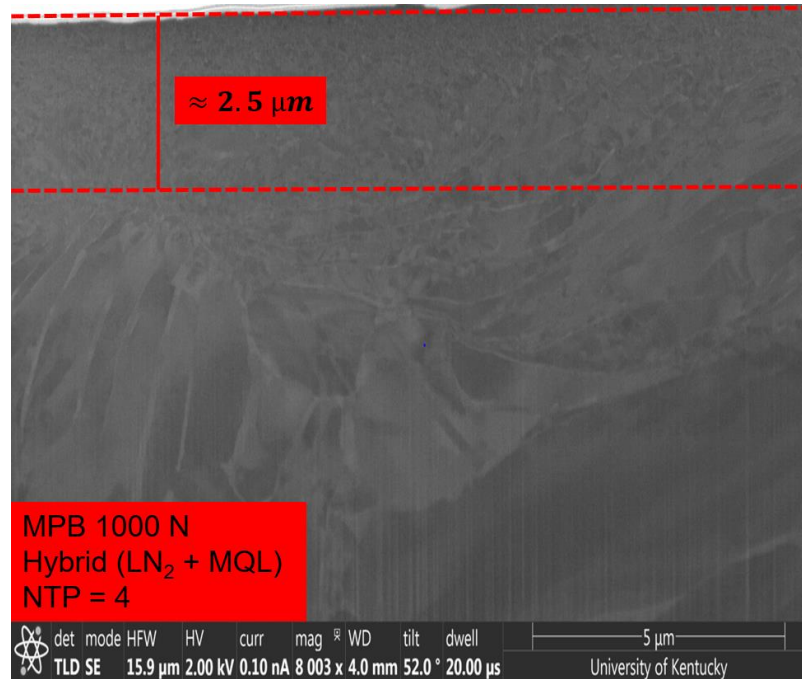


Figure 3-16. Nanocrystalline surface layer in titanium alloy *Ti-6Al-4V* after hybrid MPB at 1000 N after 4 tool passes.

For hybrid SPB at 1500 N, shallow nanostructuring was observed at depths up to 1 μm beneath the processed surface. In this layer the mean grain size varies from 54-212 nm, which impedes dislocation motion across grain boundaries through an increase in grain boundary area, leading to Hall-Petch strengthening (grain boundary strengthening). Whereby dislocation motion from grain misorientations and slip plane discontinuities is further impeded due to the increased grain boundary area associated with the finer crystallites. Larger grain sizes can accommodate an increased number of dislocations, effectively increasing the internal pressure from dislocation pile-up, and thus less force is required to initiate dislocation motion. It is worth noting that for *Ti-6Al-4V* alloy, grain sizes of below 10 nm can sometimes display an inverse Hall-Petch effect, due to the phenomena of grain boundary sliding [127]. However, the normal distribution of nanostructured grains in the layers shown did not display an inverse/softening behavior,

as evidenced by the surface microhardness values shown in Figure 3-14. Beneath the nanocrystalline surface layer, grain refinement becomes increasingly less pronounced due to decreasing strain energy, and consequently the material microstructure transitions to its bulk state. For Hybrid MPB at 1000 N, nanostructuring was observed at processing depths of up to 2.5 μm . While still relatively shallow, this represents an approximate 150% increase in the thickness of the burnishing induced nanocrystalline surface layer in comparison to SPB at 1500 N. In this layer, the measured grain size varied between 79 and 314 nanometers, which is larger than that observed in SPB at higher loading. However, statistical characterization of the relative errors associated with these grain size measurements was such that there wasn't any appreciable difference between the two data sets. Thus, it is impossible to conclude with certainty that one processing methodology was superior in terms of grain size reduction. However, there is little ambiguity in regards to the depth of the nanostructuring. Hybrid MPB, utilizing a 50% reduction in lower force, generates a substantially thicker nanocrystalline surface layer. In aeroengines, the initiation of fatigue cracks from cyclical loading and FOD typically occurs on the surface of employed components. Therefore, the thickness of the refined layer could potentially have significant fatigue life and wear resistance implications.

3.4 Sub-surface Microhardness Variation

For near surface hardness and material characterization nano-indentation techniques were employed. The accuracy of conventional Vickers based microhardness measurements is primarily a function of the indentation size, which itself is determined by the material strength and loading force. For accurate near-surface measurements, the distance between the processed surface and the center of the indentation must be at least 2.5X the length of the average diagonal. For *Ti-6Al-4V* alloy, even at the lowest loading

force, the indentation is too large for accurate measurements closer than 25 μm to the processed surface. Thus, as is illustrated in Figure 3-17, nano-indentation was used to characterize near-surface microhardness by targeted 5 μm steps from the processed surface.

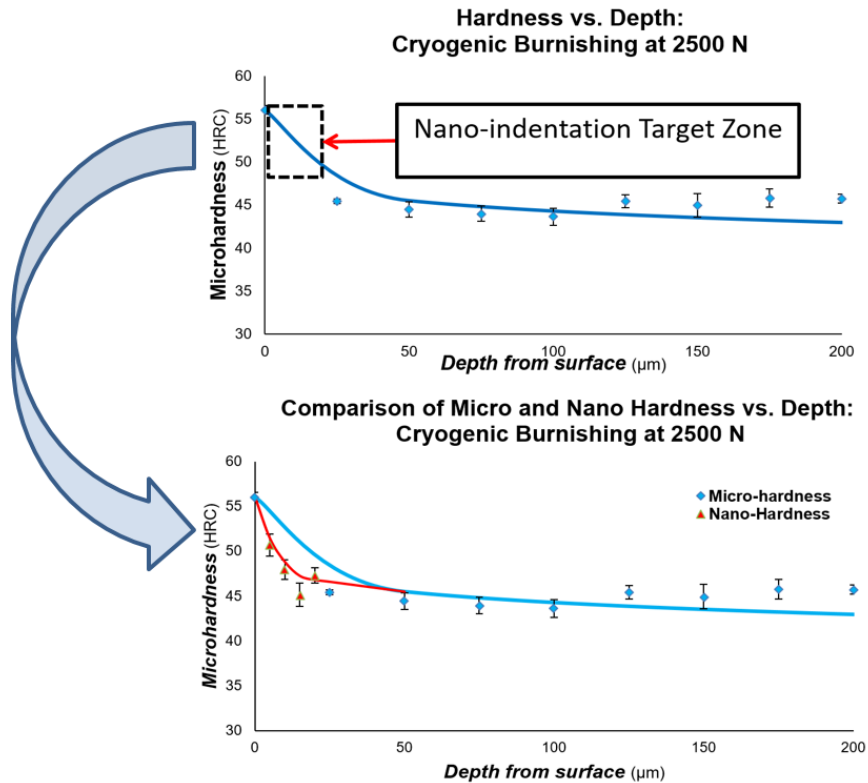


Figure 3-17. Characterization of near-surface hardness using nano-indentation.

Evaluation of sub-surface microhardness revealed no dependence on the implemented burnishing feed rate or burnishing speed. However, the utilized cooling mechanism was found to have a significant impact on the sub-surface microhardness variation of burnished *Ti-6Al-4V* alloy. While all methodologies produced enhanced microhardness from the as-received state, cryogenic and hybrid burnished workpieces exhibited substantially higher microhardness values throughout the affected layer depth (ALD). Figure 3-18 illustrates the variation of microhardness with depth using SPB at

1500 N.

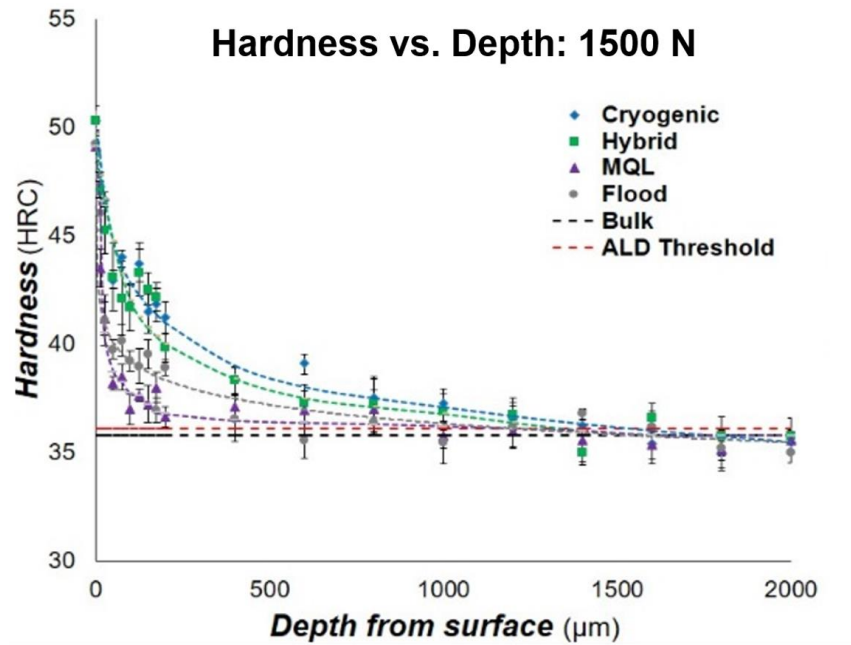


Figure 3-18. Sub-surface microhardness variation as a function of the utilized cooling mechanism in SPB at 2500 N.

Considering that both cryogenic and hybrid burnishing utilize cooling with external LN_2 , which in turn dictates the mechanisms that drive microstructural evolution and material refinement (i.e., cDRX and strain hardening rather than thermal softening), it is no surprise that both conditions exhibit similar microhardness profiles. The application of LN_2 during high strain SPD has been shown in literature to greatly improve the strain hardening capability of titanium alloys [128-130] by mitigating the normally occurring effects of thermal softening. Moreover, the formation of nanocrystalline surface layers leads to a Hall-Petch effect in the near-surface of cryogenically processed *Ti-6Al-4V* alloy. Flood-cooling and especially MQL are less effective at resisting thermal softening effects during SPD, which results in reduced microstructural and mechanical refinement in both the surface and sub-surface of the material. The large variation in observed microhardness

in the sub-surface of the burnished *Ti-6Al-4V* alloy suggests that LN₂ is far more effective at penetrating into the sub-surface of the material, and consequently can more efficiently counteract thermal softening effects beneath the processed surface. Therefore, the combination of these two mechanisms explains the observed difference in the magnitude and depth of the process-induced microhardness.

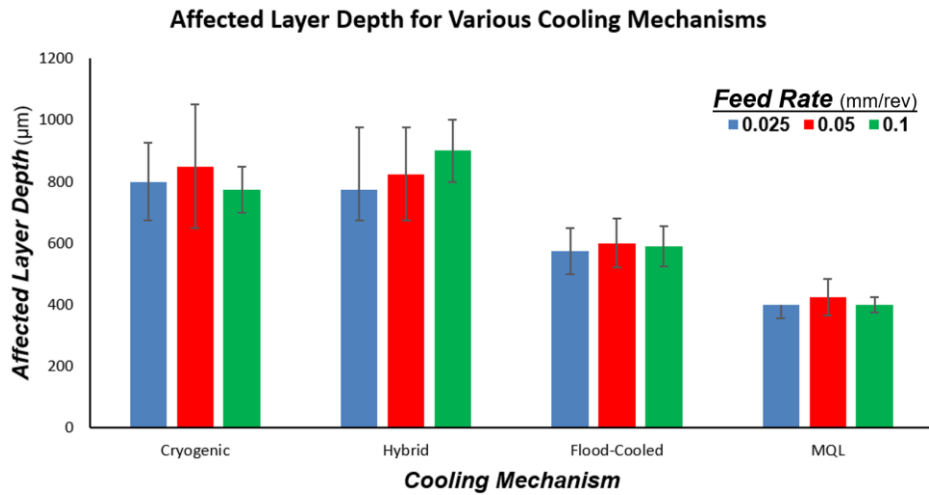


Figure 3-19. Affected layer depth as a function of utilized cooling mechanism for varying burnishing feed rates.

The measured ALD values shown in Figure 3-19 refers to the processing depth at which the material no longer displays enhanced microhardness characteristics. This depth is determined by the point of intersection between the line of best fit of the measured microhardness profile, with a 99.7% (3 standard deviations) confidence interval established around the mean of the as-received bulk hardness (In order to account for material variability). Flood-cooling and MQL displayed the least amount of hardness enhancement, likely due to the increased thermal softening effect, which counteracts grain refinement via cDRX and acts to relieve the dislocation entanglement induced within the lattice network from plastic deformation. This is particularly true in MQL burnishing, which represents a

near dry environment with no available cooling mechanism. While the reduced flow stress at increased deformation temperature facilitates improved surface quality, higher processing temperatures have a detrimental effect upon the imparted microhardness characteristics. Thus, application of LN₂ during cryogenic and hybrid burnishing allows for more significant hardness enhancement at more than twice the depth beneath the processed surface (roughly 800 μm at 1500 N).

X-ray diffraction (XRD) techniques were used to analyze the crystallographic orientation of the HCP- α and BCC- β phases in burnished *Ti-6Al-4V* alloy. In figure 3-20 the relative counts are plotted against the diffraction angle for workpieces burnished under a variety of cooling and lubrication strategies at 1500 N. Evaluation of the as-received virgin material revealed that the HCP- α phase has a preferential texture on the (100), (002), and (101) planes, while the BCC- β phase has preferred (110) orientation. Regardless of the cooling/lubrication strategy, modification to the original texture was observed as the preferential planes of the primary- α were more randomly distributed. This is particularly true for the (100) plane, which was significantly weakened relative to the (002) and (101) planes. Moreover, in the (002) and (101) planes significant peak broadening was observed for all cooling methodologies. This typically is observed as a result of a reduction in the size of the HCP crystallites [131]. However, in cryogenic and hybrid burnishing peak broadening was more extensive, likely due to the surface nanostructuring produced during processing. In fact, in samples burnished with LN₂ the (110) plane of BCC- β was completely submerged by the neighboring and broadened (002) and (101) HCP- α planes.

Phase Broadening Comparison as a function of cooling and lubrication strategies

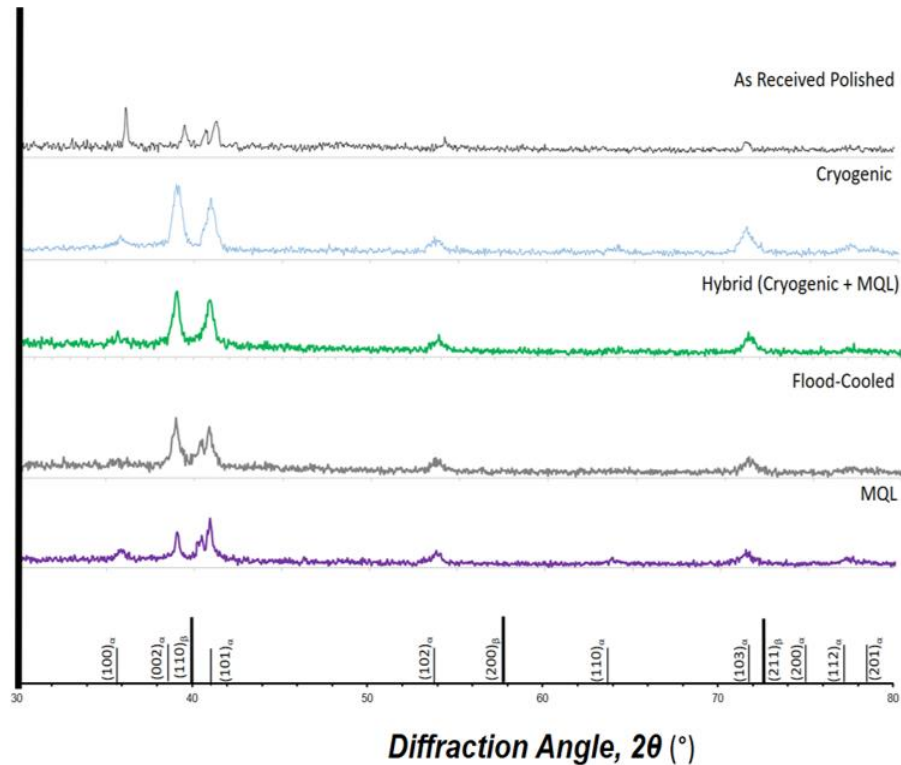


Figure 3-20. Crystallographic orientations in burnished *Ti-6Al-4V* alloy.

The sub-surface microhardness variation exhibited by hybrid MPB at 1000 N, revealed a strong dependence upon the number of tool passes as is shown in Figure 3-21. With increasing NTP and consequently TPO, the material surface and sub-surface becomes increasingly work hardened, as evidenced by the steadily increasing hardness throughout the ALD. The most pronounced increase was observed in the second tool pass, and each successive tool pass thereafter resulted in an approximate 5% increase in the mean hardness of the ALD layer. After 4 tool passes, however, no further increases in microhardness refinement were observed, as there was no observable difference in the sub-surface microhardness variation between four and eight tool passes, as is shown in Figure 3-21. Therefore, a limiting NTP exists at which the density of the dislocation network in

burnished *Ti-6Al-4V* alloy can no longer be increased with additional cold working. In fact, in comparison with SPB at 1500 N, the percent difference in mean hardness was only 0.7%. This is analogous to the surface quality observed as a function of NTP, in which subsequent tool passes beyond four produced only minimal improvements. Additionally, the ALD depth in MPB after four tool passes was approximately 25% deeper than that observed in SPB using a higher burnishing force. Thus, like was observed during analysis of surface quality in burnished *Ti-6Al-4V* alloy, MPB provides a potential means of superior surface integrity while utilizing lower loading pressures. Which further increases the application potential of this technology for processing of thin aeroengine components.

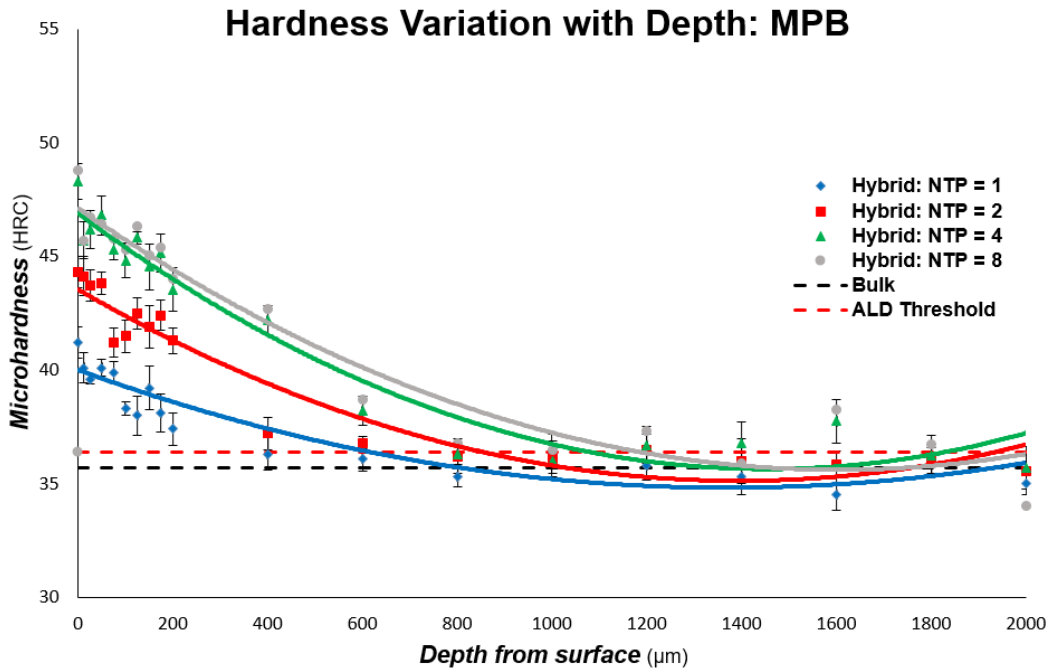


Figure 3-21. Sub-surface microhardness variation as a function of NTP for hybrid burnishing at 1000 N.

3.5 Chapter Conclusions

With this information we now have a more complete picture of the microstructural and mechanical evolution of this material during processing. Regardless of the cooling mechanism, the high pressures utilized during burnishing leads to SPD of the workpiece and consequently dislocation multiplication in the surface layer of *Ti-6Al-4V* alloy. The resulting dislocation entanglement, along with the inherent repulsion and attraction associated with each dislocation, induces significant work hardening in the surface layer of burnished *Ti-6Al-4V* alloy. In cryogenic and hybrid burnishing, application of LN₂ rapidly cools the processed surface layer and mitigates the thermal softening effect observed in flood-cooled and MQL burnishing, allowing for a more substantial accumulation of strain energy within the material microstructure. Consequently, this stored energy reduces the amount of thermal energy necessary to initiate grain refinement via cDRX, which in combination with the large strains generated during burnishing triggers the onset of grain refinement. The growth of new grains during cDRX is suppressed by the rapid removal of thermal energy during LN₂ application, as is described by Zener-Holloman, leading to the formation of nanocrystalline surface layers. Furthermore, the increased grain boundary area impedes the movement of dislocations and a Hall-Petch grain boundary strengthening of the cold worked surface layer is induced. Thus, in cryogenic and hybrid burnishing there are multiple simultaneous mechanisms driving material refinement, which his reflected in the induced nanoscale features and extremely high microhardness values of the processed surface layer, as well as in observed α -phase broadening as revealed by XRD analysis. In MQL and conventional flood-cooled burnishing significant refinement was still observed. However, the reduced cooling in comparison to LN₂ limits the both potential for grain refinement, as well as magnitude of

the induced strain hardening, by encouraging a more prominent thermal softening effect. This is supported by the reduced microhardness in the surface and sub-surface of processed *Ti-6Al-4V* alloy. Moreover, with increasing NTP lower loading forces can be utilized to achieve comparable, or even superior measures of surface integrity improvement. Furthermore, this suggests that reducing the burnishing feed rate could potentially allow for equivalent refinement by either using lower loading forces or by decreasing the NTP. Either way, a path for surface integrity optimization is evident in the experimental results, which can be tailored to the specific application in which the processed material will be employed. For aeroengine components, where material and maintenance costs are high, this would most certainly would entail an optimization strategy that focused on improved functional performance rather than throughput. As such, the likely optimization would prioritize burnishing force reduction (To more easily maintain strict processing tolerances), which would necessitate either decreased feed-rates or increased NTP.

CHAPTER 4.

NUMERICAL MODELING OF MACHINING AND BURNISHING PROCESSES

The mechanisms associated with machining and burnishing are inherently complex phenomena, defined by material non-linearity's and complicated boundary conditions. In order to more fully understand process mechanics and their underlying physics, analytic and numerical based finite element models (FEM) have been proposed in literature. For modeling of burnishing processes, numerical based FEM simulations have demonstrated far more reliability in terms of predicating relevant surface integrity metrics. Additionally, analytic models are for the most part, restricted to predicting the burnished surface quality. Whereas FEM based predictive models have been used to study a wide range of process-induced surface integrity characteristics. The structure of the FEM models reported in literature share several distinctive traits, which impact its scope, accuracy, and solution efficiency. First, essentially no models consider the effects of cooling and lubrication on the process-induced surface integrity. However, as is reflected in the preliminary experimental results, as well in the work of other researchers, these parameters have a significant effect upon a wide range of surface integrity characteristics. These omissions alone severely limit the scope of almost all published models. Moreover, frictional effects and tool geometry are almost completely neglected in most studies. Both, however, have tremendous effect upon the generation of surface tractions and heat partition characteristics, as well the observed plastic flow parameters during processing. These mechanisms in turn play a fundamental role in the process-induced surface integrity. Finally, all reported simulations were based on a Lagrangian mesh formulation. Which is largely due to the fact that it is an extremely powerful, efficient, and accurate formulation

in large deformation processes, as the individual nodes of the element mesh are attached to the workpiece and follow the material through deformation. It does, however, require continuous remeshing in order to avoid element distortion errors, which can lead to increased computational time and potentially unrealistic solutions. Eulerian formulations are seldom used in large deformation processes, due to the inaccuracies that can arise from the mesh being permanently fixed in space.

When possible, numerical models should be grounded in the relevant physics that define the process being simulated. As such, the goal should be to develop comprehensive models which not only reflect the process mechanics and dynamics, but also the necessary fluid flows, heat transfer, and their various interactions with the tool and workpiece. This would allow for a more detailed and comprehensive analysis on the impact of machining parameters and coolant/lubricant flow on surface integrity, as well as facilitate the understanding of the role of surface topographies on gas flow dynamics, fluid-structure interactions, fatigue life, and turbine efficiency, etc. To aid in this endeavor, it is often necessary to supplement commonly used FEM software packages with additional sub-models/experimentation to refine the simulation inputs.

4.1 Numerical Modeling of High Speed Machining

Ti-6Al-4V alloy is a difficult-to-machine material, which typically generates substantial heat on the cutting edge and faces of the tool, as well as upon the workpiece surface. Moreover, due to the extremely low thermal conductivity of the workpiece material, as much as 80% of the total heat in the cutting zone is absorbed by the tool, rather than removed via the chip [132]. These high temperatures can lead to rapid tool-wear and eventual catastrophic tool failure. This in turn reduces machining productivity, by limiting

the MRR that can be obtained without excessive tool replacement, and traditionally constrains cutting speeds to between 30 and 100 m/min [133]. Therefore, mitigation of thermally-activated tool-wear mechanisms would allow for more aggressive machining parameters, reduced tooling costs through tool-life enhancement, and increased machining productivity. Application of LN₂ during machining has the potential to address these issues by rapidly removing the generated heat in the cutting zone. Though there have been some significant efforts to model these effects during cryogenic machining of *Ti-6Al-4V* alloy [134-137], many aspects of the underlying physics have not been properly addressed. This includes to what degree does cooling and lubrication play in the determination of process-induced surface integrity, cutting forces, and overall machining productivity. Therefore, 3D FEM models were constructed in DEFORMTM to simulate high speed machining of *Ti-6Al-4V* alloy. The general structural hierarchy and flow chart of these models are illustrated in Figure 4-1.

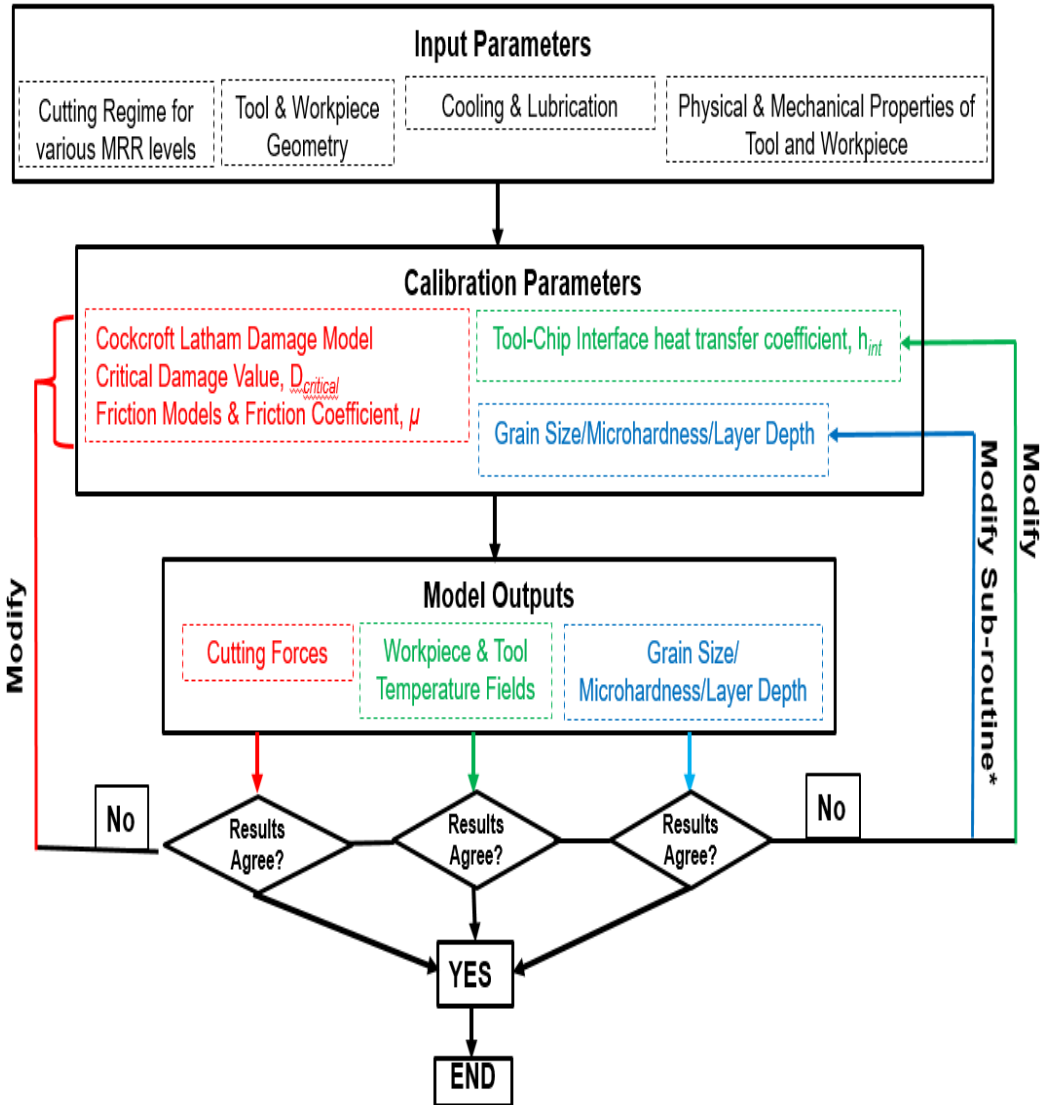


Figure 4-1. FEM flow chart and structural hierarchy.

4.1.1 Overview of Modeling Parameters

Specifically, the process being investigated is high speed milling of *Ti-6Al-4V* with an uncoated solid tungsten carbide (WC) ball nose end mill, as is depicted in Figure 4-2. This particular combination was chosen for a variety of reasons. First, this tooling is typically used for milling sculptured surfaces such as aerospace components. Secondly, the range of MRR's being investigated is quite broad in order to encompass both roughing conditions for productivity studies, as well as finishing simulations to study the effect upon

surface integrity. As such, the tooling solution should be suitable for either type of machining scenario. Lastly, the tool path, as shown in Figure 4-2, is a simple linear cut along the peripheral of the workpiece shoulder. Though a contoured tool path could have certainly been utilized, the added complexity is simply not necessary for the stated goals of the numerical simulation, but in fact could actually obscure them. Additionally, climb milling (cutter rotation is in the direction of the workpiece feed) was utilized as this is generally accepted to be superior to “conventional” milling. This is most certainly true in almost all scenarios since climb milling dictates that chip generation begins at the maximum chip thickness. In this way the force load on the cutting edge is reduced, tool-life is improved, and in general leaves a better surface quality. The tool itself is a general purpose 4-flute 3/4” diameter ball nose end mill, composed of uncoated WC, which is suitable for both rough and finish machining. As the goal was to use a single tool for simulation of both roughing and finishing, this type of generality was necessary in the tooling. Certainly more optimal roughing and finishing results could be achieved using advanced tooling solutions specifically designed for these operations, but in order to ascertain the impact of cooling and lubrication across a range of machining parameters, it is necessary for the tooling to remain constant.

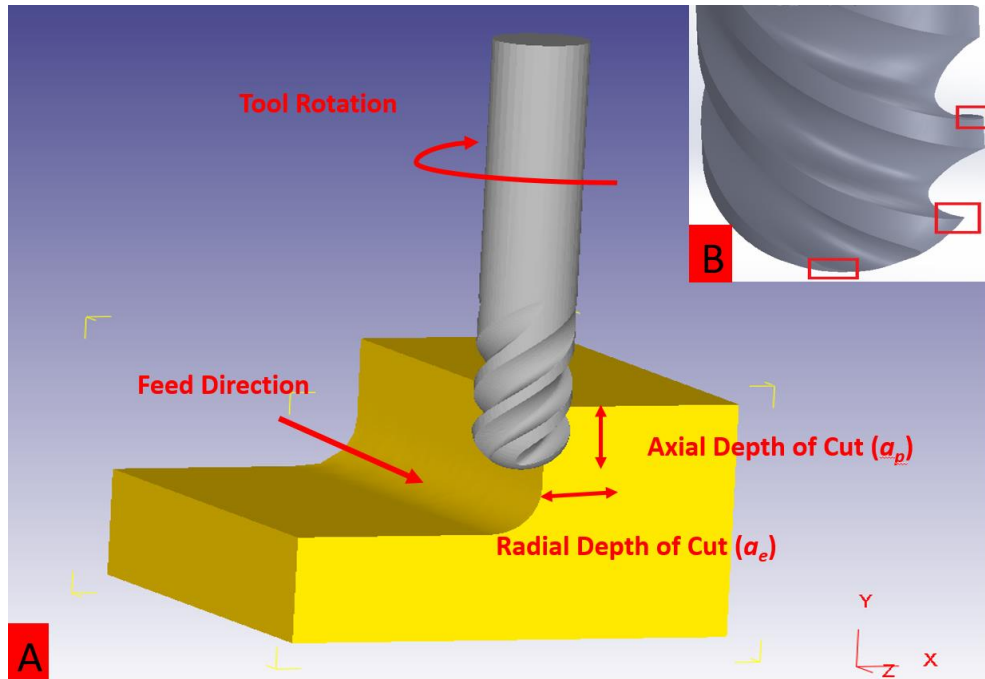


Figure 4-2. Depiction of cutting tool and workpiece geometry.

The CAD model for the end mill selected unfortunately had some inherent issues in its design. As an idealized model, the cutting edge radius was perfectly sharp, as is shown in Figure 4-2b. This can create numerous problems within the simulation due to improper contact functions at the tool workpiece interface, which can lead to inaccurate and sometimes completely unrealistic solutions. This can create many issues if the model is being calibrated, or experimentally verified, through the use of the cutting forces. As the simulated cutting forces are highly sensitive to the tool/workpiece interface conditions. Thus, the cutting edge of the tool was measured using a profilometer to be approximately 55 μm , and the CAD model was modified to reflect this more realistic cutting edge.

The workpiece and tool were modeled as plastic and rigid objects respectively, and each were discretized into 250,000 tetrahedral elements. This value was the result of an iterative mesh sensitivity analysis, where modeling accuracy was carefully balanced

against the solution efficiency. The added complexity of a 3D simulation by its very nature demands more computational time for solution convergence. From this perspective, the primary objective of a mesh sensitivity analysis is to minimize the number of elements needed to maintain an acceptable level of accuracy. As the scope of the model's outputs didn't include consideration of tool deflection or development of stresses on the cutting edges of the tool, nor in the development of residual stress fields of the workpiece, these types of material models provided the most accurate outputs in the most computationally efficient manner. In order to further increase model accuracy, though unfortunately at the expense of solution efficiency, the mesh density was further increased in the cutting zone by use of the mesh refinement windows as is shown in Figure 4-3.

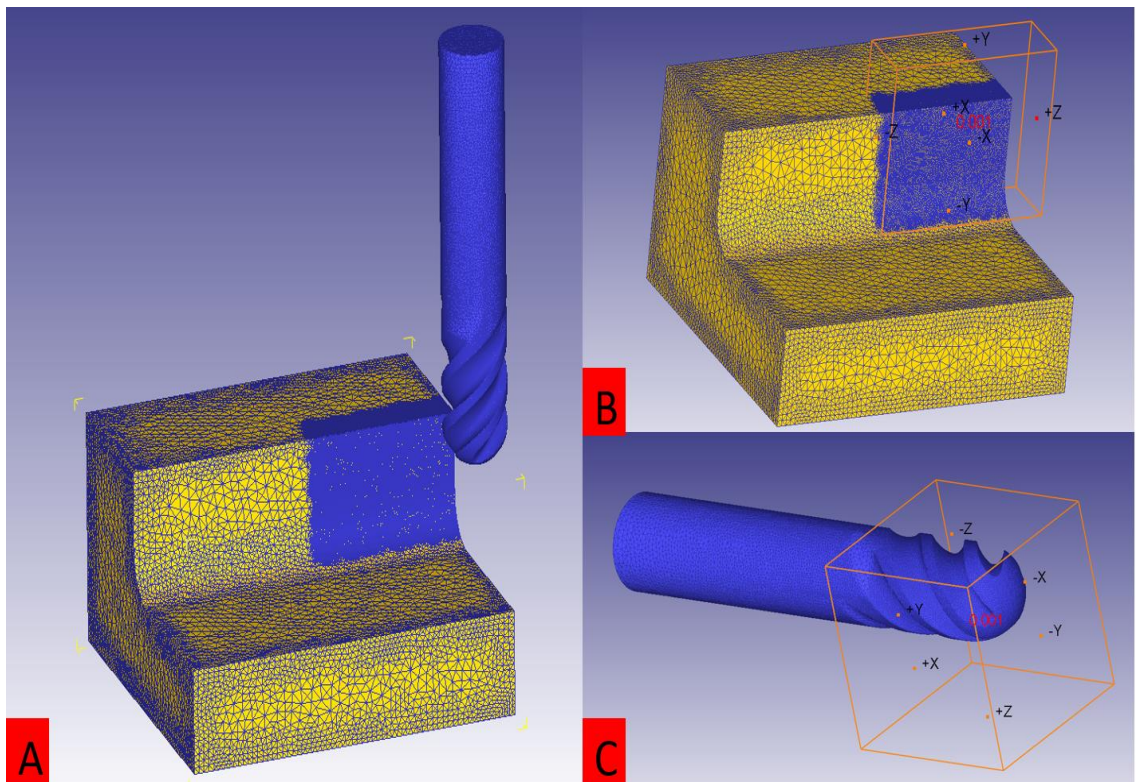


Figure 4-3. (A) Depiction of Element Mesh in the bulk region/cutting zone and implementation of refinement windows on the (B) workpiece and (C) cutting tool.

Within the refinement window the average element length was approximately 0.25 mm as shown in Figure 4-4. Consequently, a displacement based step size was assigned so that each step was 1/40th of the mean edge length. This is far more than the 1/10 ratio recommended by DEFORM [138], but the additional steps were necessary to clearly resolve the cutting forces as a function of the tool rotation angle, and therefore maintain the relevant physics of the problem being simulated. Ideally, an even finer mesh could have been implemented. As this would allow for a more accurate characterization of the simulation outputs on the surface of the workpiece. However, any further reduction in average element length resulted in drastic increases in the solution time. Regardless, the high strain and strain rates associated with high speed machining is an ideal scenario for the utilization of a Lagrangian based mesh formulation. As the element mesh follows the workpiece through deformation, and all stresses and strains are calculated incrementally as nodal locations are updated with each time/displacement step. The extensive mesh distortion that can arise in high strain machining simulations, necessitates frequent remeshing in order to obtain accurate model outputs. Though this too increases the computational time required for solution convergence, it is nonetheless necessary in order to obtain reasonable model outputs.

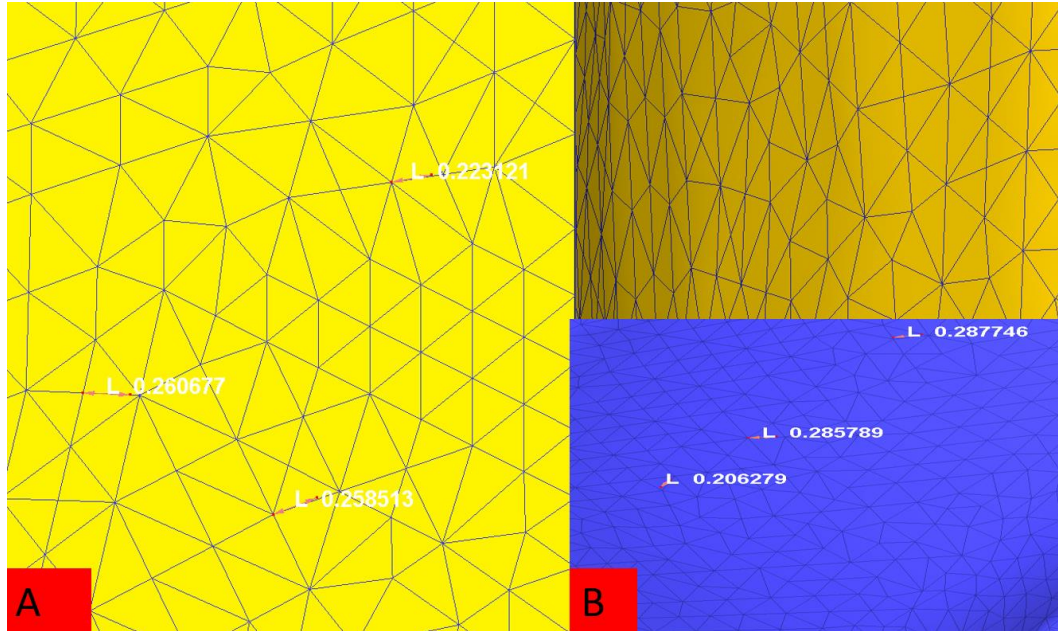


Figure 4-4. Depiction of mesh edge length.

Deformation based boundary conditions were assigned to the workpiece as illustrated Figure 4-5A. The highlighted faces have fixed velocity boundary conditions, i.e. $V_x = V_y = V_z = 0$. The general thermal boundary conditions were implemented on the tool and workpiece as shown Figure 4-5B. All highlighted faces are allowed free convective heat exchange with the environment. The convective heat transfer coefficient was assigned a value $20 \text{ W/m}^2\text{K}$, which is in the normal range of $5\text{-}25 \text{ W/m}^2\text{K}$ typically assigned to environmental heat exchange.

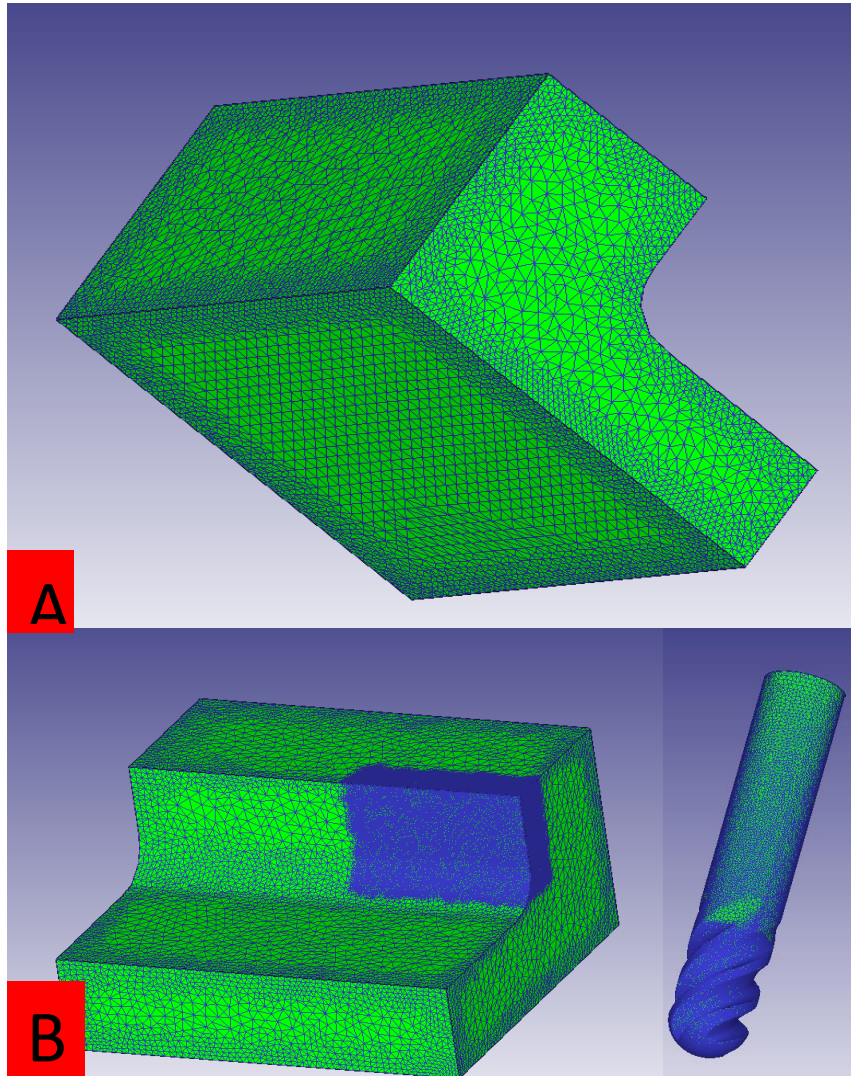


Figure 4-5. Implementation of velocity and temperature boundary conditions.

The type and magnitude of the implemented friction model has a significant effect upon the surface tractions and near-surface thermal fields generated during machining, which in turn influence the flow stress properties of the deforming workpiece and the imparted surface integrity, as well as the magnitude of the cutting forces. There have been many studies on the modeling of friction during machining. Filice et al. [139] examined the impact of various friction models on developed cutting forces, temperature, tool-chip contact length, etc., for a several workpiece materials. The most surprising result from

this study was that the choice of model had essentially no impact upon these measures, and that the magnitude of the coefficient of friction was most influential. Therefore, similar to some other investigations of cryogenic machining [140, 141], in this study a constant shear hypothesis was utilized and is described mathematically as follows (Eq. 4-1):

$$\tau = \mu\tau_0 \quad (4 - 1)$$

where τ is the shear stress formed at the tool-chip interface, μ is the coefficient of friction, and τ_0 is the shear component of the instantaneous flow stress ($\tau_0 = \frac{\sigma_0}{\sqrt{3}}$). The value of the coefficient of friction itself is as varied in literature as the number and types of friction models. Mondelin et al. [142] conducted a series of tribological experiments at different sliding velocities and lubrication strategies, in order to ascertain their impact upon the friction coefficient. The results obtained from this study are shown below in Figure 4-6.

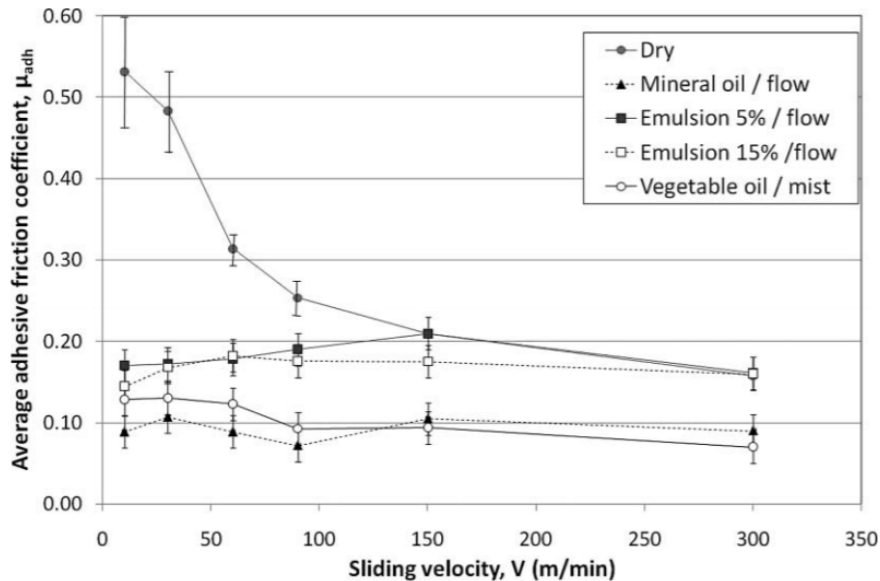


Figure 4-6. Measured friction coefficient as a function of sliding velocity and lubrication type. Reprinted from [142] with permission from Taylor & Francis.

From Figure 4-6 it is observed that the friction coefficient continuously decreases as sliding velocity increases. Dry Machining, however, has no relevant academic or industrial application in regards to difficult-to-cut alloys like *Ti-6Al-4V* alloy, as the tool cutting edge temperature under such scenarios is extremely high, and consequently tool-life is substantially decreased. However, for experiments using oil-based/emulsion flood-cooling, the average coefficient of friction remained fairly consistent regardless of the sliding velocity. Considering these results, in order to simulate the frictional conditions at the tool-chip interface a conservative value of $\mu = 0.25$ was chosen as the starting point for the calibration procedure. For cryogenic machining simulations the research is more limited, and as a consequence there is no general consensus on the proper magnitude of this coefficient. (It tends to be reported anywhere between $\mu = 0.3-0.7$). However, Hong and Ding [9, 143] determined an approximate coefficient of friction of $\mu = 0.3$ for cryogenic machining of *Ti-6Al-4V* alloy by utilizing a hybrid experimental-analytical approach. Additionally, there have been studies where cryogenic cooling during machining of *Ti-6Al-4V* alloy provided better machined surface roughness in comparison to flood-cooling [15, 144]. This is attributed to the reduction in adhesion and tool-wear from LN₂ application. However, this contradicts some of the burnishing experimental work conducted in this investigation and others [17, 18], where better surface quality was obtained using flood-cooled processing. Therefore, there is some measure of uncertainty regarding relative ability of flood-cooling and LN₂ to effectively lubricate the workpiece. This is certainly further complicated by the differing cutting tool geometries, tool types in the case of burnishing, and the specific experimental methodology (LN₂ is particularly sensitive to modifications in nozzle dimensions, distance of nozzle to workpiece, coolant flow rate,

etc.) Therefore, with no conclusive data available, it can be argued that the frictional behavior of liquid nitrogen and flood-cooling provide roughly the same level lubrication at the tool chip interface, and in order to aid in a more direct comparison of the simulated results and reduce the computational time necessary for model calibration, $\mu = 0.3$ was adopted as the starting value for both cryogenic and flood-cooled machining calibration.

Fracture was initiated using a Cockcroft-Latham Damage criterion which states that chip segmentation begins when the largest principal tensile stress over the plastic strain path reaches a critical Damage value (D_{crit}) as is shown below in Eq. 4-2:

$$\int_0^{\bar{\epsilon}_f} \sigma^* d\bar{\epsilon} = D_{crit} \quad (4 - 2)$$

During each time step the software coding determines if this critical value is reached. Once this threshold is met the fracture is initiated by deleting the appropriate element and its connections within the mesh and then smoothed via a remeshing algorithm built in to DEFORM [138]. For these simulations, an initial value of D_{crit} of 245 was chosen based upon work by Umbrello [145], which investigated the effect of D_{crit} upon the simulated cutting forces and chip morphology during machining of *Ti-6Al-4V* alloy.

Many of the material properties exhibited by *Ti-6Al-4V* alloy are strongly affected by temperature. Among the most susceptible properties to temperature dependency are its Young's modulus, heat capacity, and thermal conductivity. The assigned values for these properties are shown below in Figure 4-7.

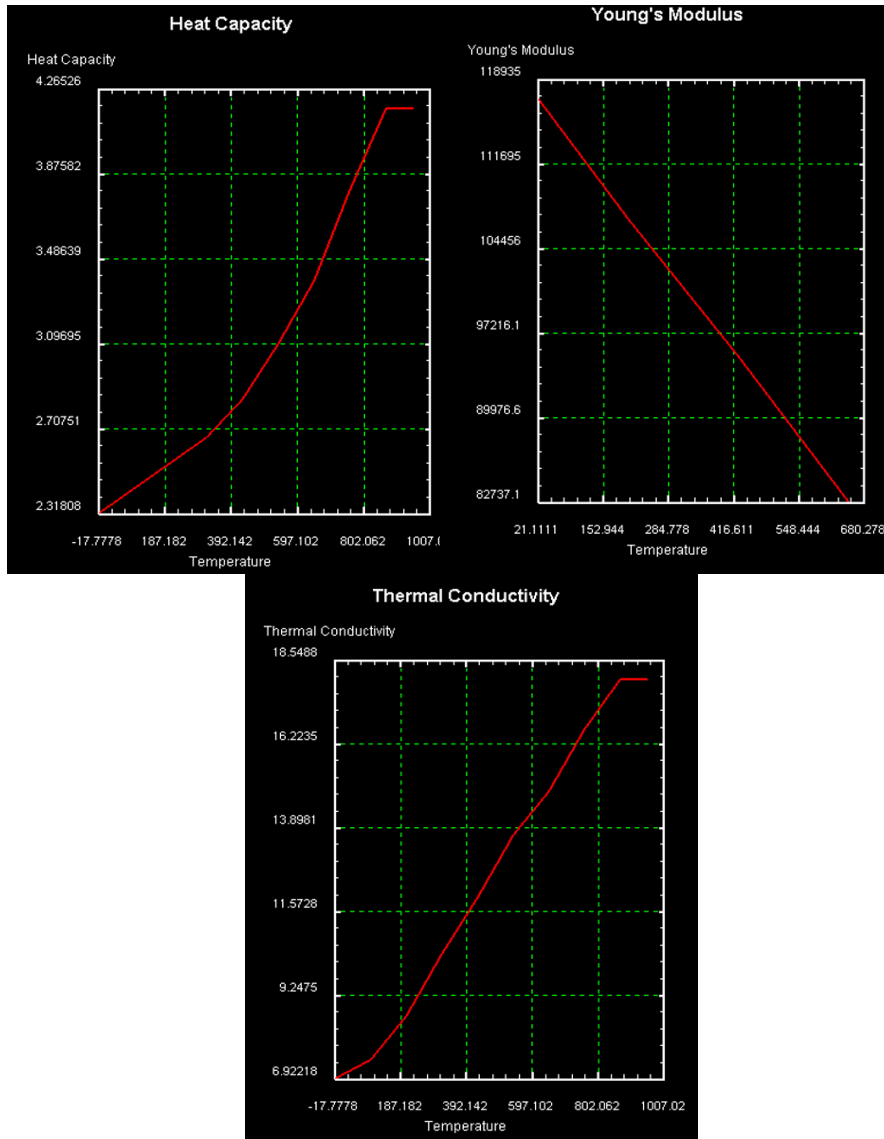


Figure 4-7. Implemented heat capacity, elasticity modulus, and thermal conductivity functions.

4.1.2 Constitutive Material Modelling

Constitutive modeling of *Ti-6Al-4V* alloy during SPD is largely characterized by the flow stress properties it exhibits. It is generally well recognized that a material's dynamic stress-strain response is highly dependent on the temperature and strain rate during deformation. Therefore, in high speed machining of difficult-to-cut alloys, where both high temperatures and strain rates will be present, it is critical that material behavior

in this regime be accurately represented. For *Ti-6Al-4V* alloy specifically, in this type of scenario the effect of temperature is even more pronounced [146]. One commonly used methodology to characterize the material behavior during machining, is to conduct an experimental study utilizing a split-Hopkinson pressure bar (SHPB) to measure these responses at high strain rates and elevated temperatures [147]. SHPB techniques have been conducted to analyze *Ti-6Al-4V* alloy by a number of researchers [146, 148-151] as well as researchers at UTRC. The latter of which was conducted under the following experimental conditions:

$$0.05 < \varepsilon < 0.4$$

$$2003 \text{ s}^{-1} < \dot{\varepsilon} < 7964 \text{ s}^{-1}$$

$$20^{\circ}\text{C} < T < 640^{\circ}\text{C}$$

However, as be seen the conditions used during SHPB experiments while extreme, do not accurately reflect the high strains and strain-rates present in machining operations. This is particularly true in high speed/high MRR machining where strains and strain-rates are typically $\varepsilon > 1$ and $\dot{\varepsilon} > 10^5 \text{ s}^{-1}$ respectively. Thus, it is almost always necessary to have some measure of extrapolation of the stress-strain relationship obtained from SHPB analysis in order to fit the data to more realistic machining scenarios. Implementation of this data into FEM simulations is typically achieved either by using the stress-strain behavior directly as tabulated data, or by fitting the experimental data into various types of flow stress models. DEFORM itself has wide variety of native material models commonly used in the modeling of machining processes. For instance, the Johnson Cook (JC) flow stress model [152] shown below in Eq. 4-3, is widely used for numerical machining simulations of *Ti-6Al-4V* alloy and is a built-in feature of the DEFORM software package

[153-156]. Here A , B , C , m , and n are constitutive constants fitted to the SHPB experimental data, ε , $\dot{\varepsilon}$, and $\dot{\varepsilon}_0$ are the equivalent plastic strain, strain-rate, and reference equivalent strain-rate respectively, and T_m and T_r are the respective melting and reference (typically room) temperatures.

$$\sigma = (A + B\varepsilon^n) \left(1 + C \ln\left(\frac{\dot{\varepsilon}}{\dot{\varepsilon}_0}\right)\right) \left(1 - \left(\frac{T - T_r}{T_m - T_r}\right)^m\right) \quad (4 - 3)$$

This model has been repeatedly shown to be highly accurate when simulating machining processes involving *Ti-6Al-4V* alloy. However, it fails to predict the phenomena of strain-softening, where a decrease in flow stress is observed with increasing strain beyond a critical strain threshold. It is hypothesized that one possible reason for this phenomena is the presence of dynamic recover and/or DRX, which results from the migration and increase in high-angle boundary locations and the consequent increase in dislocation annihilation [156, 157]. Thus, with application of LN₂ the growth of new grains during DRX can potentially be suppressed. Calamaz et al. [156] proposed a modified JC to account for this high strain behavior of *Ti-6Al-4V* alloy, as is shown below in Eq. 4-4 with material constants a , b , c , and d :

$$\sigma = \left(A + B\varepsilon^n \left(\frac{1}{\exp(\varepsilon^a)}\right)\right) \left(1 + C \ln\left(\frac{\dot{\varepsilon}}{\dot{\varepsilon}_0}\right)\right) \left(1 - \left(\frac{T - T_r}{T_m - T_r}\right)^m\right) \left(D + (1 - D) \tanh\left(\frac{1}{(\varepsilon + S)^c}\right)\right) \quad (4 - 4)$$

where $D = 1 - \left(\frac{T}{T_m}\right)^d$, and $S = \left(\frac{T}{T_m}\right)^b$. The Calamaz model does an excellent job in describing the temperature dependent stress-strain behavior beyond the critical strain threshold, and therefore it was implemented in this investigation with the value D , S , and c determined from experiments conducted in Sima and Ozel [154].

However, for cryogenic processing certain considerations must be taken to avoid

mathematically invalid flow stresses which can arise when the term $T - T_r < 0$, which can happen when contact is lost or during the initial steps of the simulation when the cutting temperatures have not risen to equilibrium. When this occurs the term $\left(\frac{T-T_r}{T_m-T_r}\right)^m$ takes on a non-real imaginary value, and the numerical simulation cannot converge to a solution beyond this time step. There are techniques, though, can be used to prevent this from occurring. One method is to conduct SHPB experiments in at cryogenic temperatures. If such data is not available, which is the more likely case, then a conditional if status can be placed on thermal boundary conditions, considering that at steady state temperatures in the cutting zone will almost assuredly be higher than room temperature. Difficulties aside, the high fidelity imparted by Johnson-Cook is the primary reason this model was chosen for these simulations, and shown below in Figure 4-8 are the fitted constants and the flow stress data used provided by UTRC.

Table 4-1. Johnson-Cook Constants from SHPB experiments.

A (MPa)	B (MPa)	C	m	N
743	1335	0.01	1.10	0.319

4.1.3 *Implementation of External Cryogenic Cooling*

Implementation of cooling and lubrication within DEFORM is performed by utilizing localized environmental windows. In these domains, nodes can be assigned specific temperatures and convective heat transfer coefficients as either constants or functions. The windows can be further tailored to reflect different cooling & lubricating scenarios, such as the configuration and number of coolant nozzles. Typically, during machining the LN₂ has a coverage area that covers a circular area with a diameter from 10-

25 mm depending on the distance of the nozzle from the target location, nozzle diameter, pressure, etc. This is generally more than sufficient to cover the entirety of the tool cutting area. Environmental heat exchange windows were implemented, as shown below in Figure 4-8, where the highlighted elements are under the constraints of the implemented thermal boundary condition. It should be noted that the heat exchange window on the WC cutting tool, moves linearly with the cutting tool along the tool path to ensure that the coolant was applied to the cutting zone for the duration of the cut.

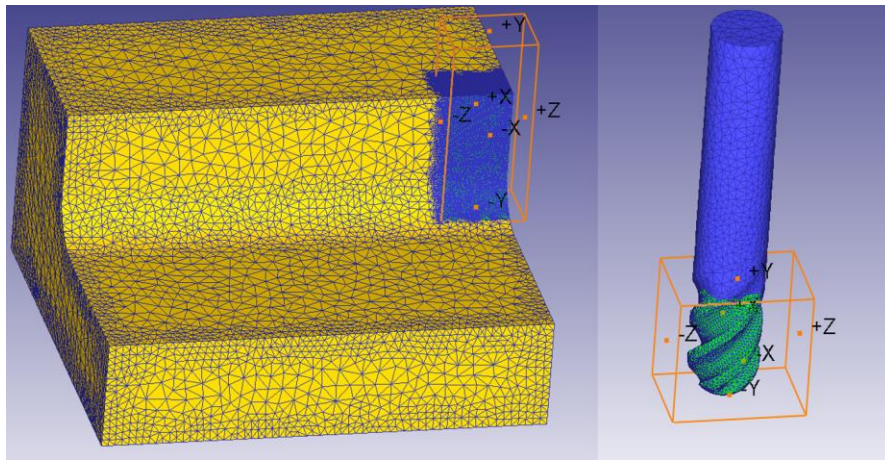


Figure 4-8. Implementation of heat exchange windows to simulate LN₂ cooling.

As mentioned previously, these heat exchange windows allow for specification of the nodal temperatures and the value of the cryogenic convective heat exchange coefficient (h_{cryo}). Both of which can be implemented as constant values or as functions of time or temperature. However, there is significant uncertainty in literature regarding the form and magnitude of the surface convective heat transfer coefficient for cryogenic machining with LN₂. Authors have reported accurate machining and burnishing simulation results for a variety of materials using values anywhere from $h_{cryo} = 3.5$ to $55,000 \text{ kW/m}^2\text{K}$ as is shown in Table 4-2.

Table 4-2. Literature survey of heat exchange coefficient in cryogenic cooling.

Author	Year	h_{cryo} (kw/m^2K)
Hong and Ding [143]	2001	23-47 (Constant)
Jin et al. [158]	2009	3.5 (Constant)
Yang [159]	2012	10000 (Constant)
Pu et al. [160]	2013	5000 (Constant)
Rotella & Umbrello [161]	2014	55000 (Constant)
Rotella & Umbrello [162]	2014	20 (Constant)
Dix et al. [163]	2014	23-40 (Constant)
Bordin et al. [134]	2015	20 (Constant)
Kheireddine et al. [164]	2015	20000 (Constant)
Sun et al. [141]	2015	10000 (Constant)
Danish et al. [165]	2017	5500 (Constant)

The surface convective heat transfer coefficient is a constant has a direct influence upon the amount of heat removed the cutting zone as is shown by Eq. 4-5.

$$q = h_{cryo}\Delta T \quad (4 - 5)$$

where q is a heat flux, or amount of thermal energy transferred per unit area per unit time, and ΔT is the temperature difference between the solid surface and liquid flow during convection. In machining applications, this temperature difference refers to the difference between the workpiece and applied coolant, and is sometimes referred to as the overheat

temperature or T_{OH} [54]. In order to increase the heat flux during machining, which equates to more efficient cooling, one can either increase the temperature difference between the workpiece surface and the coolant temperature or modify the value of h_{cryo} . This partially explains why LN₂ at -196°C can more rapidly remove heat from the cutting zone than conventional flood-cooling at approximately 25°C. Moreover, the value for h_{cryo} largely depends upon the phase composition when the LN₂ comes into contact with the tool or workpiece. As mentioned numerously, nitrogen has an extremely low saturation temperature of -196°C at standard atmospheric pressure (10⁵ Pa). Additionally, it is a supercritical fluid, meaning it has a fairly high vapor pressure and propensity to absorb heat, and has a tendency to quickly evaporate once the LN₂ flow exits the pressurized dewar. Therefore, there is some measure of uncertainty in regards to the how much of given phase is present when the coolant contacts the tool or workpiece. Furthermore, the specific physical properties of this cryogenic coolant and in particular its capacity for heat removal, are dependent upon the specific phase. Table 4-3 compares some relevant properties of liquid and gaseous nitrogen [166].

Table 4-3. Various properties of liquid and gaseous nitrogen. Adapted from [166] with permission from Taylor & Francis.

Physical Property	N ₂ (liquid)	N ₂ (gas)
Density: ρ (kg/m ³)	803.6	4.979
Viscosity: ν (Pas)	1.463E4	0.05331E-4
Specific Heat: C_p (J/kgK)	2046	1351
Thermal Conductivity: λ (W/(mK))	1.320E-1	0.07658E-1

The large amount of heat generated during machining of metallic alloys, particularly difficult-to-cut materials such as *Ti-6Al-4V* alloy, all but guarantees extremely high cutting temperatures at even low MRR values. Consequently, there will most always be a large temperature difference between the tool or chip and the LN₂ jet, which means a rapid boil of LN₂ into its gaseous phase. In comparison to conventional convective heat transfer, which is the only mechanism of heat removal in conventional cooling & lubricating strategies, boiling heat transfer has the potential to have a much higher heat flux. As the temperature difference increases, the heat flux enters a nucleate boiling phase until a critical heat flux is reached, it then enters into a transition boiling phase where the heat flux consistently drops, and upon reaching the Leidenfrost point the fluid enters a film boiling region. With the exception of research performed by Hong and Ding [167], Lu [54], Pusavec et al. [168, 169], little to no work has been focused on understanding the boiling mechanism of LN₂ in regards to its application in machining operations. Lu [54] approached this problem empirically by performing a series of cryogenic heat transfer experiments. A series of thermocouples were embedded in grooves which were machined into a magnesium *AZ31B* workpiece. The workpiece was then heated to a known temperature and LN₂ was applied at various pressures to simulate the effect of cryogenic cooling during machining. A data acquisition system was used to rapidly capture the change in temperature measured by each of the thermocouples. In this way a spatial map of the temperature gradient could be established. By strategic placement of the thermocouples the heat transfer problem was simplified to a 1-DOF inverse heat transfer problem as shown below:

$$k \frac{\partial^2 T}{\partial x^2} = \rho C_p \frac{\partial T}{\partial t} \text{ at } 0 < x < L, \text{ for } 0 < t < t_f \quad (4-6)$$

$$-k \frac{\partial T}{\partial t} = h(T - T_{LN}) = ?, \text{ at } x = 0 \quad (4-7)$$

$$-k \frac{\partial T}{\partial t} = h_{air}(T - T_{air}), \text{ at } x = L \quad (4-8)$$

$$T = T_{air} = 24^\circ C, \text{ at } t = 0, \text{ when } 0 \leq x \leq L \quad (4-9)$$

$$T(x_j, T_j) = Y_j, \text{ for } t = t_j, j = 1, 2, 3, \dots, N \quad (4-10)$$

where ρ , k , and C_p are the respective density, thermal conductivity, and specific heat capacity of the test material, x is distance from the test surface, L is the height of the specimen, h is surface heat transfer coefficient, T_{air} and T_{LN} are the temperatures of the air and saturation point of LN₂, t and t_j are the time of initial contact between the coolant and the workpiece and the time when measurements are taken respectively, x_j is the location of the test point, Y_j is the measured temperature at point x_j and time t_j , N is total number of measurements taken.

Traditionally, the most efficient way to solve an inverse heat transfer problem is by utilizing a least square based approach. However, as Oziskik and Oralnde [170] describe such solutions are very unstable and are often inaccurate. To solve this problem, Lu [54] used an oversampling methodology to reduce the sampling noise in combination with a finite difference method to calculate the temperature at each spatial and time combination. From this analysis the surface heat transfer coefficient can be determined as a function of the overheat temperature. Shown below in Figure 4-9 is a plot of the calculated h_{cryo} values versus overheat temperature at four varying LN₂ pressures.

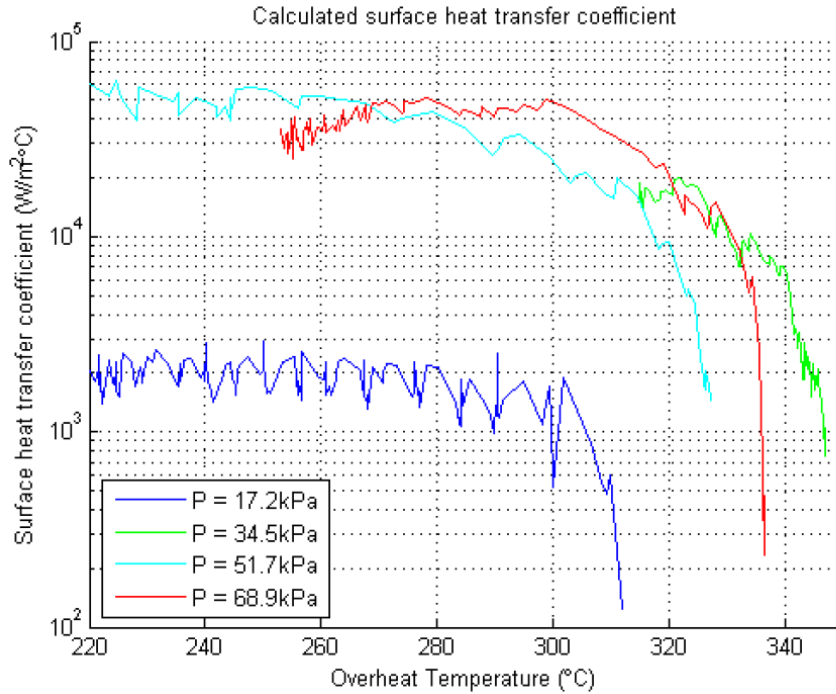


Figure 4-9. Experimentally calculated heat transfer coefficient values for various pressures. Reprinted from [54] with permission.

In comparing this data with the Nukiyama curve and the applicable overheat range of machining conditions, it can be concluded that during cryogenic machining the primary form of heat transfer is boiling heat transfer. Moreover, it is not a constant value, but rather changes depending on the type of boiling mechanism, which itself is a function of the overheat temperature. Within this domain at low T_{OH} transition boiling is the primary heat transfer mechanism, and at higher T_{OH} values film boiling is the dominant mechanism with a lower heat transfer coefficient in comparison. Nucleate boiling is not realistic as this occurs around an overheat temperature of 20°C. Unfortunately, the high temperatures associated with machining dictate that boiling heat transfer will be in almost all cases film boiling. Though in comparison to conventional convective cooling it still 10-20 times as high.

At lower LN₂ pressures the heat transfer coefficient is much lower in comparison, due to the fact that LN₂ is almost entirely in its gaseous phase with its associated diminished heat transfer capabilities. Therefore, one of the keys that must be taken away from this work, is that there must be enough pressure to ensure that the two phase flow is predominantly liquid upon contact with the hot workpiece. This is the only way to ensure that boiling heat transfer occurs, and that the heat generated from machining can be rapidly removed. Any pressure increase beyond this had no observable benefit. However, if one could significantly increase the pressures such that some measure of vapor penetration occurs one could further increase the heat flux from the cutting zone [171]. The only other means of increasing the cooling capacity of LN₂ by either modifying the flow characteristics using a laminar flow jet, but this is a difficult proposition with a two phase LN₂ flow.

Additional independent experiments using an identical methodology were conducted by Pusavec et al. [168] for *Inconel 718*. From this work the following empirical relations were determined as shown in Eq. 4-11:

$$h_{cryo} = \begin{cases} 5500T_{OH}^{1.03}, & \text{for } T_{OH} < 45^{\circ}C \\ (777963.74)e^{-0.0246T_{OH}} + (22017.91)e^{-12.78E-5T_{OH}}, & \text{for } T_{OH} \geq 45^{\circ}C \end{cases} \quad (4 - 11)$$

This empirical relationship was plotted and is shown below in Figure 4-10 for the entirety of the overheat range. It was also annotated so that individual boiling regimes as defined by the determination of a critical overheat temperatures $T_{OH} = 45^{\circ}C$ at which transition boiling begins, and $T_{OH} = 200^{\circ}C$ at which transition boiling progresses to film boiling.

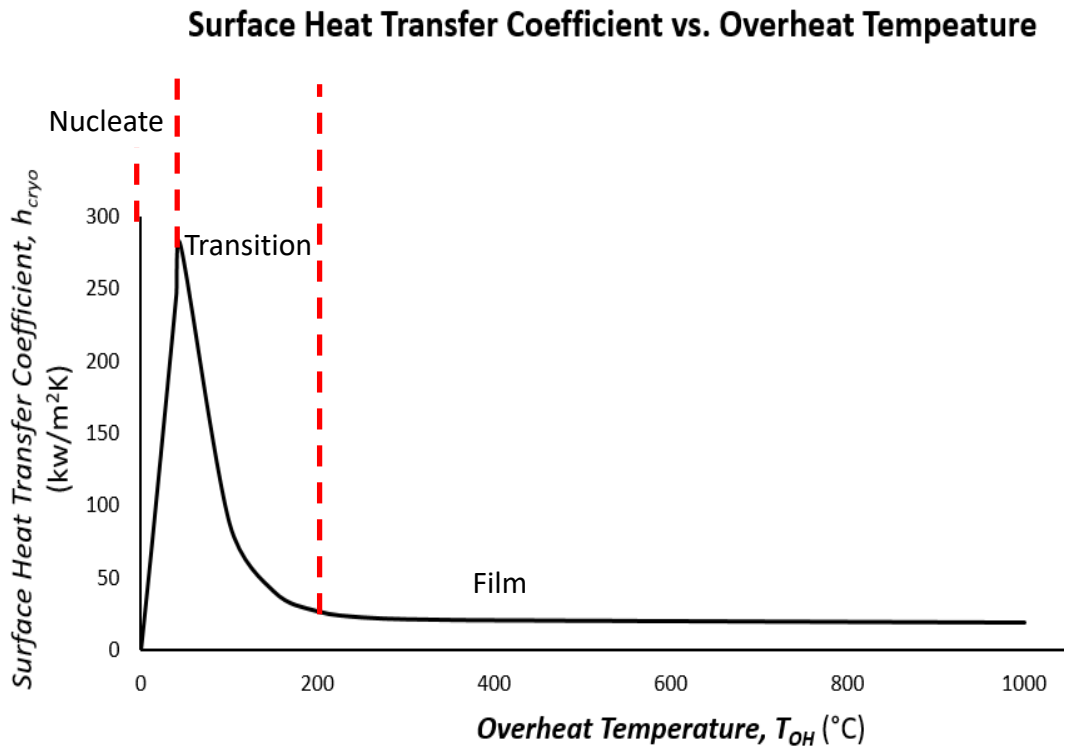


Figure 4-10. Cryogenic heat transfer coefficient for increasing values of T_{OH} . Adapted from [168] with permission from Elsevier.

4.1.4 Numerical Calibration & Experimental Validation

Numerical Calibration and Experimental validation of the constructed model was performed using the measured cutting forces from milling experiments conducted under a variety of flood-cooled machining parameters as shown in Table 4-4. During numerical calibration (Trial I), the friction coefficient $\mu = 0.3$ and D_{crit} value of 245 was iteratively modified to a value of $\mu = 0.35$ and 200 respectively, at which the percent difference between the simulated and experimental cutting forces values was at most roughly 5% as is reflected in Figure 4-11. Where the simulated feed, axial, and normal (to feed direction) components of the cutting force are plotted along with the experimentally measured cutting force values.

Table 4-4. Machining parameters utilized during numerical calibration and validation.

	Trial I: Calibration	Trial II: Validation	Trial III: Validation
Tool Diameter, DC_{ap} (mm)	19.05	19.05	19.05
Number of Teeth, Z_{EFF}	4	4	4
Cutting Speed, V_c (m/min)	10	40	40
Feed Rate, V_f (mm/min)	91.8	543.4	715.4
Feed/Tooth, f_z	0.13	0.2	0.27
Revolutions per Minute, n	167	668	668
Axial Depth of Cut, a_p (mm)	19.05	19.05	19.05
Radial Depth of Cut, a_e (mm)	1.48	1.48	1.48
MRR (mm^3/min)	2588	15320	20169

Mean Cutting Force Comparison: Numerical Calibration (Trial I)

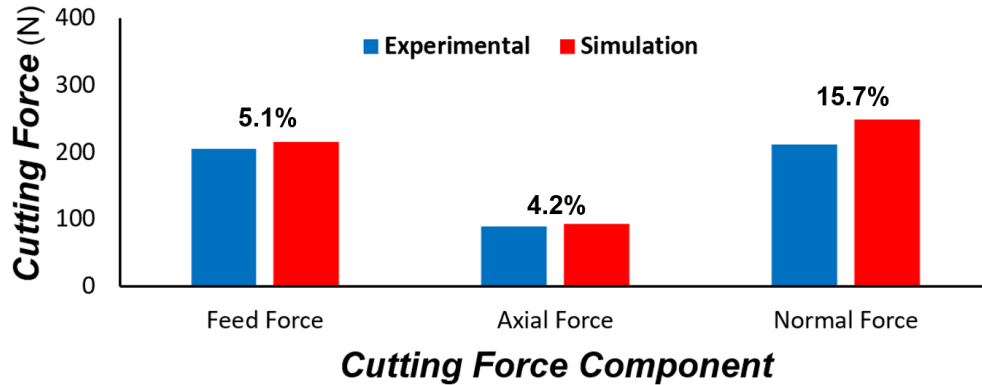


Figure 4-11. Comparison of numerical and experimental cutting forces during the modelling calibration.

As can be seen the feed and axial components of the simulated cutting force are at least within approximately 5% of the experimentally measured values. It should be noted that regardless of the modeling parameters, the simulated normal force consistently predicted cutting forces which were 15% higher than what was experimentally measured

(This is a common problem in modeling of machining operations). It was therefore necessary to neglect this force component during calibration and validation.

In order to experimentally validate the model, the machining parameters were modified to that shown for Trials II and III. As the scope of this numerical investigation was to investigate the modeling outputs at a baseline and high MRR, it was necessary that an acceptable accuracy hold for each of the for both trial II and III, in order to give confidence in its reliability to predict cutting mechanics, temperature distribution, and surface integrity across a wide range of MRR values. The cutting speed, feed rate, and feed per tooth were therefore varied to reflect a range of conventional parameters used for finish machining of *Ti-6Al-4V* alloy. More specifically, the depths of cut were held constant while the MRR was increased via appropriate increases to the feed rate, cutting speed, and feed per tooth. The mean cutting force comparisons for both trials are shown in Figures 4-12 and 4-13. As can be seen in these figures, as the MRR is increased from that utilized in Trial II to that implemented in Trial III, the percent difference in the Feed component of the cutting force varied from 3% to 2.2%, while the axial component varied from 0.98% to 3.8%. In all cases the percent difference was less than 5%, which was the desired accuracy level for the model's outputs. In fact, in both validation trials the feed and axial components were more accurate than that achieved during the calibration phase.

Mean Cutting Force Comparison: Experimental Validation (Trial II)

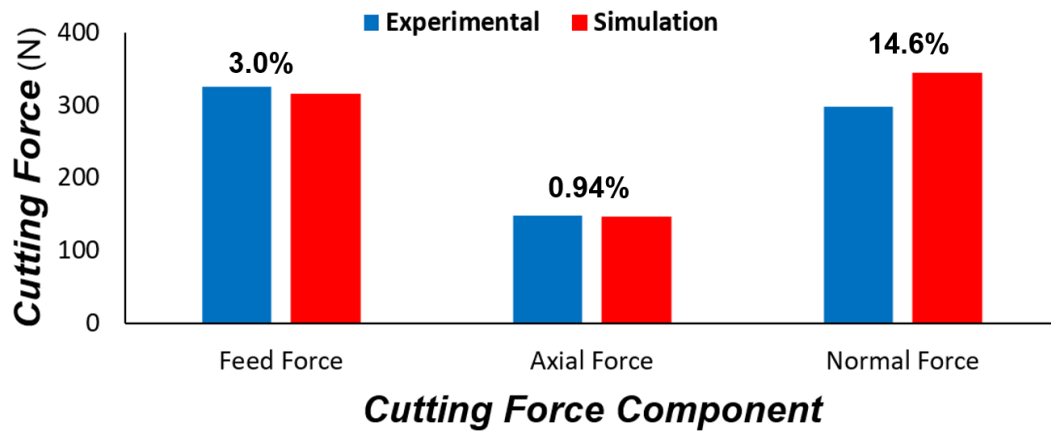


Figure 4-12. Comparison of numerical and experimental cutting forces during experimental validation for trial II.

Mean Cutting Force Comparison: Experimental Validation (Trial III)

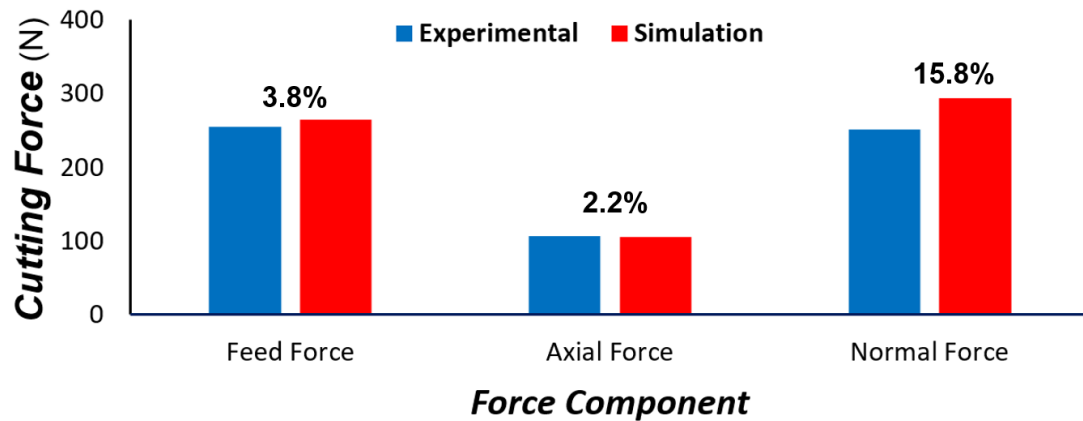


Figure 4-13. Comparison of numerical and experimental cutting forces during experimental validation for trial III.

4.1.5 Prediction of Surface Integrity Characteristics

The second phase of the calibration and model validation process involves the prediction of the machined surface integrity characteristics. As has been discussed numerously throughout this investigation, the surface integrity of machined components has a fundamental influence on the functionality of aerospace components. Furthermore, the temperature, strain, and strain-rate imparted to the workpiece during processing significantly impacts the material's surface integrity [172]. In order to accurately predict critical surface integrity characteristics, such as grain size evolution and microhardness in machined *Ti-6Al-4V* alloy, sub-routines were developed in a fashion similar to other researchers [162, 173-175]. Microstructural evolution, particularly the growth of new grains that arise from phase change and DRX, is challenging to accurately predict. For *Ti-6Al-4V* alloy, the matter is further complicated by its two phase microstructural composition. However, in all cases in literature grain size prediction models solely focus on the α (HCP) phase rather than the laminar β (BCC) for a number of reasons. First, at room temperature and the working temperatures found in machining operations, the relative volume fraction of these two phases is heavily distributed as α -grains (80-90%) [15, 176]. This is supported by the fact that the simulated workpiece temperatures only reached a maximum temperature of 429°C, which is far less than the β -transus temperature of 980°C. As such, the material microstructure almost certainly predominantly α -phase supported by laminar β -phase matrix [136].

For grain size determination in numerical simulations there are generally two phenomenological models commonly used. The first is the Johnson-Mehl-Avrami-Kolmogorov (JMAK) model which utilizes the Avrami equation to predict the growth of

new grains in the presence of phase transformation [177]. The other common approach is to utilize the Zener-Holloman parameter (Z), which is used in conjunction with a recrystallization model to define microstructural changes during SPD processing as a function of the temperature compensated strain-rate [178]. Z is expressed mathematically as is shown below in Eq. 4-11:

$$Z = \dot{\epsilon} \exp\left(\frac{Q}{RT}\right) \quad (4 - 11)$$

where $\dot{\epsilon}$ and T are the respective strain-rate and absolute temperature (K), R is the gas constant ($8.3145 \text{ J} \cdot \text{K}^{-1} \cdot \text{mol}^{-1}$), and Q is the material dependent apparent activation energy for hot deformation (KJ/mol). The value of Q is quite varied in literature, depending upon the heat treatment and the exact chemical composition of the alloy. Momeni and Abbasi [179] determined the activation energy for the HCP- α and BCC- β phases in *Ti-6Al-4V* alloy to be 530 kJ/mol and 376 kJ/mol respectively. The large reported difference is likely the result of more active slip systems and a higher diffusion coefficient in the BCC- β phase, and thus the BCC structures can more easily deform. These values were in good agreement with Seshacharyulu et al. [180] and Bruschi et al. [181]. However, they contrast significantly in comparison to those proposed by Ding et al. [182], where $Q = 218 \text{ kJ/mol}$ for the HCP- α phase. However, the mean β -grain size in this study was 1100 μm , whereas in Momeni and Abbasi [179] it was roughly 200 μm . Thus, the relative volume fraction of the individual phases, which is in large part controlled by the specific heat treatment of the alloy, has a significant impact upon the activation energy in hot deformation processing. An activation energy of 218 kJ/mol was implemented by Arisoy and Ozel [174] for prediction of microstructural evolution in 3D numerical models for face turned *Ti-6Al-4V* alloy. Whereas Rotella and Umbrello [162] used a value of 376 kJ/mol (roughly the

average of these two extremes). The β -grains exhibited by the material in this analysis, however, were more on the order of 200 μm . Therefore, a value of 530 kJ/Mol was used as the activation energy in these simulations.

The recrystallized grain size after DRX, d_{DRX} , can be determined using Eq. 4-12:

$$d_{DRX} = aZ^m \quad (4 - 12)$$

where a and m are material constants. Note that the values of a and m require a calibration procedure. The onset of DRX within the numerical simulation was initiated by a critical strain threshold, ε_{cr} . During each simulation step the induced material strain is determined and compared to this value. If the strain fails to reach this threshold the simulation carries on to the next step in the iteration. However, if the strain exceeds ε_{cr} , the subroutine calculates the new grain size using Eq. 4-12. Arisoy and Ozel [174] utilized a critical strain value of $\varepsilon_{cr} = 0.8\varepsilon_p$. Where ε_p represents the peak strain during deformation. The peak strain is itself a function of temperature, strain rate, and other constants as is expressed below in Eq. 4-13.

$$\varepsilon_p = a_1 d_0^{h_5} \dot{\varepsilon}^{m_1} \exp\left(\frac{Qm_1}{RT}\right) + C_1 \quad (4 - 13)$$

Arisoy and Ozel [174] in large measure assigned values to these constants based upon the work of Yi et al. [183], where the hot deformation behavior of Aluminum alloy 7050 was analyzed. Consequently, there must be some concern regarding the applicability of these constants in regards to *Ti-6Al-4V* alloy. Rotella and Umbrello [136] and Wang et al. [173] used a critical strain value derived from work by Momeni and Abbasi [179] on the hot flow behavior of *Ti-6Al-4V* alloy, in order to develop 2D FE models of dry and cryogenic machining of this alloy with good success. In this case, ε_p is expressed as a function Z as is shown below in Eq. 4-14:

$$\varepsilon_p = 1.4E - 2Z^{0.073} \quad (4 - 14)$$

As this empirical expression was derived entirely from the hot flow behavior of *Ti-6Al-4V* alloy, and this function was implemented into the sub-routine code for grain size prediction.

In a given time step, once the FEM code determines that the critical strain has been satisfied and the new updated grain size has been calculated, the material hardness is then determined using the Hall-Petch relationship [184] which is shown below in Eq. 4-15, where *HV* is the hardness, *H₀* is the initial workpiece hardness, and *C₁* is a calibration constant.

$$HV = H_0 + C_1 \cdot d_{DRX}^{-0.5} \quad (4 - 15)$$

The organizational flow chart for the design and implementation of this subroutine is illustrated below in Figure 4-14

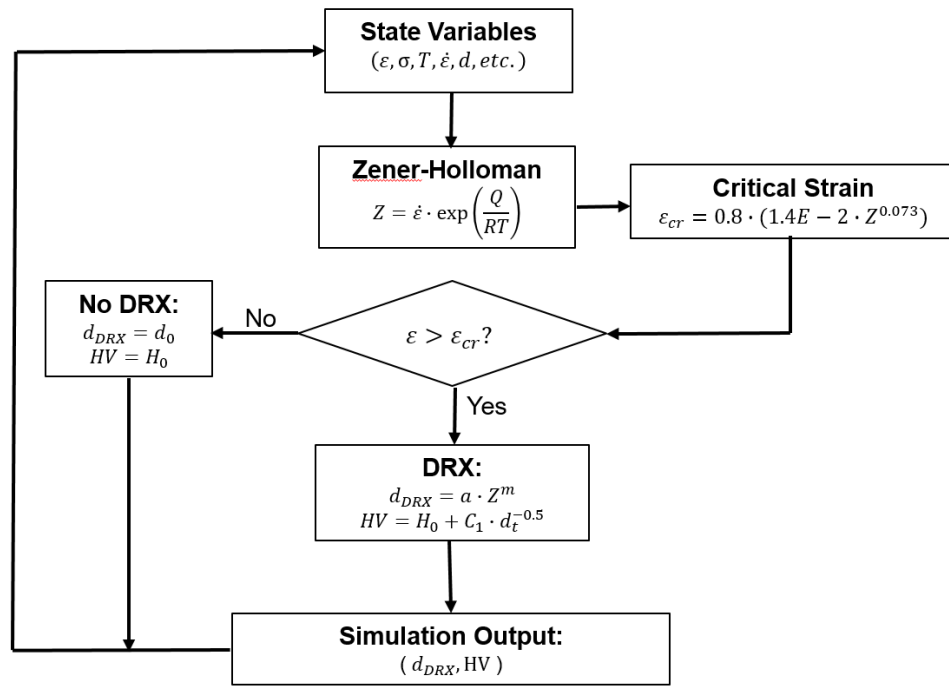


Figure 4-14. Sub-routine flowchart for prediction of surface integrity characteristics.

Numerical simulation of microstructural evolution in terms of grain size, refined layer thickness, as well as the calculated microhardness are all illustrated below in Figure 4-15 for cryogenic and flood-cooled machining using the conditions shown in trial 3. For both conditions, near-surface layers exhibiting refined microstructural and surface integrity characteristics are predicted. In terms of the magnitude of the affected layer, grain refinement was observed in cryogenic machining to a depth of 291 μm , whereas flood cooling exhibited refinement to a depth of 142 μm . Thus, with cryogenic machining the depth of refinement is roughly twice that of what can be achieved with flood-cooling.

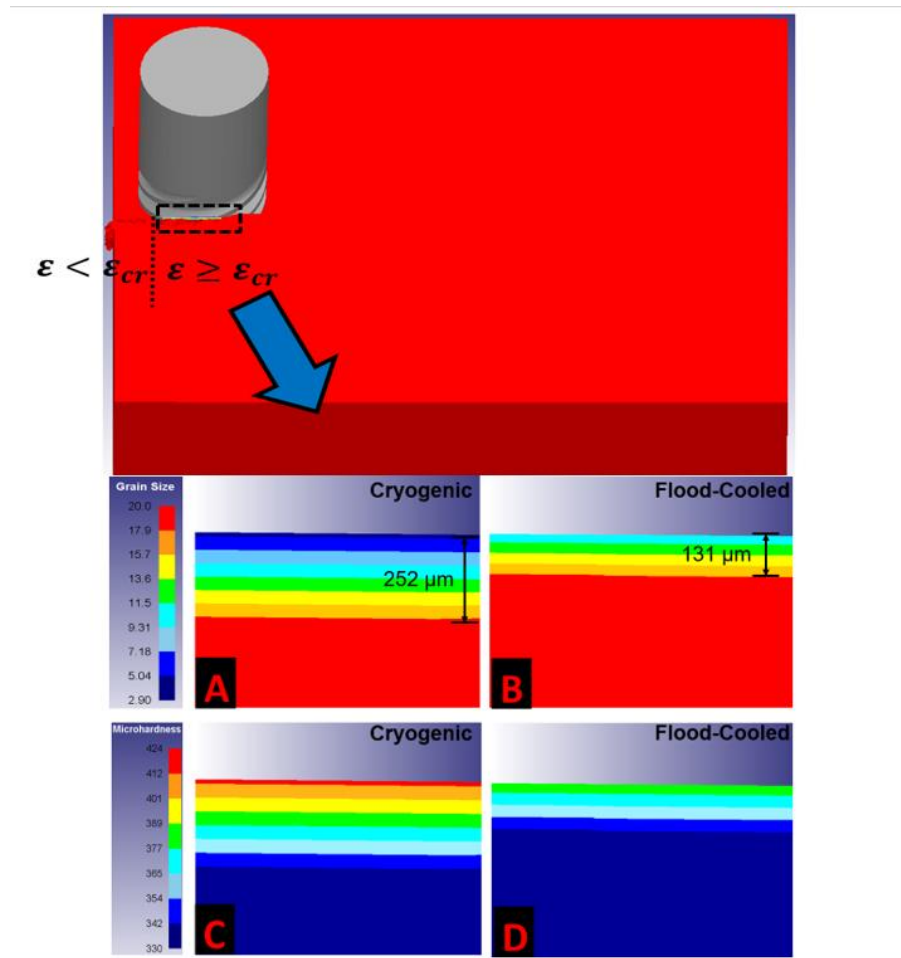


Figure 4-15. Predicted ALD and microhardness during cryogenic and flood-cooled machining.

Within each layer DRX induces α -grain refinement, specifically the growth of new grains, the size of which is consequently suppressed by the respective cooling mechanisms. As LN₂ removes significantly more heat from the cutting zone via boiling heat transfer at -196°C, as compared to flood-cooling at room temperature, it is far more effective at suppressing grain growth. During cryogenic machining, the model predicts the formation of a shallow ($\approx 20 \mu\text{m}$) layer with a mean α -grain size of $2.9 \mu\text{m}$. This is an 85% prediction from the as-received bulk size of $20 \mu\text{m}$. The smallest grains produced via flood-cooling were $15.5 \mu\text{m}$ at the processed surface, which is an approximate 20% reduction from its virgin state. With cryogenic cooling the depth of the refined layer reaches $174 \mu\text{m}$ before this grain size is reached. More concisely, at a depth of $142 \mu\text{m}$, which is the total depth of the predicted refined layer in flood-cooling, the grain size in cryogenic machining is predicted to be on average $13.6 \mu\text{m}$. Thus, there is more grain refinement at a depth of $142 \mu\text{m}$ in cryogenic machining, than there is on the processed-surface of flood-cooled work pieces. Moreover, this highlights how just effectively LN₂ can penetrate into the cutting zone and enact significant sub-surface material refinement.

In order to validate these outputs, microstructural analysis of processed samples was conducted using optical and scanning electron microscopy in conjunction with image processing techniques. This technique is illustrated below in Figures 4-16A and 4-16B for flood-cooled samples machined using the parameters in trial III. For cryogenic cooling, in order to clearly resolve α -grain boundaries in the near surface, SEM analysis was performed as shown in Figure 4-17. For both cryogenic and flood-cooled samples grain sizes were then measured to depths of $400 \mu\text{m}$ as is shown in Figure 4-18.

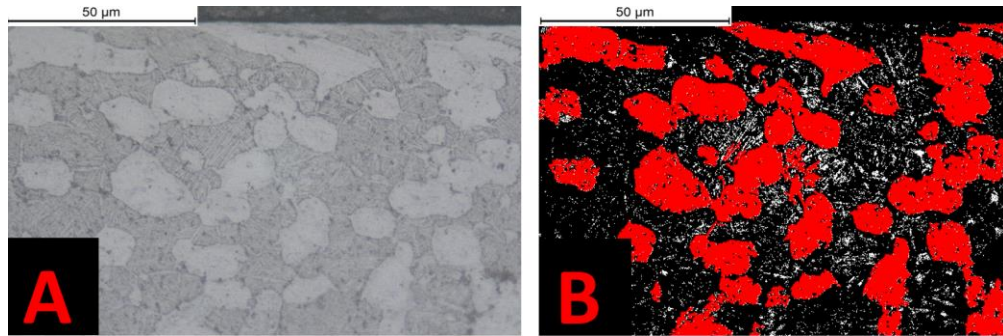


Figure 4-16. Depiction of methodology for grain size measurement in flood-cooling.

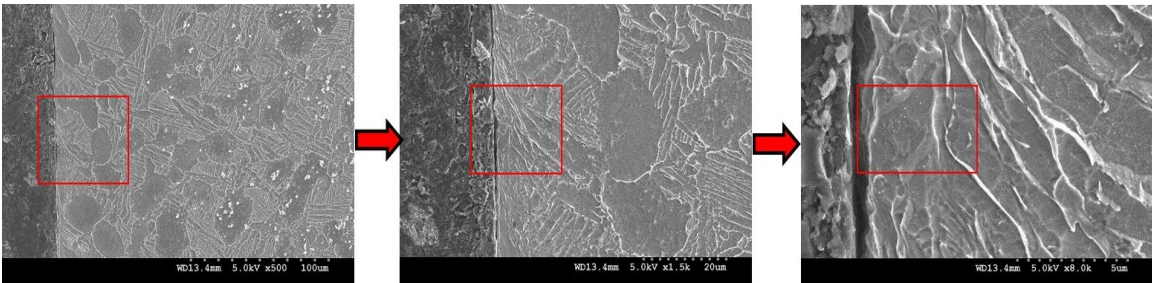


Figure 4-17. SEM analysis of near-surface microstructure in cryogenic machining.

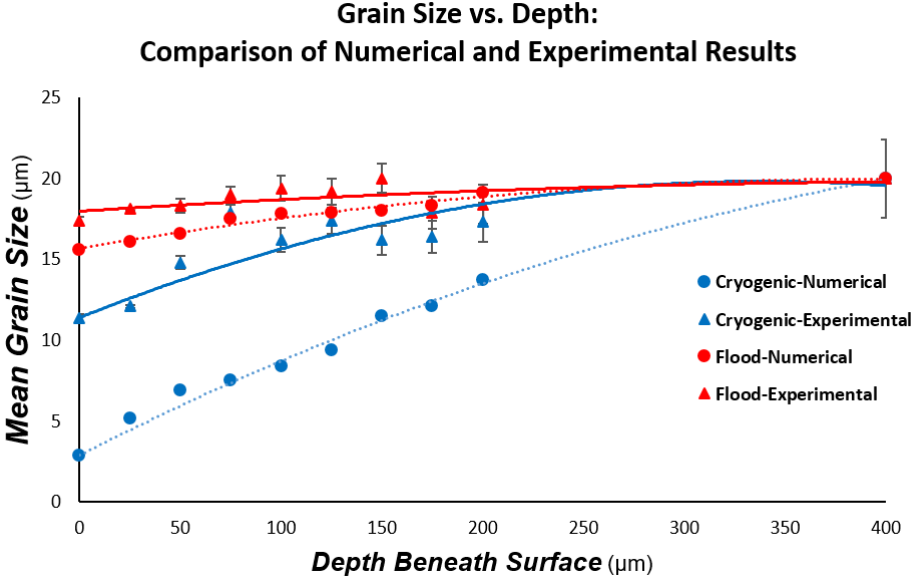


Figure 4-18. Comparison of numerically predicted and experimentally measured grain sizes in cryogenic and flood-cooled milling.

From these plots, it is observed that the deviation in the numerically predicted and experimentally measured mean α -grain size was minimal for flood-cooling (7.2% throughout the ALD). For cryogenic cooling, however the error was substantially larger. This is particularly true in the near-surface region, where the experimentally measured mean grain size was 11.4 μm , as compared to the numerically predicted value of 2.9 μm . This difference can be attributed to the near-surface mesh characteristics utilized during the simulation. A mesh sensitivity analysis was conducted during the initial stages of model development, in order to determine the point at which further increases in mesh density resulted in unacceptable solution times, while providing only minimal improvements to accuracy. Considering the large computational times necessary for solution convergence in high speed 3D machining models, and the sheer number of iterations necessary for model calibration, this sensitivity analysis was critical for developing the model in a practical time-frame. However, the scope of the initial model calibration procedure was limited to the generated cutting forces, and could not consider the machined surface integrity characteristics, as this model feature is based upon the implemented sub-routine within the larger modeling framework. Consequently, sub-routine calibration could not be undertaken until after the primary model had been calibrated, and the mesh characteristics could not be modified at this point without altering the very foundation of the model itself. As shown in Figure 4-4, the end result of the mesh sensitivity procedure was mesh elements in the cutting zone with an average length of 0.25 mm. The predicted ALD depth was itself, however, 252 μm . This is far too coarse to accurately characterize surface integrity characteristics as a function of minute changes in processing depth. For such an analysis, the ideal element length would be no larger than

10 μm [137]. The flood-cooled simulations did not exhibit such large error, simply because the experimentally measured grain size measurements were all within the error bounds of the mean grain size in the as-received virgin material (i.e., minimal grain size refinement was induced during processing, and thus the predicted grain size was less sensitive to the calibration coefficients in Eq. 4-12). Unfortunately, even with state-of-the-art CPU's, utilizing a mesh density this fine is impractical for calibration, due to the computational size of 3D machining models and the resulting solution times. The predictive scope, in essence, is limited by the model's complexity. In general, it is simply not possible to efficiently develop a single comprehensive model that can accurately predict all desired outputs, when the model features that generate those outputs cannot all be calibrated in the same procedure. In such instances 2D models are typically employed, as the reduced model complexity allows for significantly increased mesh density while maintaining reasonable solution times.

The microstructural evolution depicted in Figure 4-15 corresponds to changes in the microhardness of the material as is shown in Figure 4-19. As DRX drives the formation of new grains, the growth of which are limited by the application of external cooling, this in turn directly affects the predicted microhardness via a Hall-Petch relationship. Though the accuracy of the numerically predicted grain size is questionable, within the model grain size and microhardness are only partially coupled. Meaning that even though the hardness determination is based on the simulated grain size, the calibration constant C_I in Eq. 4-15 allows for accurate calibration of the microhardness sub-routine, even in the presence of inaccurate grain sizes (as long as those grain sizes are not chaotic and follow a specific pattern). Moreover, since the Hall-Petch is only dependent upon a single calibration

coefficient, the calibration procedure is less time and computationally expensive. Thus, smallest predicted grains near the surface exhibit elevated hardness, which progressively decreases until both hardness and grain size reach their as-received states. These numerical predictions are validated by experimental measurements of microhardness where the percent error deviates from 2.5% and 1.62% for flood-cooled and cryogenically machined work pieces respectively.

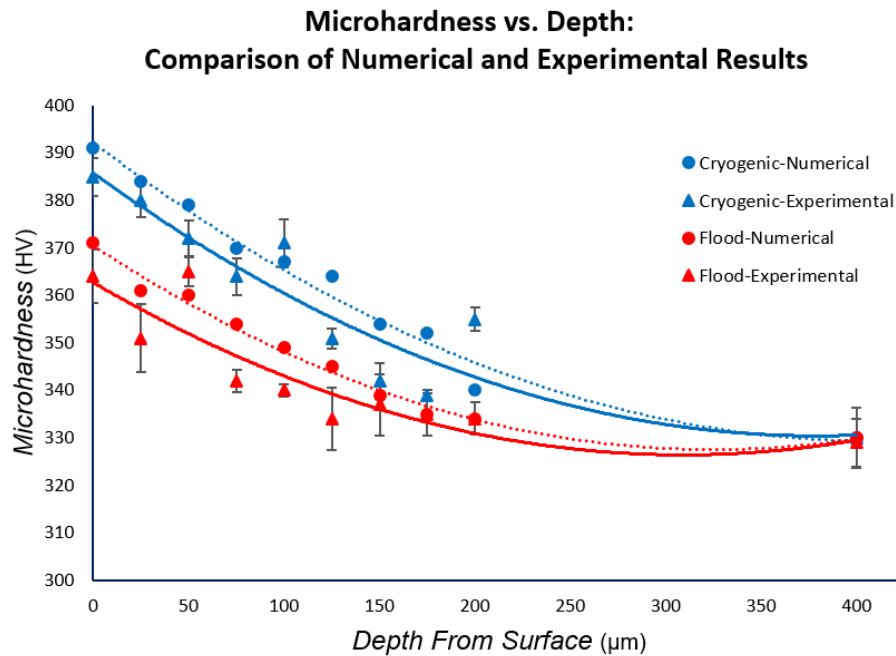


Figure 4-19. Comparison of numerically predicted and experimentally measured microhardness variation.

4.1.6 Impact of High MRR on Cutting Forces and Thermal Fields

The machining parameters were chosen so as to achieve two different MRR rates. Baseline MRR's for standard roughing and finishing operations and a high MRR representing 3X the baseline value. With machining of *Ti-6Al-4V* alloy the most efficient way of achieving this is by increased feed and speed. To study the effect of these parameters the radial and axial depth of cut and chip load were kept constant, and the feed

and tool RPM were varied. Moreover, in order to facilitate a more accurate comparison of cooling and lubrication for both roughing and finishing identical feed and speed values were used as inputs. However, the cutting dynamics are significantly different between these two operations due to the aggressive radial depth of cut simulated during roughing. In this case it represents 30% of the tool cutting diameter, whereas during finishing the radial depth of cut was only 7%. The specific machining parameters used during these simulations are shown in Table 4-5.

Table 4-5. Machining parameters for high MRR simulations.

	Machining Parameter	Flood (Baseline)	Flood (3X MRR)	Cryogenic (3X MRR)
Roughing	Feed, V_f (mm/min)	800	2400	2400
	Axial Depth of Cut, a_p (mm)	11.11	11.11	11.11
	Radial Depth of Cut, a_e (mm)	5.715	5.715	5.715
	RPM	1003	3008	3008
	Cutting Speed, V_c (m/min)	60	180	180
	Feed per tooth, f_z (mm)	0.2	0.2	0.2
	MRR (mm³/min)	50800	152400	152400
Finishing	Feed, V_f (mm/min)	800	2400	2400
	Axial Depth of Cut, a_p (mm)	23.8125	23.8125	23.8125
	Radial Depth of Cut, a_e (mm)	1.3335	1.3335	1.3335
	RPM	1003	3008	3008
	Cutting Speed, V_c (m/min)	60	180	180
	Feed per tooth, f_z (mm)	0.2	0.2	0.2
	MRR (mm³/min)	25400	76200	76200

The low thermal conductivity exhibited by titanium alloy *Ti-6Al-4V*, and the tendency for the vast majority of the cutting heat to accumulate on the cutting tool, highlights the need to characterize the distribution of thermal fields on the tool and workpiece. Shown below in Figures 4-20 and 4-21 are the thermal profiles generated on the tool and work piece temperatures for the baseline MRR (60 m/min) and 3X MRR (180

m/min) for flood-cooled and cryogenic machining in both roughing and finishing machining scenarios.

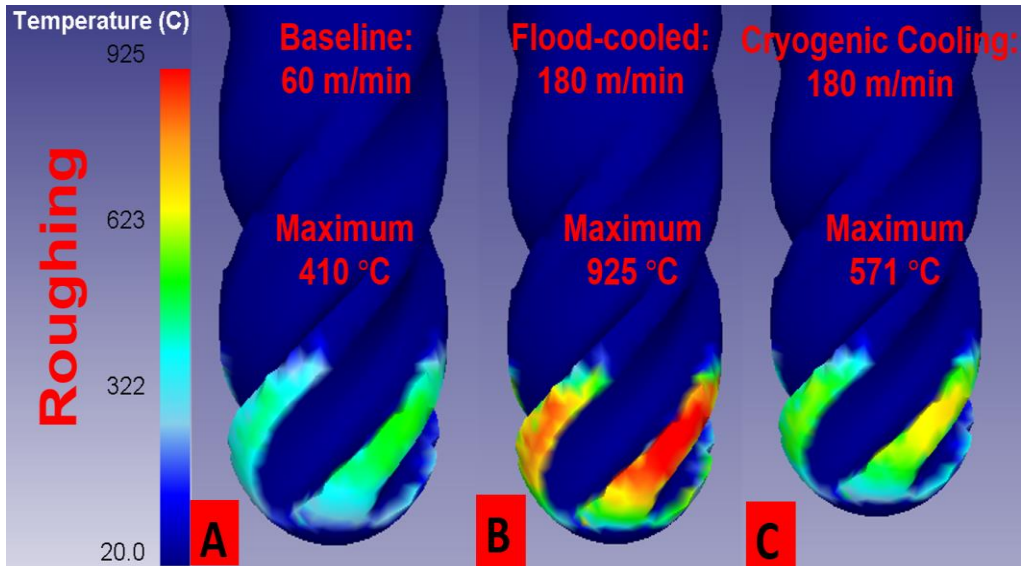


Figure 4-20. Simulated tool temperature distribution for cryogenic and flood-cooled rough machining.

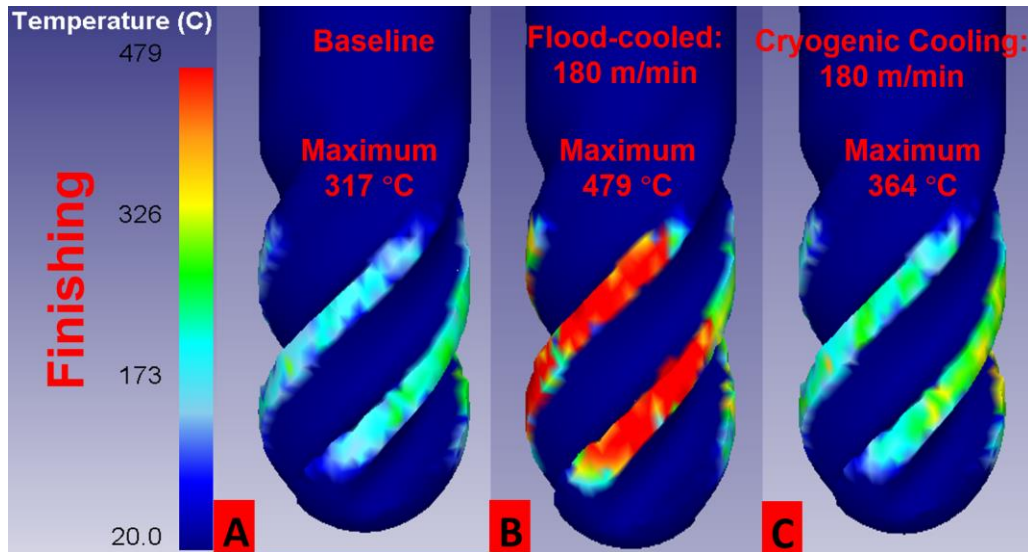


Figure 4-21. Simulated tool temperature distribution for cryogenic and flood-cooled finish machining.

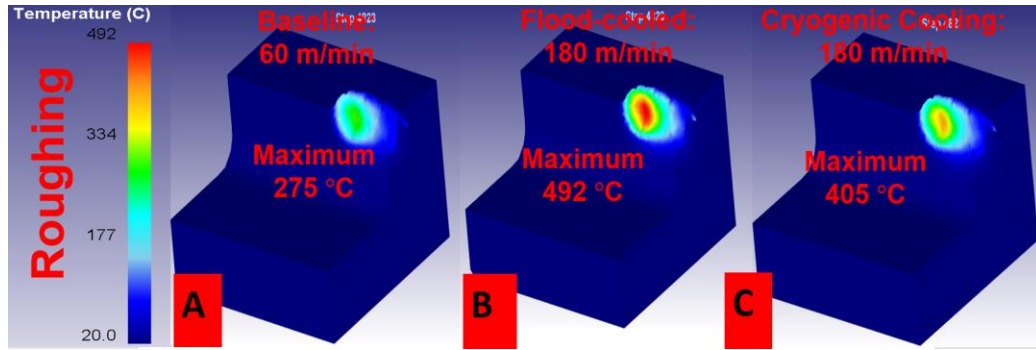


Figure 4-22. Simulated workpiece temperature distribution for cryogenic and flood-cooled rough machining.

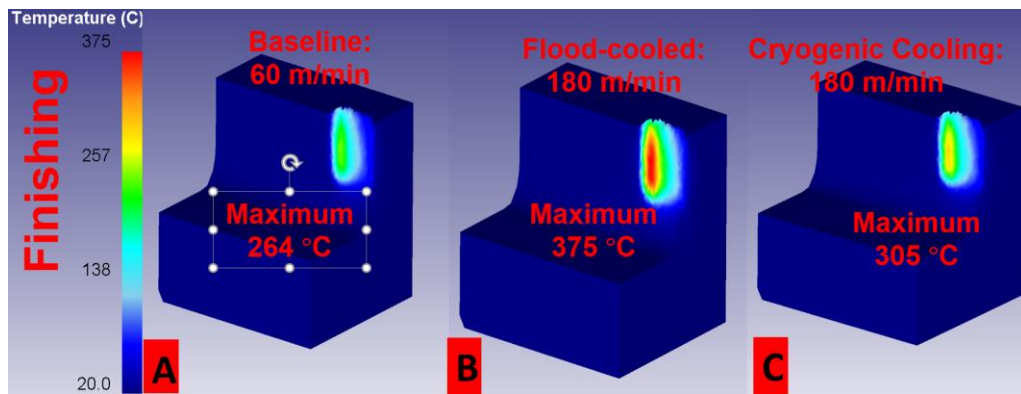


Figure 4-23. Simulated tool temperature distribution for cryogenic and flood-cooled finish machining.

In comparing the predicted temperature fields and maximum temperatures shown in Figures 4-20 through 4-23 several important conclusions can be drawn. Roughly 65%-70% of the heat generated in both roughing and finish machining of *Ti-6Al-4V* alloy. This is explained by The low thermal conductivity exhibited in this material in comparison to the Tungsten Carbide cutting tool. The large amount heat accumulated on the cutting edges of the tools highlight the significant challenge facing high speed machining of *Ti-6Al-4V* alloy. This is particularly true in flood-cooled machining at 180 m/min. High speed roughing using flood-cooling generates significant amount of heat in relatively large areas

of the cutting edges. This would almost certainly allow thermally activated tool-wear mechanisms to initiate rapid losses in tool-life and eventual catastrophic tool failure.

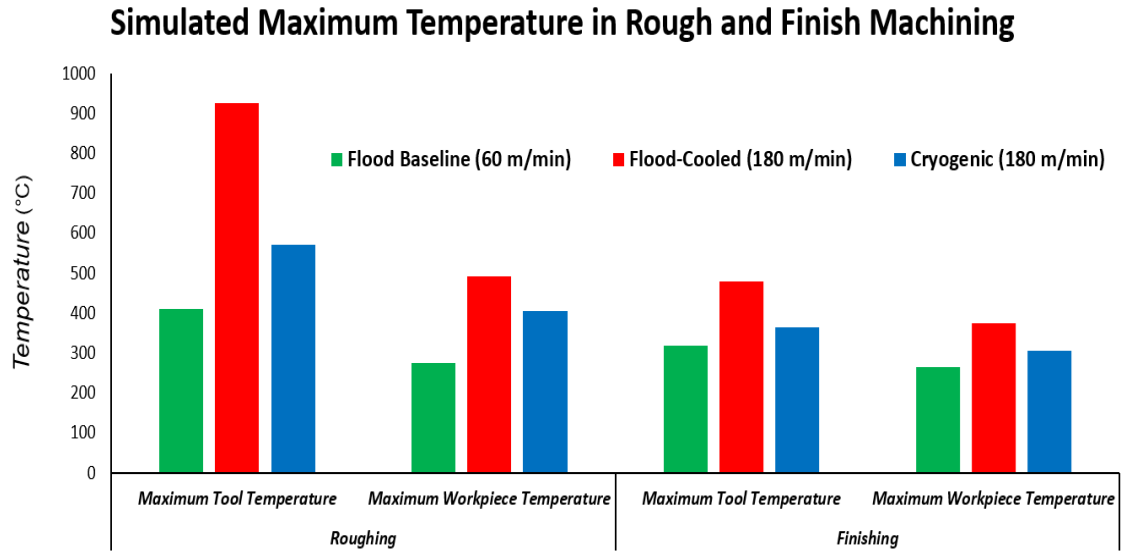


Figure 4-24. Simulated maximum tool and workpiece temperatures in flood-cooled and cryogenic machining as a function of cutting speed for rough and finish machining.

The maximum simulated cutting temperature on the cutting tool and workpiece are plotted in Figure 4-24. It is observed that for rough machining at 180 m/min, flood-cooled machining generates a maximum temperature of 925°C, well beyond the ideal temperature for carbide tools. Whereas, with cryogenic temperature a maximum temperature of 562°C was observed. This represents a 38% decrease in maximum tool temperature. Moreover, this temperature is within the ideal working parameters for WC. Therefore, it can be expected that the likely tool-life and general overall machining productivity would be greatly enhanced in comparison to flood-cooling. For finish machining, both flood cooling and external cryogenic cooling provide sufficient cooling to maintain a working tool temp below the WC ideal temperature. Even so, however, cryogenic cooling still produces maximum temperatures that are 24% lower. As such, it would certainly be possible to

increase the MRR/cutting speed even more using cryogenic cooling to further increase productivity while maintaining a comparable tool-life.

There is a modest amount of uncertainty in literature regarding the impact of cryogenic cooling on the measured cutting forces. Some experimental based works conclude that LN₂ application in machining of *Ti-6Al-4V* alloy leads to an increase in the measured cutting force in comparison to flood-cooling [9, 132], possibly due to an increase in hardness and strength in the workpiece from flow stress modification. Whereas other research concludes that some components and of force are increased, while other components decrease or are unaffected, or even all components of force decrease while utilizing cryogenic cooling [57, 185, 186]. The reduction in force could be attributable to modifications in the frictional behavior of the material at decreased temperature, or reduction in the tool-chip contact length from physically lifting the chip away. Considering that the properties of LN₂ are highly sensitive to even slight changes in experimental methodology, without any uniformity in experimental technique, it is impossible to make any conclusion with absolute certainty. For numerical simulations within DEFORM, the cooling windows used to implement cryogenic cooling cannot capture the effect of physically lifting the chip. Moreover, as the same friction models were used in these simulations to represent cryogenic and flood-cooled machining, this hypothesis cannot be tested either. Leaving only the impact of cooling upon the imparted flow stress properties as a possible factor to explore.

The simulated mean feed and axial components of the cutting force for rough and finish machining are shown respectively below in Figures 4-25 and 4-26. The normal force was omitted due to the inability to properly calibrate this component.

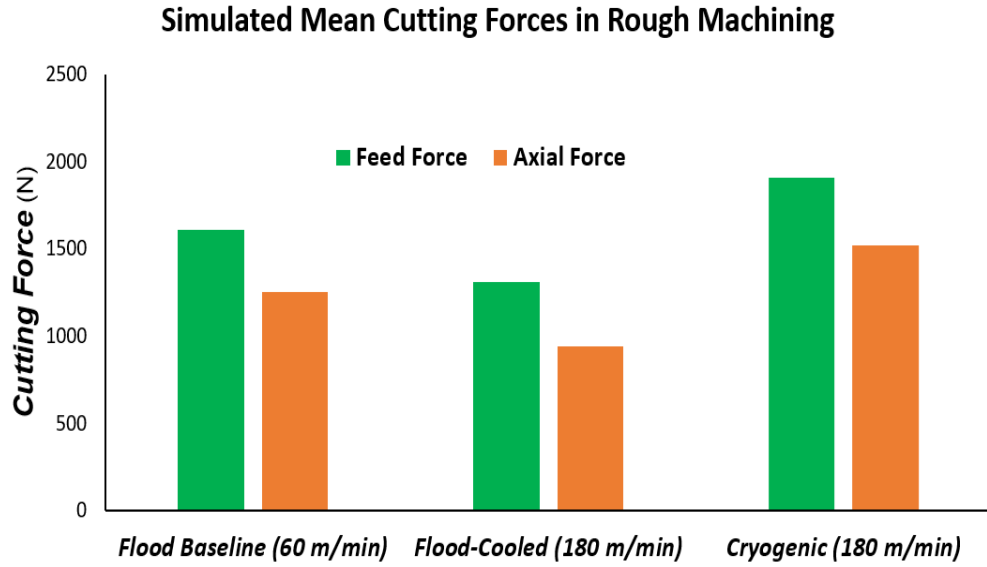


Figure 4-25. Simulated mean cutting forces in high MRR rough machining for flood and cryogenic cooling.

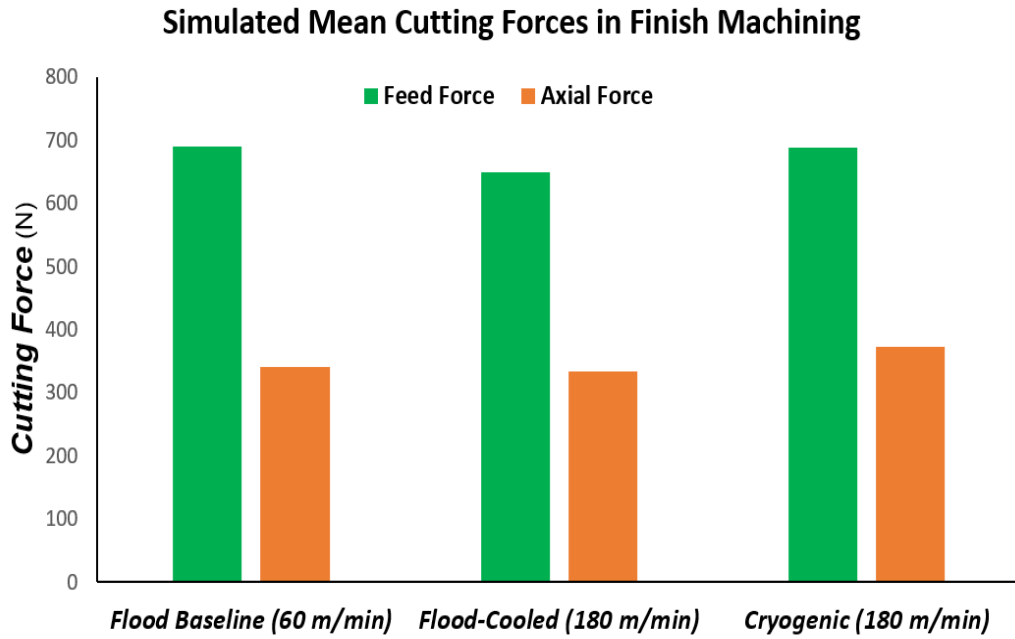


Figure 4-26. Simulated mean cutting forces in high MRR finish machining for flood and cryogenic cooling.

There are some significant conclusions that can be drawn from these two plots. For flood-cooling, an increase in cutting speed from 60 to 180 m/min resulted in a reduction in simulated cutting force for both roughing and finishing operations. This is certainly due to an increase in thermal softening of the workpiece at the higher cutting temperatures, which were observed in Figures 4-22 through 4-24. Application of cryogenic cooling did in fact lead to significant increases in both the feed and axial component of the cutting forces in these simulations. This likely a consequence of the increased flow stress exhibited at decreased temperatures, as a stronger material will more readily resist deformation from the cutting tool which can lead to higher cutting forces. However, it should be noted that all of these studies were on uninterrupted cutting operations such as turning. While the milling operation being investigated represents an interrupted cut. The different cutting dynamics and the ability to successfully apply LN₂ into the cutting zone will almost certainly effect the measured cutting forces. Therefore, further studies need to be conducted with experimental plans tailored specifically to cutting force investigation in turning and milling operations, while utilizing a consistent methodology for LN₂ application. The latter of which has a direct effect upon the lubricating and frictional characteristics in cryogenic machining, which itself needs further study.

4.2 Residual Stress Modelling in Burnished Titanium Alloy Ti-6Al-4V

In aerospace applications, perhaps the most important aspect of surface integrity is the process-induced residual stress state. The tensile residual state that is generated from conventional finish machining operations, necessitates that post-processing strategies (Such as burnishing, shot-peening, laser-shock-peening, etc.) be implemented in order to induce compressive residual stress state in the near-surface regions of employed components. This is largely due to the fact that tensile stress states facilitate the formation

and propagation of fatigue cracks, whereas the initiation and growth of such cracks is inhibited within in compressive stress fields. As aeroengine components are routinely subjected to HCF at elevated temperatures, the nature of the residual stresses which remain after burnishing can potentially have significant fatigue life implications. Unfortunately, characterization of residual stresses, particularly in terms of its variation with processing depth, is an extremely complex and resource expensive process. Thus, development of robust and accurate models which can accurately predict the residual stress state developed from burnishing processes could potentially provide great insight into the feasibility of burnishing as a replacement processing strategy for more conventional operations.

4.2.1 *Development of Numerical Model*

2D numerical (FEM) models were constructed in DEFORM for the purpose of simulating the residual stress fields in burnished *Ti-6Al-4V* alloy. Initially, 3D models were implemented so as to characterize the full stress tensor, but the increased model complexity in conjunction with the developed procedure for residual stress determination was far too computationally expensive. However, even modelling this process in two dimensions is a very time intensive process for numerous reasons which will be discussed subsequently. In any case, though, it has been shown in literature that 2D burnishing models designed for residual stress prediction can be extremely accurate [103, 104]. The general overview of the model designed in this investigation is illustrated in Figure 4-27.

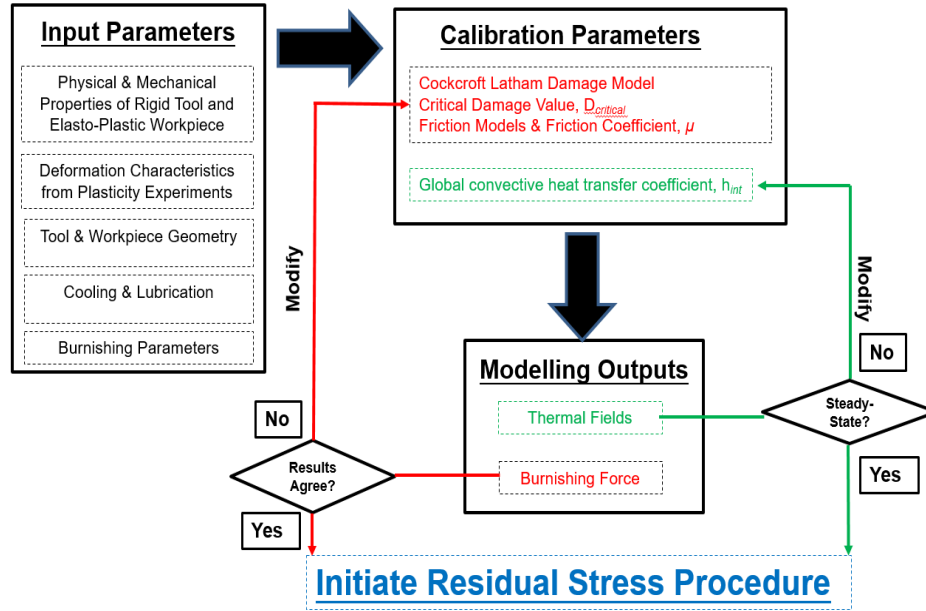


Figure 4-27. General modeling overview and calibration procedure.

In terms of the general model calibration, the 2D models developed for prediction of burnishing induced residual stresses share some commonalities with the 3D models designed for simulation of high speed machining of *Ti-6Al-4V* alloy. Namely, in both cases force based calibration was facilitated by modification to the critical damage value, D_{crit} , and the application friction coefficient μ . Moreover, they both utilize the modified Johnson Cook material model developed by Calamaz et al. [156] which is shown in Eq. 4-4, with numerical constants ascertained from SHPB experiments conducted at UTRC. However, beyond these characteristics the models share essentially no other significant similarities.

For modelling of burnishing-induced residual stresses, the workpiece was thermo-mechanically analyzed in DEFORM using an elasto-plastic material model to allow for non-uniform plastic deformation. The comparatively larger out-of-plane z-dimension (i.e., the length of the workpiece), depicted in Figure-4-28, allows for the implementation of

plane strain conditions, and thus $\varepsilon_{xz} = \varepsilon_{yz} = \varepsilon_{zz} = 0$ and the full strain tensor is reduced accordingly (Eq. 4-17):

$$\varepsilon_{ij} = \begin{bmatrix} \varepsilon_{11} & \varepsilon_{12} & \varepsilon_{13} \\ \varepsilon_{21} & \varepsilon_{22} & \varepsilon_{23} \\ \varepsilon_{31} & \varepsilon_{32} & \varepsilon_{33} \end{bmatrix} \rightarrow \begin{bmatrix} \varepsilon_{11} & \varepsilon_{12} \\ \varepsilon_{21} & \varepsilon_{22} \end{bmatrix} \quad (4 - 17)$$

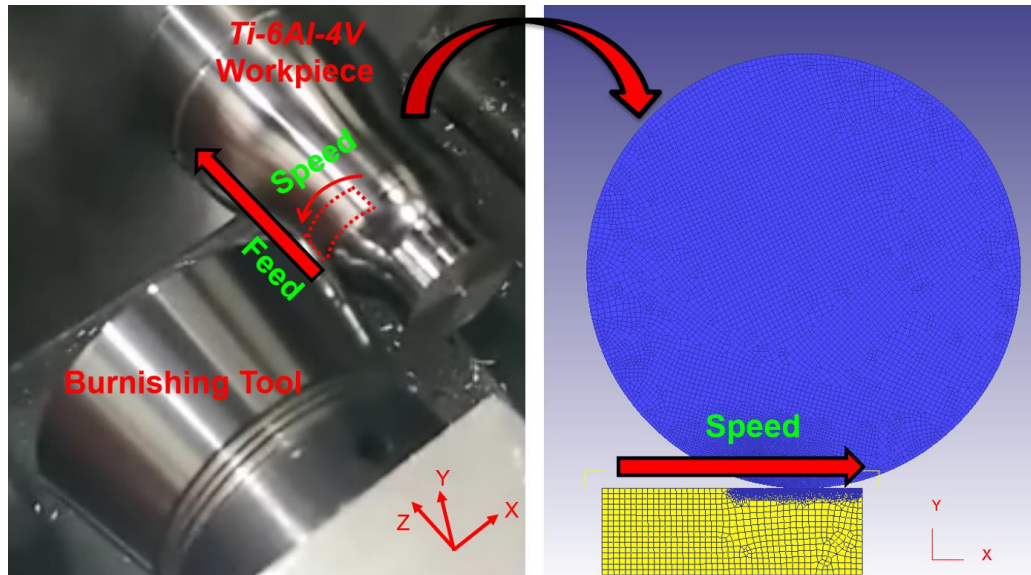


Figure 4-28. 2D plane strain representation of 3D burnishing process.

The workpiece and burnishing tool were each modeled using 10,000 linear quadrilateral elements. Mesh refinement windows were used to significantly increase the mesh density (24X) in the tool-workpiece surfaces as well as in the near-surface regions of the burnished workpiece. Thus, for the workpiece, the mean element length in the undeformed virgin region was roughly 0.6 mm, whereas in the SPD zone the element length varied between 15 and 20 μm . In this way, accurate characterization of the residual stress distribution in the sub-surface of the material is facilitated. Depiction of the mesh implemented for both the tool and workpiece are shown in Figure 4-29.

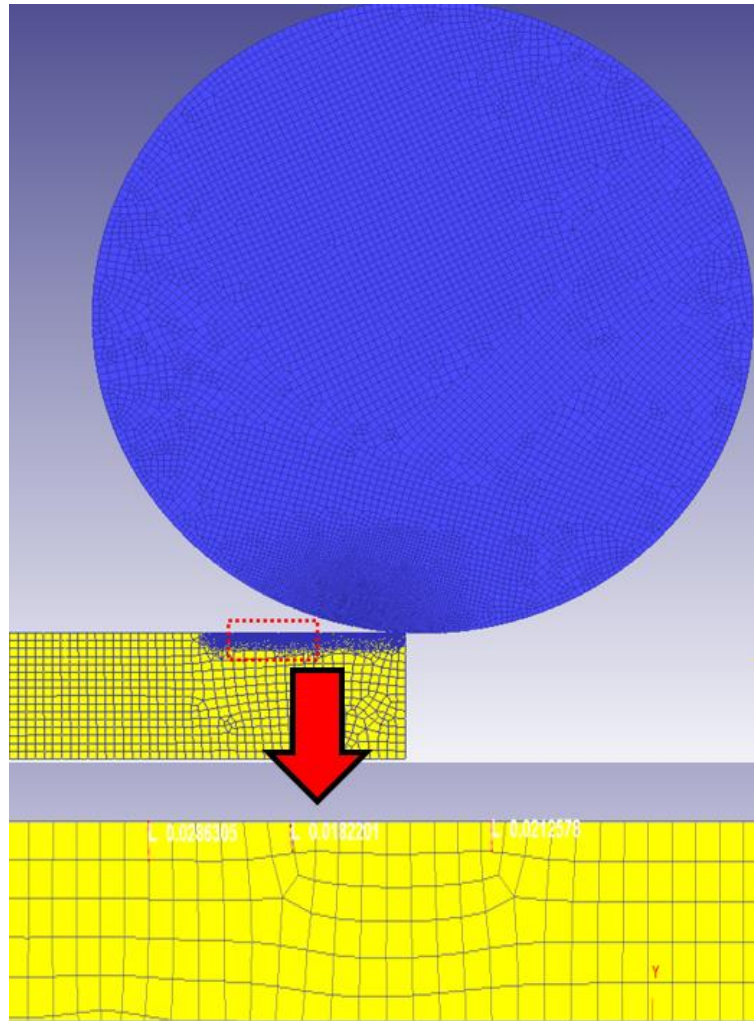


Figure 4-29. Depiction of mesh characteristics in burnishing tool and workpiece.

Burnishing simulations were conducted using methodologies which were adopted from literature and subsequently modified to reflect the specific nature of the burnishing process conducted in this investigation. This not only includes conventional ball burnishing, but also chip generating processes such as orthogonal machining operations [98, 187-189]. As DEFORM lacks any built-in software features to calculate residual stresses, the most common technique requires mechanical and thermal unloading of the workpiece after processing. This required mechanically unloading of the workpiece by shifting the tool away from the contact zone, after which the thermal fields in the workpiece

were allowed to reach equilibrium temperature with the environment (20 °C). The residual stress values at specific depths were then extracted from the simulation as functions of burnishing force, cutting speed, and NTP. Unfortunately, the employed methodology prevents residual stress characterization as a function of feed rate (As the feed direction is out-of-plane in the 2D model).

In literature, residual stress modeling of burnishing processes is typically facilitated by depicting the burnishing mechanism as a series of discrete indentations. Implementation of this technique in FEM is discussed in Sartkulvanich et al. [103], whereby after each indentation the workpiece is mechanically and thermally unloaded, after which the tool is shifted by the burnishing feed rate. This methodology is illustrated in Figure 4-30 for ten indentations. This type of 2D burnishing model is only possible with spherical rollers with no movement constraints. Given that the circular cross section of the tool is equivalent for regardless of the plane from which it is taken, models can be constructed with either feed or speed as the tool control variable. However, with cylindrical rollers, burnishing speed is the only available variable for tool repositioning, due to the fact that tool rotation would be out of plane for any other relevant cross section. In any case, the discrete indentation methodology utilized in literature, while certainly effective at estimating the burnishing mechanism (As evidenced by the good agreement between the simulation and experimental results), is not truly representative of the actual burnishing process. Regardless of the tool geometry, once the tool penetrates into the subsurface of the workpiece (i.e., indentation), the tool is not unloaded from the workpiece until processing has occurred over the entire tool path. This could potentially significantly affect residual stress values, as the dynamic

effects of material side-flow are obscured (Which occurs due to workpiece rotation, i.e., burnishing speed, as well from the tool step-over rate determined by the burnishing feed).

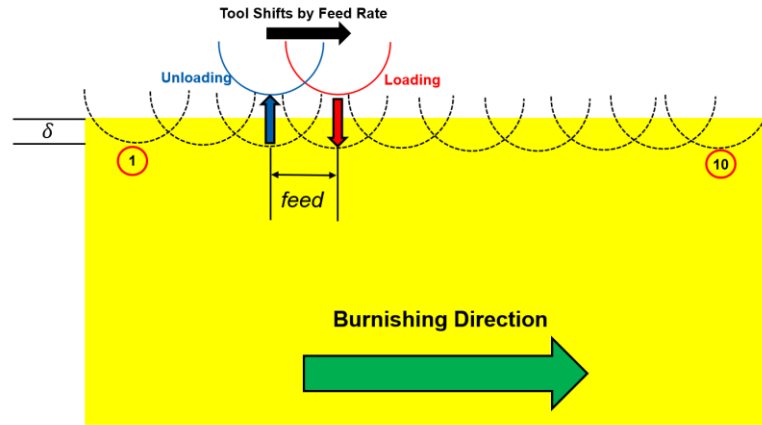


Figure 4-30. Depiction of modelling methodology typically used in literature to characterize the impact of burnishing force on residual stress.

4.2.2 Implementation of Displacement-Control and Calibration

For numerical modelling of burnishing processes, both force and displacement based controls of the burnishing tool are utilized. In a force-controlled methodology, a specific burnishing force is imparted to the workpiece, which then deforms plastically to a depth prescribed by the load. However, this methodology is inherently flawed, as it consistently under predicts the amount of plastic deformation generated during burnishing [103, 190, 191], due to the effect of elastic spring-back in the processed workpiece. Considering this, generally displacement-control of the burnishing tool is often a more effective method for 2D numerical modelling of the burnishing process, as the prescribed deformation (Penetration depth of the burnishing tool into the sub-surface of the workpiece) for a given loading force remains constant throughout the process. However, in literature this value is derived using either analytical or additional numerical models [103, 109, 192], and while this is certainly a valid strategy in the absence of the known

material behavior under different burnishing conditions, experimentally derived values would likely give a more realistic representation of the underlying physics of the burnishing process. Therefore, in this investigation displacement-based controls were implemented using the experimentally measured plastic deformation characteristics shown in Figures 3-8 and 3-9. Specifically, the experimentally measured maximum plastic deformation depths were used to assign constant maximum tool penetration depths as is depicted in Figure 4-32.

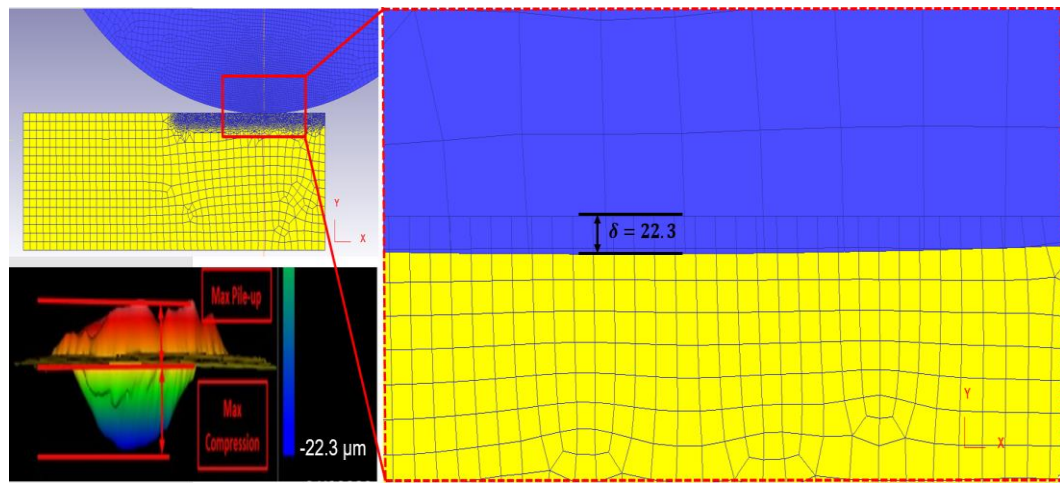


Figure 4-31. Implementation of displacement-control procedure for burnishing simulation using 1500 N loading force.

The predicted burnishing forces were then compared to the known loads on which the deformation-control schemes were based. For burnishing forces of 1000, 1500, 2000, and 2500 N, the mean percent difference between the simulated burnishing forces at steady-state and the experimentally applied burnishing force was less than 1% as is shown in Figure 4-33. The high level of inherent accuracy of the model eliminated the need for any type of calibration procedure. The natural fidelity displayed by the model is likely the result of a well-designed control scheme, good experimental methodology, and an accurate material model.

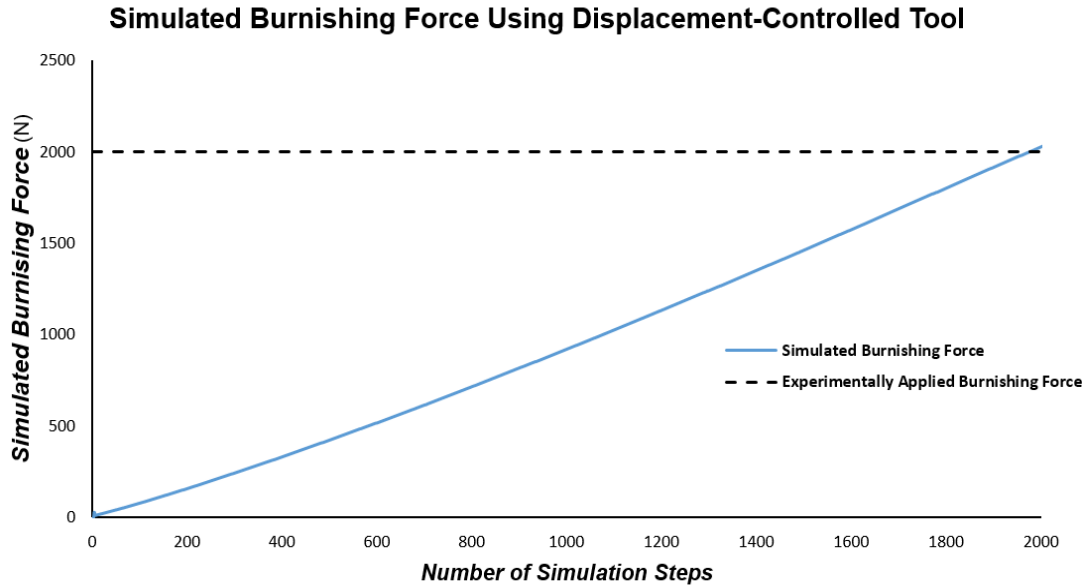


Figure 4-32. Comparison of experimental and simulated burnishing forces using a displacement-control scheme.

As mentioned previously, most burnishing models in literature utilize a discrete indentation-based mechanism. However, to improve upon the inherent shortcomings in this methodology (i.e., the neglect of any material side-flow effects), a burnishing scheme was simulated in which the effects of both the maximum penetration depth and material side-flow were captured. This scheme is illustrated in Figure 4-33.

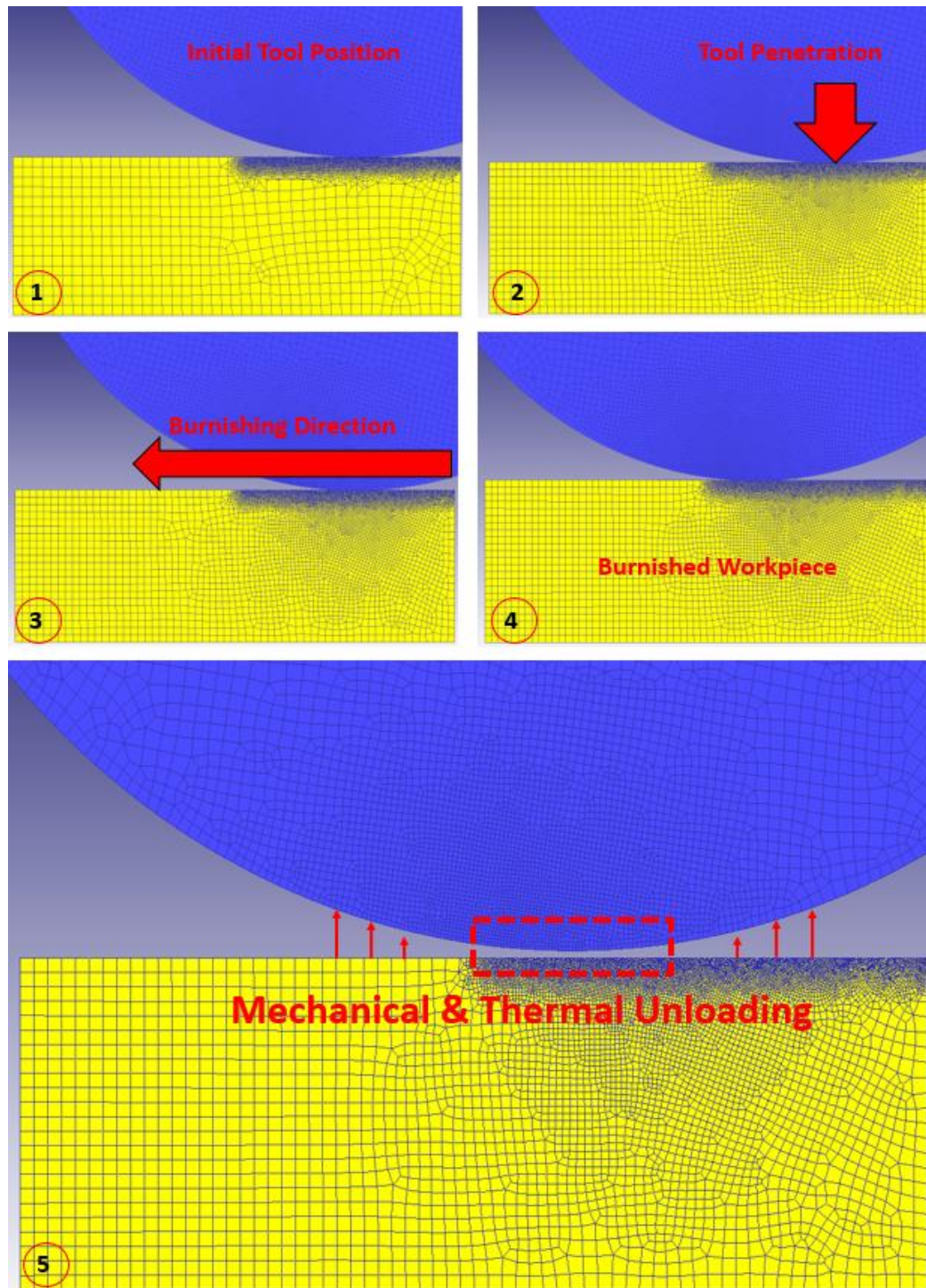


Figure 4-33. Five-step depiction of burnishing methodology employed during numerical investigation of residual stresses.

As can be seen in Figure 4-33, the burnishing simulation can be divided into five distinct steps which are summarized below:

- 1.) Initial tool positioning
- 2.) Tool Penetration into workpiece sub-surface to a maximum penetration depth determined by experimental indentation experiments
- 3.) Initiation of burnishing process (Note the tool is rotated accordingly)
- 4.) End of Burnishing Simulation
- 5.) Workpiece is mechanically and thermally unloaded

In order to determine the appropriate burnishing simulation parameters for steps 3 and 4, it was first necessary to determine the transition point from non-steady-state to steady-state conditions. As accurate prediction of the residual stress state in burnished *Ti-6Al-4V* alloy required steady-state processing conditions, determining this transition point was critical to the validity of all simulation results. To determine this value, burnishing simulations were conducted over a 12 mm tool path (Which is the entire length of the refined mesh region), and the predicted burnishing force was extrapolated. The transition point to steady-steady was then determined based upon the number of simulations steps necessary for burnishing force convergence to a constant value, as is shown in Figure 4-34. Unfortunately, elasto-plastic convergence is extremely sensitive to the implemented time-step. Consequently, the simulations were conducted on a ten millionth of a second scale. Specifically, the step size was set to 4.5×10^{-7} s, which necessitated approximately 8,000 simulation steps at a 100 m/min burnishing speed in order reach steady-state conditions. Moreover, the predicted force was again in essentially perfect agreement with the experimental load and associated deformation on which the tool-control was assigned.

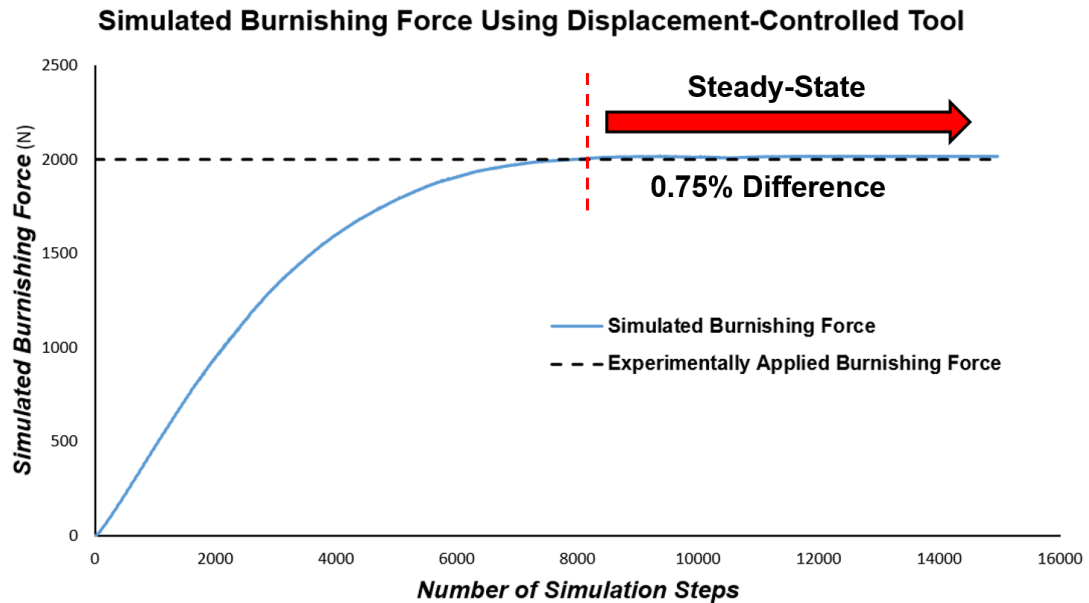


Figure 4-34. Comparison of experimental and simulated burnishing forces to determine transition point to steady-state.

4.2.3 Numerical Characterization of Residual Stresses

The residual stress state was characterized as function of processing depth for MQL, flood-cooled, and cryogenic burnishing using a 1500 N loading force and burnishing speed of 100 m/min. After which, the speed, loading force, and NTP were varied from 50-200 m/min, 1000-2000 N, and 2-4 tool passes respectively (The cooling strategy, namely external LN₂ application, was kept constant). Implementation of flood-cooled and cryogenic cooling followed an identical strategy to that used in the high speed machining models shown in section 4.1.3, where heat transfer environmental windows were used to assign specific temperatures and heat transfer characteristics to the workpiece nodes within their domains. The mean residual stress was then determined in both the tangential and axial directions from 10 extrapolated data points evenly distributed across the steady-state regime as illustrated in Figure 4-35. This process was repeated with a depth variation step

size of 25 μm (The approximate average length of near-surface element lengths) until the residual stress state displayed an as-received profile.

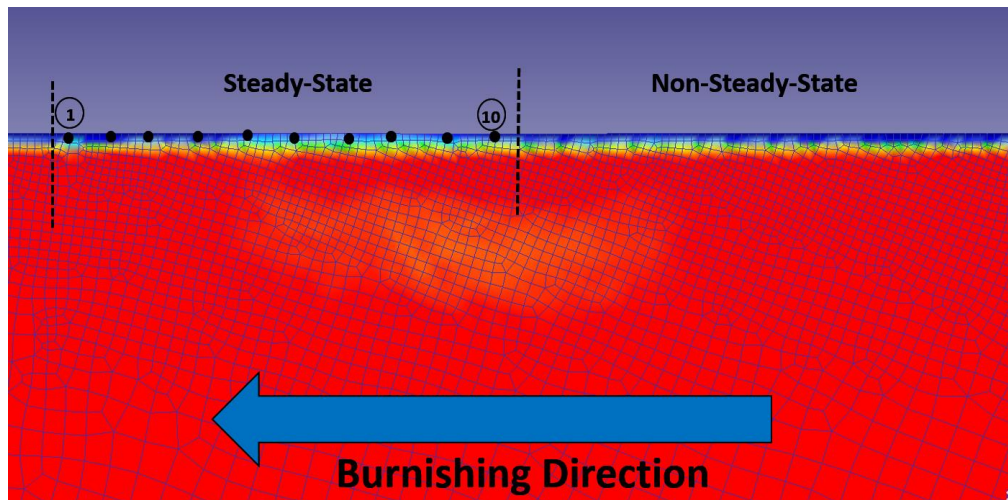


Figure 4-35. Methodology for data extraction in residual stress prediction models.

The FE model predicted significant levels of compressive stresses on the material surface and sub-surface regions. Analysis of the residual stress distribution as functions of the cooling mechanism and burnishing speed, in the both the tangential and axial directions, showed no notable dependency on the utilized cooling strategy. In all cases the residual stress state in the normal direction where insignificant. For cryogenic, flood-cooled, and MQL burnishing the maximum predicted residual stresses in the tangential direction and axial direction were approximately -815 MPa and -420 MPa. as is illustrated in Figure 4-36 for cryogenic burnishing. Regardless of the residual stress component, the peak stress was observed at approximately 50 μm beneath the processed surface, with a total refined layer depth of roughly 100 μm . The lack of dependency upon the utilized burnishing speed was also observed during the experimental investigation of the impact of burnishing parameters on the surface integrity.

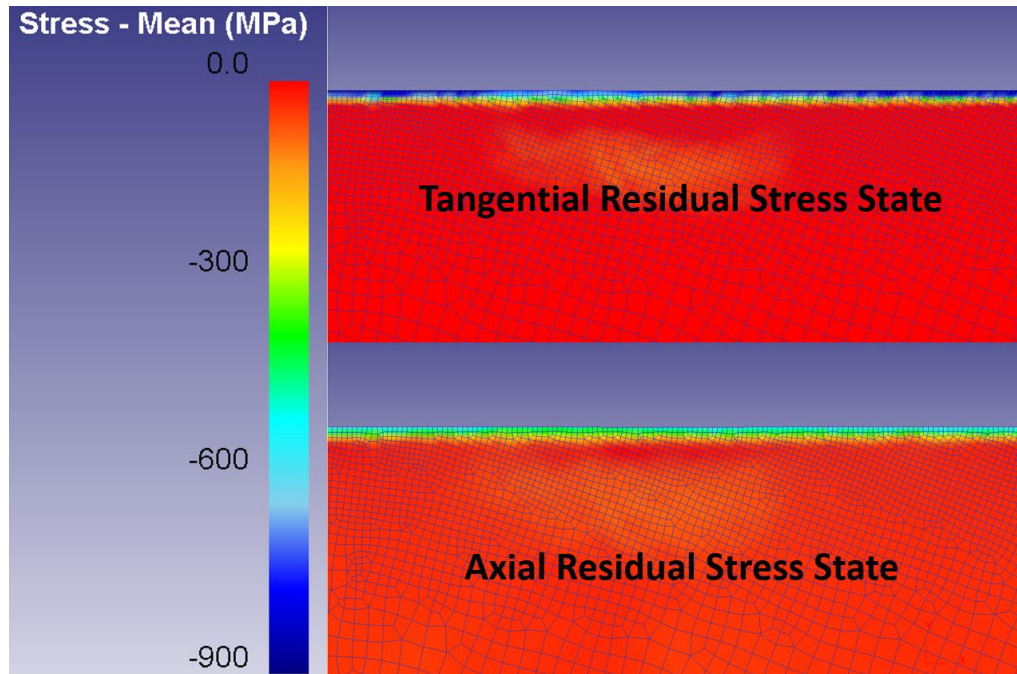


Figure 4-36. Depiction of numerically simulated compressive residual stresses for cryogenically burnished *Ti-6Al-4V* alloy in the tangential and axial directions.

As loading force was varied, however, significant deviations in the simulated stress state were observed. As the loading force was decreased to 1000 N the peak stresses in the tangential and axial directions, likewise decreased to -630 and -235 MPa respectively. However, as the loading force was increased to 2000 N the residual stress state only marginally increased (< 1%) from that observed at 1500 N. This likely indicates that the peak stresses obtained at 1500 N approached a limiting refinement threshold for *Ti-6Al-4V* alloy. In Figure 4-37 the simulated residual stresses are shown as a function of depth. In general, all the simulated conditions display a similar trend. In that the compressive stress state on the material surface becomes increasingly compressive to a processing depth of 50 μm . At this depth the nature of the compressive stress field reverses, and the material displays a sharp transition to its unburnished state. Moreover, as expected, the higher pressures associated with larger burnishing forces are more effective at inducing a higher magnitude of compression within the material.

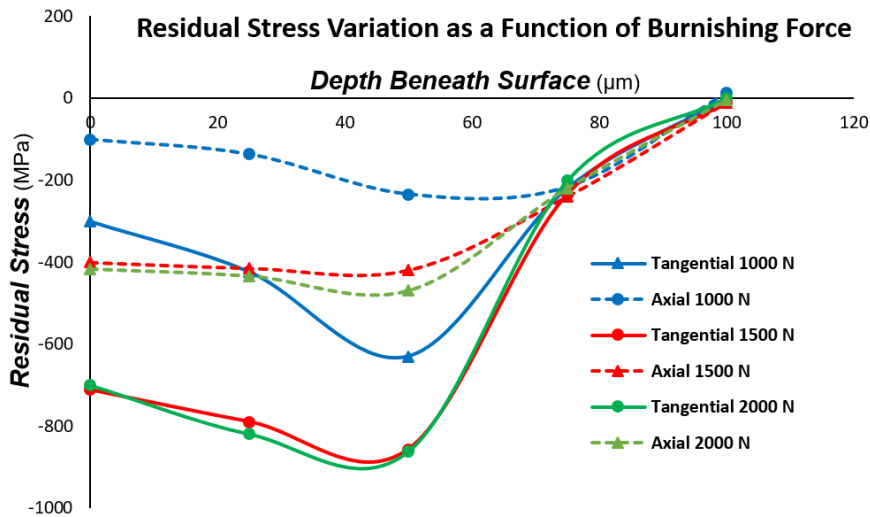


Figure 4-37. Simulated residual stress depth variation for various loading forces.

An interesting stress-stacking phenomena is observed when characterizing the effect of NTP on the residual stress profile of burnished *Ti-6Al-4V* alloy. Like the results shown in Figure 3-21, in which the processed sub-surface became increasingly work hardened with increasing NTP, increasing NTP also produced more compressive peak stresses in the near surface regions of the material. Additionally, the residual stress ALD was significantly larger in MPB. After 4 tool passes at 1000 N, the magnitude of the residual stress was similar to that simulated at 1500 N with a single tool pass. Moreover, the simulation predicts the presence of deep layer of compressive stress in the material sub-surface from roughly 300 to 800 μm. These results are shown in Figures 4-38 and 4-39. While the exact fidelity of this secondary compressive layer is questionable to some degree, as it highly unlikely that the residual stress field would transition to its as-received state and then become compressive yet again deeper in the sub-surface, it does however highlight the possibility of a mechanism driving the stress-state deeper into the material sub-surface.

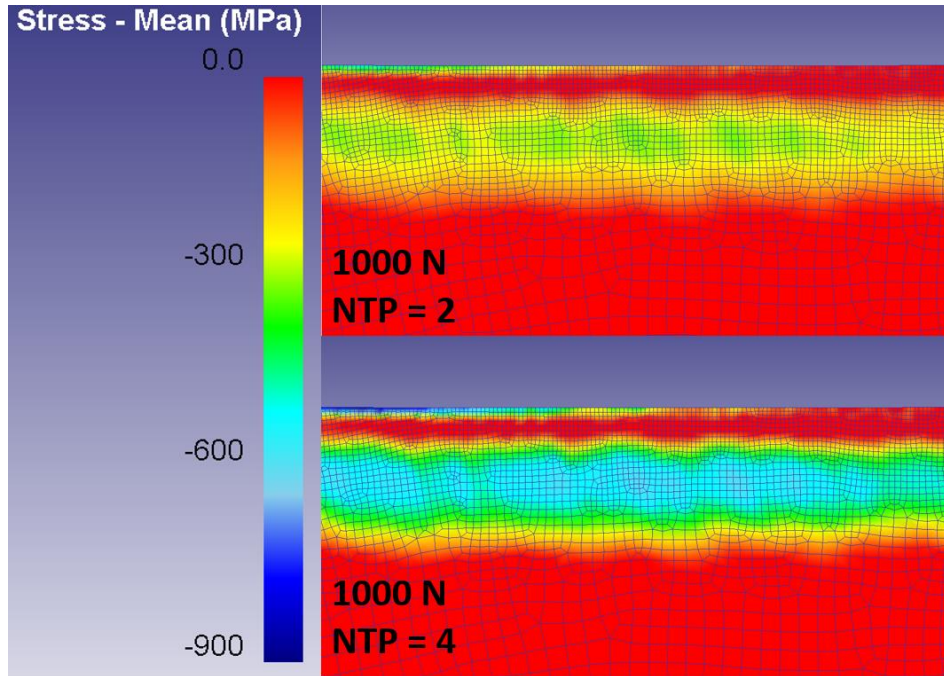


Figure 4-38. Depiction of tangential residual stress fields in MPB.

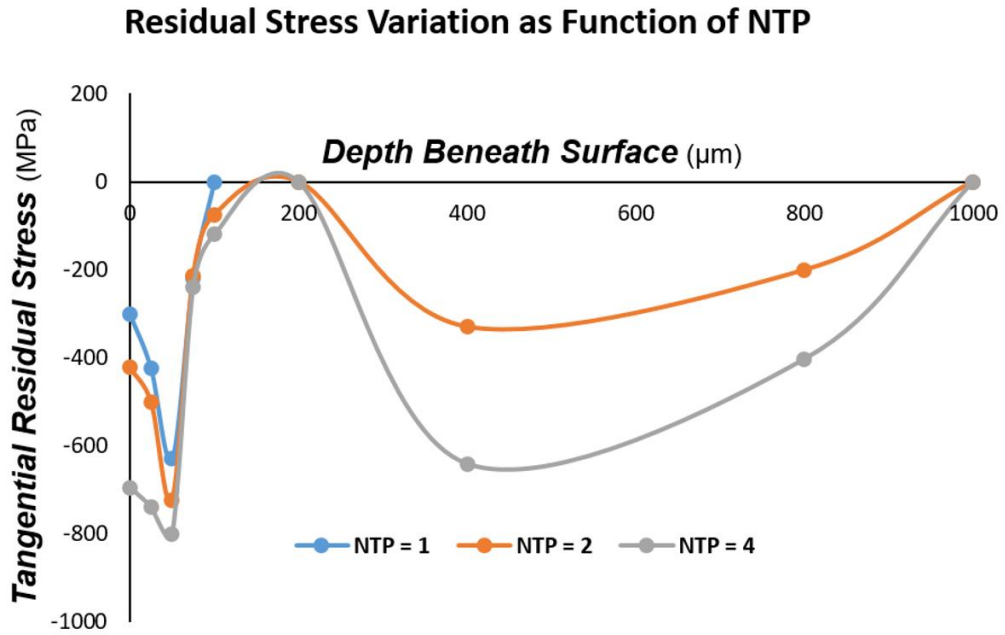


Figure 4-39. Simulated residual stress variation in MPB.

These simulations suggest that the residual stress fields in burnished *Ti-6Al-4V* alloy are strongly influenced by both the loading pressure and the number of tool passes. The latter of which has potentially significant implications in terms of the fatigue life of thin aerospace components processed using this technology. As mentioned previously, maintaining part tolerances is extremely important during manufacturing, and using lower loading forces is one means of facilitating this requirement. While implementing high loading forces would certainly induce a greater level of surface integrity improvement, it would however drastically increase the probability of part distortion. By utilizing additional tool passes at lower loading forces to obtain a comparable level of material refinement, both surface integrity and distortion allowances can be achieved during processing. Moreover, the potential presence of deeper a stress-state in MPB would likely provide additional fatigue-life benefits.

CHAPTER 5.

CHARACTERIZATION OF RESIDUAL STRESS FIELDS IN MACHINED & BURNISHED

TITANIUM ALLOY *Ti-6Al-4V*

Residual stresses are self-equilibrating internal stresses that remain in a material once an applied load (force, temperature gradients, etc.) is removed. These stresses form as a response to either plastic deformation processes, non-uniform cooling of material that is processed at elevated temperatures, or from cooling induced phase transformation [193]. Thus, cryogenic machining or burnishing of *Ti-6Al-4V* alloy can alter the internal stress state by several possible avenues. Practically, for aerospace applications, the process-induced residual stress state which results from machining, post-processing, or other manufacturing operations, alters the in-service stresses that components would normally experience. The implication being that residual stresses can be either beneficial or detrimental to the fatigue life of a component, depending upon their impact to the tensile stress fields that facilitate crack initiation, and are commonly generated during the normal service life a component. If a manufacturing process induces tensile stresses in a component, the fatigue life will likely be significantly decreased, due the fact that these stresses will be superimposed onto the in-service tensile field experienced due to loading. Consequently, this will lead to an acceleration in crack formation and propagation on the surface and near-surface layers of the material. Compressive stresses, conversely, can significantly increase the service life of employed components by counteracting these tensile stresses, allowing for the effective absorption of any detrimental stress and thus the suppression of fatigue cracks. Depending upon the respective level of the tensile stress experienced, and magnitude of the sub-surface compressive state of the material, it is

certainly possible if not likely, that any tensile stresses that arise due to loading would be experienced by the component as in-plane compressive stress, and thus completely retarding the formation of fatigue cracks [194]. This is particularly important in aerospace applications, where components are routinely subjected to cyclical loading at elevated temperatures. Therefore, accurate measurement of residual stresses is extremely important from both a product and process design perspective. Generation of residual stresses during processing is inherently a thermo-mechanical process, with each independently having significant influence on the induced residual stress profile [195-197]. Increased thermal loading, which is at its maximum on the surface of the workpiece, tends to generate a tensile stress state. Therefore, tool geometry, friction, wear, etc., all of which influence the thermal load experienced during machining, can significantly influence the residual stress state. The mechanical component of the experienced loading, however, tends to generate compressive stresses into the sub-surface of the material. Thus, the actual residual stress profile developed during processing is complex combination of the individual and combined effects of thermal and mechanical loading.

5.1 Measurement Techniques

Measurement of residual stresses can be broadly categorized into non-destructive and destructive techniques [194, 198]. In the latter, the most commonly utilized technique is the hole-drilling method, in which a hole is drilled through the surface of the material to a prescribed depth, while strain gauges measure the distortion that occurs during deformation. Relaxation of residual stresses that occurs from material removal can be back-calculated using theoretical correlation coefficients relating the tri-axial strains to the principal stresses in the drilling direction. However, beyond destroying the component and preventing further analysis, the most significant drawback with this technique is that

implementation of the correlation coefficients introduces significant error into the analysis. Moreover, due to the nature of this methodology, it cannot accurately characterize compressive residual stress when the magnitude is greater than 50% of the material's yield stress [198]. As has been shown by Nalla et al. [126], burnishing of *Ti-6Al-4V* alloy induces stress a state that well exceeds this 50% threshold. Therefore, this method is not a suitable choice for characterization of residual stress depth profiles in burnished *Ti-6Al-4V* alloy.

Of the non-destructive techniques employed, X-ray diffraction (XRD) is the most commonly utilized [199]. This is a macroscopic methodology which determines the mean stress in an irradiated volume defined by the surface area and penetration depth of the X-ray beam. It is characterized by the interactions between high frequency X-rays and the crystal lattice of the metal under investigation in accordance with Bragg's Law, as is shown in Eq. 5-1:

$$n\lambda = nd' \sin \theta \quad (5 - 1)$$

The planes of atoms within the lattice network cause destructive and/or non-destructive interference, depending upon the interplanar spacing of the atoms (d) and the specific wave length of the X-ray (λ) as is shown below in Figure 5-1.

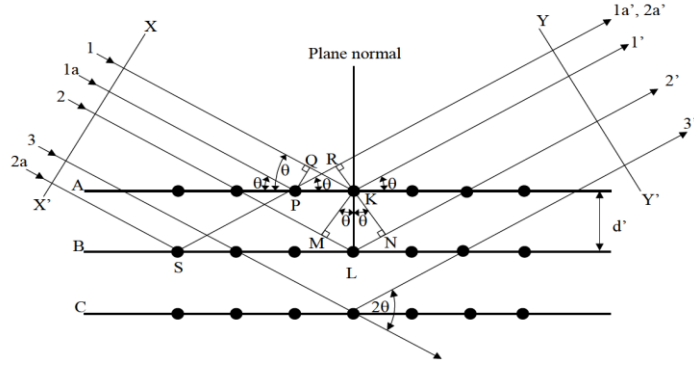


Figure 5-1. Diffraction of X-rays in crystal lattice. Reprinted from [199] with permission.

The stresses in any direction can be determined based upon the interplanar spacing measurements on planes normal to (d_n) and in the direction of the desired stress (d_ψ) using the following expression (Eq. 5-2):

$$\sigma_\phi = \frac{E}{(1 + \nu)\sin^2\psi} \left(\frac{d_\psi - d_n}{d_n} \right) \quad (5 - 2)$$

According to Fitzpatrick et al. [199], the $\sin^2\psi$ method is the most commonly employed non-destructive technique for measuring residual stress. A series of XRD measurements are taken at varying psi angles, from which $\sin^2\psi$ is then plotted against the interplanar spacing (or 2θ position) as is shown in Figure 5-2.

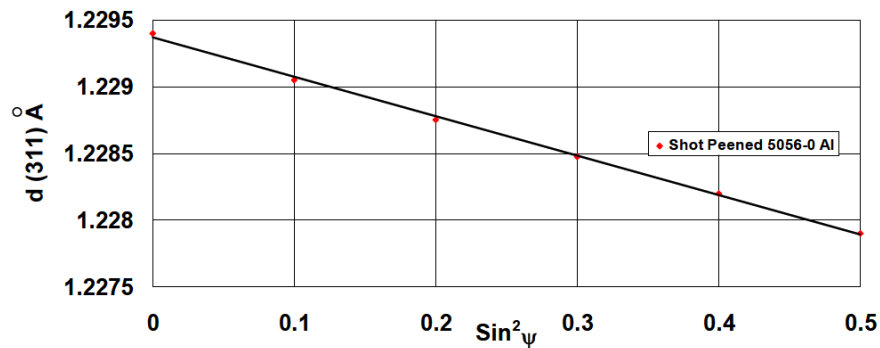


Figure 5-2. Example of $\sin^2\psi$ plot as a function of interplanar spacing. Reprinted from [199] with permission.

Residual stress is then determined by taking the gradient of the plotted line, m , and using material properties of the measured material as is shown below in Eq. 5-3. This methodology is generally native in most software packages used for XRD analysis, and only minimal human calculation is generally necessary.

$$\sigma_{\phi} = \left(\frac{E}{1 + \nu} \right) m \quad (5 - 3)$$

For the *Ti-6Al-4V* alloy under investigation in this study, lattice strain measurements were made using Cu-K $_{\alpha}$ radiation on the (221) planes of the HCP- α phase. Unfortunately, the geometric constraints of the XRD unit and the processed sample prevented analysis of the axial component of residual stress. Therefore, all stress values shown in this experimental investigation represent the stress component in the tangential direction. The stresses in the radial direction were assumed to be zero in accordance with the plane-stress assumptions typically used during XRD analysis.

In terms of reducing the formation and propagation of fatigue cracks, the residual stress state in the material's sub-surface can be just as significant as that induced on the material's surface. As X-ray radiation can only make minimal penetration into the sub-surface of a material (For titanium alloys the approximate penetration depth is 15-20 μm), in order to characterize the residual profile as a function of depth, material layers must be successively removed to the desired depth for XRD analysis. However, mechanically removing layers of material can significantly alter the residual stress state imparted during processing. Therefore, in order to accurately correlate processing parameters with their impact upon residual stress depth variation, material removal must be as minimally invasive as possible. In this scenario, electropolishing is the most common method for material removal. This process is defined by submerging a sample in an electrolyte bath

of an acid or salt solution (the exact chemical depends on the material being analyzed and there is often a number of suitable solutions for a given material), a specific voltage and current is then applied to the solution and over time the material is gradually removed. However, the process can sometimes be more complicated due to variations in MRR, material pitting, chemical deposits on sample, etc., and thus experimentation is often necessary to determine the proper combination of polishing parameters. [199].

In this investigation, a methanol solution with 5% perchloric acid was carefully prepared and material samples were electropolished under various voltage and currents until the desired material response was achieved. A chemical mask, which resists the electrolyte attack, was attached to the surface of the workpiece sample, such that only a specific region of the material surface was susceptible to material removal. Scanning white light interferometry was then utilized in order to build a 3D model of the electropolished surface topography, as is shown in Figure 5-3, from which the depth of the layer removal could then be measured.

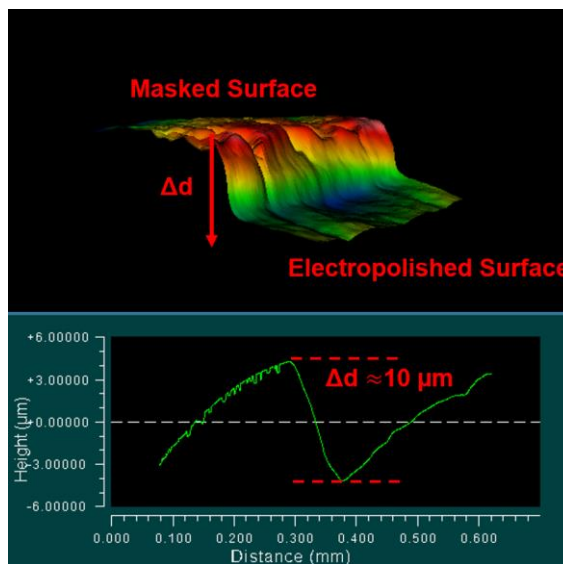


Figure 5-3. 3D surface topography of electropolished *Ti-6Al-4V* alloy.

Ti-6Al-4V alloy samples were then polished at various time steps to a maximum of 5 minutes in order to build an electropolishing calibration curve based on the utilized parameters which is illustrated in Figure 5-4.

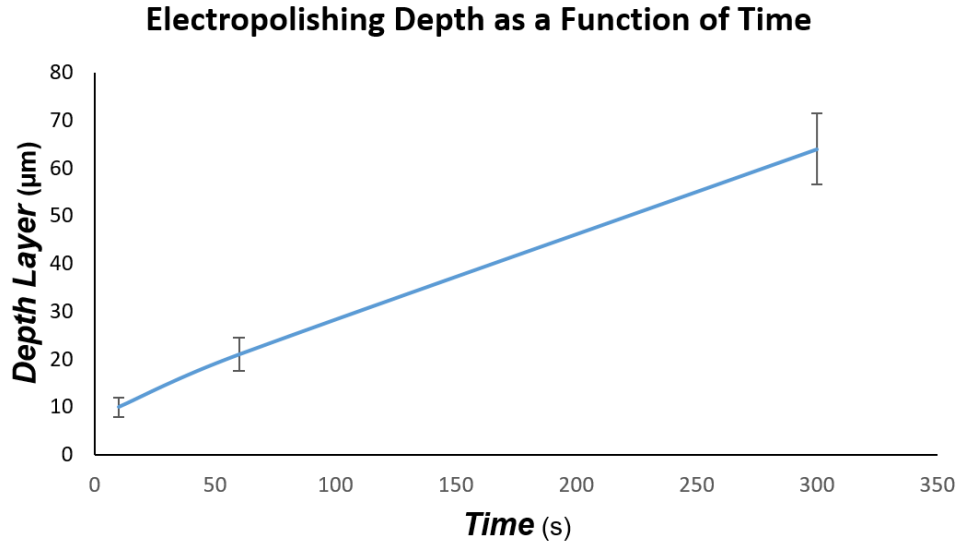


Figure 5-4. Electropolished material removal calibration curve in *Ti-6Al-4V alloy*.

As each successive layer of material is removed, exposing a new surface for XRD analysis, the magnitude of the residual stress field is relieved. The magnitude of the stress relaxation must be mathematically accounted to ensure an accurate depiction of the residual stress fields. Moore and Evans [200] proposed a closed-form solution for correction of residual stresses in numerous geometries. This includes solid cylindrical bodies, such as the titanium alloy *Ti-6Al-4V* workpieces under investigation in this study, as shown in Eq. 5-4.

$$\sigma_z(r_1) = \sigma_{zm}(r_1) - 2 \int_{r_1}^R \frac{\sigma_{zm}(r) dr}{r} \quad (5 - 4)$$

Where dr is the radius of the removed cylindrical shell, r_1 is the radius at the depth of interest, and R is the total radius of the sample. As long as dr is small, the correction error is minimal, as is seen in numerous experimental works [201]. However, this error

significantly increases with increasing layer thickness. Mathematically, this is reflected in a Taylor expansion of the integrand, where the later terms increase the error exponentially.

5.2 *Impact of Cutting Edge Radius*

In order to examine the influence of burnishing parameters on the induced residual stress state, it is helpful to first gain insight into the impact of machining processes. From an aerospace perspective, burnishing is a post-processing operation that is utilized after finish machining or grinding. Therefore, in order to characterize the combined effect of these processes, their independent effects must first be ascertained. Tool geometry, specifically the cutting edge preparation, has a significant effect upon the generated surface tractions, cutting forces, temperature distributions, and consequently residual stresses [202-205]. Kishawy [206] investigated the impact of tool edge radius on the cutting temperatures for sharp and honed tools. It was observed that as the cutting radius was decreased the localized contact area also decreased, this was accompanied by an increase in cutting temperatures. Conversely, as cutting edge radius increased, a temperature reduction was noted. In terms of cutting forces, Wyen and Wegener [207] examined the impact of cutting edge radius on the developed cutting forces in orthogonal turning of *Ti-6Al-4V* alloy. Both the main and feed cutting force components increased with cutting edge radius. Additionally, even in sharp tools, ploughing forces were found to be highly susceptible to cutting edge radius. Therefore, in order to quantify the impact of cutting edge radius upon residual stress, orthogonal turning experiments were conducted at a cutting speed of 100 m/min and a feed rate/depth of cut of 0.06 mm. Three sharp tools were prepared with cutting edge radii of 50 μm , 28 μm , and $<5 \mu\text{m}$. For all conditions hybrid cooling was utilized in order to investigate the impact of cryogenic cooling on the known propensity of thermal loads to generate tensile stresses on the processed surface.

For comparison on this front, a baseline turning using flood-cooling was analyzed. No consideration was given to tool geometry, as the workpiece was simply lightly finish turned to the prescribed R_a used for all burnishing experimentation. Residual stress was characterized as a function of depth for these conditions and is shown in Figure 5-5.

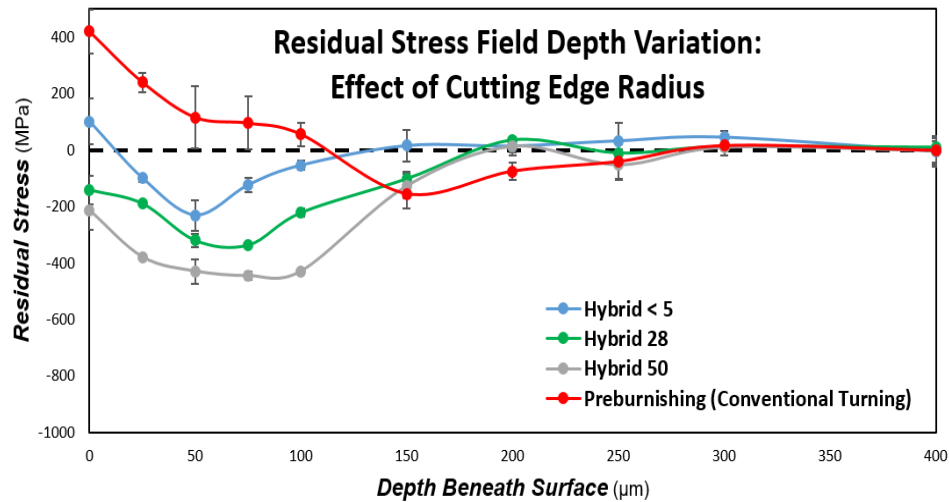


Figure 5-5. Impact of cutting edge radius on residual stress in machined *Ti-6Al-4V* alloy.

Analysis revealed that as cutting edge radius increased, the stress state in the processed workpiece became increasingly more compressive, owing to the increased amount of material being compressed onto the surface ahead of the cutting tool. This aligns with previous literature results in which more compressive loading was found with higher cutting radius values [208]. Moreover, tensile stresses were observed on the surface and near-surface layers of samples machined using flood-cooling, as well during hybrid cooling with the sharpest tool ($< 5\mu\text{m}$). These results mesh well with the known tendency for increased thermal loading to generate tensile stresses during machining. Flood-cooling relies primarily on standard convection cooling, which has a significantly lower heat transfer capability in comparison to boiling heat transfer in cryogenic cooling. Consequently, the cutting temperatures on both the workpiece and cutting tool are typically

significantly higher in flood-cooling. This is supported by the numerical models presented in this work and shown in Figures 4-20 through 4-23. This increased thermal load on the material surface leads directly to increased tensile stresses on the surface layers of machined *Ti-6Al-4V* alloy. Additionally, tensile stresses were observed under hybrid cooling using the sharpest tool ($< 5 \mu\text{m}$), though the magnitude of the maximum stress was significantly less tensile than that in flood-cooling. This indicates that cryogenic is unable to completely mitigate the intense and localized cutting heat generated while using an extremely sharp tool. In both cases, these tensile surface stresses are extremely problematic from a fatigue life perspective. Fatigue cracking can only occur in a tensile stress field, and thus in aerospace applications it is necessary for machined/ground components to undergo some type of finishing process in order to alter the stress state. As the cutting edge radius increases, however, the stress-state becomes entirely compressive in the near-surface machined layers to a depth of approximately 150-200 μm . Additionally, the largest cutting edge radius also induced microstructural refinement in the surface layers of machined *Ti-6Al-4V* alloy. Focused ion beam (FIB) microscopy was used to mill a cross section of the near-surface, and analysis revealed the presence of shallow ($< 5 \mu\text{m}$) surface layers with reduced grain size. Though no nanostructuring was present, like that observed in hybrid single pass and MPB, grain refinement was still present in these layers as is depicted in Figure 5-6. Such grain refinement has been shown to be effective at mitigating fatigue crack formation and propagation at elevated working temperatures [126].

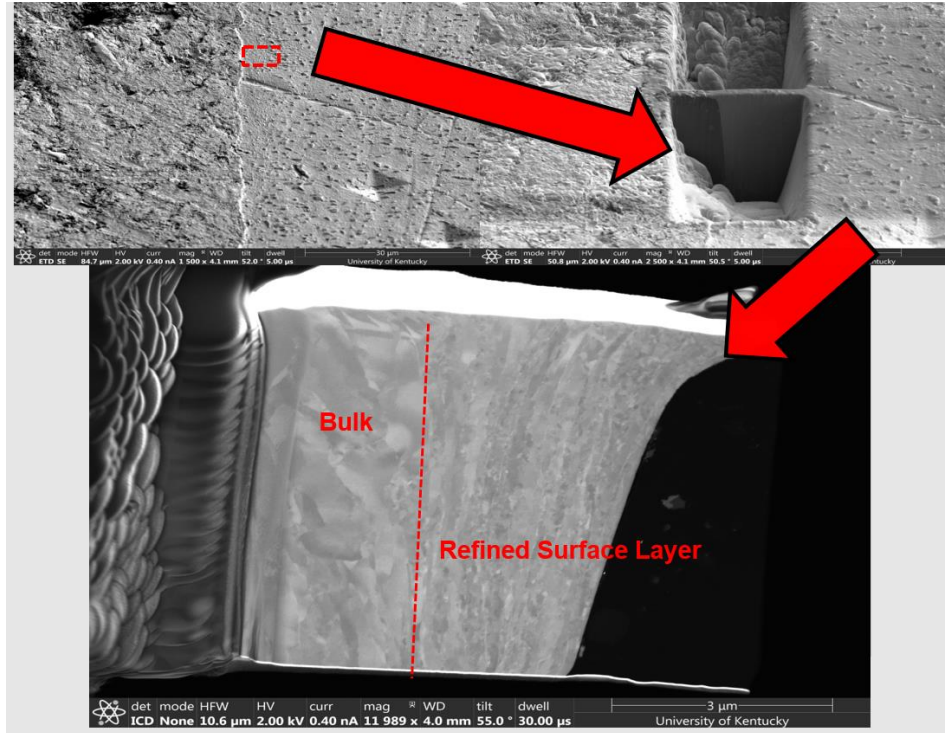


Figure 5-6. FIB based microstructure analysis of hybrid machined *Ti-6Al-4V* alloy with 50 μm cutting edge radius.

In summary, the combination of increased ploughing force with increasing cutting edge radius and lower cutting temperature in the presence of LN₂ cooling, facilitates the formation of deep layers of compressive residual stress. Furthermore, larger cutting edge tools generate surface layers exhibiting grain refinement, which can help to maintain fatigue life at elevated temperatures. Thus, in terms of maximizing both component functionality and fatigue life, tools with larger cutting edge radii are more advantageous, considering that compressive stress fields will effectively negate detrimental tensile stresses and retard the formation and propagation of fatigue cracks. Additionally, these observations will provide further insight during XRD characterization burnishing induced residual stress fields.

5.3 *Residual Stress Fields in Burnished Ti-6Al-4V Alloy*

Aeroengine components are routinely subjected cyclical loading over a range of working temperatures, leading to fatigue in both low cycle and high cycle regimes. Which, along with foreign object damage (FOD) from ingested debris, facilitates the formation and propagation of fatigue cracks, significantly limiting the functional performance and fatigue life of components. This is a pressing concern for aerospace companies, due to the high costs associated with component maintenance and replacement. Moreover, it reinforces the need for components that can tolerate high temperature cyclical loading and FOD with minimal losses in fatigue life.

As fatigue cracks are generated on surfaces which are in tension, an effective mechanism to mitigate crack formation and propagation, and consequently to increase fatigue life, is to impart compressive residual stresses into the surface layers of employed components [37, 209-214]. Compressive stresses counteract the in-service tensile stresses experienced during operation and suppress the formation and growth rate of fatigue cracks. As has been discussed previously, typically in aerospace applications shot-peening or laser-shock-peening are used to induce shallow layers of compressive residual stress [210, 215, 216]. However, shot-peening has a tendency to degrade surface quality, which can consequently lead to a reduction in fatigue life (particularly at elevated temperatures). [217, 218]. Burnishing, on the other hand, has consistently been shown to significantly improve surface quality [18, 80, 219]. Moreover, burnishing has also proven to be an effective means of increasing the fatigue life of aerospace components, by generating deep cold worked layers of material which exhibit highly compressive residual stress fields. Additionally, as shown by Nalla et al. [126] and Nikitin et al. [210], the depth of the peak compressive stress is more than twice that observed in laser-shock-peened *Ti-6Al-4V* and

AISI 304 alloys, and roughly 20-25% larger than that observed for shot-peening as reported by Wagner et al. [73].

It can be surmised that in aerospace applications, the nature and magnitude of the residual stress fields induced from manufacturing processes, significantly impacts the fatigue life and functional performance of components subjected to HCF. However, little no research has been conducted that considers the impact of cooling mechanisms upon the residual stress state of processed materials. It has been shown repeatedly that reduced processing temperatures mitigate the normally occurring effects of thermal softening, allowing for increased strain hardening during burnishing of *Ti-6Al-4V* alloy. Processing temperature also effects the flow stress behavior of *Ti-6Al-4V* alloy, as there is a sharp decrease in the exhibited flow stress with increasing temperature, and conversely as temperature decreases. Consequently, application of LN₂ (which possesses a boiling temperature of -196°C at standard atmospheric pressure), enacts severe increases to the flow stress during machining. The end result being that elastic energy facilitates the formation of nanocrystalline surface layers by reducing the temperature necessary for DRX. As shown during this investigation, burnishing at cryogenic temperatures resulted in increased microstructural and mechanical refinement. In order to ascertain the effects of LN₂ application upon the burnishing-induced residual stress state of *Ti-6Al-4V* alloy, XRD was utilized to characterize depth variation of tangential residual stresses for a variety of cooling mechanisms and burnishing parameters, as is shown in Figure 5-7.

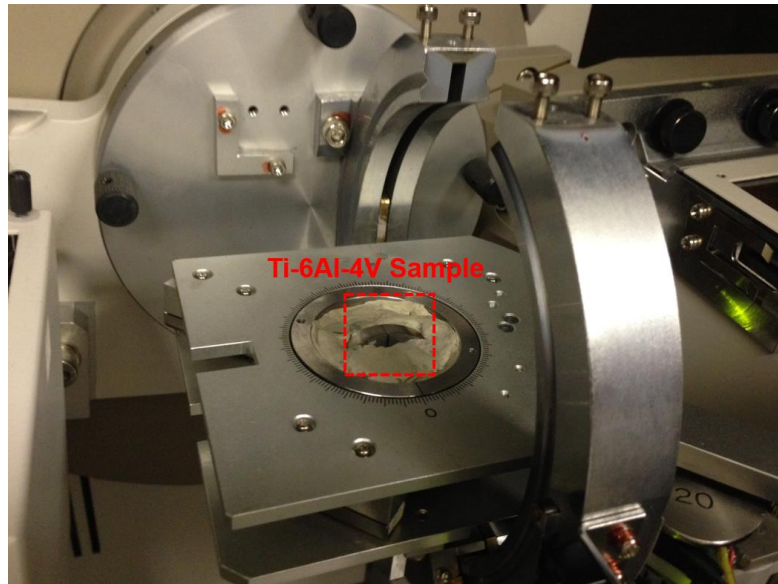


Figure 5-7. Experimental setup for XRD analysis of burnished *Ti-6Al-4V* alloy.

In regards to the impact of cooling mechanisms upon the imparted stress state of burnished *Ti-6Al-4V* alloy, the results of which are shown in Figure 5-8, many important conclusions can be drawn. First, for all examined cooling mechanisms, burnishing produced deep layers of compressive residual stress in the material sub-surface, with the peak stress occurring within the near-surface stress-hook. Though the general profile of these stress states depending upon the cooling mechanism, all burnished samples had significantly deeper and more compressive residual stress fields than the laser-shock-peened *Ti-6Al-4V* alloy sample reported in Nalla et al. [126] and show here in Figure 5-9. Moreover, the peak compressive stress of workpiece samples burnished in this study are comparable to the deep rolled peak stress shown in Figure 5-9. The implications of these findings are significant, as shot-peening and laser-shock peening are the predominant means of inducing compressive states into aerospace components to increase fatigue life. The larger compressive state generated by burnishing can more effectively mitigate the tensile stresses produced during conventional finish machining, as well as those

experienced during its service life. Therefore, in comparison to shot-peening and laser-shock-peening, burnishing can potentially provide better functional performance and fatigue life in components employed in aerospace applications.

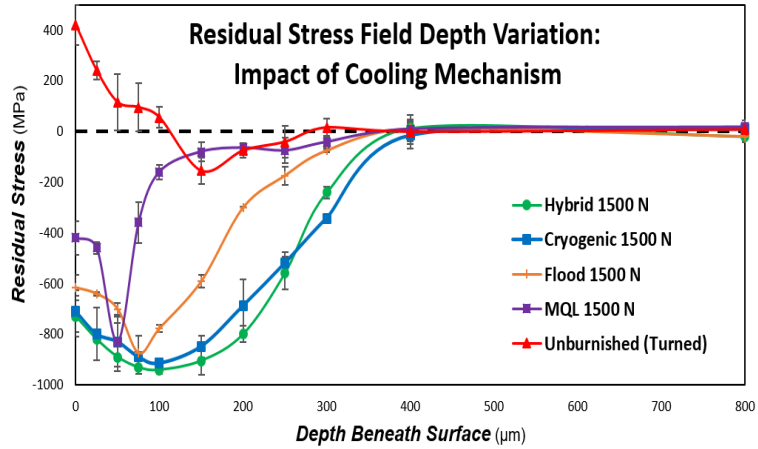


Figure 5-8. Residual stresses in burnished *Ti-6Al-4V* alloy for various cooling mechanisms.

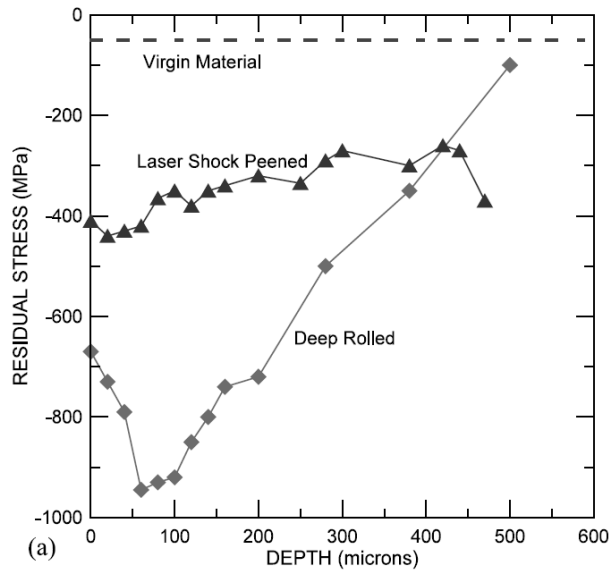


Figure 5-9. Residual stresses in laser-shock-peened and deep rolled *Ti-6Al-4V* alloy. Reprinted from [126] with permission from Elsevier.

The observed surface residual stresses show a strong dependency on the utilized cooling technique. This is in stark contrast to the numerical residual stress models developed in the previous chapter, where the implemented cooling methodology had no impact of the residual stress state. As mentioned previously, high thermal loads during machining have a tendency to generate tensile residual stresses on the surface of processed materials. However, cryogenic and hybrid burnishing produced surface compressive stress values of -710 MPa and -730 MPa respectively, whereas flood-cooling and MQL respectively generated values of -615 MPa and -420 MPa, as is shown in Figure 5-10. This signifies a 73% increase in the peak surface compressive stress when comparing near-dry MQL to external LN₂ application. The unburnished workpiece sample, which was finish machined using conventional flood-cooling, displayed a peak tensile residual stress of 418 MPa. Overall, the observed trend was that with increased cooling the stress state in the burnished surface became increasingly compressive. On the surface of the material the effect of cooling is most pronounced, and thus the largest percentage of the machining-induced tensile stress is mitigated while burnishing with LN₂. As the formation and propagation of fatigue cracks is predominantly on the surface and near-surface of aerospace components experiencing tensile stresses, the marked increase in compressive residual stress in these surface layers while utilizing cryogenic cooling could significantly suppress fatigue-based cracking.

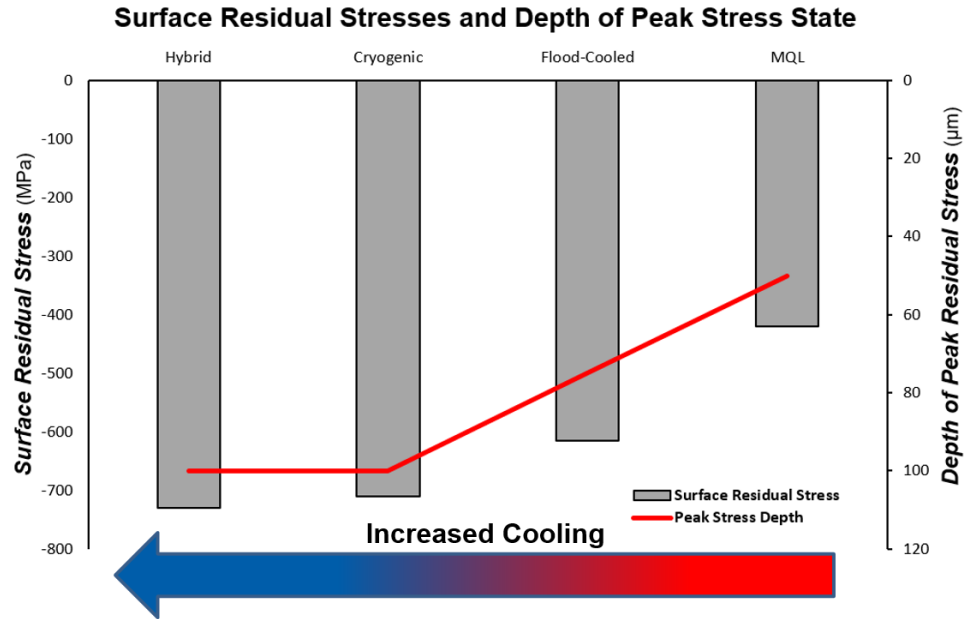


Figure 5-10. Surface residual stresses and depths of peak compressive stresses in burnished *Ti-6Al-4V* alloy.

The stress profile conventional flood-cooled burnishing resulted in a maximum compressive stress of -911 MPa at a processing depth of 75 µm. In comparison to shot peening and laser-shock-peening, this represents a significant increase in the peak sub-surface compressive residual stress, and this is particularly true for laser-shock-peening (as this value is more than twice the observed peak compressive stress). Moreover, the depth of the peak stress is 4-5 times that typically observed in shot-peening [73]. The magnitude, and the depth beneath the processed surface at which it occurs, is almost identical that observed by Nalla et al. [126] and Nikitin et al. [210] in deep rolled *Ti-6Al-4V* alloy, however the depth of the peak stress more shallow in comparison. Considering that these stress states likely corresponded to significant increases in the measured fatigue life of *Ti-6Al-4V* alloy, it can be inferred that similar or even superior increases would be generated in the workpiece samples analyzed in this investigation. For hybrid and cryogenic

burnishing, peak stresses of -931 MPa and -915 MPa were observed. In both cases the peak compressive stresses were observed at a depth of 100 μm , which represents a 25% increase from that observed in flood-cooling. The near-dry environment of MQL burnishing, with no available cooling mechanism, still produced a maximum compression comparable to other tested methodologies. However, the depth of the peak stress was only 50 μm . In all cases, the total compressive depth, or the depth at which the material's stress state returns to its as-received state, in all samples is roughly 400 μm . The lack of variability exhibited in the peak stress values under different cooling mechanisms tends to suggest in terms of the peak compressive stress, the most significant factor almost certainly the loading pressure imparted by the burnishing tool, as this parameter largely dictates the penetration depth of the hydrostatic stress wave generated during burnishing. In addition to the surface residual stress values illustrated in Figure 5-10, the depth at which the peak residual stress occurs (also denoted in Figure 5-10), and the rate at which the peak stress transitions to its as-received state (as reflected in a general broadening of the near-surface stress-hook) also appear to be significantly affected by the cooling mechanism. As stated previously, the depth at which the peak compressive stress is observed varies from 50 μm in MQL burnishing to approximately 100 μm in cryogenic and hybrid burnishing. The unburnished finish machined sample displayed a tensile stress field to a processing depth of approximately 115 μm . This suggests that thermal effects, though most pronounced on the material surface, were still prominent in the sub-surface of *Ti-6Al-4V* alloy. As the observed depth of the peak stress increased with increasing cooling, the deeper stress state in cryogenic and hybrid burnished *Ti-6Al-4V* alloy indicates that LN_2 can more effectively penetrate into the sub-surface of the workpiece material. Moreover, in samples burnished

with LN₂, the stress-hook is extremely broad, indicating a more compressive stress states exist throughout the ALD. In flood-cooling, and particularly MQL, the hook is extremely narrow in comparison, and consequently the peak compressive stresses decays rapidly with increasing processing depth.

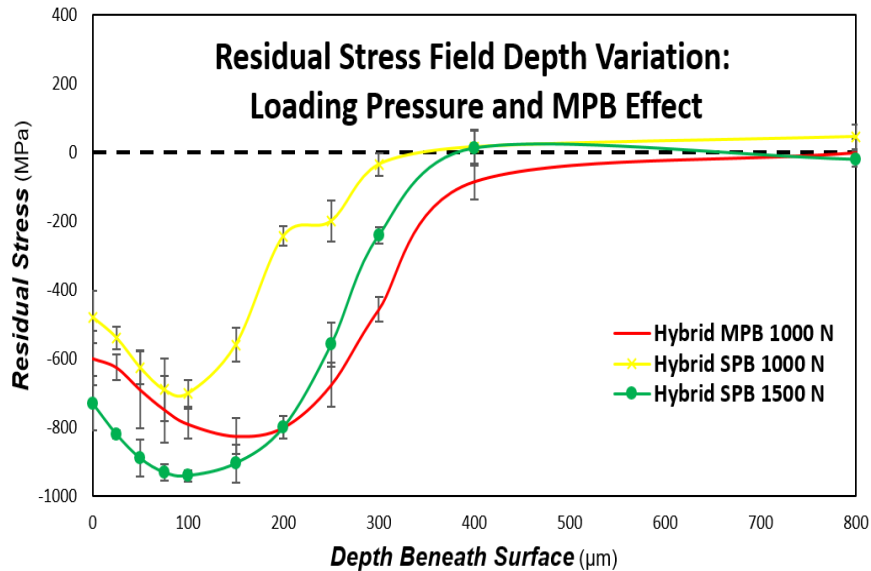


Figure 5-11. Impact of burnishing force and the NTP on the residual stress state in burnished *Ti-6Al-4V* alloy.

The effect of loading force and NTP for hybrid burnishing upon the residual stress state is shown in Figure 5-11. Some very interesting observations can be made regarding observed stress variation. First, and as expected, with a reduced loading force the peak stress significantly decreased, which is depicted in the stress profile exhibited by hybrid burnishing at 1000 N. This supports the previous conclusion that the loading force is the most influential factor in determining the peak compressive state during burnishing. Additionally, the surface and peak stress values are very similar to those numerically predicted at various loading forces (Though the depth of the ALD was severely under

predicted in the numerical simulations). Specifically, the mean percent difference is approximately 10% for most of the comparisons, which is illustrated in Figure 5-12.

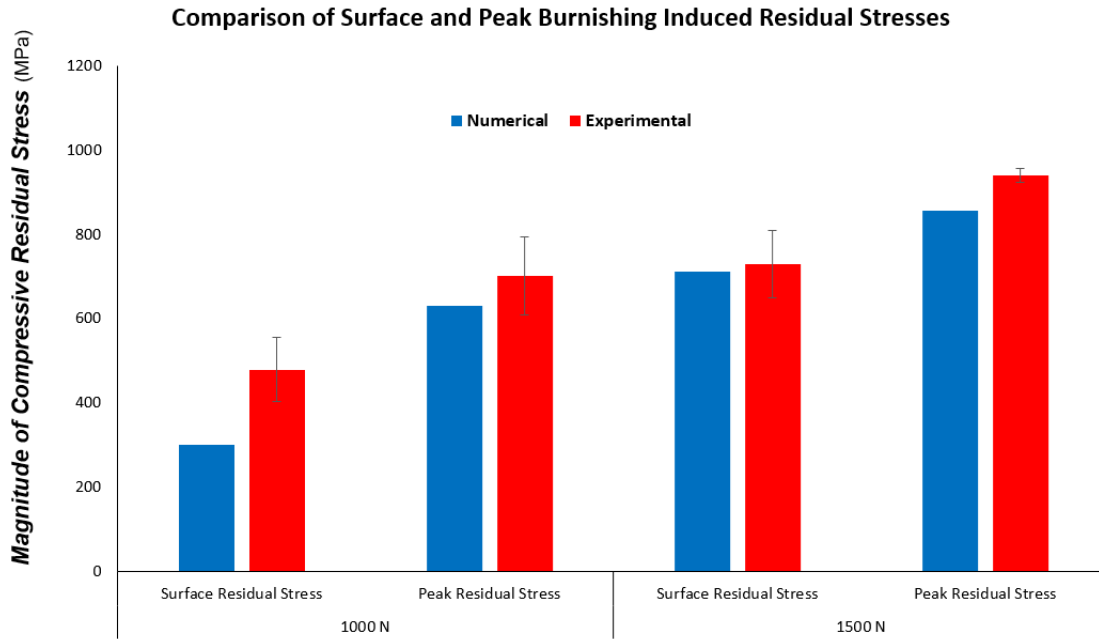


Figure 5-12. A comparison of surface and peak residual stresses in numerical simulations and experimentally measured.

Though the difference in peak stress is negligible, in MPB after four tool passes a stress-stacking phenomena is observed, in which the peak stress depth is substantially increased and the shape of the residual stress hook is further broadened. In hybrid burnishing at 1500 N the peak depth occurs at roughly 100 μm . However, as the NTP increases, the peak stress depth progressively shifts deeper into the sub-surface of the material. After four tool passes the peak stress depth is observed at 150 μm beneath the processed surface. This represents a 50% increase compared to all other analyzed workpiece samples. and is twice the depth observed in conventional flood-cooling at higher loading pressures. Moreover, as the stress-state is pushed deeper into the burnished workpiece, the depth of the total effected layer is extended by 50% to approximately 600

μm . Thus, with MPB deeper effected layers can be generated while utilizing lower loading forces. This is extremely important from a practical application perspective. Burnishing of thin aeroengine components such as turbine and compressor blades, which must be processed within strict tolerances, is more feasible with lower loading forces (as this reduces the chance of unwanted part distortion). Moreover, this observed material behavior has significant implications in regards to the performance of burnished materials that have undergone stress relaxation at elevated temperatures.

Aerospace components are typically subjected to wide range of loading scenarios. In high pressure gas turbine applications, of particular importance is their functional performance at elevated in-service temperatures. Unfortunately, there are very studies in literature focused on understanding the impact of elevated service temperature upon the compressive residual stress fields of burnished *Ti-6Al-4V* alloy. Nalla et al. [126] and Altenberger et al. [34] examined the phenomena of stress relaxation in burnished *Ti-6Al-4V* alloy over a range of temperatures to maximum values of 450°C and 550°C respectively. It was discovered that the beneficial compressive residual stresses that were imparted before temperature elevation, depending upon the temperature, were at least partially if not completely relieved. This is certainly the case for samples isothermally heated to the highest tested temperatures, as the *Ti-6Al-4V* alloy samples were essentially annealed into their virgin states. Interestingly, it was observed that the work-hardened surface layers and microstructural evolution remained largely unaffected by these temperatures as evidenced by the FWHM data. The generated nanostructures remained impressively stable after mechanical fatigue cycling up to temperatures of 450°C, and for brief durations of isothermal heating to 900°C. This is probably the most profound

conclusion drawn in Nalla et al. [126], as nanocrystalline surface layers can reduce the experienced plastic strain amplitude during operation and thus limit fatigue damage. Unfortunately, stress relaxation at elevated temperatures is certainly detrimental from a fatigue life perspective, as any real component employed in a turbine assembly will almost certainly experience such temperatures during their service life. Therefore, any relevant post-processing methodologies used solely to enhance component fatigue life through generation of compressive residual stresses, would have limited influence on such components. This was the observed case for laser-shock-peened samples in Nalla et al. [126], in which no nanostructuring of surface layers was observed. For laser-shock-peening, microstructural refinement is based solely on increased dislocation density and entanglement [210, 220]. Aggressive shot-peening, however, has been shown by Liu et al. [221] to produce shallow nanocrystalline surface layers in *Ti-6Al-4V* alloy. Unfortunately, this refinement is accompanied by a severe degradation in surface quality, which will significantly reduce the fatigue life of processed aerospace components. Considering these findings, the overall benefit of shot-peening and laser-shock-peening is likely extremely limited, if not completely inconsequential, for aeroengine components which operate at elevated working temperatures. Burnishing, on the other hand, has a demonstrated ability of generating superior surface finishes and highly cold worked nanocrystalline surface layers, and can thus endure compressive stress relaxation from fatigue cycling and elevated temperatures (The combination of both at very high temperature results in a near total relaxation), and still provide superior fatigue performance due to the reduction in experienced plastic strain amplitude in burnished materials with nanocrystalline surface layers. As the findings in this study suggest that the NTP and the utilized cooling

mechanism have a significant effect on the residual stress state in burnished *Ti-6Al-4V* alloy, it is therefore necessary to investigate the effect of thermal relaxation on samples burnished under these conditions. Using a similar methodology as in Nalla et al. [126], selected workpiece samples were subjected to gradual isothermal heating to a temperature 500°C (approximately 30-45 minutes) and then held for an additional 45 minutes once the steady-state temperature was reached. Residual stresses were then measured and characterized as a function of depth as shown in Figure 5-13.

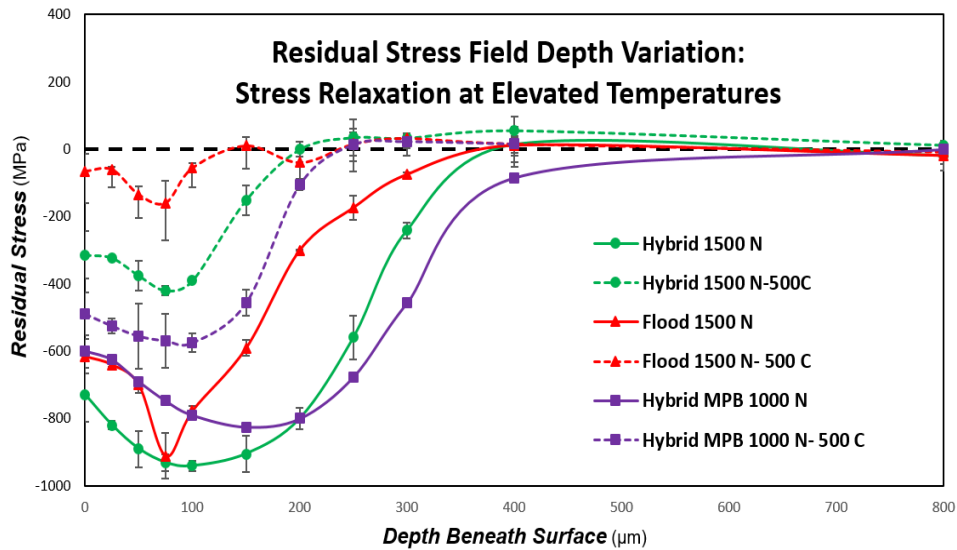


Figure 5-13. Residual Stresses in burnished *Ti-6Al-4V* alloy after isothermal heating.

In order to ascertain the effects of thermal relaxation of residual stresses as a function of cooling mechanism, workpiece samples burnished under hybrid and flood-cooling conditions at 1500 N, as well as hybrid MPB at 1000 N, were analyzed after isothermal heating. Like the results shown in Nalla et al. [126] and Altenberger et al. [34], flood-cooled samples were almost completely annealed after isothermal heating (80% reduction in peak stress) at 500°C for 45 minutes, as the deep layers of compressive residual stress underwent almost total thermal relaxation. As the yield stress of titanium

alloy *Ti-6Al-4V* significantly decreases with increasing temperature, the stored residual stress beyond this reduced yield accelerates the rate of relaxation, and therefore the vast majority of the thermal relaxation occurs near the material surface, where the compressive stress-state before isothermal heating was highest. However, an interesting material behavior was observed in hybrid SPB at 1500 N. Though there was certainly some measure of thermal relaxation (55% reduction in peak stress), in comparison to flood-cooled samples, hybrid burnished *Ti-6Al-4V* alloy retained appreciably more of the original compressive stress state. After isothermal heating, in the workpiece sample burnished under flood-cooling, the surface and peak compressive residual stresses were respectively -65 MPa and -160 MPa. Whereas in the hybrid burnished material, the surface and peak residual stresses were -314 MPa and -420 MPa (In both cases the depth of the peak stress after thermal relaxation was reduced to 75 μm). Thus, the compressive stress field displayed in hybrid burnished *Ti-6Al-4V* alloy after thermal relaxation at 500°C, was roughly equivalent to that obtained during laser shock peening with no thermal relaxation in Nalla et al. [126] and shown in Figure 5-9. Therefore, cryogenically burnished *Ti-6Al-4V* alloy retained a larger percentage of the burnishing-induced compressive residual stress field after isothermal heating, and also exhibited nanocrystalline surface modification. The end result of these combined effects is that hybrid burnishing of *Ti-6Al-4V* alloy offers a far more promising processing strategy for generating increased fatigue life in aeroengine components composed of this alloy than laser-shock-peening or shot shot-peening. In the former no nanostructuring is observed, while in the latter nanostructuring can only be generated at the expense of reduced surface quality, and in both cases isothermal heating resulted in a complete relaxation of residual stresses (However it should be noted that the

combined effect of fatigue cycling at elevated temperatures was not investigated in this study).

Before isothermal heating, flood-cooled and hybrid burnished *Ti-6Al-4V* alloy at 1500 N displayed roughly the same residual stress profile in terms of the peak value of the compressive stress and the total ALD. The only observable differences between the two methodologies was that with LN₂ application surface nanostructures were generated, the observed depth of the peak compressive stress was approximately 35% deeper (100 μm vs. 75 μm), and a deeper layer of highly compressive residual stress was generated in the near surface (< 200 μm), which was reflected in the broader shape of the stress-hook of the residual stress depth variation. In terms of fatigue life enhancement, the primary benefit of surface nanostructuring is thought to be a reduced plastic strain amplitude by impeding dislocation movement during loading, which helps to suppress fatigue crack initiation in the HCF regime [73]. However, for a purely thermal loading scenario in which the material was unconstrained, plastic strains cannot be generated, and nanostructuring cannot explain the differences observed in the residual stress profiles after isothermal heating. Consequently, the only plausible explanation for these observations is the nature of the residual stress distribution, i.e., the deeper and more uniform stress state was able to more effectively resist thermal relaxation and maintain a more compressive residual stress at elevated temperatures. This hypothesis is further supported when analyzing the stress relaxation behavior in hybrid MPB at 1000 N.

In Figures 5-11 and 5-13, it is shown that after four tool passes, hybrid burnishing at 1000 N produced a peak residual stress of -825 MPa at a depth of 150 μm and a total ALD of 600 μm. In comparison to flood-cooled and hybrid burnishing at 1500 N, this

represents an increase in peak stress depths of 100% and 50% respectively. Moreover, after thermal relaxation, the observed peak stress was -570 MPa at a peak stress depth of 100 μm . This is an increase of approximately 35% and 350% relative to hybrid and flood-cooled burnishing at 1500 N. Thus, when considering the effect of thermal relaxation, with hybrid MPB lower loading forces can be employed during to obtain deeper and more compressive residual stresses. As the deeper stress state in hybrid MPB at 1000 N, even though it has a lower peak stress in comparison to hybrid and flood-cooled burnishing at 1500 N, can more effectively resist thermal exposure. Considering that aeroengine components routinely must operate at elevated temperatures, this revelation has significant implications for the potential use of this technology in aerospace applications. The ability to maintain enhanced mechanical properties at elevated working temperatures, rather than suffer losses in functional performance, significantly increases the fatigue life and functionality of processed components employed in such applications. Therefore, in terms of real world applications of this technology, with MPB it is possible to utilize lower burnishing forces to enact greater mechanical refinement than higher pressure single pass burnishing, and consequently more easily maintain the tight tolerances associated with the manufacturing of gas turbine components. Moreover, at these level of elevated temperature it was the FWHM values remained thermally stable as is illustrated in Figure 5-14, indicating that the highly cold worked surface layers were unaffected by thermal exposure. Thus, the microstructural evolution and formation of nanocrystalline surface layers during cDRX were not affected. Consequently, the micro/nano hardness and the resulting FOD resistance imparted by the cryogenic burnishing process, likely loses none of its effectiveness at elevated temperatures. Considering the ever increasing demand for

greater thermal efficiencies in jet engines as materials are pushed to higher operating temperatures, mitigation of a key constraint like residual stress relaxation will potentially allow for increased functional performance of employed components.

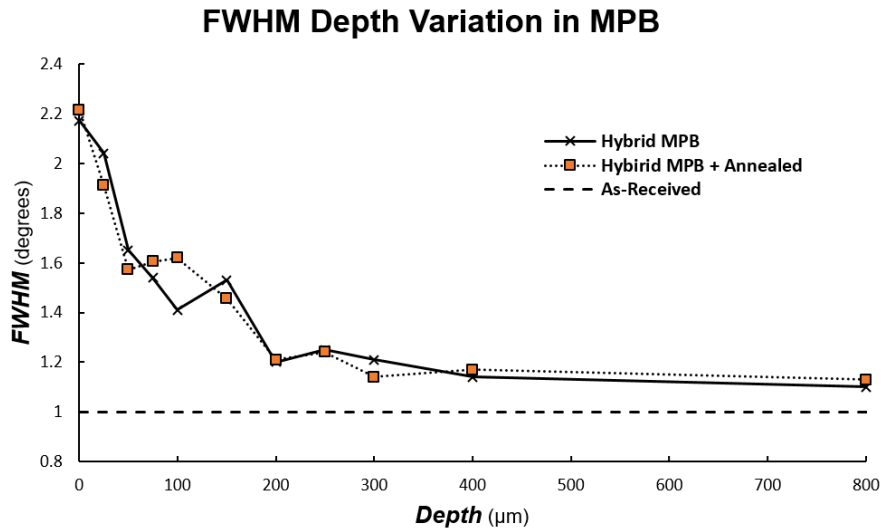


Figure 5-14. Comparison of FWHM variation in hybrid burnished *Ti-6Al-4V* alloy before and after isothermal heating.

5.4 Fatigue Life Implications in Aerospace Applications

Components in rotating machinery, such as those employed in gas turbine applications, typically experience LCF and HCF due to the mean and vibratory stresses they experience during operation. Furthermore, in aeroengines the fatigue state is often exacerbated by damage from fretting, foreign objects, etc. For titanium based compressor and turbine blades, there is a well-established connection to these loading scenarios and eventual part failure [222]. This is largely due to the fact that such extreme loading scenarios lead to the formation and propagation of fatigue cracks, the growth of which inevitably becomes untenable, leading to fracture and catastrophic component failure. According to Cowles [223], this is the most prevalent failure mechanism in modern commercial and military aircraft. Moreover, in turbine engines there are many avenues for

HCF damage to occur. This includes but is not limited to, aerodynamic excitation from pressure fluctuations, mechanical vibration, airfoil flutter, and acoustic fatigue. Depending on the operational parameters, some or all of these HCF sources may contribute to the experienced fatigue of aeroengine components [223]. This makes identification of the root cause of fatigue challenging in most cases, and underscores the importance of utilizing mechanical surface treatments to increase a components resistance to fatigue crack initiation and propagation. One of the most effective means of mitigating the fatigue damage experienced by aerospace components, and thus improve aircraft safety while reducing the economic impact of component maintenance/replacement, is by introducing compressive residual stress fields into a components surface layers. Miller [224] characterized the life of a fatigue crack from initiation and growth into three distinct stages:

- (i) Stress driven crack initiation at the component surface
- (ii) Transient growth of fatigue cracks
- (iii) Subsequent tensile/shear driven growth of fatigue cracks

For aerospace applications, HCF is of particular importance to the functional life of employed components. Unlike LCF, in which the plastic strain and eigenstrain's responsible for the formation of the residual stress field tend to be negated within the first load cycles by large amplitude plastic strains, components experiencing HCF (such as those found turbine assemblies e.g.) tend to be fairly sensitive to variation in residual stress, due to the fact that such systems are typically stress controlled and involve rotating machinery [225]. Moreover, aerospace parts and assemblies almost always contain detectable fatigue cracks, or are assumed to have some measure of micro-cracks just below the threshold size for detection. It is therefore vital for engineers to have a clear picture of how the

combination of operational stresses and cycle rate affect the formation and growth of cracks over the life-cycle of the component.

Analysis of fracture mechanics is generally divided into Linear Elastic (LEFM) and Elasto-Plastic (EPFM) methodologies [226]. LEFM accounts for small scale yielding near the crack tip and thus is quite useful in aerospace applications where components are relatively thin. Fatigue crack propagation is typically characterized by analyzing the crack growth rate per number of cycles (da/dN) as a function the stress intensity factor (ΔK), which is expressed in Eqs. 5-5 and 5-6 as shown by Paris [227].

$$\Delta K = K_{max} - K_{min} \quad K_{min} > 0 \quad (5 - 5)$$

$$\Delta K = K_{max} \quad K_{min} \leq 0 \quad (5 - 6)$$

where K_{max} and K_{min} represent the minimum and maximum stress values respectively. The distinction between Eq. 5-5 and 5-6 is due to the phenomena of crack tip closure, in which the crack tip is closed during some portion of a given fatigue cycle ($K_{min} < 0$ or $K_{min} < K_{OP}$, where the latter denotes the minimum tensile stress factor to open a crack tip). Withers [225] states that if the stress fields are sufficiently compressive, then the crack faces will come into contact over some portion of the fatigue cycle, and in effect shield a portion of the crack tips from loading. As no fatigue damage can occur under compression, $K=0$ serves as the dividing point dictating whether compression or tension is transmitted across the faces of a fatigue crack. When the crack tip is closed no fatigue damage can occur, and this is generally denoted when the crack tip is in a compressive (negative) portion of fatigue cycle. By plotting da/dN vs. $\log \Delta K$, as is shown in Figure 5-15, three distinct stages of crack propagation are realized [37, 225].

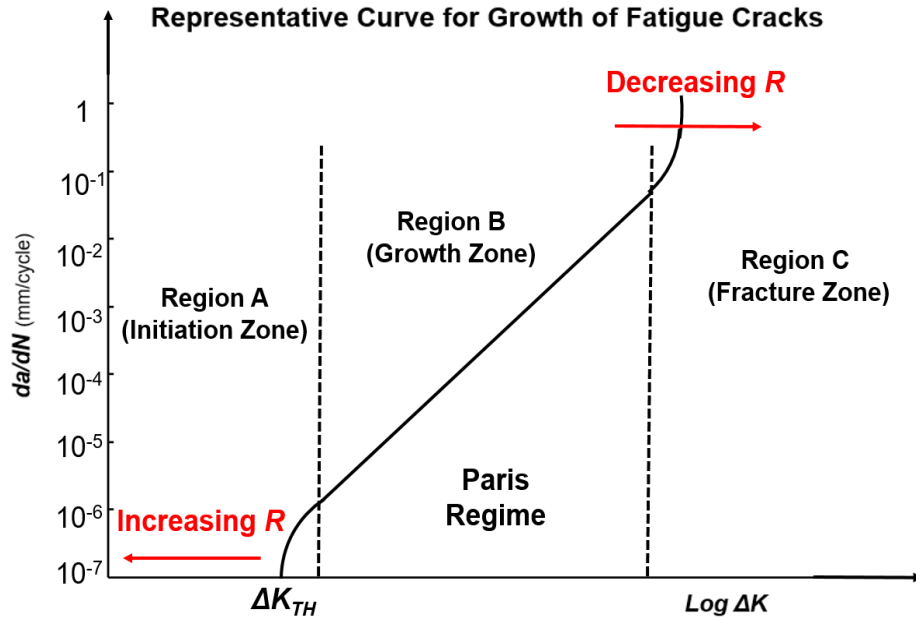


Figure 5-15. Representative curve for crack initiation and growth.

In region A, ΔK_{TH} represents the threshold stress intensity factor necessary for crack initiation (For virgin *Ti-6Al-4V* alloy this value tends to be reported as approximately $4 \text{ MPa m}^{1/2}$ [228]). Region C is defined by a rapid progression in the crack growth rate with an increasing number of cycles, as K_{max} quickly approaches the limiting fracture toughness of the material where catastrophic failure will likely soon occur. Both region A and C tend to be strongly influenced by the load factor R given by Eq. 5-7 and 5-8.

$$R = \frac{K_{min}}{K_{max}} \quad K_{min} > 0 \quad (5 - 7)$$

$$R = 0 \quad K_{min} \leq 0 \quad (5 - 8)$$

As the load factor increases, regions A and C consequently shift to lower values of ΔK , and thus accelerate both crack initiation (reduction in ΔK_{TH}) and crack growth rate (for a given value of ΔK). Due to the rapid growth rate of fatigue cracks in region C, once fatigue cracks have initiated focus tends to be placed upon region B, where the most of the

usable fatigue life of a component will be spent [225]. In this region a linear relationship is displayed as described mathematically by Paris and Erdogan [229] and is shown in Eq. 5-9:

$$\frac{da}{dN} = C(\Delta K)^m \quad (5 - 9)$$

where C and m are material dependent constants. To account for crack tip closure effects the Paris Law is modified accordingly as shown below in Eq. 5-10:

$$\frac{da}{dN} = C(\Delta K_{eff})^m \quad (5 - 10)$$

where ΔK_{eff} represents the case where the crack tip remains closed during some portion of the tensile fatigue load (K_{OP}), as is shown in Figure 5-16. Thus, these variables can be related to the maximum stress intensity factor:

$$\Delta K_{eff} = K_{max} - K_{op} \quad (5 - 11)$$

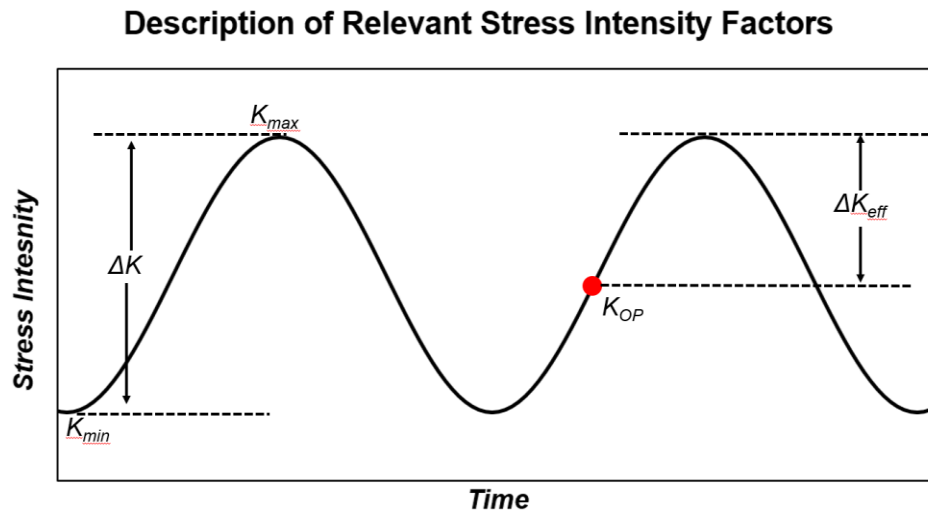


Figure 5-16. Graphical depiction of relevant stress intensity factors.

In the presence of residual stress fields, the principle of superposition is utilized to modify the fatigue stresses generated during the portion of the fatigue cycle at which the

crack remains open. This occurs not through alterations to the overall stress range, but rather by modifying K_{max} and K_{min} by the residual stress value [230]. This is accounted for in changes to the applied load factor and the stress intensity range at which crack the remains open during loading ($K_{min} + K_{res} > 0$), as is shown in Eqs. 5-12 and 5-13.

$$\Delta K = K_{max} - K_{min} \quad (5 - 12)$$

$$R_{eff} = \frac{K_{min} + K_{res}}{K_{max} + K_{res}} \quad (5 - 13)$$

where K_{res} is the stress intensity factor due to the presence of residual stresses. For tensile residual stress fields, such as those that arise from thermal effects during flood-cooled machining, K_{res} is positive and thus $R_{eff} > R$. Consequently, regions A and C shift to lower ΔK values. In this scenario, less applied stress is required to initiate crack formation (ΔK_{TH} is reduced) and rate of crack propagation increases. This is unacceptable in any industry, but it is particularly a problem in aerospace applications, and thus further explains the need for post-processing techniques such as burnishing to negate the tensile stresses that can be produced in finish machining. Conversely, when compressive residual stresses are present in a material, higher stress intensity factors are required to initiate crack formation and crack growth rate is effectively reduced. Thus, when $K_{min} + K_{res} \leq 0$ the stress intensity factor range and load factors are respectively modified to that shown in Eqs. 5-14 and 5-15:

$$\Delta K = K_{max} + K_{res} \quad (5 - 14)$$

$$R = 0 \quad (5 - 15)$$

When $K_{min} + K_{res} < 0$, the resultant stress intensity factor is typically set to zero to simulate fatigue crack closure [231]. Application of this is described in Webster and Ezeilo [213], and reflected in Figure 5-17, where compressive residual stresses delay the onset of

crack formation and significantly decrease crack growth rate for given stress intensity factor.

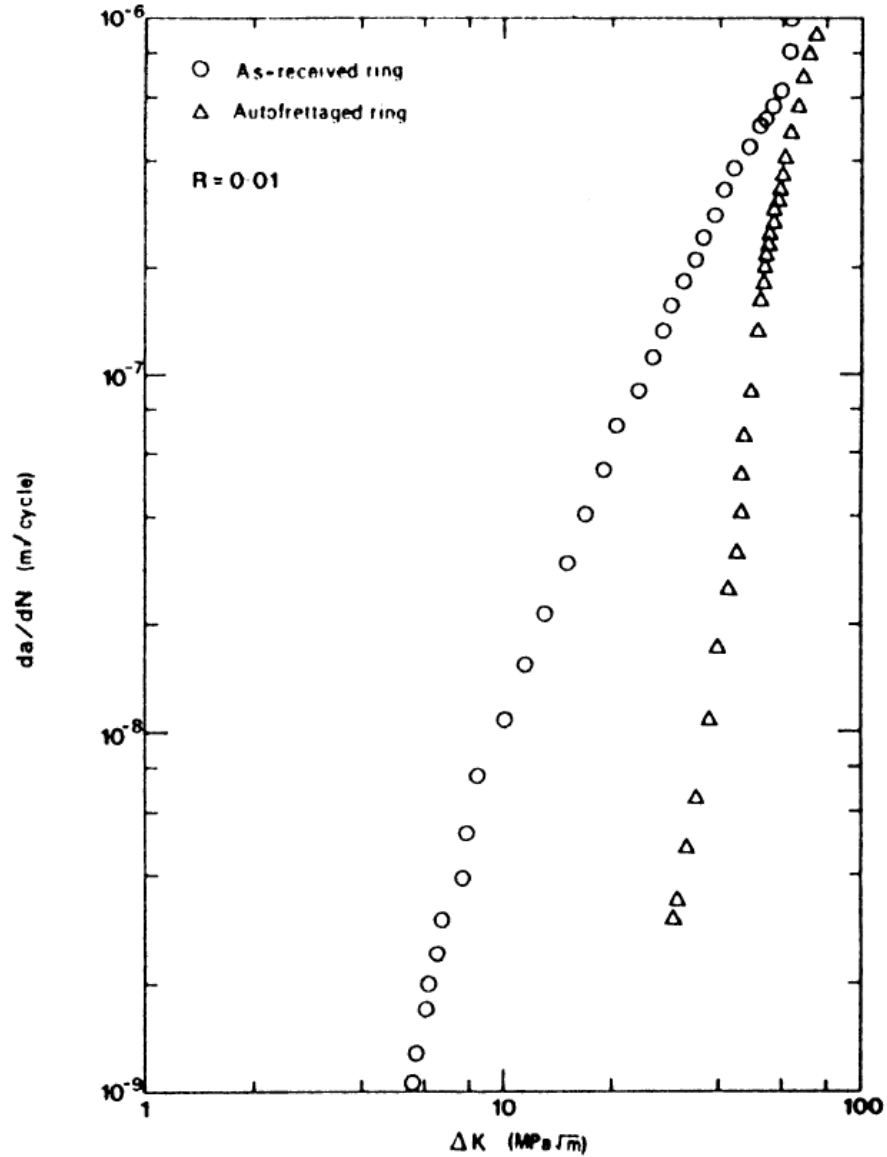


Figure 5-17. Depiction of crack growth suppression due to autofretting. Reprinted from [213] with permission from Elsevier.

Considering the mechanisms of fatigue crack formation and propagation, it can be inferred that the residual stress fields developed in burnished *Ti-6Al-4V* alloy could potentially lead to substantial increases in the fatigue life of employed components. The

presence of residual stresses acts to decrease the load ratio, and therefore delay the onset of fatigue crack initiation by increasing the threshold stress intensity factor at which crack initiation begins. Moreover, once crack initiation begins, the growth rate can be significantly suppressed due to crack closure effects, in which the effective stress intensity factor is greatly reduced. In Ruschau et al. [232], residual stresses in laser-shock peened *Ti-6Al-4V* alloy induced crack closure for over 85% of the fatigue cycle, which consequently resulted in large reductions to ΔK_{eff} . Considering the magnitude of the compressive stress fields induced in burnishing, where the peak residual stress was more than twice that has been shown in literature for laser-shock peening processes, a logical conclusion would be that even more pronounced crack closure effects could be obtained using burnishing techniques. This is particularly true in hybrid MPB, where deep layers of residual stress remained even after high temperature thermal exposure.

One tool utilized by design engineers to predict the cyclical fatigue life of components is the Goodman Diagram, in which the number of cycles to failure is predicted as functions of both the mean stress load and alternating stresses for various load factors. An example of a Goodman Diagram is presented in Figure 5-18 for an a particular aerospace application, where Nicholas and Zuiker [222] show the combined effects of LCF and HCF on predicted cyclical fatigue life of *Ti-6Al-4V* alloy. In Figure 5-18, N denotes the total number of LCF cycles and n represents is the total number of HCF cycles per LCF cycle.

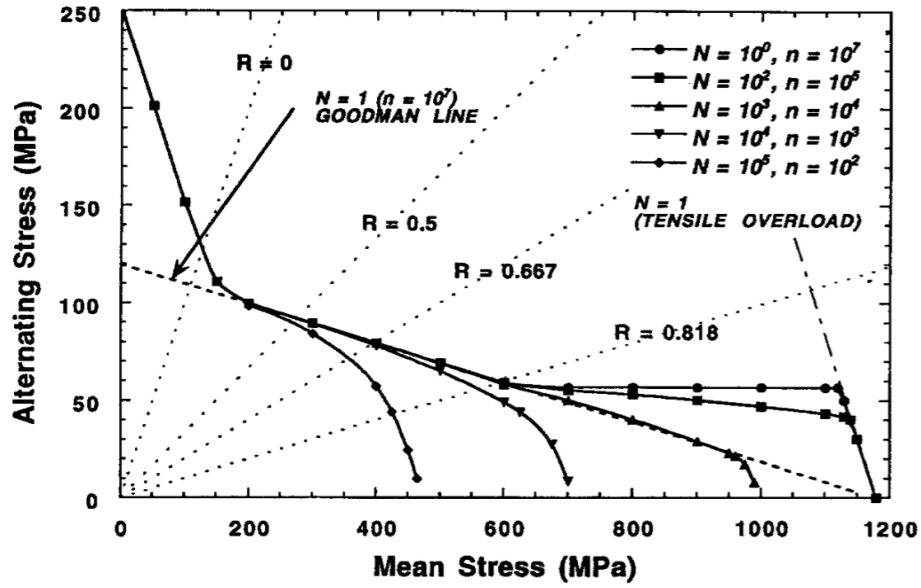


Figure 5-18. Illustration of Goodman Diagram for *Ti-6Al-4V* alloy. Reprinted from [222] with permission from Elsevier.

In order to develop a clearer picture of the in-service application potential of burnishing technologies, the residual stress field developed from hybrid MPB and subsequently thermally relaxed to replicate the effect of elevated operational temperatures, was compared to the fatigue life predicted in the Goodman Diagram. Of course this is an idealized comparison, as there are many other potential sources of fatigue damage (FOD, fretting, surface quality, etc.) that are not accurately captured within the design envelope of the Goodman diagram. Nevertheless, it is an effective measure of the relative impact of residual stress fields on the applied load factor and predicted fatigue life. The peak compressive residual stress induced from MPB after thermal relaxation was -570 MPa. This value was used in accordance with Eq. 5-13 and 5-15 to determine the impact of the imparted residual stress upon the applied load factors, which was then superimposed onto the Goodman Diagram in Figure 5-178. As expected, the load factors were drastically reduced due to the highly compressed stress state in burnished *Ti-6Al-4V* alloy. In fact, at

low mean stress values ($\sigma_m < 630$ MPa), for all alternating stresses the load factor was negative, indicating the crack tip would in compression and thus shielded from fatigue stress if no other sources of fatigue damage were present. This is indicated by the region highlighted in green in Figure 5-19.

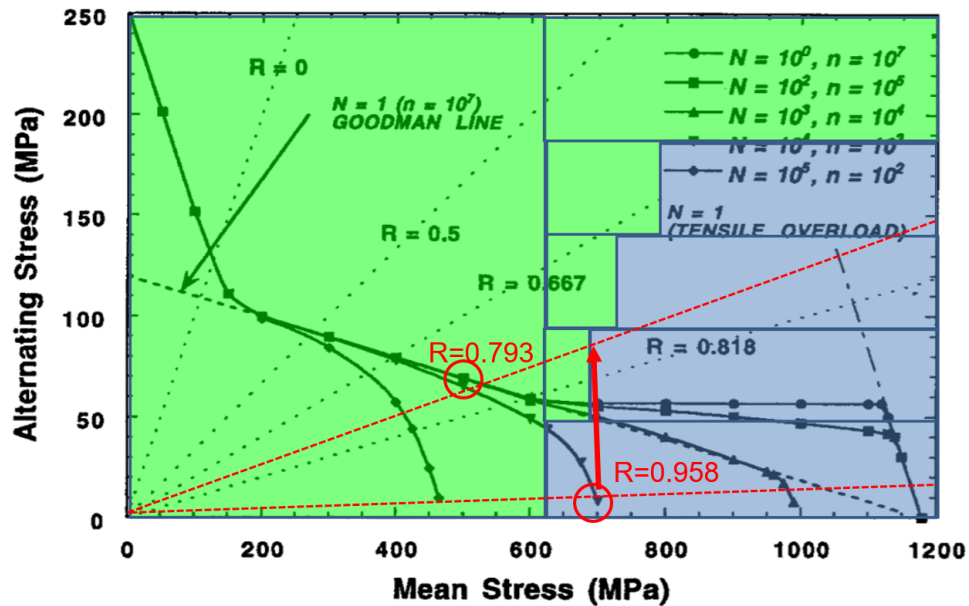


Figure 5-19. Modified Goodman diagram based on compressive residual stress field developed from hybrid burnishing. Adapted from [222] with permission from Elsevier.

For the region in which the compressive residual stress field was not sufficiently a compressive to completely negate the in-service tensile stresses (determined by $R_{eff} > 0$ and highlighted in blue), a substantial load factor reduction was still observed. The predicted combination of LCF and HCF cycles is consequently modified to allow for an increased stress level while maintain the same expected fatigue life. This is described by the annotations shown in Figure 5-19. At a mean stress value of 700 MPa and load factor of $R = 0.958$, the predicted number of LCF and HCF cycles before failure is 10^4 and 10^7 cycles respectively. This fatigue life corresponds to a maximum alternating stress value of 15 MPa. However, in the presence of the residual stress field induced from MPB, R_{eff} is

effectively reduced to 0.793. Therefore, for this specific mean stress, the maximum alternating stress can be increased to approximately 80 MPa with no alteration to the expected fatigue life. In Figure 5-20, the load ratio reduction due the effect of compressive residual stress is plotted as a function of mean stress for various alternating stress values. As the residual stress field in Hybrid MPB was only partially relieved after thermal relaxation, it was still sufficiently compressive to significantly reduce the applied load factor for all combinations of mean and alternating stresses. Specifically, load factors were reduced from 20-40% to over 90% over the analyzed stress ranges. Moreover, as reductions in load factor correlate strongly with increasing stress intensity thresholds, it can be expected that such large reductions in load factors could result in significant increases to the stresses necessary to initiate fatigue cracking. Thus, providing increased flexibility to the in-service operational design envelope for titanium alloy *Ti-6Al-4V* based aerospace components.

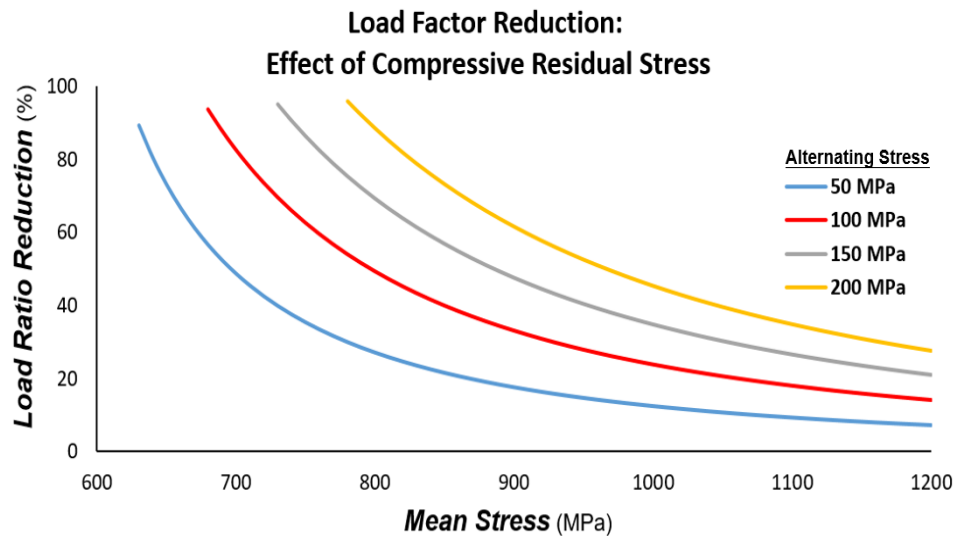


Figure 5-20. Potential load factor reduction in *Ti-6Al-4V* alloy based aerospace components due to the presence of compressive residual stresses from MPB.

5.5 Chapter Conclusions

In previous sections it has been shown that the cooling strategy implemented during burnishing has a significant effect upon the depth of the peak stress and the overall compression in the near surface regions of the ALD. The extremely low boiling temperature of LN₂, in comparison to conventional flood-cooling and MQL, more effectively negates the tensile thermal loads generated on the machined sample before burnishing. Moreover, nanocrystalline surface layers generated in hybrid SPB and MPB not only help negate the in-service plastic strain amplitude experienced by components (and thus reduce the driving force for fatigue damage), but also help mitigate fatigue cracking from FOD by facilitating significant increases in hardness. These nanostructures likely remain thermally stable during high temperature isothermal heating, which is indicated by the FWHM profiles shown in Figure 5-14. This in turn has significant implications for the potential use of this processing technology for components utilized in high temperature applications. The combined effects of cryogenic cooling with the stress stacking effects exhibited by MPB, effectively increases the peak stress depth to more than twice that observed in higher pressure SPB. Consequently, after isothermal heating to a temperature that reflects the in-service operational temperatures experienced by aeroengine components, the deeper stress state imparted by MPB resulted in significantly less overall relaxation. Therefore, in high temperature aerospace applications, MPB with LN₂ has the potential to drastically suppress both crack initiation and fatigue crack propagation, and thus prolong the useful service life of aerospace components and allow for greater thermal efficiencies in gas turbine engines.

CHAPTER 6.

CONCLUSIONS AND FUTURE WORK

6.1 Conclusions

The operational requirements for materials utilized in aerospace gas turbine applications dictates that components have ample wear and fatigue resistance in order to mitigate the damages incurred from high temperature cyclical loading and impacts from unavoidable debris ingestion. This is traditionally accomplished by using shot-peening and other similar post-processing techniques, to impart upon the processed workpieces work hardened surface layers which exhibit near-surface compressive residual stresses. In order to address the inherent shortcomings prevalent in these traditional methodologies, namely surface quality degradation, shallow effected layers depths with relatively minimal mechanical refinement, and unstable near-surface microstructures, roller burnishing was investigated as an alternative means of increasing the functional performance and fatigue life of *Ti-6Al-4V* alloy components employed in aerospace applications. Therefore, a comprehensive characterization of surface integrity was conducted in order to ascertain the impact of processing parameters and cooling and lubricating mechanisms on the process-induced surface quality, microstructure, microhardness variation, and residual stress fields. In aerospace applications, surface integrity is a critical metric in determining the functional performance and fatigue life of components subject to high temperatures and cyclical loading. The key findings of this investigation can be summarized as follows:

- The impact of cryogenics upon the life-cycle of aerospace components processed using MPB is quite profound. With the right processing conditions, LN₂ cooling can help maximize the process-induced surface integrity characteristics of this alloy.

In doing so, the fatigue life of processed aerospace components can potentially be significantly increased via increasing the threshold stress intensity necessary for fatigue crack initiation and by decreasing the rate of fatigue crack propagation. Both of which, in turn, can prolong the use phase of a product's life-cycle, which consequently increases the overall product sustainability characteristics.

- Conventional oil-based MWF have a significant and detrimental impact upon sustainability. The indiscriminate use of such coolants has negative implications for the environment, worker health, as well as for both the short and long-term costs respectively associated with the treatment and disposal of coolants, and from producing inferior components with decreased functional performance and fatigue life. LN₂ is a far more sustainable coolant for manufacturing process, not only in terms of replacing harmful MWF's, but by facilitating the production of aerospace components with superior fatigue and performance capabilities.
- Feed rate, loading force, NTP, and cooling/lubrication are the primary means of controlling the process-induced surface integrity.
- As feed rate decreases and loading force increases, the center line distance between consecutive indentations becomes small compared to the plastic contact area, which in turn allows for more overlapping passes and a greater improvement in surface quality.
- The flow stress of exhibited by *Ti-6Al-4V* alloy during processing is highly dependent on the processing temperature. At cryogenic temperatures an increase in flow stress results in less material plasticity and higher surface roughness in single pass burnishing. However, at higher loading forces the increased contact pressure and associated rise in thermal energy in the contact zone become the dominant processing parameter, leading to large improvements in surface quality regardless of the cooling strategy.
- As the NTP increases surface quality improves until an optimum is reached. Subsequent tool passes beyond this produces material spalling and surface quality degradation in MQL and flood-cooled burnishing. Application of LN₂

during processing increases the yield strength of *Ti-6Al-4V* alloy, allowing for more significant strain hardening, which in effect extends the optimum number of passes without catastrophic surface failure. Thus, the largest reduction in Ra observed during this investigation was achieved using hybrid MPB burnishing, in which nano-level surface finishes (≈ 100 nm) were achieved.

- The large pressures and mechanical strains produced during burnishing facilitate microstructural evolution and grain refinement via continuous dynamic recrystallization (cDRX) processes. Application of LN_2 during cDRX suppresses the nucleation and growth of new grains resulting in shallow nanostructured surface layers with high dislocation densities. This can be described mathematically using a Zener-Holloman expression, in which decreasing grain-size and processing temperature are directly related. This was verified using FIB and SEM to characterize the nanocrystalline surface layers produced in cryogenic and hybrid burnishing (No nanostructuring was observed using conventional cooling methodologies).
- Characterization of micro/nanohardness in these surface layers is explained by Hall-Petch grain boundary strengthening, as near-surface nanostructures and comparatively higher dislocation density result in appreciably higher hardness in these layers for samples burnished using LN_2 . This is apparent in not only the surface of the processed material, but in the hardness variation with cross-sectional depth. Cryogenically burnished samples exhibit sustained hardness enhancement at significantly greater depths beneath the processed surface. For aerospace applications, the increased hardness associated with cryogenic processing will promote greater resistance to wear and FOD, and thus increase the likely functional performance and fatigue life of gas turbine components.
- The low thermal conductivity exhibited by *Ti-6Al-4V* alloy, along with the reduced heat flux (cooling capacity) associated with flood-cooled and MQL burnishing, results in a localized annealing of the material due to the accumulation of thermal energy. Consequently, the dislocation network is continuously relieved leading to decreased strain-hardening using conventional cooling techniques.

- Machining and burnishing induced residual stress depth variation was characterized using nondestructive XRD techniques using a $\sin^2\psi$ methodology. Electropolishing was used to remove thin layers of material in steps (10 μm) with minimal disturbance to the stress state imparted by processing. However, some measure of stress relaxation occurs regardless. This is accounted for by applying closed-form analytic solutions for stress correction unique to specific geometry being studied.
- For sharp tools, the impact of cutting edge radius on the developed residual stresses was investigated. Three samples were machined using hybrid (LN_2+MQL) cooling, and the residual stress fields were shown to be highly sensitive to the cutting edge geometry. The sharpest tool ($< 5 \mu\text{m}$) generated tensile stress field on the surface of the workpiece, which gradually became compressive in the material sub-surface. As the cutting edge radius increased, the stress field became increasingly compressive, owing to the increased plowing force. The largest tested radii of 50 μm generated compressive stresses at the surface to a depth of approximately 200 μm . An additional sample was machined using flood-cooling with no consideration given to tool geometry. The near-surface residual stress was highly tensile (More than 3X that observed with cryogenic machining with the sharpest cutting edge). This highlights the ability of LN_2 to mitigate the tensile thermal stresses generally associated with machining.
- Burnishing, regardless of the implemented cooling strategy, induced deep layers of compressive residual stresses for all tested workpiece samples. The magnitude of the peak stress was found to be highly dependent upon the burnishing force, and under the right processing conditions was more than twice that generally reported for laser-shock-peening techniques as well as those observed in cryogenic machining with large cutting edge radii.
- Surface residual stresses in burnished samples were found to be strongly affected by the cooling mechanism utilized. As the effect of cooling is most pronounced on the material surface, it is here that the tensile surface stresses associated with machining generally undergo the most mitigation. Therefore, though the maximum

compression in the subsurface is approximately equal, regardless of the cooling method, on the surface itself cryogenic and hybrid burnishing produced far more compressive surface layers due to the increased mitigation of thermal energy (almost twice that observed in MQL processing). Consequently, the depth of the maximum residual stress was slightly deeper (25-50 μm) with a more sustained compressive field in the sub-surface (as is indicated by the general broadness of the residual stress profile).

- Hybrid MPB displayed a stress-stacking effect, in which the maximum depth of the peak residual stress value shifted to deeper into the material subsurface with subsequent tool passes. After four tool passes the maximum depth of the residual stress field was 150 μm . This is roughly twice that observed in any other analyzed condition. This includes conventional cooling methodologies and higher pressure single pass burnishing.
- Isothermal heating of burnished workpiece samples at 500°C for 45 minutes resulted in significant relaxation of the compressive residual stress fields. For flood-cooled samples the material was essentially annealed into its virgin state, as roughly 80% of the imparted residual stress was relieved. However, the hybrid burnished workpiece samples were only partially relaxed in comparison (55% reduction). This is attributed to the deeper state of the residual stress observed in samples processed with cryogenic cooling. Furthermore, owing the deeper state of the compressive stress in hybrid MPB, after thermal relaxation only minimal relaxation was observed (25%). In fact, after thermal relaxation the stress state in MPB was more compressive than that obtained using higher loading forces in SPB. This is certainly one of the most significant revelations regarding the residual stress distributions produced from burnishing. As it sheds light on a possible methodology for minimizing part distortion (which is a significant concern for processing of thin aerospace components such as turbine or compressor blades) without sacrificing surface integrity and fatigue life improvement.
- Characterization of FWHM values in hybrid MPB workpieces displayed little to variation before and after isothermal heating. This reflects a high degree of thermal

stability in the work hardened surface layers, likely including the burnishing-induced surface nanostructures. Thus, it can generally be expected that beneficial microstructural and mechanical improvements imparted in *Ti-6Al-4V* alloy from hybrid MPB will likely remain well into the usable life of components employed in high temperature applications.

- To facilitate the processing of thin aerospace components with strict processing tolerances, it is advantageous to use lower loading forces that minimize the chance for part distortion. MPB allows for superior surface integrity improvement, while utilizing lower working pressures, thus making it an ideal processing choice for improving the functionality of thin components such as turbine blades.

6.2 *Future Work*

6.2.1 *Comprehensive Investigation of NTP and Stress Relaxation on Residual Stress Fields and Fatigue Life*

It can be argued that the most significant finding in this investigation was that MPB generated deeper subsurface residual stress states with lower working pressures. As this in turn allows for a greater compressive state after thermal relaxation, which more accurately portrays the true operational environment of a component employed in high temperature aerospace applications. By utilizing lower working pressures to achieve greater surface integrity improvement, processing of thin aerospace components is more tenable, as it is easier in such a scenario to maintain tight tolerances without unwanted part distortion. Thus, this avenue of research should certainly be explored more comprehensively. The residual stress distribution should be characterized as a function of increasing NTP under various cooling and loading scenarios, as only four tool passes were analyzed in this study. In this way optimum levels of residual stress can be established for a given loading scenario, which can then be compared to limiting load (based on the geometric and structural constraints) during component manufacturing. This would consequently allow for the development of

the ideal processing strategy to maximize fatigue life for a given component.

Moreover, investigations into stress relaxing processes should be greatly expanded. Thermal relaxation of residual stresses should ideally be quantified as a functions of both temperature and of time. This would provide insight into the thermal restoration mechanisms such as those provided by the Zener-Wert-Avrami models depicted in Eq. 6-1 [233-235].

$$\frac{\sigma^{RS}(t, T)}{\sigma^{RS}(t = 0)} = \exp[-(At)^m] \quad (6 - 1)$$

where $\sigma^{RS}(t=0)$ is the residual measured residual before annealing, $\sigma^{RS}(t, T)$ is the residual stress after thermal relaxation for time t and Temperature T , m is a numerical parameter that varies depending upon the dominant relaxation mechanism. Additionally, A is the material relaxation function given by Eq. 6-2:

$$A = B \exp\left(-\frac{\Delta H}{kT}\right) \quad (6 - 2)$$

where B is material constant, k is the Boltzmann constant ($8.617\text{E-}5 \text{ eV}\text{K}^{-1}$), and T is the Temperature during relaxation. Log-log plots of heating time vs temperature relaxation can be created which to determination of nature of the relaxation phenomena for this particular process as well as provide insight into the nature of the activation enthalpy. Most importantly, however, it would allow for a quantitative comparison of thermal stability in the work hardened surface layer and the residual stress fields, which could then be compared to similar procedures undertaken in literature for shot-peened and laser-shock-peened alloys.

Moreover, additional avenues of stress relaxation should be explored for MPB samples. In aerospace applications many sources of stress relaxation are possible, but the

most prominent are fatigue cycling and FOD. In the former, normal operational tensile stresses placed upon a component, will over time reduce the compressive state imparted during processing. Thus, it is certainly necessary to quantify, independently, these effects upon the stress state of burnished *Ti-6Al-4V* alloy. Moreover, FOD from debris ingestion in turbine engines have a well-documented history of being ideal locations for fatigue crack initiation [236]. The near surface tensile stresses generated on turbine blades from high velocity debris impact should be characterized for different cases of surface compressive residual stress induced from MPB. Finally, the combined effects of thermal relaxation, fatigue cycling, and FOD should be explored on the stress relaxation of MPB samples. As this will provide the most realistic depiction of the in-service residual stresses, and it would consequently allow for the development of comprehensive models to predict the residual stress characteristics of critical aerospace components throughout their respective service lives. Ideally, such an investigation should be accompanied by an in-depth microstructural analysis (including FIB/SEM/TEM). It has been shown that the microstructural changes induced via burnishing mechanisms were not affected by thermal relaxation. However, the validity of this conclusion should be examined independently, and in conjunction with, different stress relaxation mechanisms.

In the work presented here the impact of burnishing parameters on the residual stress characteristics of processed components was investigated. These imparted characteristics, in turn, were used to infer the likely impact upon the fatigue life of aerospace components. However, the current understanding of these mechanisms is such that it's not possible to predict the actual fatigue life with exact precision. Unfortunately, the sheer number of potential sources of fatigue damage, and the complex interplay with the material properties

of components being fatigued, dictate that expensive and time-consuming experimentation is still necessary. Therefore, cyclical fatigue tests should be performed on burnished samples. In this way a direct correlation could be established between the mechanisms that define the burnishing process and the quantifiable measures of fatigue crack initiation, propagation, and eventual catastrophic failure.

6.2.2 *Comparison of Conventionally Wrought and Additively Produced Titanium Alloy Ti-6Al-4V*

The complex geometric profiles associated with most aerospace components, particularly turbine and compressor blades, make conventional subtractive manufacturing difficult and costly [237, 238]. Additive manufacturing offers increased weight savings through the redesign of component assemblies into single parts and the ability to fabricate complex parts and features with equal or superior functionality [237]. By producing near-net shape components, material utilization is improved. Newly developed turbine engines, such as the GENx gas turbine engine, feature a multitude of additively produced components. All of these advantages are highly relevant to the aerospace industry, especially considering the high raw material costs of aerospace alloys and increasing energy costs [238-240]. However, additive processing has also been shown to produce unacceptable dimensional tolerances, poor surface finish and highly variable material properties, due to repeated melting and solidification during fabrication, which induces numerous phase changes and thus highly variable microstructures.

Surface integrity of metallic aerospace components, especially microstructure (including grain size and orientation), microhardness and residual stress fields, has a significant influence on their functional performance, including wear-rate, corrosion and/or fatigue resistance, etc. These parameters can be enhanced to achieve the most desirable

surface integrity by the selection and control of involved process variables. With increasing use of additively manufactured components, the importance of correlating additive processing parameters with as-printed microstructure and mechanical properties has been well documented. At the same time, the ability of subtractive processes to induce beneficial surface layers and other functionally relevant surface integrity parameters in conventionally produced (cast/wrought) metals has been widely studied, yet no effort has been devoted to establishing the effect of subtractive post-processing techniques such as burnishing on additively produced metals. Due to the surface finish and tolerance requirements of *Ti* alloy aerospace components, which are routinely subjected to thermo-mechanical cyclical loads, some subtractive finishing is generally required. Thus, exploring the effects of additional post-processing techniques that are commonly performed on conventionally wrought alloys, is the next logical step in ensuring that additively produced components can meet the stringent manufacturing requirements of the aerospace industry.

REFERENCES

- [1] Choragudi A, Kuttolamadom MA, Jones JJ, Mears ML, Kurfess T. *Investigation of the machining of titanium components in lightweight vehicles*. in *SAE International Congress*. 2010.
- [2] Jaffery S, Mativenga P, *Assessment of the machinability of Ti-6Al-4V alloy using the wear map approach*. The International Journal of Advanced Manufacturing Technology, 2009. 40(7-8): p. 687-696.
- [3] Lütjering G WJ, *Titanium*. 2nd ed. 2007, New York, NY.
- [4] Shaw MC, Cookson J, *Metal cutting principles*. Vol. 2. 2005: Oxford university press New York.
- [5] Hong SY, Markus I, Jeong W-c, *New cooling approach and tool life improvement in cryogenic machining of titanium alloy Ti-6Al-4V*. International Journal of Machine Tools and Manufacture, 2001. 41(15): p. 2245-2260.
- [6] Shokrani A, Dhokia V, Newman ST, *Investigation of the effects of cryogenic machining on surface integrity in CNC end milling of Ti-6Al-4V titanium alloy*. Journal of Manufacturing Processes, 2016. 21: p. 172-179.
- [7] Bermingham M, Kirsch J, Sun S, Palanisamy S, Dargusch M, *New observations on tool life, cutting forces and chip morphology in cryogenic machining Ti-6Al-4V*. International Journal of Machine Tools and Manufacture, 2011. 51(6): p. 500-511.
- [8] Aggarwal A, Singh H, Kumar P, Singh M, *Optimization of multiple quality characteristics for CNC turning under cryogenic cutting environment using desirability function*. J. Mater. Process. Technol., 2008. 205(1-3): p. 42-50.
- [9] Hong SY, Ding Y, Jeong W-c, *Friction and cutting forces in cryogenic machining of Ti-6Al-4V*. International Journal of Machine Tools and Manufacture, 2001. 41(15): p. 2271-2285.
- [10] Su Y, He N, Li L, Li XL, *An experimental investigation of effects of cooling/lubrication conditions on tool wear in high-speed end milling of Ti-6Al-4V*. Wear, 2006. 261(7): p. 760-766.
- [11] Field M, Kahles J, *The surface integrity of machined-and ground high-strength steels(Surface integrity of machined and ground high strength steels)*. 1964., 1964: p. 54-77.
- [12] Jawahir I, Brinksmeier E, M'saoubi R, Aspinwall D, Outeiro J, Meyer D, Umbrello D, Jayal A, *Surface integrity in material removal processes: Recent advances*. CIRP annals, 2011. 60(2): p. 603-626.
- [13] Bordin A, Bruschi S, Ghiotti A, Bariani P, *Analysis of tool wear in cryogenic machining of additive manufactured Ti6Al4V alloy*. Wear, 2015. 328: p. 89-99.
- [14] Courbon C, Pusavec F, Dumont F, Rech J, Kopac J, *Tribological behaviour of Ti6Al4V and Inconel718 under dry and cryogenic conditions—Application to the context of machining with carbide tools*. Tribology International, 2013. 66: p. 72-82.
- [15] Rotella G, Dillon O, Umbrello D, Settineri L, Jawahir I, *The effects of cooling conditions on surface integrity in machining of Ti6Al4V alloy*. The International Journal of Advanced Manufacturing Technology, 2014. 71(1-4): p. 47-55.

- [16] Schoop J, Ambrosy F, Zanger F, Schulze V, Jawahir I, Balk T, *Increased surface integrity in porous tungsten from cryogenic machining with cermet cutting tool*. Mater. Manuf. Processes, 2016. 31(7): p. 823-831.
- [17] Caudill J, Huang B, Arvin C, Schoop J, Meyer K, Jawahir I, *Enhancing the surface integrity of Ti-6Al-4V alloy through cryogenic burnishing*. Procedia CIRP, 2014. 13: p. 243-248.
- [18] Caudill J, Schoop J, Jawahir I, *Correlation of surface integrity with processing parameters and advanced interface cooling/lubrication in burnishing of Ti-6Al-4V alloy*. Advances in Materials and Processing Technologies, 2018: p. 1-14.
- [19] Boyer R, *Titanium for aerospace: rationale and applications*. Advanced Performance Materials, 1995. 2(4): p. 349-368.
- [20] Donachie MJ, *Titanium±a Technical Guide, 1988*. ASM, Metals Park, OH.
- [21] Peters M, Kumpfert J, Ward CH, Leyens C, *Titanium alloys for aerospace applications*. Adv. Eng. Mater., 2003. 5(6): p. 419-427.
- [22] Williams JC, Starke Jr EA, *Progress in structural materials for aerospace systems I*. Acta Mater., 2003. 51(19): p. 5775-5799.
- [23] Design M. <https://www.machinedesign.com/motorsdrives/what-s-difference-between-turbine-engines>. 2016.
- [24] Hornbach DJ, Prevey PS, Loftus EF. *Application of low plasticity burnishing (LPB) to improve the fatigue performance of Ti-6Al-4V femoral hip stems*. in *1st Symposium - Fatigue and Fracture of Medical Metallic Materials and Devices, November 1, 2005 - November 1, 2005*. 2007. Dallas, TX, United states: ASTM International.
- [25] Prev y PS, Jayaraman N, Cammett J. Overview of low plasticity burnishing for mitigation of fatigue damage mechanisms. 2005, DTIC Document.
- [26] Drechsler A, D rr T, Wagner L, *Mechanical surface treatments on Ti-10V-2Fe-3Al for improved fatigue resistance*. Materials Science and Engineering: A, 1998. 243(1-2): p. 217-220.
- [27] Nikitin I, Scholtes B, *Deep rolling of austenitic steel AISI 304 at different temperatures-near surface microstructures and fatigue*. HTM Journal of Heat Treatment and Materials, 2012. 67(3): p. 188-194.
- [28] Sato M, Tsuji N, Minamino Y, Koizumi Y, *Formation of nanocrystalline surface layers in various metallic materials by near surface severe plastic deformation*. Science and Technology of Advanced Materials, 2004. 5(1-2): p. 145.
- [29] Valiev R, Alexandrov I, Enikeev N, Murashkin MY, Semenova I, *Towards enhancement of properties of UFG metals and alloys by grain boundary engineering using SPD processing*. Rev. Adv. Mater. Sci, 2010. 25: p. 1-10.
- [30] Yang S, Dillon Jr OW, Puleo DA, Jawahir IS, *Effect of cryogenic burnishing on surface integrity modifications of Co-Cr-Mo biomedical alloy*. Journal of Biomedical Materials Research - Part B Applied Biomaterials, 2013. 101 B(1): p. 139-152.
- [31] Altenberger I, Scholtes B, Martin U, Oettel H, *Cyclic deformation and near surface microstructures of shot peened or deep rolled austenitic stainless steel AISI 304*. Materials Science and Engineering: A, 1999. 264(1-2): p. 1-16.

- [32] Fu Y, Loh NL, Batchelor AW, Liu D, Xiaodong Z, He J, Xu K, *Improvement in fretting wear and fatigue resistance of Ti–6Al–4V by application of several surface treatments and coatings*. Surf. Coat. Technol., 1998. 106(2–3): p. 193-197.
- [33] Kloos KH, Kaiser B. *Influence of Shot Peening on the Fatigue Strength of Spring Steel under Decarburization and Heat Treatment Conditions*. 1st International Conference on Shot Peening. 1982. Paris, Fr: Pergamon Press.
- [34] Altenberger I, Nalla RK, Sano Y, Wagner L, Ritchie RO, *On the effect of deep-rolling and laser-peening on the stress-controlled low- and high-cycle fatigue behavior of Ti–6Al–4V at elevated temperatures up to 550 °C*. Int. J. Fatigue, 2012. 44: p. 292-302.
- [35] Novovic D, Dewes RC, Aspinwall DK, Voice W, Bowen P, *The effect of machined topography and integrity on fatigue life*. International Journal of Machine Tools and Manufacture, 2004. 44(2-3): p. 125-134.
- [36] Vogelesang LB, Vlot A, *Development of fibre metal laminates for advanced aerospace structures*. J. Mater. Process. Technol., 2000. 103(1): p. 1-5.
- [37] Webster G, Ezeilo A, *Residual stress distributions and their influence on fatigue lifetimes*. Int. J. Fatigue, 2001. 23: p. 375-383.
- [38] Brinksmeier E, Meyer D, Huesmann-Cordes A, Herrmann C, *Metalworking fluids—Mechanisms and performance*. CIRP Annals, 2015. 64(2): p. 605-628.
- [39] Jones FD, Oberg E, Horton HL. Machinery's handbook. 2004, Industrial Press, Incorporated.
- [40] Astakhov VP, *Tribology of metal cutting*. Vol. 52. 2006: Elsevier.
- [41] El Baradie M, *Cutting fluids: Part I. characterisation*. J. Mater. Process. Technol., 1996. 56(1-4): p. 786-797.
- [42] Jawahir I, Attia H, Biermann D, Duflou J, Klocke F, Meyer D, Newman S, Pusavec F, Putz M, Rech J, *Cryogenic manufacturing processes*. CIRP annals, 2016. 65(2): p. 713-736.
- [43] Grzesik W, *Advanced machining processes of metallic materials: theory, modelling and applications*. 2008: Elsevier.
- [44] Hong SY, Broomer M, *Economical and ecological cryogenic machining of AISI 304 austenitic stainless steel*. Clean Products and Processes, 2000. 2(3): p. 157-166.
- [45] Feng SC, Hattori M. *Cost and process information modeling for dry machining*. in *Proceedings of International Workshop on Environment and Manufacturing*. 2000.
- [46] Pusavec F, Kramar D, Krajnik P, Kopac J, *Transitioning to sustainable production—part II: evaluation of sustainable machining technologies*. Journal of Cleaner Production, 2010. 18(12): p. 1211-1221.
- [47] Meza F, Chen L, Hudson N, *Investigation of respiratory and dermal symptoms associated with metal working fluids at an aircraft engine manufacturing facility*. American journal of industrial medicine, 2013. 56(12): p. 1394-1401.
- [48] Shokrani A, Dhokia V, Newman ST, *Environmentally conscious machining of difficult-to-machine materials with regard to cutting fluids*. International Journal of Machine Tools and Manufacture, 2012. 57: p. 83-101.
- [49] Rivero A, Aramendi G, Herranz S, de Lacalle LL, *An experimental investigation of the effect of coatings and cutting parameters on the dry drilling performance of*

- aluminium alloys*. The International Journal of Advanced Manufacturing Technology, 2006. 28(1-2): p. 1-11.
- [50] Sharma VS, Dogra M, Suri N, *Cooling techniques for improved productivity in turning*. International Journal of Machine Tools and Manufacture, 2009. 49(6): p. 435-453.
- [51] De Lacalle LL, Angulo C, Lamikiz A, Sanchez J, *Experimental and numerical investigation of the effect of spray cutting fluids in high speed milling*. J. Mater. Process. Technol., 2006. 172(1): p. 11-15.
- [52] Yuan S, Yan L, Liu W, Liu Q, *Effects of cooling air temperature on cryogenic machining of Ti-6Al-4V alloy*. J. Mater. Process. Technol., 2011. 211(3): p. 356-362.
- [53] Timmerhaus KD, Reed RP, *Cryogenic engineering: fifty years of progress*. 2007: Springer Science & Business Media.
- [54] Lu T, *A metrics-based sustainability assessment of cryogenic machining using modeling and optimization of process performance*. 2014.
- [55] Hong SY, *Economical and ecological cryogenic machining*. Journal of Manufacturing Science and Engineering, 2001. 123(2): p. 331-338.
- [56] Wang Z, Rajurkar K, *Cryogenic machining of hard-to-cut materials*. Wear, 2000. 239(2): p. 168-175.
- [57] Ke Y-L, Dong H-Y, Gang L, Zhang M, *Use of nitrogen gas in high-speed milling of Ti-6Al-4V*. Transactions of Nonferrous Metals Society of China, 2009. 19(3): p. 530-534.
- [58] Pusavec F, Kopac J, *Achieving and implementation of sustainability principles in machining processes*. Journal of Advances in Production Engineering and Management, 2009. 3: p. 58-69.
- [59] Zhao Z, Hong S, *Cooling strategies for cryogenic machining from a materials viewpoint*. J. Mater. Eng. Perform., 1992. 1(5): p. 669-678.
- [60] Hong SY, Zhao Z, *Thermal aspects, material considerations and cooling strategies in cryogenic machining*. Clean Products and Processes, 1999. 1(2): p. 107-116.
- [61] Hong SY, *Lubrication mechanisms of LN₂ in ecological cryogenic machining*. Machining science and technology, 2006. 10(1): p. 133-155.
- [62] Dhananchezian M, Kumar MP, *Cryogenic turning of the Ti-6Al-4V alloy with modified cutting tool inserts*. Cryogenics, 2011. 51(1): p. 34-40.
- [63] Hong SY, Ding Y, Jeong J, *Experimental evaluation of friction coefficient and liquid nitrogen lubrication effect in cryogenic machining*. Machining Science and Technology, 2002. 6(2): p. 235-250.
- [64] Venugopal K, Paul S, Chattopadhyay A, *Growth of tool wear in turning of Ti-6Al-4V alloy under cryogenic cooling*. Wear, 2007. 262(9-10): p. 1071-1078.
- [65] Venugopal K, Paul S, Chattopadhyay A, *Tool wear in cryogenic turning of Ti-6Al-4V alloy*. Cryogenics, 2007. 47(1): p. 12-18.
- [66] Schoop J, Sales WF, Jawahir I, *High speed cryogenic finish machining of Ti-6Al4V with polycrystalline diamond tools*. J. Mater. Process. Technol., 2017. 250: p. 1-8.
- [67] Iqbal S, Mativenga P, Sheikh M, *A comparative study of the tool-chip contact length in turning of two engineering alloys for a wide range of cutting speeds*. The International Journal of Advanced Manufacturing Technology, 2009. 42(1-2): p. 30.

- [68] Sadik MI, Isakson S, Malakizadi A, Nyborg L, *Influence of Coolant Flow Rate on Tool Life and Wear Development in Cryogenic and Wet Milling of Ti-6Al-4V*. Procedia CIRP, 2016. 46: p. 91-94.
- [69] Su Y, He N, Li L, Li X, *An experimental investigation of effects of cooling/lubrication conditions on tool wear in high-speed end milling of Ti-6Al-4V*. Wear, 2006. 261(7-8): p. 760-766.
- [70] Yuan SM, Yan LT, Liu WD, Liu Q, *Effects of cooling air temperature on cryogenic machining of Ti-6Al-4V alloy*. J. Mater. Process. Technol., 2011. 211(3): p. 356-362.
- [71] Nikitin I, Altenberger I, *Comparison of the fatigue behavior and residual stress stability of laser-shock peened and deep rolled austenitic stainless steel AISI 304 in the temperature range 25–600 °C*. Materials Science and Engineering: A, 2007. 465(1–2): p. 176-182.
- [72] Mhaede M, Sano Y, Altenberger I, Wagner L, *Fatigue Performance of Al7075-T73 and Ti-6Al-4V: Comparing Results after Shot Peening, Laser Shock Peening and Ball-Burnishing*. 2011.
- [73] Wagner L, Mhaede M, Wollmann M, Altenberger I, Sano Y, *Surface layer properties and fatigue behavior in Al 7075-T73 and Ti-6Al-4V: Comparing results after laser peening; shot peening and ball-burnishing*. International Journal of Structural Integrity, 2011. 2(2): p. 185-199.
- [74] Abrão A, Denkena B, Köhler J, Breidenstein B, Mörke T, *The influence of deep rolling on the surface integrity of AISI 1060 high carbon steel*. Procedia CIRP, 2014. 13: p. 31-36.
- [75] El-Khabeery MM, El-Axir MH, *Experimental techniques for studying the effects of milling roller-burnishing parameters on surface integrity*. International Journal of Machine Tools and Manufacture, 2001. 41(12): p. 1705-1719.
- [76] El-Taweel T, El-Axir M, *Analysis and optimization of the ball burnishing process through the Taguchi technique*. The International Journal of Advanced Manufacturing Technology, 2009. 41(3-4): p. 301-310.
- [77] Tsuji N, Tanaka S, Takasugi T, *Effect of combined plasma-carburizing and deep-rolling on notch fatigue property of Ti-6Al-4V alloy*. Materials Science and Engineering: A, 2009. 499(1–2): p. 482-488.
- [78] Nemat M, Lyons A, *An investigation of the surface topography of ball burnished mild steel and aluminium*. The International Journal of Advanced Manufacturing Technology, 2000. 16(7): p. 469-473.
- [79] El-Tayeb NSM, Low KO, Brevern PV, *Influence of roller burnishing contact width and burnishing orientation on surface quality and tribological behaviour of Aluminium 6061*. J. Mater. Process. Technol., 2007. 186(1–3): p. 272-278.
- [80] Revankar GD, Shetty R, Rao SS, Gaitonde VN, *Analysis of surface roughness and hardness in ball burnishing of titanium alloy*. Measurement, 2014. 58: p. 256-268.
- [81] Shirsat U, Ahuja B, *Parametric analysis of combined turning and ball burnishing process*. 2004.
- [82] Hassan AM, Maqableh AM, *The effects of initial burnishing parameters on non-ferrous components*. J. Mater. Process. Technol., 2000. 102(1): p. 115-121.
- [83] Brinksmeier E, Garbrecht M, Meyer D, *Cold surface hardening*. CIRP Annals-Manufacturing Technology, 2008. 57(1): p. 541-544.

- [84] Hassan AM, *The effects of ball- and roller-burnishing on the surface roughness and hardness of some non-ferrous metals*. J. Mater. Process. Technol., 1997. 72(3): p. 385-391.
- [85] Meyer D, *Cryogenic deep rolling—An energy based approach for enhanced cold surface hardening*. CIRP Annals-Manufacturing Technology, 2012. 61(1): p. 543-546.
- [86] Grzesik W, Żak K, *Producing high quality hardened parts using sequential hard turning and ball burnishing operations*. Precision Engineering, 2013. 37(4): p. 849-855.
- [87] Pu Z, Yang S, Song G-L, Dillon O, Puleo D, Jawahir I, *Ultrafine-grained surface layer on Mg–Al–Zn alloy produced by cryogenic burnishing for enhanced corrosion resistance*. Scripta Mater., 2011. 65(6): p. 520-523.
- [88] Huang B, Kaynak Y, Sun Y, Jawahir I, *Surface layer modification by cryogenic burnishing of Al 7050-T7451 alloy and validation with FEM-based burnishing model*. Procedia CIRP, 2015. 31: p. 1-6.
- [89] Merchant M, *An interpretive look at 20th century research on modeling of machining*. Machining Science and Technology, 1998. 2(2): p. 157-163.
- [90] Moaveni S, *Finite element analysis theory and application with ANSYS, 3/e*. 2011: Pearson Education India.
- [91] Dixit PM, Dixit US, *Modeling of metal forming and machining processes: by finite element and soft computing methods*. 2008: Springer Science & Business Media.
- [92] Arrazola PJ, Özel T, Umbrello D, Davies M, Jawahir IS, *Recent advances in modelling of metal machining processes*. CIRP Annals - Manufacturing Technology, 2013. 62(2): p. 695-718.
- [93] Brenner S, Scott R, *The mathematical theory of finite element methods*. Vol. 15. 2007: Springer Science & Business Media.
- [94] Kukielka L, *Designating the field areas for the contact of a rotary burnishing element with the rough surface of a part, providing a high-quality product*. Journal of Mechanical Working Technology, 1989. 19(3): p. 319-356.
- [95] Luo H, Liu J, Wang L, Zhong Q, *Investigation of the burnishing force during the burnishing process with a cylindrical surfaced tool*. Proceedings of the Institution of Mechanical Engineers, Part B: Journal of Engineering Manufacture, 2006. 220(6): p. 893-904.
- [96] Korzynski M, *Modeling and experimental validation of the force–surface roughness relation for smoothing burnishing with a spherical tool*. International Journal of Machine Tools and Manufacture, 2007. 47(12–13): p. 1956-1964.
- [97] Black AJ, Kopalinsky EM, Oxley PLB, *Analysis and experimental investigation of a simplified burnishing process*. International Journal of Mechanical Sciences, 1997. 39(6): p. 629-641.
- [98] Outeiro JC, Umbrello D, M'Saoubi R, Jawahir I, *Evaluation of present numerical models for predicting metal cutting performance and residual stresses*. Machining Science and Technology, 2015. 19(2): p. 183-216.
- [99] Rao JM, Reddy ACK, Rao PR, Mayuri B, *FINITE ELEMENT APPROACH FOR THE PREDICTION OF RESIDUAL STRESSES IN ALUMINUM WORK PIECES PRODUCED BY ROLLER BURNISHING*. International Journal of Design and Manufacturing Technology (IJDMT), ISSN: p. 0976-6995.

- [100] Bouzid W, Tsoumarev O, Sai K, *An investigation of surface roughness of burnished AISI 1042 steel*. The International Journal of Advanced Manufacturing Technology, 2004. 24(1-2): p. 120-125.
- [101] Maximov J, Dunchева G, *Finite element analysis and optimization of spherical motion burnishing of low-alloy steel*. Proceedings of the Institution of Mechanical Engineers, Part C: Journal of Mechanical Engineering Science, 2012. 226(1): p. 161-176.
- [102] Roettger K. Rolling Hard-Turned Surfaces, in WZL. 2002, Aachen: RWTH.
- [103] Sartkulvanich P, Altan T, Jasso F, Rodriguez C, *Finite Element Modeling of Hard Roller Burnishing: An Analysis on the Effects of Process Parameters Upon Surface Finish and Residual Stresses*. Journal of Manufacturing Science and Engineering, 2007. 129(4): p. 705-716.
- [104] Beres W, Li J, Patnaik P. *Numerical Simulation of the Low Plasticity Burnishing Process for Fatigue Property Enhancement*. in ASME Turbo Expo 2004: Power for Land, Sea, and Air. 2004. American Society of Mechanical Engineers.
- [105] Mohammadi F, Sedaghati R, Bonakdar A, *Finite element analysis and design optimization of low plasticity burnishing process*. The International Journal of Advanced Manufacturing Technology, 2014. 70(5-8): p. 1337-1354.
- [106] Klocke F, Liermann J, *Roller burnishing of hard turned surfaces*. International Journal of Machine Tools and Manufacture, 1998. 38(5): p. 419-423.
- [107] Balland P, Tabourot L, Degre F, Moreau V, *Mechanics of the burnishing process*. Precision Engineering, 2013. 37(1): p. 129-134.
- [108] Zhuang W, Wicks B, *Multipass low-plasticity burnishing induced residual stresses: three-dimensional elastic-plastic finite element modelling*. Proceedings of the Institution of Mechanical Engineers, Part C: Journal of Mechanical Engineering Science, 2004. 218(6): p. 663-668.
- [109] Sayahi M, Sghaier S, Belhadjsalah H, *Finite element analysis of ball burnishing process: comparisons between numerical results and experiments*. The International Journal of Advanced Manufacturing Technology, 2013. 67(5-8): p. 1665-1673.
- [110] Huang B, Kaynak Y, Sun Y, Jawahir IS, *Surface Layer Modification by Cryogenic Burnishing of Al 7050-T7451 Alloy and Validation with FEM-based Burnishing Model*. Procedia CIRP, 2015. 31: p. 1-6.
- [111] Yen YC, Sartkulvanich P, Altan T, *Finite Element Modeling of Roller Burnishing Process*. CIRP Annals - Manufacturing Technology, 2005. 54(1): p. 237-240.
- [112] Froes FH, Eylon D, Bomberger H, *Titanium technology: present status and future trends*. Titanium Development Association, 1985, 1985: p. 191.
- [113] Némat M, Lyons CA, *An Investigation of the Surface Topography of Ball Burnished Mild Steel and Aluminium*. The International Journal of Advanced Manufacturing Technology. 16(7): p. 469-473.
- [114] Lin YC, Wang SW, Lai H-Y, *The relationship between surface roughness and burnishing factor in the burnishing process*. The International Journal of Advanced Manufacturing Technology, 2004. 23(9): p. 666-671.
- [115] Yeldose BC, Ramamoorthy B, *An investigation into the high performance of TiN-coated rollers in burnishing process*. J. Mater. Process. Technol., 2008. 207(1-3): p. 350-355.

- [116] Hassan AM, *The effects of ball-and roller-burnishing on the surface roughness and hardness of some non-ferrous metals*. J. Mater. Process. Technol., 1997. 72(3): p. 385-391.
- [117] El-Axir M, Othman O, Abodiena A, *Study on the inner surface finishing of aluminum alloy 2014 by ball burnishing process*. J. Mater. Process. Technol., 2008. 202(1-3): p. 435-442.
- [118] Sun H, Shi Y-N, Zhang M-X, Lu K, *Plastic strain-induced grain refinement in the nanometer scale in a Mg alloy*. Acta Mater., 2007. 55(3): p. 975-982.
- [119] Sakai T, Belyakov A, Kaibyshev R, Miura H, Jonas JJ, *Dynamic and post-dynamic recrystallization under hot, cold and severe plastic deformation conditions*. Prog. Mater. Sci., 2014. 60: p. 130-207.
- [120] Hardwick D, Tegart WM, *Structural changes during the deformation of copper, aluminium and nickel at high temperatures and high strain rates*. J Inst Met, 1961. 90: p. 17-21.
- [121] Jonas J, Sellars C, Tegart WM, *Strength and structure under hot-working conditions*. Metallurgical Reviews, 1969. 14(1): p. 1-24.
- [122] McQueen H, Jonas J, *Recovery and recrystallization during high temperature deformation*, in *Treatise on Materials Science & Technology*. 1975, Elsevier. p. 393-493.
- [123] Mishra A, Kad B, Gregori F, Meyers M, *Microstructural evolution in copper subjected to severe plastic deformation: Experiments and analysis*. Acta Mater., 2007. 55(1): p. 13-28.
- [124] Yang S, Dillon OW, Puleo DA, Jawahir IS, *Effect of cryogenic burnishing on surface integrity modifications of Co-Cr-Mo biomedical alloy*. Journal of Biomedical Materials Research Part B: Applied Biomaterials, 2013. 101(1): p. 139-152.
- [125] Pu Z, Yang S, Song GL, Dillon Jr OW, Puleo DA, Jawahir IS, *Ultrafine-grained surface layer on Mg-Al-Zn alloy produced by cryogenic burnishing for enhanced corrosion resistance*. Scripta Mater., 2011. 65(6): p. 520-523.
- [126] Nalla RK, Altenberger I, Noster U, Liu GY, Scholtes B, Ritchie RO, *On the influence of mechanical surface treatments—deep rolling and laser shock peening—on the fatigue behavior of Ti-6Al-4V at ambient and elevated temperatures*. Materials Science and Engineering: A, 2003. 355(1-2): p. 216-230.
- [127] Zhu YT, Langdon TG, *Influence of grain size on deformation mechanisms: An extension to nanocrystalline materials*. Materials Science and Engineering: A, 2005. 409(1-2): p. 234-242.
- [128] Wang Y, Ma E, Valiev RZ, Zhu Y, *Tough nanostructured metals at cryogenic temperatures*. Adv. Mater., 2004. 16(4): p. 328-331.
- [129] Wei Q, Cheng S, Ramesh K, Ma E, *Effect of nanocrystalline and ultrafine grain sizes on the strain rate sensitivity and activation volume: fcc versus bcc metals*. Materials Science and Engineering: A, 2004. 381(1-2): p. 71-79.
- [130] Zehetbauer MJ, Valiev RZ, *Nanomaterials by severe plastic deformation*. 2006: John Wiley & Sons.
- [131] Li R, Riester L, Watkins TR, Blau PJ, Shih AJ, *Metallurgical analysis and nanoindentation characterization of Ti-6Al-4V workpiece and chips in high-*

- throughput drilling*. Materials Science and Engineering: A, 2008. 472(1-2): p. 115-124.
- [132] Dhananchezian M, Rajadurai A, *Experimental investigation of cryogenic cooling by liquid nitrogen in the orthogonal machining process*. International Journal of Recent Trends in Engineering, 2009. 1(5): p. 55.
- [133] Kitagawa T, Kubo A, Maekawa K, *Temperature and wear of cutting tools in high-speed machining of Inconel 718 and Ti · 6Al · 6V · 2Sn*. Wear, 1997. 202(2): p. 142-148.
- [134] Bordin A, Imbrogno S, Rotella G, Bruschi S, Ghiotti A, Umbrello D, *Finite element simulation of semi-finishing turning of electron beam melted Ti6Al4V under dry and cryogenic cooling*. Procedia CIRP, 2015. 31: p. 551-556.
- [135] Bordin A, Bruschi S, Ghiotti A, Bariani PF, *Analysis of tool wear in cryogenic machining of additive manufactured Ti6Al4V alloy*. Wear, 2015. 328-329: p. 89-99.
- [136] Rotella G, Umbrello D, *Finite element modeling of microstructural changes in dry and cryogenic cutting of Ti6Al4V alloy*. CIRP Annals, 2014. 63(1): p. 69-72.
- [137] Imbrogno S, Sartori S, Bordin A, Bruschi S, Umbrello D, *Machining simulation of Ti6Al4V under dry and cryogenic conditions*. Procedia CIRP, 2017. 58: p. 475-480.
- [138] V11.2 S-D. DEFORM, User Manual. 2018, Scientific Forming Technologies Corporation Ed.: Columbus, OH, USA.
- [139] Filice L, Micari F, Rizzuti S, Umbrello D, *A critical analysis on the friction modelling in orthogonal machining*. International Journal of Machine Tools and Manufacture, 2007. 47(3-4): p. 709-714.
- [140] Pu Z, Umbrello D, Dillon OW, Lu T, Puleo DA, Jawahir IS, *Finite element modeling of microstructural changes in dry and cryogenic machining of AZ31B magnesium alloy*. Journal of Manufacturing Processes, 2014. 16(2): p. 335-343.
- [141] Sun Y, Huang B, Puleo D, Jawahir I, *Enhanced machinability of Ti-5553 alloy from cryogenic machining: comparison with MQL and flood-cooled machining and modeling*. Procedia CIRP, 2015. 31: p. 477-482.
- [142] Mondelin A, Claudin C, Rech J, Dumont F, *Effects of lubrication mode on friction and heat partition coefficients at the tool-work material interface in machining*. Tribology Transactions, 2011. 54(2): p. 247-255.
- [143] Hong SY, Ding Y, *Cooling approaches and cutting temperatures in cryogenic machining of Ti-6Al-4V*. International Journal of Machine Tools and Manufacture, 2001. 41(10): p. 1417-1437.
- [144] Dhananchezian M, Pradeep Kumar M, *Cryogenic turning of the Ti-6Al-4V alloy with modified cutting tool inserts*. Cryogenics, 2011. 51(1): p. 34-40.
- [145] Umbrello D, *Finite element simulation of conventional and high speed machining of Ti6Al4V alloy*. J. Mater. Process. Technol., 2008. 196(1-3): p. 79-87.
- [146] Lee W-S, Lin C-F, *Plastic deformation and fracture behaviour of Ti-6Al-4V alloy loaded with high strain rate under various temperatures*. Materials Science and Engineering: A, 1998. 241(1): p. 48-59.
- [147] Davies E, Hunter S, *The dynamic compression testing of solids by the method of the split Hopkinson pressure bar*. Journal of the Mechanics and Physics of Solids, 1963. 11(3): p. 155-179.

- [148] Seo S, Min O, Yang H, *Constitutive equation for Ti–6Al–4V at high temperatures measured using the SHPB technique*. International journal of impact engineering, 2005. 31(6): p. 735-754.
- [149] Lesuer D, *Experimental investigation of material models for Ti-6Al-4V and 2024-T3*. Livermore: University of California, Lawrence Livermore National Laboratory, 1999: p. 1-36.
- [150] Peirs J, Verleysen P, Degrieck J, Coghe F, *The use of hat-shaped specimens to study the high strain rate shear behaviour of Ti–6Al–4V*. International Journal of Impact Engineering, 2010. 37(6): p. 703-714.
- [151] Liu X, Tan C, Zhang J, Hu Y, Ma H, Wang F, Cai H, *Influence of microstructure and strain rate on adiabatic shearing behavior in Ti–6Al–4V alloys*. Materials Science and Engineering: A, 2009. 501(1-2): p. 30-36.
- [152] Cook W. *A constitutive model and data for metals subjected to large strains, high strain rates and high temperatures*. in *Proceedings of the seventh international symposium on ballistics, Hague*. 1983.
- [153] Zhang Y, Outeiro J, Mabrouki T, *On the selection of Johnson-Cook constitutive model parameters for Ti-6Al-4 V using three types of numerical models of orthogonal cutting*. Procedia CIRP, 2015. 31: p. 112-117.
- [154] Sima M, Özel T, *Modified material constitutive models for serrated chip formation simulations and experimental validation in machining of titanium alloy Ti–6Al–4V*. International Journal of Machine Tools and Manufacture, 2010. 50(11): p. 943-960.
- [155] Chen G, Ren C, Yang X, Jin X, Guo T, *Finite element simulation of high-speed machining of titanium alloy (Ti–6Al–4V) based on ductile failure model*. The International Journal of Advanced Manufacturing Technology, 2011. 56(9): p. 1027-1038.
- [156] Calamaz M, Coupard D, Girod F, *A new material model for 2D numerical simulation of serrated chip formation when machining titanium alloy Ti–6Al–4V*. International Journal of Machine Tools and Manufacture, 2008. 48(3-4): p. 275-288.
- [157] Kassner M, Wang M, Perez-Prado M-T, Alhajeri S, *Large-strain softening of aluminum in shear at elevated temperature*. Metallurgical and Materials Transactions A, 2002. 33(10): p. 3145-3153.
- [158] Jin T, Hong J-p, Zheng H, Tang K, Gan Z-h, *Measurement of boiling heat transfer coefficient in liquid nitrogen bath by inverse heat conduction method*. Journal of Zhejiang University-SCIENCE A, 2009. 10(5): p. 691-696.
- [159] Yang S, *Cryogenic burnishing of Co-Cr-Mo biomedical alloy for enhanced surface integrity and improved wear performance* Theses and Dissertations--Mechanical Engineering, 2012. Paper 10.
- [160] Pu Z, Umbrello D, Dillon Jr O, Lu T, Puleo D, Jawahir I, *Finite element modeling of microstructural changes in dry and cryogenic machining of AZ31B magnesium alloy*. Journal of Manufacturing Processes, 2014. 16(2): p. 335-343.
- [161] Rotella G, Umbrello D. *Numerical simulation of surface modification in dry and cryogenic machining of AA7075 alloy*. in *2nd CIRP Conference on Surface Integrity, CSI 2014, May 28, 2014 - May 30, 2014*. 2014. Nottingham, United kingdom: Elsevier.

- [162] Rotella G, Umbrello D, *Finite element modeling of microstructural changes in dry and cryogenic cutting of Ti6Al4V alloy*. CIRP Annals - Manufacturing Technology, 2014. 63(1): p. 69-72.
- [163] Dix M, Wertheim R, Schmidt G, Hochmuth C, *Modeling of drilling assisted by cryogenic cooling for higher efficiency*. CIRP Annals, 2014. 63(1): p. 73-76.
- [164] Kheireddine A, Ammouri A, Lu T, Dillon O, Hamade R, Jawahir I, *An experimental and numerical study of the effect of cryogenic cooling on the surface integrity of drilled holes in AZ31B Mg alloy*. The International Journal of Advanced Manufacturing Technology, 2015. 78(1-4): p. 269-279.
- [165] Danish M, Ginta TL, Habib K, Carou D, Rani AMA, Saha BB, *Thermal analysis during turning of AZ31 magnesium alloy under dry and cryogenic conditions*. The International Journal of Advanced Manufacturing Technology, 2017. 91(5-8): p. 2855-2868.
- [166] Weisend JG, Weisend J, *Handbook of cryogenic engineering*. Vol. 325. 1998: Taylor & Francis Philadelphia, PA.
- [167] Hong SY. *Advancement of economical cryogenic machining technology*. in *Proceedings of 3rd International Conference on Manufacturing*. 1995.
- [168] Pusavec F, Lu T, Courbon C, Rech J, Aljancic U, Kopac J, Jawahir IS, *Analysis of the influence of nitrogen phase and surface heat transfer coefficient on cryogenic machining performance*. J. Mater. Process. Technol., 2016. 233: p. 19-28.
- [169] Hribersek M, Sajn V, Pusavec F, Rech J, Kopac J, *The Procedure of Solving the Inverse Problem for Determining Surface Heat Transfer Coefficient between Liquefied Nitrogen and Inconel 718 Workpiece in Cryogenic Machining*. Procedia CIRP, 2017. 58: p. 617-622.
- [170] Ozisik MN, *Inverse heat transfer: fundamentals and applications*. 2018: Routledge.
- [171] Chen S-J, Tseng AA, *Spray and jet cooling in steel rolling*. Int. J. Heat Fluid Flow, 1992. 13(4): p. 358-369.
- [172] Jawahir I, Brinksmeier E, M'saoubi R, Aspinwall D, Outeiro J, Meyer D, Umbrello D, Jayal A, *Surface integrity in material removal processes: Recent advances*. CIRP Annals-Manufacturing Technology, 2011. 60(2): p. 603-626.
- [173] Wang Q, Liu Z, Wang B, Song Q, Wan Y, *Evolutions of grain size and micro-hardness during chip formation and machined surface generation for Ti-6Al-4V in high-speed machining*. The International Journal of Advanced Manufacturing Technology, 2016. 82(9-12): p. 1725-1736.
- [174] Arısoy YM, Özel T, *Prediction of machining induced microstructure in Ti-6Al-4V alloy using 3-D FE-based simulations: Effects of tool micro-geometry, coating and cutting conditions*. J. Mater. Process. Technol., 2015. 220: p. 1-26.
- [175] Pan Z, Liang SY, Garmestani H, Shih DS, *Prediction of machining-induced phase transformation and grain growth of Ti-6Al-4 V alloy*. The International Journal of Advanced Manufacturing Technology, 2016. 87(1-4): p. 859-866.
- [176] Kim JH, Semiatin S, Lee YH, Lee CS, *A self-consistent approach for modeling the flow behavior of the alpha and beta phases in Ti-6Al-4V*. Metallurgical and Materials Transactions A, 2011. 42(7): p. 1805-1814.
- [177] Fanfoni M, Tomellini M, *The johnson-mehl-avrami-kohnogorov model: a brief review*. Il Nuovo Cimento D, 1998. 20(7-8): p. 1171-1182.

- [178] Chang C, Lee C, Huang J, *Relationship between grain size and Zener–Holloman parameter during friction stir processing in AZ31 Mg alloys*. Scripta Mater., 2004. 51(6): p. 509-514.
- [179] Momeni A, Abbasi S, *Effect of hot working on flow behavior of Ti–6Al–4V alloy in single phase and two phase regions*. Materials & Design, 2010. 31(8): p. 3599-3604.
- [180] Seshacharyulu T, Medeiros S, Frazier W, Prasad Y, *Microstructural mechanisms during hot working of commercial grade Ti–6Al–4V with lamellar starting structure*. Materials Science and Engineering: A, 2002. 325(1-2): p. 112-125.
- [181] Bruschi S, Poggio S, Quadrini F, Tata M, *Workability of Ti–6Al–4V alloy at high temperatures and strain rates*. Mater. Lett., 2004. 58(27-28): p. 3622-3629.
- [182] Ding R, Guo Z, Wilson A, *Microstructural evolution of a Ti–6Al–4V alloy during thermomechanical processing*. Materials Science and Engineering: A, 2002. 327(2): p. 233-245.
- [183] Yi Y-p, Fu X, Cui J-d, Chen H, *Prediction of grain size for large-sized aluminium alloy 7050 forging during hot forming*. Journal of Central South University of Technology, 2008. 15(1): p. 1-5.
- [184] Hughes G, Smith S, Pande C, Johnson H, Armstrong R, *Hall-Petch strengthening for the microhardness of twelve nanometer grain diameter electrodeposited nickel*. Scripta Metallurgica, 1986. 20(1): p. 93-97.
- [185] Bermingham MJ, Kirsch J, Sun S, Palanisamy S, Dargusch MS, *New observations on tool life, cutting forces and chip morphology in cryogenic machining Ti-6Al-4V*. International Journal of Machine Tools and Manufacture, 2011. 51(6): p. 500-511.
- [186] Strano M, Chiappini E, Tirelli S, Albertelli P, Monno M, *Comparison of Ti6Al4V machining forces and tool life for cryogenic versus conventional cooling*. Proceedings of the Institution of Mechanical Engineers, Part B: Journal of Engineering Manufacture, 2013. 227(9): p. 1403-1408.
- [187] Stenberg N, Proudian J, *Numerical Modelling of Turning to Find Residual Stresses*. Procedia CIRP, 2013. 8: p. 258-264.
- [188] Umbrello D, Outeiro J, M'saoubi R, Jayal A, Jawahir I, *A numerical model incorporating the microstructure alteration for predicting residual stresses in hard machining of AISI 52100 steel*. CIRP annals, 2010. 59(1): p. 113-116.
- [189] Outeiro JC, Umbrello D, M'Saoubi R, *Experimental and numerical modelling of the residual stresses induced in orthogonal cutting of AISI 316L steel*. International Journal of Machine Tools and Manufacture, 2006. 46(14): p. 1786-1794.
- [190] Yen YC, Sartkulvanich P, Altan T, *Finite Element Modeling of Roller Burnishing Process*. CIRP Annals, 2005. 54(1): p. 237-240.
- [191] Lim A, Castagne S, Cher Wong C, *Effect of Deep Cold Rolling on Residual Stress Distributions Between the Treated and Untreated Regions on Ti–6Al–4V Alloy*. Journal of Manufacturing Science and Engineering, 2016. 138(11): p. 111005-111005-111008.
- [192] Sai WB, Sai K, *Finite element modeling of burnishing of AISI 1042 steel*. The International Journal of Advanced Manufacturing Technology, 2005. 25(5-6): p. 460-465.

- [193] Ladous DA, Apelian D, *The effect of residual stress on the fatigue crack growth behavior of Al-Si-Mg cast alloys—Mechanisms and corrective mathematical models*. Metallurgical and Materials Transactions A, 2006. 37(1): p. 133-145.
- [194] Niku-Lari A, Lu J, Flavenot JF, *Measurement of residual-stress distribution by the incremental hole-drilling method*. Exp Mech, 1985. 25(2): p. 175-185.
- [195] Okushima K, Kakino Y, *Study of the residual stress produced by metal cutting*. Mem. Fac. Eng. Kyoto Univ., 1972. 34(2): p. 234-248.
- [196] M'saoubi R, Outeiro J, Changeux B, Lebrun J, Dias AM, *Residual stress analysis in orthogonal machining of standard and resulfurized AISI 316L steels*. J. Mater. Process. Technol., 1999. 96(1-3): p. 225-233.
- [197] Jacobus K, DeVor R, Kapoor S, *Machining-induced residual stress: experimentation and modeling*. Journal of Manufacturing Science and Engineering, 2000. 122(1): p. 20-31.
- [198] Withers PJ, Bhadeshia H, *Residual stress. Part 1—measurement techniques*. Mater. Sci. Technol., 2001. 17(4): p. 355-365.
- [199] Fitzpatrick M, Fry A, Holdway P, Kandil F, Shackleton J, Suominen L, *Measurement good practice guide No. 52. Determination of residual stresses by X-ray diffraction*, 2005(2): p. 6.
- [200] Moore M, Evans W, *Mathematical correction for stress in removed layers in X-ray diffraction residual stress analysis*. SAE transactions, 1958: p. 340-345.
- [201] Prevey PS, *X-ray diffraction residual stress techniques*. ASM International, ASM Handbook., 1986. 10: p. 380-392.
- [202] Nasr MN, Ng E-G, Elbestawi M, *Modelling the effects of tool-edge radius on residual stresses when orthogonal cutting AISI 316L*. International Journal of Machine Tools and Manufacture, 2007. 47(2): p. 401-411.
- [203] Sharman A, Hughes J, Ridgway K, *The effect of tool nose radius on surface integrity and residual stresses when turning Inconel 718™*. J. Mater. Process. Technol., 2015. 216: p. 123-132.
- [204] Thiele JD, Melkote SN, Peascoe RA, Watkins TR, *Effect of cutting-edge geometry and workpiece hardness on surface residual stresses in finish hard turning of AISI 52100 steel*. Journal of Manufacturing Science and Engineering, 2000. 122(4): p. 642-649.
- [205] Jang D, Watkins T, Kozaczek K, Hubbard C, Cavin O, *Surface residual stresses in machined austenitic stainless steel*. Wear, 1996. 194(1-2): p. 168-173.
- [206] Kishawy H, *An experimental evaluation of cutting temperatures during high speed machining of hardened D2 tool steel*. 2002.
- [207] Wyen C-F, Wegener K, *Influence of cutting edge radius on cutting forces in machining titanium*. CIRP annals, 2010. 59(1): p. 93-96.
- [208] Wyen C-F, Jaeger D, Wegener K, *Influence of cutting edge radius on surface integrity and burr formation in milling titanium*. The International Journal of Advanced Manufacturing Technology, 2013. 67(1-4): p. 589-599.
- [209] Morikage Y, Igi S, Oi K, Jo Y, Murakami K, Gotoh K, *Effect of Compressive Residual Stress on Fatigue Crack Propagation*. Procedia Engineering, 2015. 130: p. 1057-1065.

- [210] Nikitin I, Scholtes B, Maier HJ, Altenberger I, *High temperature fatigue behavior and residual stress stability of laser-shock peened and deep rolled austenitic steel AISI 304*. Scripta Mater., 2004. 50(10): p. 1345-1350.
- [211] Roland T, Retraint D, Lu K, Lu J, *Fatigue life improvement through surface nanostructuring of stainless steel by means of surface mechanical attrition treatment*. Scripta Mater., 2006. 54(11): p. 1949-1954.
- [212] Suresh S, *Fatigue of materials (Cambridge solid state science series)*. Cambridge: Press Syndicate of the University of Cambridge, 1991.
- [213] Webster GA, Ezeilo AN, *Residual stress distributions and their influence on fatigue lifetimes*. Int. J. Fatigue, 2001. 23: p. 375-383.
- [214] Zhu L, Jia M-P, *A new approach for the influence of residual stress on fatigue crack propagation*. Results in Physics, 2017. 7: p. 2204-2212.
- [215] Kobayashi M, Matsui T, Murakami Y, *Mechanism of creation of compressive residual stress by shot peening*. Int. J. Fatigue, 1998. 20(5): p. 351-357.
- [216] Torres M, Voorwald H, *An evaluation of shot peening, residual stress and stress relaxation on the fatigue life of AISI 4340 steel*. Int. J. Fatigue, 2002. 24(8): p. 877-886.
- [217] Novovic D, Dewes R, Aspinwall D, Voice W, Bowen P, *The effect of machined topography and integrity on fatigue life*. International Journal of Machine Tools and Manufacture, 2004. 44(2-3): p. 125-134.
- [218] Lai J, Huang H, Buising W, *Effects of microstructure and surface roughness on the fatigue strength of high-strength steels*. Procedia Structural Integrity, 2016. 2: p. 1213-1220.
- [219] Lin Y, Wang S, Lai H-Y, *The relationship between surface roughness and burnishing factor in the burnishing process*. The International Journal of Advanced Manufacturing Technology, 2004. 23(9-10): p. 666-671.
- [220] Altenberger I, Stach E, Liu G, Nalla R, Ritchie R, *An in situ transmission electron microscope study of the thermal stability of near-surface microstructures induced by deep rolling and laser-shock peening*. Scripta Mater., 2003. 48(12): p. 1593-1598.
- [221] Liu YG, Li MQ, Liu HJ, *Nanostructure and surface roughness in the processed surface layer of Ti-6Al-4V via shot peening*. Mater. Charact., 2017. 123: p. 83-90.
- [222] Nicholas T, Zuiker J, *On the use of the Goodman diagram for high cycle fatigue design*. International Journal of Fracture, 1996. 80(2-3): p. 219-235.
- [223] Cowles B, *High cycle fatigue in aircraft gas turbines—an industry perspective*. International Journal of Fracture, 1996. 80(2-3): p. 147-163.
- [224] Miller KJ, *The three thresholds for fatigue crack propagation*, in *Fatigue and Fracture Mechanics: 27th volume*. 1997, ASTM International.
- [225] Withers P, *Residual stress and its role in failure*. Rep. Prog. Phys., 2007. 70(12): p. 2211.
- [226] Farahmand B, *Fracture mechanics of metals, composites, welds, and bolted joints: application of LEFM, EPFM, and FMDM theory*. 2012: Springer Science & Business Media.
- [227] Parker A, *Stress intensity factors, crack profiles, and fatigue crack growth rates in residual stress fields*, in *Residual stress effects in fatigue*. 1982, ASTM International.

- [228] John R, Jata K, Sadananda K, *Residual stress effects on near-threshold fatigue crack growth in friction stir welds in aerospace alloys*. Int. J. Fatigue, 2003. 25(9-11): p. 939-948.
- [229] Paris P, Erdogan F, *A critical analysis of crack propagation laws*. Journal of basic engineering, 1963. 85(4): p. 528-533.
- [230] Thompson SR, Ruschau JJ, Nicholas T, *Influence of residual stresses on high cycle fatigue strength of Ti-6Al-4V subjected to foreign object damage*. Int. J. Fatigue, 2001. 23: p. 405-412.
- [231] LaRue J, Daniewicz S, *Predicting the effect of residual stress on fatigue crack growth*. Int. J. Fatigue, 2007. 29(3): p. 508-515.
- [232] Ruschau JJ, John R, Thompson SR, Nicholas T, *Fatigue crack nucleation and growth rate behavior of laser shock peened titanium*. Int. J. Fatigue, 1999. 21: p. S199-S209.
- [233] Zhou Z, Bhamare S, Ramakrishnan G, Mannava SR, Langer K, Wen Y, Qian D, Vasudevan VK, *Thermal relaxation of residual stress in laser shock peened Ti-6Al-4V alloy*. Surf. Coat. Technol., 2012. 206(22): p. 4619-4627.
- [234] Maawad E, Sano Y, Wagner L, Brokmeier H-G, Genzel C, *Investigation of laser shock peening effects on residual stress state and fatigue performance of titanium alloys*. Materials Science and Engineering: A, 2012. 536: p. 82-91.
- [235] Nikitin I, Besel M, *Residual stress relaxation of deep-rolled austenitic steel*. Scripta Mater., 2008. 58(3): p. 239-242.
- [236] Boyce BL, Chen X, Peters JO, Hutchinson JW, Ritchie RO, *Mechanical relaxation of localized residual stresses associated with foreign object damage*. Materials Science and Engineering: A, 2003. 349(1-2): p. 48-58.
- [237] Atzeni E, Salmi A, *Economics of additive manufacturing for end-usable metal parts*. The International Journal of Advanced Manufacturing Technology, 2012. 62(9): p. 1147-1155.
- [238] Campbell T, Williams C, Ivanova O, Garrett B, *Could 3D printing change the world*. Technologies, Potential, and Implications of Additive Manufacturing, Atlantic Council, Washington, DC, 2011.
- [239] Frazier WE, *Metal Additive Manufacturing: A Review*. J. Mater. Eng. Perform., 2014. 23(6): p. 1917-1928.
- [240] Zhai Y, Lados DA, LaGoy JL, *Additive manufacturing: making imagination the major limitation*. JOM, 2014. 66(5): p. 808-816.

VITA

James Robert Caudill received his Bachelor of Science in Mechanical Engineering from the University of Kentucky in 2013. Upon graduation he joined the research team headed by Dr. I.S. Jawahir of the Institute for Sustainable manufacturing (ISM) at the University of Kentucky, while pursuing a PhD in Mechanical Engineering. He was the lead researcher in two major research projects. The first was in partnership with GE Aviation, tasked with exploring the process-induced surface integrity of burnished titanium alloy *Ti-6Al-4V*. The second was in partnership with Lightweight Innovations for Tomorrow (LIFT), examining the impact of cryogenic cooling on material removal rates in high speed machining of *Ti-6Al-4V* alloy. His research is focused on sustainable manufacturing processes, such as cryogenic and hybrid processing of difficult-to-cut materials, as well as analytical and numerical (FEM) modelling of high speed machining and burnishing processes.

LIST OF PUBLICATIONS

Published Journal Paper

Caudill J, Schoop J, Jawahir I, *Correlation of surface integrity with processing parameters and advanced interface cooling/lubrication in burnishing of Ti-6Al-4V alloy*. Advances in Materials and Processing Technologies, 2018: p. 1-14

Accepted Journal Paper

Uysal A, Caudill, J., Schoop, J., I.S. Jawahir, *Minimizing carbon emissions and machining costs with improved human health in sustainable machining of austenitic stainless steel through multi-objective optimization* IJSM Special Edition, 2019.

Upcoming Journal Papers

Caudill J., Jawahir, I.S. . *Thermally Stable Nanocrystalline Surface Layers and Residual Stress Fields in Cryogenic Multipass Burnishing of Ti-6Al-4V*.

Caudill, J., Chen, G., Schoop, J., Jawahir, I.S. *Impact of Cutting Edge Radius on Residual Stress Fields in Cryogenic Turning of Ti-6Al-4V Alloy*.

Caudill, J., Jawahir, I.S. *Numerical Modeling of Surface Integrity in High Speed End Milling of Ti-6Al-4V Alloy*. *Advances in Materials and Processing Technologies*

Conference Papers

Caudill J, Huang B, Arvin C, Schoop J, Meyer K, Jawahir I, *Enhancing the surface integrity of Ti-6Al-4V alloy through cryogenic burnishing*. *Procedia CIRP*, 2014. 13: p. 243-248. (Published)

Caudill J, I.S. Jawahir. *Multipass Cryogenic Burnishing of Ti-6Al-4V Alloy for Improved Surface Integrity in Aerospace Components*, in *AMPT 2016*. 2017. (Published) (Keynote)

Chen G, Chen, S., Caudill, J., I.S. Jawahir. *Effect of Cutting Edge Radius and Cooling Strategies on surface integrity in orthogonal machining of Ti-6Al-4V alloy*, in *Procedia CIRP*. 2019. (Accepted)

Caudill J, Schoop, J., I.S. Jawahir. *Numerical Modelling of Cutting Forces and Temperature Distribution in High Speed Cryogenic and Flood-cooled Milling of Ti-6Al-4V*, in *Procedia CIRP*. 2019. (Accepted)

Caudill J, Schoop, J., I.S. Jawahir. *Producing Sustainable Nanostructures in Ti-6Al-4V Alloys for Improved Surface Integrity and Functional Performance in Aerospace Applications*, in *26th CIRP Life Cycle Engineering Conference*. (Accepted)